Geographia Technica

Geographia Technica

Technical Geography

an International Journal for the Progress of Scientific Geography

2020 – No. 2

Cluj University Press

C o n t e n t s

Geographia Technica

APPLICATION OF ANFIS TECHNIQUE FOR PREDICTION OF RAINFALL IN THE SOUTH TANGERANG CITY

Wayan SUPARTA[1]* , RESDIANSYAH[2] and Safitri JAYA[3]

ABSTRACT:
Flood phenomenon is an annual scourge that often occurs at several critical points in the territory of Indonesia, one of which is in the South Tangerang City, Banten. This paper aims to predict rainfall as an early detection model by exploring the application of artificial intelligence techniques such as the Adaptive Neuro-Fuzzy Inference System (ANFIS). The proposed technique was built with various input structures and membership functions, then trained and tested to evaluate its capabilities. Daily meteorological data such as relative humidity, temperature, and partial pressure of water vapour are chosen as intermediate parameters to predict rainfall. While rainfall measurement data is used as a comparison or validation. By analysing the three scenarios that have been carried out, it was found that rainfall can be estimated well. The prediction results with ANFIS Fuzzy-C-Means (FCM) algorithm are promising to detect floods that can later be integrated with more complex systems, especially types of floods at various points in the City of South Tangerang and surrounding areas.

Key-words: *ANFIS, Rainfall, Urban Floods, South Tangerang City.*

1. INTRODUCTION

Indonesia is clearly a country with a disaster-prone zone, starting from floods, landslides, earthquakes to tsunamis. With a remarkable tropical climate where the country tends to be hot, the temperature is not the main parameter of climate in this country. In other words, rainfall plays an important role in climate change, especially during the rainy season, where rainfall occurs quite high in each year. The rainy season usually triggers frequent of a natural disaster such as landslides and floods. Floods can be caused by various factors such as the condition of the catchment area, rain duration and intensity, land cover, topographic conditions, and drainage network capacity (Ghazavi et al., 2016; Fujiki and Renard, 2018). While the basic factor of a disaster is the result of climate change. Among the types of floods that are very upsetting besides flash floods are urban floods, where people's lands have now shifted to various types of new housing.

Based on flood forecasts in Indonesia, December, January and February throughout the year are potentially high flood months. Similar to neighboring cities like Jakarta, the South Tangerang is also no exception to this flood phenomenon. The South Tangerang City is located in the eastern part of Banten Province, at the coordinates of 106°38"- 106°47"E and 06°13'30" - 06°22'30"S. Most of this area is lowland and has a relatively flat topography with a slope of 0 - 3% (average) while the altitude of the region is between 0-25 m above sea level. Looked from the climate condition, the intensity of the sun is around 50% and the highest rainfall (December - January) is reaching 264.4 mm. Until 2019, there are 13 locations are regularly subscribed to flooding because of inadequate drainage (Kompas, 2018). The Ciputat Block is the most flood point and other areas adjacent to the Universitas Pembangunan Jaya (UPJ) are Jombang and Cantiga Blocks.

With the above climatic and topographic conditions, the development of an early warning system (EWS) that can provide fast, accurate, targeted, easily accepted and understood, reliable and sustainable information is indispensable. The previous system was works by measuring the water

---

[1,3]*Universitas Pembangunan Jaya, Department of Informatics, South Tangerang City, Banten 15413, Indonesia, Corresponding author: wayan.suparta@upj.ac.id, safitri.jaya@upj.ac.id*

[2] *Universitas Pembangunan Jaya, Department of Civil Engineering, South Tangerang City, Banten 15413, Indonesia, resdiansyah.mansyur@upj.ac.id.*

level in the river and then classified according to the danger level. The disadvantage of this system is that new flooding can be predicted if the river's water level is at an almost overflowing height. This causes the warning given too short and the community does not have time to prepare self-preservation. In addition, the existing monitoring system in this region cannot be recorded automatically so that long-term historical data cannot be utilized for the benefit of future investigations. In this study, a softcomputing method will be proposed with consideration of low costs, easy to analyze and still have good accuracy. One form of hybrid softcomputing technique to be developed is an Adaptive Neuro Fuzzy Inference System (ANFIS) model. ANFIS is a combination of fuzzy logic and artificial neural networks. Exploration of the ANFIS model in this study is expected to predict flooding.

ANFIS model has been proposed to develop a forecasting seasonal rainfall in Victoria of southern Australia to anticipate floods (Mekanik et al., 2015) and for spatial flood predictions such as Hong et al. (2017) and Bui et al. (2018). However, the model applied is also very dependent on regional characteristics. The purpose of this study is to predict urban flood trough rainfall parameter using ANFIS. These urban floods become a driver in the development of a softcomputing in order to improve the accuracy of the flood early detection system. The focus of research is to obtain the capability of the models built to predict future flooding based on the data that has been trained. The data collected will also be analyzed to carry out patterns and flood trends. For preliminary investigation, rainfall in the South Tangerang City will be used as a testing model (training and validation). The model developed will help provide alternative prediction in anticipating floods that can be used as references by decision makers in flood mitigation and educate the public or users with the aim of providing early weather warnings, especially related to flooding.

2. METHODS

2.1. Dataset and location

A number of measurement data is collected to support the study. The primary data are obtained from Indonesia Agency for Meteorology, Climatology and Geophysics or BMKG (*Badan Meteorologi, Klimatologi dan Geofisika*).
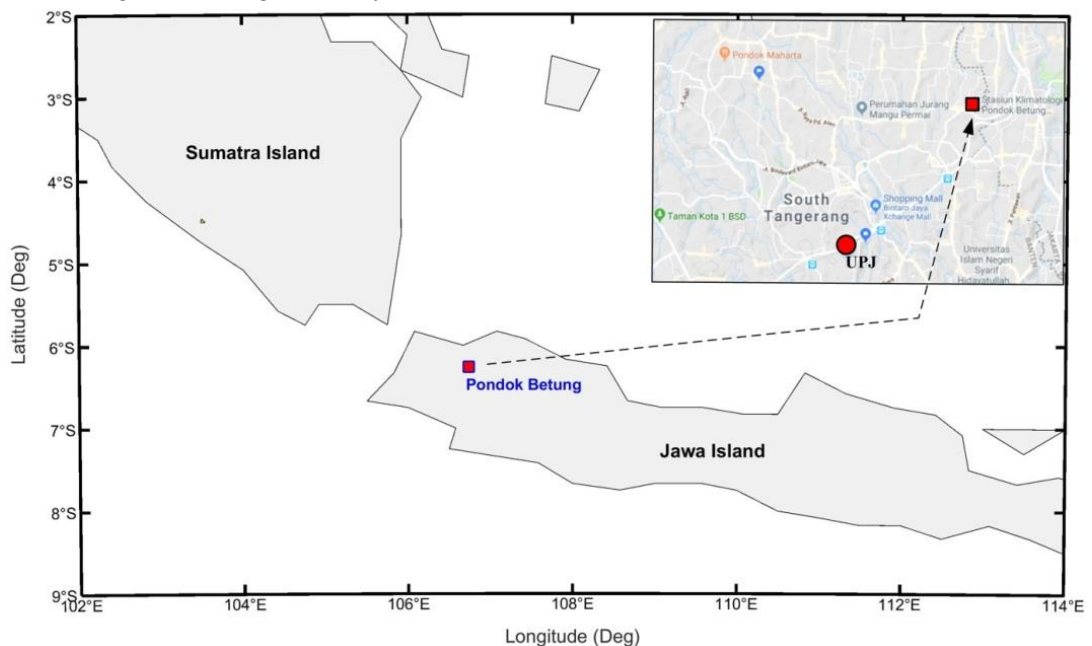
Fig. 1. The location of study and floods point by Google Maps in South Tangerang City.

The data collected includes rainfall, relative humidity, and surface temperature. Because the BMKG in one district only managed one weather station, this study will use data at the South Tangerang City which located in Pondok Betung station (geographically: 6°15'40.22"S, 106°44'56.26"E). The meteorological data provided by BMKG is available on a daily basis. This existing data is utilized entirely to predict floods. In this work, ten years of data will be employed to make an accurate prediction of rainfall. The location of meteorology station used in this study is depicted in **Fig.1**.

Since no surface pressure data provided free by BMKG, the partial pressure of water vapour (P_w) is employed. It can be obtained from the relative humidity (RH) and temperature as recommended by the World Meteorological Organization (WMO) Technical Note No. 8 as in Suparta et al. (2008) and defines as follows:

$$P_w = \frac{RH}{100}\exp\left(-37.2465 + 0.213166\,T_K - 2.56908\,x10^{-4}\,T_K^2\right) \tag{1}$$

where P_w is in mbar and T_K is mean temperature in Kelvin.

2.2. ANFIS model development for rainfall predictions

The approach used for rainfall prediction is the utilization of ANFIS techniques rather than Artificial Neural Network (ANN) (Tierra, 2016). One of the advantages of ANFIS, it has a similar concept to the concept of human thinking where they can learn something from the data that has trained. Furthermore, it can self-learning effectively and memory abilities of neural networks and brings a more stable training process (Huang et al., 2018). This is the idea of Tagaki-Sugeno-Kang (Jang, 1993; Jang & Sun, 1995) which apply the first order of the ANFIS model. The approach can use types of supervised learning and unsupervised learning algorithms. In this work, a neural multilayer advanced feed network with supervised learning processes will be selected. From the various types of supervised learning algorithms, the backpropagation-learning algorithm (BPL) is chosen as a flood prediction system. The choice of BPL is because it has been widely applied. About 90% of backpropagation has been successfully applied in many fields, such as finance, handwriting pattern recognition, voice pattern recognition, system control, medical image processing, and light prediction made by NASA.

Fig. 2 shows the basic ANFIS architecture with two inputs and one output. In general, ANFIS is constructed with five layers, i.e. the input layer as antecedent parameters, three hidden layers with two constant parameters and one consequent parameter, and one output layer. In more detail about the ANFIS concept, authors can refer to Suparta and Alhasa (Suparta & Alhasa, 2013; 2016a; 2016b, 2013; Suparta & Putro, 2017). In brief, the model can be explanation as follows.

Layer 1: Every node in this layer transforms input into degree between 0 and 1 (fuzzification) which so-called premise parameter. It is an activation function with membership function such as gauss, triangular, trapezoidal, and generalized Bell. The node output is given by,

$$O_{1,i} = \mu_{Ai}(x), \quad i = 1,2 \text{ and } \quad O_{1,i} = \mu_{Bi-2}(y), i = 3,4 \tag{1}$$

where x or y is the input to the node i; A_i or B_{i-2} is a linguistic label of fuzzy set associated with this node, $O_{1,\,i}$ is the membership functions (MFs) grade of fuzzy set. Assuming the Gaussian membership function is used.

$$\mu_{Ai}(x) = exp\left[-\left(\frac{x-c_i}{2a_i}\right)^{2b}\right] \quad \mu_{Bi-2}(x) = exp\left[-\left(\frac{x-c_i}{2a_i}\right)^{2b}\right] \tag{2}$$

where $\{a_i,\,b_i,\,c_i\}$ are the parameter set of the membership function in premise parameter that can change the shape of the membership function. As the value of these parameters' changes, the gauss shaped functions will vary accordingly
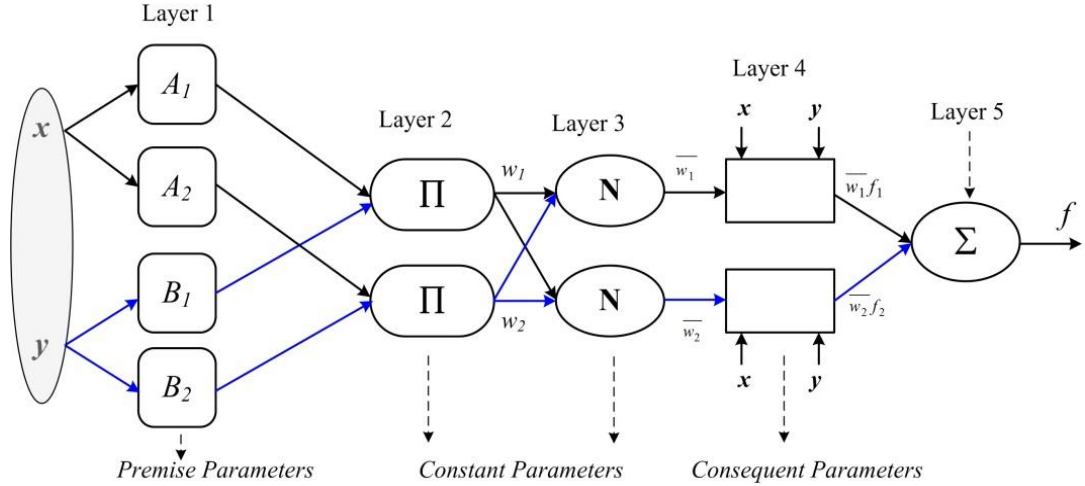
Fig. 2. Basic ANFIS architecture with two inputs and one output.

Layer 2: Every node in this layer will estimate of each incoming signal to each neuron using the product operator (Π) or T-norm operator. The output is the product of <u>multiplying</u> the incoming signals to entire node and demonstrates the firing strength of a rule.

$$O_{2,i} = w_i = \mu_{Ai}(x) * \mu_{Bi}(y), i = 1,2 \tag{3}$$

Layer 3: Every node in this layer labelled N will normalize all input signals to calculate the ratio of each ith rule's firing strength to the sum of all rules firing strengths as

$$O_{3,1} = \overline{w_i} = \frac{w_i}{w_1 + w_2}, i = 1,2 \tag{4}$$

where, w_i is the firing strengths of the second layer, and $\overline{w_i}$ is taken as the normalized firing strength.

Layer 4: Each node in the fourth layer calculates the contribution of the ith rules toward the total output and the function is defined as

$$O_{4,i} = \overline{w}_i f_i = \overline{w}_i (p_i x + q_i y + r_i) \tag{5}$$

where $(p_i x + q_i y + r_i)$ are the parameter set on first order of Sugeno fuzzy inference system model.

The parameters in this layer are referred to as consequent parameters.

Layer 5: The single node in this layer labelled Σ will summarize all the weighted output values from overall of all incoming signals.

$$O_{5,i} = \sum_i \overline{w}_i f_i = \frac{\sum_i w_i f_i}{\sum_i w_i} \tag{6}$$

2.3. ANFIS Fuzzy C–Means clustering algorithm

Specifically, this work employed an ANFIS based on Fuzzy C–Means clustering algorithm (ANFIS FCM) for rainfall prediction. ANFIS FCM is one of the artificial intelligence algorithms that is proven successful in predicting the relationship between input and output parameters (Fattahi, 2016). Bezdek et al. (1984) has been introduced the FCM algorithm as a data clustering in which each data point belongs to a cluster to a degree specified by a membership grade. FCM partitioned the collection of n vector Y_i, i = 1, 2..., n into C fuzzy groups and finds a cluster center in each group, it then minimizes a cost function of inequality measure. The stages of FCM algorithm are (1) the cluster

centers, c_i, $i = 1,2,...,C$ is randomly chosen from n points $\{Y_1,\ Y_2,\ Y_3,,..,\ Y_n\}$. The membership of matrix **U** is then computed following the equation:

$$U_{ij} = \frac{1}{\sum_{k=1}^{c}\left(d_{ij}/d_{kj}\right)^{\frac{2}{m-1}}}$$

(7)

where, $d_{ij} = \|c_i - c_j\|$ is the Euclidean distance between i_{th} cluster center and j_{th} data point, and m is the fuzziness index. Then, the cost function according to the equation (3) is computed. The process is stopped if it is below a certain threshold.

$$J(U, c_1, ..., c_3) = \sum_{\substack{k=1 \\ i}}^{c} J = \sum_{i=1}^{c}\sum_{j=1}^{n}\mu_{ij}^{m}d_{ij}^{2}$$

(8)

Finally, a new C fuzzy cluster centers c_i, $_{i} = 1,2,..., C$ is computed using the following equation:

$$C_i = \frac{\sum_{j=1}^{n}\mu_{ij}^{m}x_j}{\sum_{j=1}^{n}\mu_{ij}^{m}}$$

(9)

2.4. Data processing

In this study, meteorological parameters that were selected will be trained and tested to find which combinations of parameters have the best correlation with the highest accuracy to be selected as the input of model. The size of the data being trained is ten years with 70% for training and 30% for testing. The output of the system will be tested to match with the target given to the system. If not, then the learning algorithm will be improved by providing new network architecture or learning. The results of rainfall prediction through the ANFIS method are also evaluated with the RMSE (Root Mean Squared Error) and Mean Squared Error (MSE). Mathematically, RMSE and MSE are expressed as (Wang & Lu, 2018).

$$RMSE = \sqrt{\frac{1}{n}\sum_{k=1}^{n}(y_k - \hat{y}_k)^2}\ \ and\ \ MSE = \frac{1}{n}\sum_{k=1}^{n}(y_k - \hat{y}_k)^2$$

(10)

where $\hat{y}_k$ is the prediction value, y_k is the actual value, and n is the data number.

Note that both RMSE and MSE express the average model prediction error in the unit of the observed variable. The MSE parameter is used when data contains unexpected values that must be considered, i.e. the value is too high or too low. In this case, rainfall data on certain days can reach extreme values. The value of both parameters can range from 0 to ∞ and ignores the direction of the error. Prediction results will obtained better if both values are close to zero. On the other hand, if RMSE is small enough, ANFIS is considered to have succeeded in carrying out the training process.

The detailed process of developing a rainfall prediction model using ANFIS, it can be applied as a system for early detection of flooding. For this work, three scenarios of combination input by using surface temperature, relative humidity, and partial pressure of water to predict rainfall are employed as shown in Fig. 3. The first scenario of learning process, it has been used one input, i.e. relative humidity (RH). The second scenarios is with two inputs (temperature average (T_{avg}) and RH). While the third scenario is using three inputs (minimum temperature (T_{min}), RH, and partial pressure of water vapour (P_w)). The selection of these parameters is based on trial and error to find which parameter is best as an intermediary. Overall, each output is predicted using ANFIS through the learning process of training, testing, and validation.
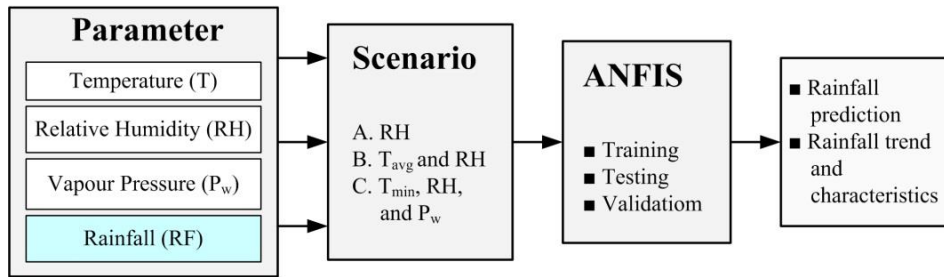
Fig. 3. The scenario of research to predict rainfall.

3. RESULT AND DISCUSSION

Based on the scenario in **Fig. 3**, the daily data for 10 years (2009 – 2018) is divided into 70% (2556 data) for training and 30% (1096 data) for validation. Furthermore, 70% of training data is also divided into 70% for training (1789 data) and 30% for testing (767 data). The training set is used to fit the model to sees how the model learns from this data. While the validation set is used to evaluate a given model. On the other hand, the test set is used to provide an unbiased evaluation of a final model fit on the training dataset. It is only used once a model is completely trained (using the train and validation sets). The estimation results of rainfall that has been carried out with three scenarios (A, B, and C) are presented in **Fig. 4**. As shown in the figure, the rainfall prediction (blue) follows the trend of rainfall data (gray) in (a) training, (b) testing, and (c) validation. However, the daily rainfall from measurement is around 34% higher than the rainfall with the estimation technique using ANFIS.
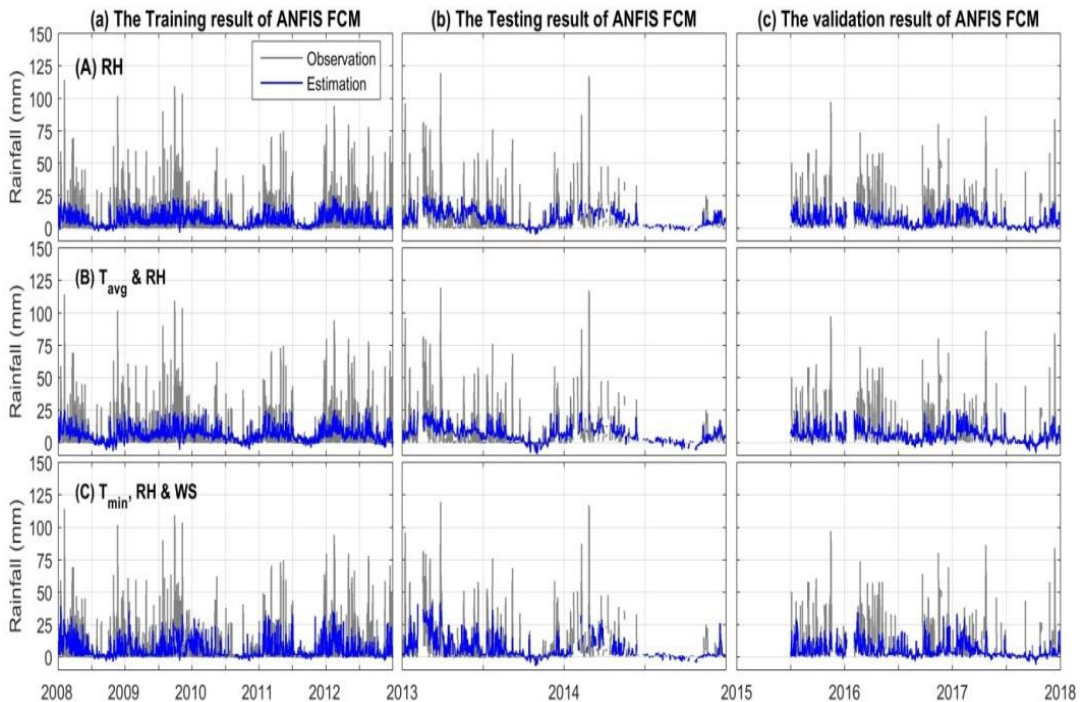
Fig. 4. Daily variation of rainfall estimated from ANFIS FCM model compared with daily rainfall data at BMKG Pondok Betung station during the (a) training, (b) testing and (c) validation process for the input of (A) RH, (B) T_{avg} and RH, and (C) T_{min}, RH, and P_w.

The relationship rainfall together with MSE values between observation and estimation for the three scenarios during the training, testing, and validation processes is depicted in **Fig. 5**. The result shows that overall correlation coefficients (*r*) to have a low relationship at the 99% confidence level with almost similar MSE values except for *scenario C* where during the training process shows a moderate relationship with a small MSE value. The figure also shows that good learning outcomes in the training process will also produce good estimates. In the case of using daily rainfall, it appears that the estimated daily rainfall value for the three scenarios is almost the same. With due regard to cost efficiency, measurement equipment, and time, with almost the same results, relative humidity can be considered as the best input model or intermediate parameter to estimate rainfall values.

Because the daily data in **Fig. 4** can only see rainfall trends between measurements and estimations and the correlation is also low, the monthly data is processed to show clearly the variations and differences in values between observations and estimates. **Fig. 6** shows the monthly average rainfall results in the training, testing and validation processes for each scenario. The figure also shows the correlation coefficient (r), MSE and the difference in rainfall between observations and estimated average (δ). It is clear that the rainfall data from the measurement is still higher around 28 mm than the estimated average. However, rainfall trends clearly follow one another. Note that the testing result show a strong correlation where the training result is with moderate relationship. Note that the testing results show a strong correlation while the training results show a moderate relationship.
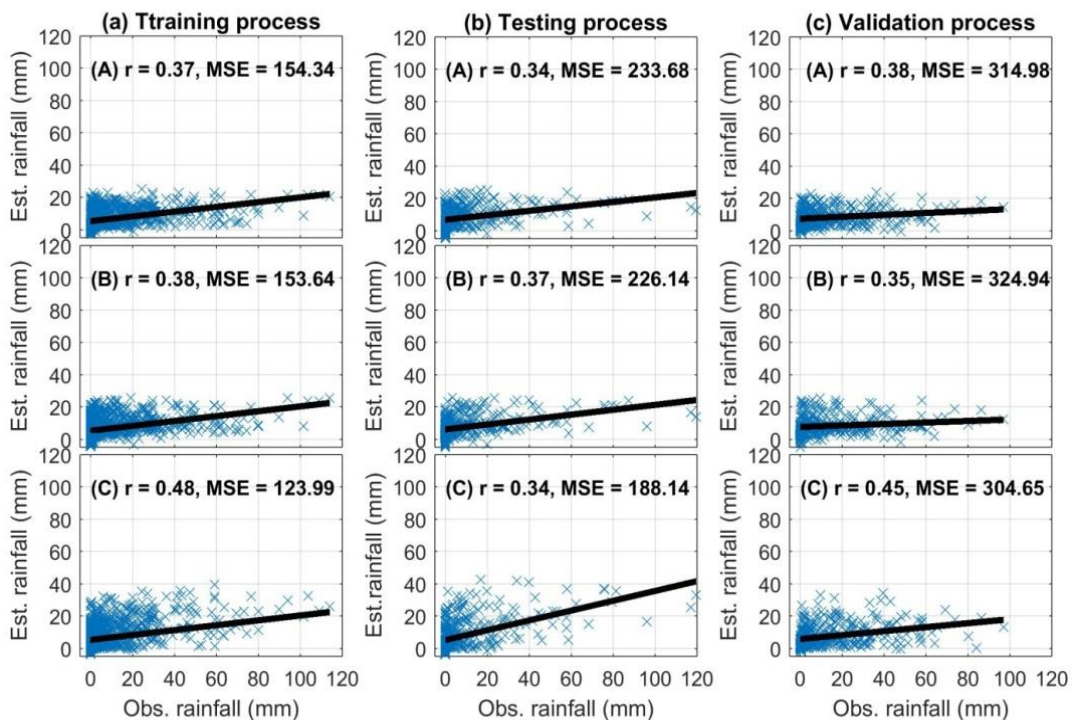
Fig. 5. The relationship of rainfall between observation and estimation for the three scenarios during the training, testing, and validation processes.

Table 1 shows the RMSE value obtained during the learning process for training, testing, and validation. It is seen that the RMSE value for daily and monthly data is similar for training and testing. In the validation process, the RMSE value for monthly is 38% lower than the daily RMSE. This indicates that the monthly RMSE value provides better accuracy of the predicted results.
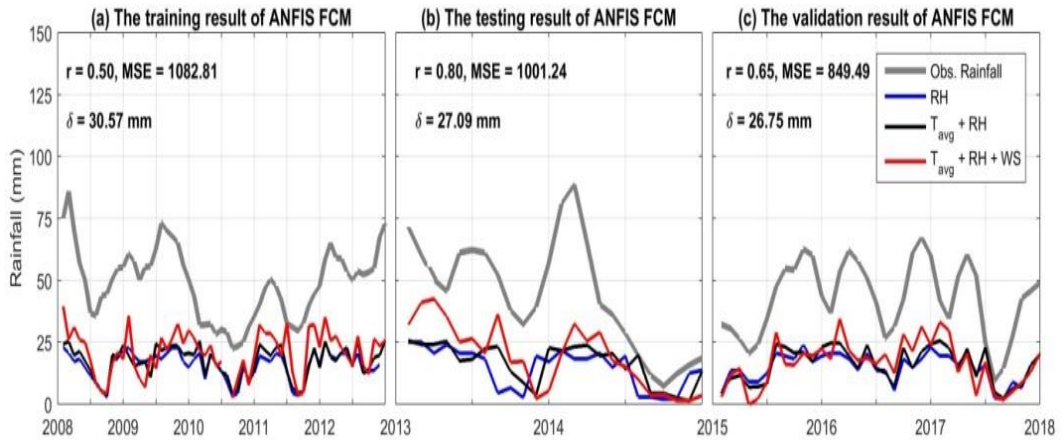
Fig. 6. Monthly average of variation of rainfall estimated from ANFIS FCM model compared with daily rainfall data at BMKG Pondok Betung station during the (a) training, (b) testing, and (c) validation process for the input of (A) RH, (B) T_{avg} and RH, and (C) T_{min}, RH, and P_w.

Table 1.

RMSE results from daily and monthly rainfall based on three scenarios (A, B, and C) during training, testing, and validation for a period of 10 years (2009 - 2018)

Learning Process	The evaluation of the model in each scenario					
	Daily			Monthly		
	A	B	C	A	B	C
Training	12.20	12.17	10.43	12.20	12.17	10.42
Testing	11.92	11.73	10.53	11.92	11.73	10.53
Validation	17.75	18.03	17.45	11.03	11.21	10.71

Focusing on daily analysis, in each case, the model learns well the sample data (training dataset) where the testing result (test dataset) is capable to capture all the training data in their estimation. This is indicated by almost similar RMSE in each scenario, except for the validation result where the bias or error is 32% higher as compared to training and testing results. Prediction of rainfall using scenarios A and B are different in error by 9% and 8% as compared to scenario C respectively. Overall, the combination input with T_{min}, RH, and P_w or scenario C is the best result for the prediction of rainfall in South Tangerang City.

5. CONCLUSIONS

Using the ANFIS Fuzzy-C-Means (FCM) technique, rainfall data on a daily basis in South Tangerang City, Indonesia has been successfully estimated. From all the scenarios, the RSME of training and testing and validation processes of prediction on a daily basis is around 11% and 18% respectively. The model is capable to estimate rainfall with accuracy more than 80%.

However, the model that have been built with membership structures and functions are still not able to capture or predict extreme rainfall. This condition is possible because the intermediate parameters chosen are only limited to the amount of data available namely temperature, humidity and partial pressure of water. In future, other meteorological parameters such as station surface pressure

and other parameters need to be inputted and combined with other existing parameters such as temperature and humidity and the results of the estimation can also be compared with hydrological data such as water level. At present, meteorological data in the form of surface pressure are not provided free of charge by BMKG. Further analysis will also look at what rainfall categories potentially triggering urban flash floods.

ACKNOWLEDGMENTS

R E F E R E N C E S

Bezdek, J. C., Ehrlich, R. & Full, W. (1984) FCM: Fuzzy C-Means Clustering Algorithm. *Computer & Geosciences,* 10(2-3), 191-203.

Bui, D. T. et al. (2018) New Hybrids of ANFIS with several optimization algorithms for flood susceptibility modeling. *Water,* 10, 1210, doi:10.3390/w10091210.

Fattahi, H. (2016) Adaptive neuro fuzzy inference system based on fuzzy c–means clustering algorithm, a technique for estimation of tbm penetration rate. *Int. J. Optim. Civil Eng*., 6, 159-171.

Fujiki, K., & Renard, F. (2018) A geographic analysis of post-disaster social impacts on a municipal scale – a case study of a potential major flood in the Paris region (France). *Geographia Technica*, 13 (2), 31-51.

Ghazavi, R., Rabori, A. M. & Reveshty, M. A. (2016) Modelling and assessment of urban flood hazards based on rainfall intensity-duration-frequency curves reformation. *Nat. Hazards Earth Syst. Sci. Discuss.,* doi: 10.5194/nhess-2016-304.

Hong, H., Panahi, M., Shirzadi, A., Ma, T., Liu, J., Zhu, A.-X., Chen, W., Kougias, I. & Kazakis, N. (2017) Flood susceptibility assessment in hengfeng area coupling adaptive neuro-fuzzy inference system with genetic algorithm and differential evolution. *Sci. Total Environ.* 621, 1124–1141.

Huang, M., Zhang, T., Ruan, J. & Chen. X. (2017) A new efficient hybrid intelligent model for biodegradation process of DMP with fuzzy wavelet neural networks. *Sci. Rep.*, 7, 41239, doi: 10.1038/srep41239.

Jang, J. S. R. (1993) ANFIS: adaptive network-based fuzzy inference systems. *IEEE Transactions on Systems Man and Cybernetics,* 23, 665–685.

Jang, J. S. & Sun, C. T. (1995) Neuro-fuzzy modeling and control. *Proceedings of the IEEE* 83(3), 378-406.

Kompas (2018) Flood-prone points in South Tangerang. "https://megapolitan.kompas.com/read/2018/10/26/19180951/ini-titik-titik-rawan-banjir-di-tangerang-selatan"

Mekanik, F., Imteaz, M. A. & Talei, A. (2015) Seasonal rainfall forecasting by adaptive network-based fuzzy inference system (ANFIS) using large scale climate signals. *Clim. Dyn*. 1-15.

Suparta, W., Abdul Rashid, Z. A., Mohd Ali, M. A., Yatim, B., & Fraser, G. J. (2008) Observations of Antarctic precipitable water vapor and its response to the solar activity based on GPS sensing. *Journal of Atmospheric and Solar- Terrestrial Physics,* 70, 1419-1447.

Suparta, W. & Alhasa, K. M. (2013) A comparison of ANFIS and MLP models for the prediction of precipitable water vapor. *Proceeding of the 2013 IEEE International Conference on Space Science and Communication (IconSpace),* 243-248.

Suparta, W. & Alhasa, K. M. (2016a) *Modeling of Delays Using ANFIS. Germany: Springer International*.

Suparta, W. & Alhasa, K. M. (2016b) Precipitable water vapor using an adaptive neuro-fuzzy inference system in the absence of the GPS network. *Journal of Applied Meteorology and Climatology* 55(10), 2283-2300, doi: 10.1175/JAMC-D-15-0161.1.

Suparta, W. & Putro, W. S. (2017) Comparison of tropical thunderstorm estimation between multiple linear regression, Dvorak, and ANFIS. *Bulletin of Electrical Engineering and Informatics* 6(2), 149-158, doi: 10.11591/eei.v6i2.648.

Tierra, F., (2016) Nonlinear and discontinuities modeling of time series using artificial neural network with radial basis function. *Geographia Technica*, 11 (2), 102 -112.

Wang, W. & Lu, Y. (2018) Analysis of the mean absolute error (MAE) and the root mean square error (RMSE) in assessing rounding model. *IOP Conference Series: Materials Science and Engineering*, 324 (2018) 012049, doi:10.1088/1757-899X/324/1/012049.

BUSINESS CYCLE IMPACT ON POLLUTION LEVELS
IN THE CITY OF MADRID USING FUNCTIONAL DATA

Betancourt ALEJANDRO [1] ⓘ *, Ramos JAVIER [2], Wirth ESZTER [2]* ⓘ

ABSTRACT :

The aim of this paper is to analyse whether the evolution of NO_2 and PM_{10} emission levels in the Madrid metropolitan area with heavy traffic are affected by business cycles (comprised of a boom, recession and recovery). Therefore, we explore if economic developments act as automatic environmental stabilizers in an urban context in order to provide guidelines for environmental policymaking in large cities. Considering the continuous nature of the particles that this paper analyses, functional data have been used and the most suitable statistical method has been applied to this information's typology. The aim is to capture the behaviour of $NO2$ and PM_{10} particles throughout the booming years (2001-2005), the recession (2008-2012) and the recovery (2014-2018) periods. The results obtained through the Kendall's functional Tau statistic have revealed that the similarities and differences found between the booming years, the recession and the recovery prove the effect of the economy's cyclical fluctuations on pollution levels. This is due to the fact that the negative and close to zero correlations obtained through these periods represent a sign that pollution levels regarding these two particles are significantly different during the phases of business cycles.

***Key-words:** Pollution, Urban Environmental Policy, Business Cycle, Functional Data, Kendall Correlation.*

1. INTRODUCTION

NO_2 and PM_{10} particles represent two of the pollutants that have concerned international scientific communities the most (Medina, Zanobetti & Schwartz, 2006; Lelieveld et al, 2002; EEA, 2018) due to their negative effects on global warming and human health (World Health Organization, 2014). When it comes to NO_2, scientists have highlighted its role in generating other harmful particles such as O_3 and PM_5 (Hysenaj, 2019, Archer, Brodie & Rauscher, 2019). This substance, which can be found in urban air, mainly comes from NO rusting, whose main sources are emissions by automobile combustion engines, especially those that run on diesel.

During year 2018 in Madrid, the city that is the focus of this research, 7 out of the 24 air monitoring stations that measure NO_2 levels surpassed the annual threshold value recommended by the World Health Organization (WHO) (Ceballos et al, 2018; ACDGMAS, 2018). This particle's highest value (55 µg/m^3) was detected within the area covered by the Escuela Aguirre air monitoring station (Central Madrid). When it comes to PM_{10}, 4 out of the 13 air monitoring stations recorded figures that also exceeded the annual threshold value recommended by the WHO (Ceballos M.A, et al., 2018; Spain Government, Ministry for Ecological Transition, 2018).

Economic activities play an outstanding role in this economic context with high production and consumption levels seriously damaging environmental health. An empirical study that was carried out throughout this document brought to light that high pollution rates of certain particles, such as NO_2 and PM_{10}, vary according to the economy's business cycle (see Figures 2 and 3).

[1] *Universidad Pontificia Comillas, Departament of Quatitative Methods mabetancourt@comillas.edu*

[2]*Universidad Pontificia Comillas, Economic Departament, ajramos@icade.comillas.edu, ewirth@comillas.edu*

These particles' pollution levels are higher during the economic booms than during crises and recoveries. Pollution levels are increasing anew during the current recovery period, although at a slower pace than throughout the previous intensive economic boom.

If this fact was true from a statistical point of view, the following hypothesis could be contemplated: Do business cycles act as automatic regulators for certain particles' pollution levels? With a view to answering this formulation, this study aims at showing if the evolution of NO_2 and PM_{10} pollution levels in Central Madrid's heavy traffic zones is affected by business cycles (comprised of a boom, recession and recovery).

Research studies including mathematical and statistical techniques have a crucial role in shedding light on the behaviour and trends of polluting substances in such circumstances. The search for patterns through mathematical models considering the specific features of the orography and meteorological conditions in the places that are the focus of our study have been deeply analysed by many authors (Salvador et al, 2015).

However, almost all the articles published so far consider NO_2 and PM_{10} pollution levels as a discrete variable over time, and consequently apply traditional statistical techniques. This problem entails the lack of those scientific methods that could enable a more thorough research on these particles' behaviour. This is the reason why this article takes into account the continuous nature of the particles, and therefore the data are considered as functions. This particularity requires the application of statistics on functional data, such as the KFT, developed by Valencia, Lillo & Romo, (2019).

2. STUDY AREA AND DATA

Daily studies on NO_2 and PM_{10} particles were carried out during the time frames 2001-2005, 2008-2012 and 2014-2018, which correspond to the stages of boom, recession and recovery of the last 20-year business cycle, respectively (see **Fig. 1a and 1b**). To do so, 5 air quality-monitoring stations were selected (Escuela Aguirre, Cuatro Caminos, Plaza de España, and Barrio del Pilar), all located in the urban core of Madrid City. These stations were selected because they correspond to those areas that are affected by the heaviest traffic levels in the capital. Any interested reader can access the most up-to-date data on the web page of Madrid City Council, which is regularly collected and made available by the Comprehensive Air Quality System. Data was processed with MATLAB V18b software system.

Figs. 1a and 1b depict the average annual NO_2 and PM_{10} pollution levels between years 2001 and 2017 for the 5 air monitoring stations that are considered in this study. On both charts it can be observed that during the Spanish economy's boom (2001-2005) the levels remained stable and substantially exceeded the WHO's regulation. However, through the economic crisis (2008-2012) both pollutants suffered a downward trend until registering a slight increase since year 2014, which corresponds to the recovery stage. Each phase of the Spanish economy's business cycle can be observed in **Figs. 2a and 2b**.

Fig.2a displays nominal GDP annual growth rates in Madrid City, the Community of Madrid and Spain from 2000 until 2017, while **Fig. 2b** represents national real GDP growth rates during the same time frame. We can observe the three stages of the last Spanish business cycle on both charts: an intense economic growth prior to the 2008 crisis; a substantial fall in production (and employment) throughout the 2008-2013 global economic crisis; and followed by an economic recovery since 2014, blurred by an uncertain outlook nowadays.

The existence of three clearly defined periods, each comprised of 5 years, justify the choice of polluting particle emission samples for each one of them. By analysing each period, we will be able to study the impact of each stage of the business cycle (economic growth, economic crisis and recovery) on pollution levels and thus, determine if business cycles can be considered as automatic regulators of pollution levels.
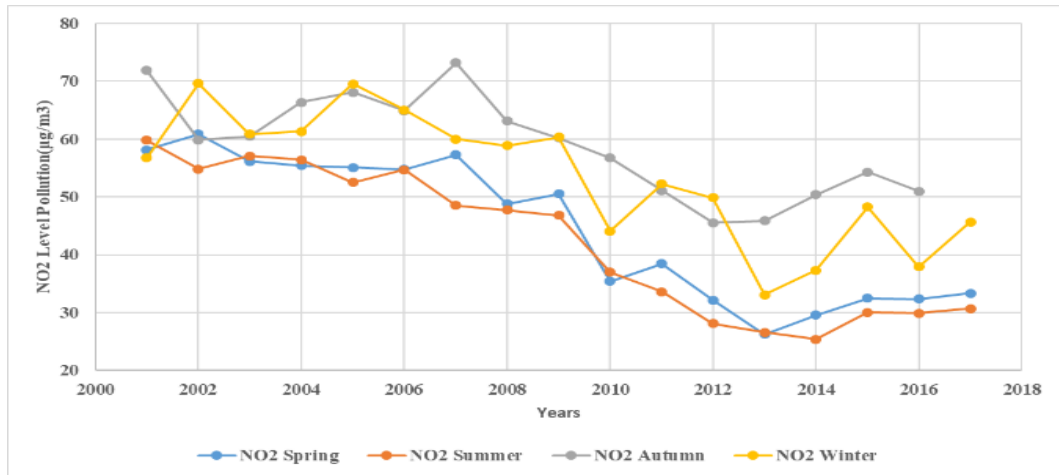
Fig. 1a. Annual average, NO_2 in Madrid (2001-2017).
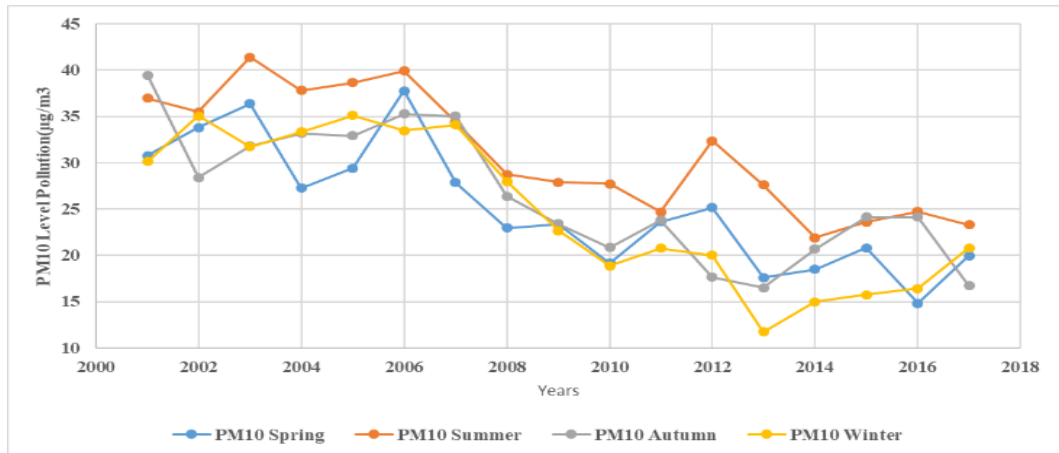
Fig. 1b. Annual average, PM_{10} in Madrid (2001-2017).
(Source: authors' calculations based on data)

3. METHODOLOGY

3.1 Functional Kendall's Tau Correlation

Even though the evolution of many variables of interest takes place over a continuous time period, in the context of scientific investigations their study is often carried out from a more transversal and discrete perspective, which leads to a loss of relevant information regarding the 'natural' behavior of the phenomenon under study (Kovács, 2018; Fontana, Tavoni & Vantini, 2019). Therefore, the choice to resort to functions as a mathematical tool seems to be natural for a scientist who aims at capturing the continuous-time behaviour of a phenomenon (Li & Chow, 2005). Once we allow ourselves to interpret the observations of a process as function realizations, the tools adopted for the statistical analysis must be consistent with the available data type.
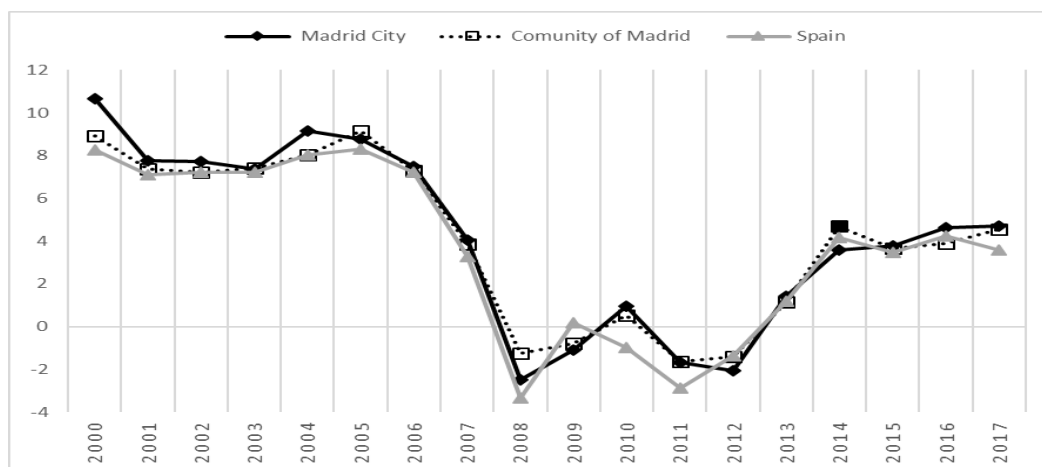
Fig 2a. Nominal GDP annual growth rates (%).
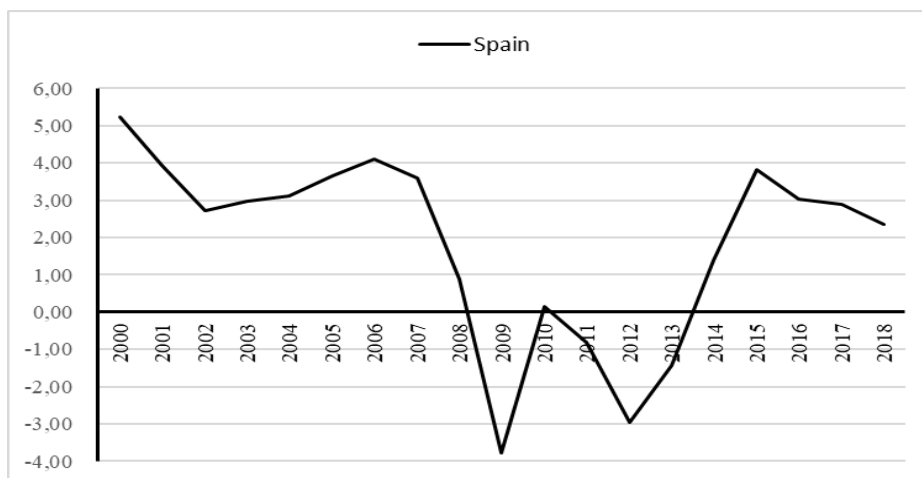
Fig 2b. Real GDP annual growth rates, Spain (%).
(Source: authors' calculations based on data from the Spanish Statistical Institute)

For example, this is the case for the techniques adopted by regression analysis (Escabias, Aguilera &Valderrama, 2004), by the measures of depth (López-Pintado & Romo, 2009) and by the dependency and correlation analysis (Leurgans, Moyeed & Silverman, 1993; Li & Chow, 2005; Valencia, Lillo & Romo, 2019). Specifically, in recent years in each of these contexts classical statistics techniques have been extended to the scope of functional analysis.

For the kind of investigation that we aim to do in our work, which requires us to study the relationships between the pollution behaviors of NO_2 and PM_{10} particles and the air quality in different geographical districts of the MMA, we chose to implement the Functional Kendall's Tao (FKT), proposed by Valencia, Lillo & Romo (2019). The FKT is the extension to a functional context of the classic Kendall's Tao coefficient (Kendall, 1955), which relies on the distinction between concordant and discordant observations between two sets of data. In particular, the FKT is inspired by the idea that the sets to be analyzed are discrete realizations along curves.

Functional Kendall's Tau (FKT): If $(X_1, Y_1)(X_2, Y_2)$ are copies of a stochastic bivariate process $\{(X(t), Y(t): t \in I\}$, where $I = [a, b]$. The population version of the Functional Kendall's Tao (FKT) would be:

$$\tau = [P\{X_1 \prec X_2, Y_1 \prec Y_2\} + P\{X_2 \prec X_1, Y_2 \prec Y_1\}] - 1 \qquad (1)$$

In particular, if we consider a sample $(x_1, y_1) \dots (x_n, y_n)$ of a bivariate random process $(X, Y) = \{(X(t), Y(t): t \in I\}$ within the compact interval $I = [a, b]$, then the empirical version of the Functional Kendall Tau would be given by

$$\tau = \binom{n}{2}^{-1} \sum_{i<j}^{n} [2I(x_1 \prec x_2, \ y_1 \prec y_2) + 2I(x_2 \prec x_1, \ y_2 \prec y_1)] - 1 \qquad (2)$$

The realizations of the stochastic process are taken as functions. When the FKT takes 1 as a value then the sets of functions are perfectly positively correlated. Instead, if $\hat{\tau}$ is equal to -1 when their correlation is perfectly negative and if equal to 0 when they display absence of correlation. When the FKT takes increasing values between 0 and 1 (-1), this indicates increasing positive (negative) degrees of correlation between the pair of sets.

Finally, the KTF is robust, which means it displays low sensitivity to the presence of data outliers. Robustness is an important property for these kinds of coefficients, since any point value that is erroneously captured will not significantly affect the overall analysis and conclusions. These and other properties of the functional coefficient are discussed by Valencia, Lillo & Romo, (2019).

4. RESULTS AND DISCUSSIONS

The use of functions as baseline information that describe daily pollution levels in each air monitoring station, justified by the information's nature, allows us to take into account the evolution of NO_2 an PM_{10} in a continuous way over time. On the contrary, the conventional statistics (average, standard deviation), often used and applied on discrete data, are sensitive to extreme values. In many cases their calculation makes it impossible to describe everything that occurs concerning pollution in the medium-long run. In contrast, some of the statistics defined as functions allow to capture their whole evolution over the study period as it has been proved by Valencia, Lillo & Romo (2019).

For the functional correlation analysis each air monitoring station's data correspond to three sets of 5 curves each, which describe the daily pollution levels over the periods 2001-2005, 2008-2012 and 2014-2018. These periods have been selected in order to match them with the three stages of the Spanish and Madrilenian business cycle. Each function contains approximately 365 discretisation points that correspond to the total days of a year. The Kendall Tau coefficient between business cycles is calculated through functional data. This way correlation coefficients between each stage of the business cycle are thoroughly studied in order to analyse pollution behaviours under each stage's effects. The results were obtained by programming the proposed functional statistic on MATLAB18b.

Each pair of the business cycle's stages for the same air monitoring station displaying a low correlation or a negative correlation explains that pollution behaviours are very different between them, and thus, are a sign that business cycles act as automatic regulators on certain particles' pollution levels. **Tables 1-7** show for each study period the Kendall Tau's most relevant results for air monitoring stations located in those areas of Madrid City that suffer from heavy traffic.

Table 1 and 2 depict the correlations between periods 2001-2005 and 2008-2012 for NO_2 and PM_{10} substances in the Cuatro Caminos air monitoring station. In case of the former pollutant, the correlation between the two periods is -0.2, which indicates a weak linkage between pollution levels during the economic boom and the recession. As for the second pollutant, the correlation is moderately negative (-0.8), which means that during most of the booming years (2001-2005) pollution trends are the opposite to the trends during the recession period (2008-2012), as it can be observed in **Table 2**.

Similar results are shown in the Escuela Aguirre, Plaza de España and Barrio del Pilar air monitoring stations, whose results are reflected in **tables 3 to 6**, respectively.

<div align="right">

Table 1.

</div>

Kendall Functional Correlation for NO$_2$.

Station (Years)	Cuatro Caminos (14-18)	Cuatro Caminos (08-12)	Cuatro Caminos (01-05)
Cuatro Caminos (01-05)	0,8	-0,2	1
Cuatro Caminos (08-12)	-0,4	1	-0,2
Cuatro Caminos (14-18)	1	-0,4	0,8

<div align="right">

Table 2.

</div>

Kendall Functional Correlation for PM$_{10}$.

Station (Years)	Cuatro Caminos (14-18)	Cuatro Camino s (08-12)	Cuatro Caminos (01-05)
Cuatro Caminos (01-05)	0,4	-0,8	1
Cuatro Caminos (08-12)	-0,2	1	-0,8
Cuatro Caminos (14-18)	1	-0,2	0,4

<div align="right">

Table 3.

</div>

Kendall Functional Correlation for NO$_2$.

Station (Years)	Escuelas Aguirre (14-18)	Escuelas Aguirre (08-12)	Escuelas Aguirre (01-05)
Escuelas Aguirre (01-05)	-0,2	0,2	1
Escuelas Aguirre (08-12)	0,2	1	0,2
Escuela Aguirre (14-18)	1	0,2	-0,2

<div align="right">

Table 4.

</div>

Kendall Functional Correlation for PM$_{10}$.

Station (Years)	Escuelas Aguirre (14-18)	Escuelas Aguirre (08-12)	Escuelas Aguirre (01-05)
Escuelas Aguirre(01-05)	0,6	-0,6	1
Escuelas Aguirre (08-12)	-0,2	1	-0,6
Escuela Aguirre (14-18)	1	-0,2	0,6

<div align="right">

Table 5.

</div>

Kendall Functional Correlation for NO$_2$.

Station (Years)	Plaza España (14-18)	Plaza España (08-12)	Plaza de España (01-05)
Plaza España (01-05)	0	0,4	1
Plaza España (08-12)	0,2	1	0,4
Plaza España (14-18)	1	0,2	0

<div align="right">

Table 6.

</div>

Kendall Functional Correlation for NO₂.

Station (Years)	Barrio del Pilar (14-18)	Barrio del Pilar (08-12)	Barrio del Pilar (01-05)
Barrio del Pilar (01-05)	-0,4	0	1
Barrio del Pilar (08-12)	0,2	1	0
Barrio del Pilar (14-18)	1	0,2	-0,4

On the other hand, the Escuela Aguirre air monitoring station displays correlations of 0.2 and -0.2 (NO₂ and PM₁₀) when it comes to the recession and recovery (2008-2012 and 2014-2018), which proves that pollution trends are practically unrelated. In other words, even if pollution levels had decreased during the crisis (see **Figs. 3a and 3b**), throughout the recovery phase they started to increase anew, although it is worth highlighting that this increase has been less intense than during the booming years preceding the crisis.
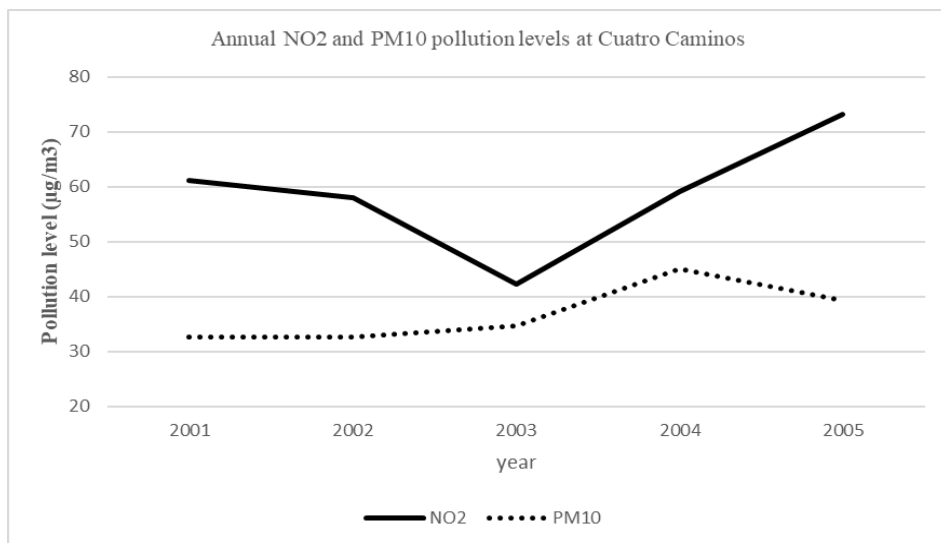
Fig. 3a. Average annual pollution during the economic boom
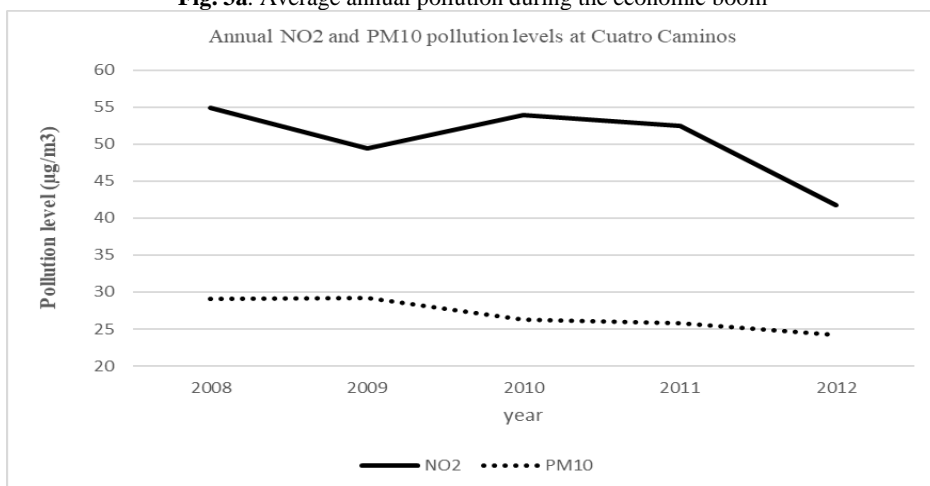
Fig. 3b. Average annual pollution during the recession.
(Source: authors' calculations based on data).

From a statistical point of view, on **Table 1** we can observe significant differences. As an example, **Table 7** displays the significant differences that exist between average PM_{10} pollution levels during the analysed time frames at the Cuatro Caminos air monitoring station. This fact statistically confirms the differences regarding pollution levels for each phase of the business cycle. Hence, it is crucial to take into consideration the phase of the business cycle in the city under study when analysing environmental policy effectiveness, as these policies can be misinterpreted.

Table 7.

Mean differences between time frames.

Monitoring Station	Daily average ozone ($\mu g /m^3$)	N	p-value
Cuatro Caminos (PM_{10}). (2001-2005)	35.95	1584	0.00
Cuatro Caminos (PM_{10}). (2008-2012)	27.27		
Cuatro Caminos (PM_{10}). (2001-2005)	35.95	1584	0.00
Cuatro Caminos (PM_{10}). (2014-2018)	19.58		
Cuatro Caminos (PM_{10}). (2008-2012)	27.27	1584	0.00
Cuatro Caminos (PM_{10}). (2014-2018)	19.58		

5. CONCLUSIONS

After having used functional data in order to represent PM_{10} and NO_2 pollution levels during the Spanish economy's boom, recession and recovery, and having selected the air monitoring stations located in Madrid City's areas suffering from heavy traffic, we could establish the similarities and differences in pollution levels for each phase of the business cycle. It is worth pointing out that this type of study involving environmental data framed within a functional context had never been done before.

The FKT coefficients calculated between different phases of the business cycle relative to those areas of Madrid that experience heavy traffic allow us to confirm that the inherent features to each phase of the business cycle act as automatic regulators of PM_{10} and NO_2 pollution levels. In this sense it should be noted that during the booming years pollution levels regarding these substances were higher than during the crisis (negative correlations or close to zero correlations). The similarities found between the economic boom and the recovery prove the effect that economic activities, basically production and consumption, exert on pollution levels. This is due to the fact that the negative and close to zero correlations that we obtained regarding PM_{10} and NO_2 levels between these two periods reflect that pollution levels differ significantly. Moreover, the follow-up of this study will allow to check what could happen to pollution levels depending on the current phase of the business cycle and will contribute to environmental policy decision-making in an urban context.

R E F E R E N C E S

ACDGMAS (2018). Dirección General de Medio Ambiente y Sostenibilidad - Área de Calidad Atmosférica (2019). "Informe anual sobre la calidad del aire de la Comunidad de Madrid. Año 2018" http://gestiona.madrid.org/azul_internet/ (viewed August 3rd, 2019).

Archer, C. L., Brodie, J. F., & Rauscher, S. A. (2019). Global Warming Will Aggravate Ozone Pollution in the U.S. Mid-Atlantic. *Journal of Applied Meteorology & Climatology*, 58(6), 1267–1278. https://doi.org/10.1175/JAMC-D-18-0263.1.

Ceballos M. A., Segura P., Alarcón E., Gutiérrez E., Gracia J. C., Ramos P., Reaño M., García B., Villeta C., García M., Aranda J. A., Prima H., Veiras X., Bárcena J., García J., Belmonte P., Luengo P., Navascués E. & Hernández K. (2018a) "La calidad del aire en el Estado español durante 2018". *Ecologistas en Acción*, https://www.ecologistasenaccion.org/?p=96516.

EEA (2018). "Air quality in Europe – 2018 Report". *European Environment Agency Reports*, No 12/2018, ISSN 1977-8449. https://www.eea.europa.eu/publications/air-quality-in-europe-2018.

Fontana, M., Tavoni, M., & Vantini, S. (2019). Functional Data Analysis of high-frequency load curves reveals drivers of residential electricity consumption. PLoS ONE, 14(6), 1–16. https://doi.org/10.1371/journal.pone.0218702.

Hysenaj, M. (2019). Dispersion model prospective of air pollution in Tirana. *Geographia Technica*, 14 (2), 10-19. doi: 10.21163/GT_2019.142.02.

Kendall, M. (1955). "A New Measure of Rank Corr elation". *Biometrika*. 30 (1–2): 81–89. https://doi.org/10.1093/biomet/30.1-2.81.

Kovács K.D. (2018). Evaluation of burned areas with Sentinel-2 using snap: the case of Kineta and Mati, Greece, july 2018. *Geographia Technica*, 14(2), 20-38. doi: 10.21163/gt_2019.142.03.

Lelieveld, J., Berresheim, H., Borrmann, S., Crutzen, P. J., Dentener, F. J., Fischer, H., Feichter, J., Flatau, P. J., Heland, J., Holzinger, R., Korrmann, R., Lawrence, M. G. , Levin, Z., Markowicz, K. M., Mihalopoulos, N., Minikin, A., Ramanathan, V., de Reus, M., Roelofs, G. J., Scheeren, H. A., Sciare, J., Schlager, H., Schultz, M. ., Siegmund, P., Steil, B., Stephanou E. G., Stier, P., Traub, M.,Warneke, C.,Williams, J., & Ziereis, H. (2002). Global air pollution crossroads over the Mediterranean, *Science* 298, 794–799.

Li, R., & Chow, M. (2005). Evaluation of reproducibility for paired functional data. Journal of Multivariate Analysis, 93(1), 81–101. https://doi.org/10.1016/j.jmva.2004.01.010.

López-Pintado, S., & Romo, J. (2009). On the Concept of Depth for Functional Data. *Journal of the American Statistical Association*, 104(486), 718–734. https://doi.org/10.1198/jasa.2009.0108.

Medina-Ramón M., Zanobetti A., & Schwartz J., (2006) "The Effect of Ozone and PM_{10} on Hospital Admissions for Pneumonia and Chronic Obstructive Pulmonary Disease: A National Multicity Study". *American Journal of Epidemiology*, 163 (6), pp 579–588, https://doi.org/10.1093/aje/kwj078.

Salvador, P., Artíñano, B., Viana, M. M., Alastuey, A., & Querol, X. (2015). Multicriteria approach to interpret the variability of the levels of particulate matter and gaseous pollutants in the Madrid metropolitan area, during the 1999–2012 period. Atmospheric Environment, 109, 205–216. https://doi.org/10.1016/j.atmosenv.2015.03.008.

Spain Government, Ministry for Ecological Transition, 2018 (2018). "Evaluación de la calidad del aire en España – Ano 2018", https://www.miteco.gob.es/es/calidad-y_evaluacion-ambiental/temas/atmosfera-y-calidad-del-aire/calidad-del_aire/visor/default.aspx (viewed August 3rd, 2019).

Valencia, D., Lillo, R. E., & Romo, J. (2019). "A Kendall correlation coefficient between functional data". *Advances in Data Analysis and Classification*. https://doi.org/10.1007/s11634-019-00360-z.

World Health Organization (2014). Burden of disease from ambient air pollution for 2012. Geneva, Public Health, Social and Environmental Determinants of Health Department, World Health Organization, Available from: http://www.who.int/phe/health_topics/outdoorair/databases/AAP_BoD_results_March2014.pdf?ua=1.

THE EFFECT OF AIR QUALITY ON THE INCIDENCE OF ACUTE RESPIRATORY INFECTION (ARI) IN PONTIANAK CITY

Rurika Widya Ningrum PALURENG[1], Arie Dipareza SYAFEI[1] ⓘ*, Abdu Fadli ASSOMADI* ⓘ*,*
Rachmad BOEDISANTOSO, Joni HERMANA, Wayan SUPARTA[2] ⓘ

ABSTRACT:
The Regional Health Office of Pontianak City stated that in 2017, acute respiratory infection (ARI) was the most common disease in the community with 83,128 cases, highest incidence in West Kalimantan. Air is the transmission medium of ARI. The incidence of ARI increases with population growth which can be a source of air pollution due to the many activities. This study aimed to determine the effect of air quality and the effect of the season on the incidence of ARI disease in Pontianak and policies that can be established by relevant government agencies to deal with ARI. The research used secondary data, consisted of air quality and ARI incidence data. The determination was analyzed using multiple linear regression statistical methods using the RStudio software application. The results found that air quality affected 46.71% of the ARI incidence in Pontianak. Influential pollutants are NO_2, SO_2, and CO_2. Analysis of the effect of the season showed that the air quality during the rainy season affected 65.76%, while in the dry season affected 22.67% of the ARI incidence in Pontianak. So to reduce the incidence of ARI in Pontianak, the action that we can take is by improving the air quality.

Key-words: *Acute Respiratory Infection (ARI), Air quality, Multiple linear regression, RStudio.*

1. INTRODUCTION

The World Health Organization (WHO) has reported that as many as 1.9 million children aged less than five die from acute respiratory infection (ARI) each year. Around 70% of ARIs occur in Africa and Southeast Asia. Based on epidemiological studies, the incidence of ARI in developing countries is estimated to reach 25% in children under the age of five years.

Indonesia is ranked as the country with the fifth-highest ARI incidence in the world (Anggraeni, 2017). ARI is among the top 10 diseases in hospitals. A mortality survey in 2013 placed ARI as the largest cause of mortality among children under five in Indonesia, causing 32.10% of deaths. Based on data from the Pontianak City Health Office (2018), the most common illness among people living in Pontianak City in 2017 was ARI. The data is based on reports from all community health centers in Pontianak. There were 83,128 cases of ARI in that year. Based on the RISKESDAS by the Indonesian Ministry of Health (2018) it was stated that Pontianak is the city with the highest ARI prevalence in West Kalimantan Province.

ARI attacks the body through the upper and lower respiratory tract, from the nose to the alveoli, including the adnexa, the sinus of the middle ear cavity, and the pleura. This infection is acute, lasting up to 14 days. ARI is usually caused by a virus or bacterium (Gagarani, 2015). Dinayah (2014) stated that the health status of a person is influenced by environmental factors, health behavior, available health services, and genetic factors. Of these, environmental factors have a greater influence on ARI. Poor environmental health and extreme climatic conditions can contribute greatly to health status (Haidu, 2009). Environmental factors also include air pollution (Hysenaj, 2019). According to Anggraeni (2017), air is a transmission medium for the cause of ARI, whether it is dust, bacteria, or viruses. Air is therefore a major environmental component in the spread of ARI.

Air quality is a problem closely related to the urban situation in Indonesia. Pontianak is the capital city of West Kalimantan Province that has a population of 637,723, with an annual growth rate of

[1]*Institut Teknologi Sepuluh Nopember, Department of Environmental Engineering, 60111, Surabaya, Indonesia, dipareza@enviro.its.ac.id.*

[2] *Universitas Pembangunan Jaya, Department of Informatics, South Tangerang City, Banten 15413, Indonesia, Corresponding author: wayan.suparta@upj.ac.id*

1.84% (BPS Pontianak City, 2019). According to Aprianto et al. (2018), the presence of a large number of residents in a city can be a source of air pollution because of the many activities that occur, including industrial activities, offices, land fires, and transportation. Based on the Indonesian National Board for Disaster Management (2018), forest fires occur in Pontianak City every year and in 2018 there are 21 incidents with the number of transportation which is grow every year. Therefore, this study was conducted with the aim of determining and identifying the effect of air quality ARI incidence in Pontianak, determining and identifying the effect of seasons on incidence, and determining policies that can be established by the relevant government agencies to deal with ARI.

2. METHODOLOGY

2.1 Study Area

This study used a research design based on ecological time trend study. Ecological study according to time is a research study design used to determine the relationship between the frequency of illness or death due to a type of disease in society over time (Adriyani, 2012). The research was located in Pontianak City. Pontianak City is the capital of West Kalimantan Province. The total area of Pontianak City is 107.82 km^2. Pontianak City is situated on the equator line, with latitude coordinates of $00^002'24"$ N – $00^05'37"$ S and longitude coordinates of $109^016'25"$ E – $109^023'04"$ E. Pontianak City is divided into six subdistricts: Pontianak Kota, Pontianak Barat, Pontianak Selatan, Pontianak Tenggara, Pontianak Timur, and Pontianak Utara, with a total of 29 urban villages (BPS Kota Pontianak, 2018). As a fulfillment of its health facilities aspect, Pontianak City is equipped with 23 community health centers.

Fig. 1. Map of Pontianak City *(Source: BPS Kota Pontianak, 2018).*

As an effort to manage air quality and control air pollution, Pontianak City has an air quality monitoring device commonly called the Air Quality Management System (AQMS). This tool is located in the Pontianak Tenggara Subdistrict Office, in accordance with the criteria for the placement of ambient air quality monitoring instruments in the State Minister of Environment Regulation No. 12 of 2010 concerning the Implementation of Air Pollution Control in the Region. The sampling inlet is ± 6 meters from the ground and free from barriers, with an open angle of 120^0.

The AQMS tool detects Pontianak City air quality concentrations in the form of sulfur dioxide (SO_2), nitrogen dioxide (NO_2), carbon monoxide (CO), ozone (O_3), and particulate matter (PM_{10}) concentrations. The raw data is sent every 30 minutes to the national Ministry of Environment and Forestry server, which displays the Air Pollution Index (API) figures daily at 3 pm. This can be accessed by the entire community so that the public can obtain information about air quality status.

2.2 Statistical Analysis

This research used secondary data to identify the effect of air quality in the form of SO_2, NO_2, CO, O_3, and PM_{10} concentrations on ARI incidence from 2012–2018 in Pontianak City, based on monthly report data. Respiratory disease data were obtained from the Pontianak City Health Office and air quality data were obtained from the Pontianak City Environment Office.

The analysis used univariate and bivariate analysis. Univariate analysis was performed to determine the frequency distribution, minimum value, maximum value, and average value of air quality variables. The results are presented as a monthly trend graph. Bivariate analysis was performed to identify the relationship between air quality and the ARI incidence in Pontianak, conducted with multiple linear regression methods using the RStudio application. The multiple linear regression models is used to examine the relationship or effect of two or more independent variables on the dependent variable. The general form of multiple linear regression models is as follows (Kutner, 2004):

$$Y_i = \beta_0 + \beta_1 X_{i\,1} + \beta_2 X_{i\,2} + \cdots + \beta_n X_{i\,n} + \varepsilon_i \tag{1}$$

where
Y_i	=	dependent variable for the i-th observation, for i = 1, …, n.
$\beta_0, \beta_1, …, \beta_n$	=	regression parameters or coefficients
$X_{i\,1}, X_{i\,2}, …, X_{i\,n}$	=	independent variable
ε_i	=	the remainder (errors) for the i-th observation.

Known variables in this study are as follows:

- Dependent variable (Y_i)
  The dependent variable in this study is ARI, which consists of pneumonia, severe pneumonia, or not pneumonia.
- Independent variable ($X_{i\,n}$)
  The independent variables in this study include air quality data and meteorological data. The air quality data includes the concentration of air pollutant parameters at the API station, namely CO ($\mu g/m^3$), O_3 ($\mu g/m^3$), NO_2 ($\mu g/m^3$), SO_2 ($\mu g/m^3$), and PM_{10} ($\mu g/m^3$).

4. RESULTS AND DISCUSSIONS

4.1 Univariate Analysis of Each Concentration

Univariate analysis results provide an overview of each research variable in the form of air quality concentration, namely SO_2, NO_2, CO, O_3, and PM_{10}.
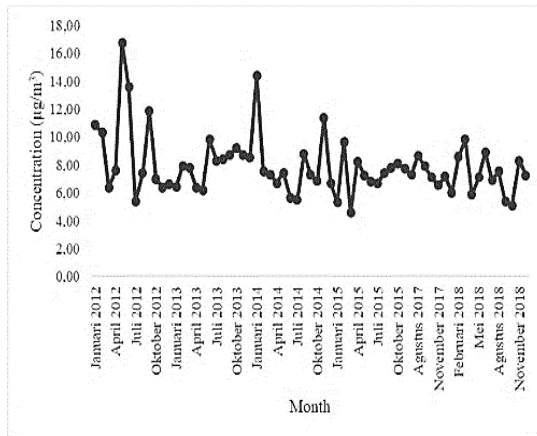
Fig. 2. NO₂ air quality in Pontianak City, 2012–2018.
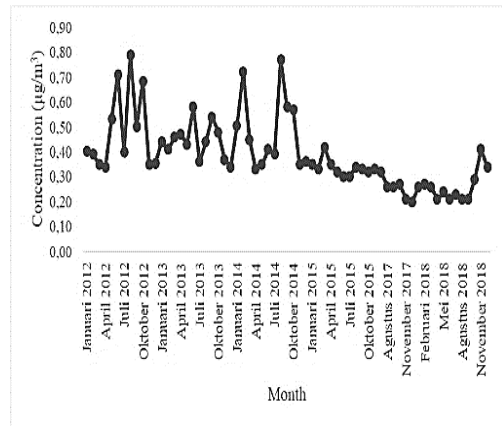
Fig. 3. CO air quality in Pontianak City, 2012-2018.

The results of the analysis based on the **Fig. 2** showed an average value of NO_2 of 7.90 µg/m³ with a standard deviation of 7.90. The lowest NO_2 concentration was 4.57 µg/m³ while the highest was 16.74 µg/m³. The average value of NO_2 when converted to API figures became TD (not specified), which based on the Decree of the Minister of Environment No. KEP-45/MENLH 10/1997 is in the 'good' category.

The results of the analysis based on the **Fig.3** showed an average value of CO of 0.39 mg/m³ with a standard deviation of 0.14. The lowest NO_2 concentration was 0.20 mg/m³ while the highest was 0.79 mg/m³. The average value of NO_2 when converted to API figures became 3.9, which based on the Decree of the Minister of Environment No. KEP-45/MENLH 10/1997 is in the 'good' category.
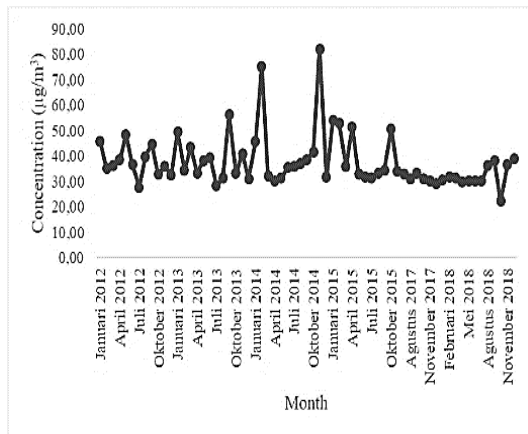
Fig. 4. O₃ air quality in Pontianak City, 2012–2018.
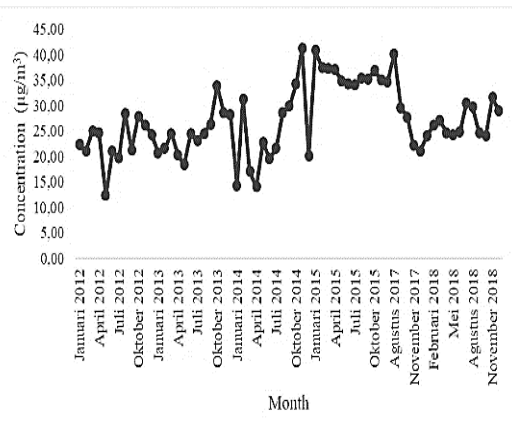
Fig. 5. SO₂ air quality in Pontianak City, 2012–2018.

The results of the analysis based on the **Fig.4** showed an average value of O_3 of 37.61 µg/m³ with a standard deviation of 7.90. The lowest O_3 concentration was 22.28 µg/m³ while the highest was 82.08 µg/m³. The average value of O_3 when converted to API figures became 15.67, which based on the Decree of the Minister of Environment No. KEP-45/MENLH 10/1997 is in the 'good' category.

The results of the analysis based on the **Fig.5** showed an average value of SO_2 of 27.04 µg/m³ with a standard deviation of 7.90. The lowest SO_2 concentration was 12.32 µg/m³ while the highest was 41.22 µg/m³.

The average value of SO_2 when converted to API figures became 16.9, which based on the Decree of the Minister of Environment No. KEP-45/MENLH 10/1997 is in the 'good' category. The results of the analysis based on the **Fig.6** showed an average value of PM_{10} of 41.26 μg/m³ with a standard deviation of 7.90. The lowest PM_{10} concentration was 12.25 μg/m³ while the highest was 146.54 μg/m³. The average value of PM_{10} when converted to API figures became 41.26, which based on the Decree of the Minister of Environment No. KEP-45/MENLH 10/1997 is in the 'good' category but approaching 'moderate'.
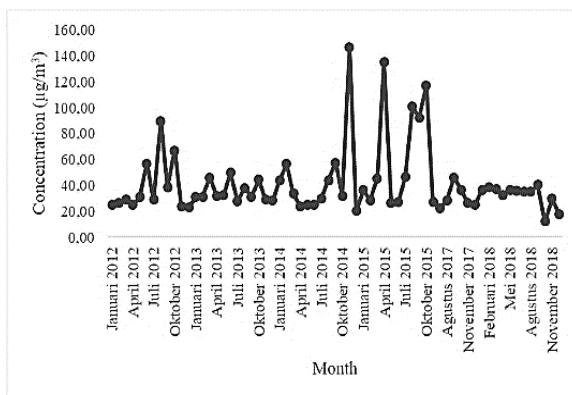
Fig. 6. PM_{10} air quality in Pontianak City, 2012–2018.

4.2 Bivariate Analysis and Effect of Air Quality on ARI Incidence in Pontianak City

Before analyzing the effect of air quality on ARI incidence in Pontianak using multiple linear regression models, a correlation analysis test was performed as shown in **Table 1** to get correlation between two variables, independent variable and the dependent variable. If the p-value is smaller than the significance value (α=0.05), so there's a correlation between the two variables.

Based on **Table 1**, all the independent variables have a correlation with the dependent variable. Then the estimation results of multiple linear regression models regarding the impact of air quality NO_2, CO, O_3, SO_2, and PM_{10} in Pontianak on ARI incidence can be seen in **Table 2**.

Table 1.
**The correlation analysis between air quality parameters
with the ARI incidence in Pontianak.**

	p-value	Correlation Analysis
NO$_2$	0,0077	0,3275
CO	0,0020	0,3756
O$_3$	0,0009	0,4007
SO$_2$	0,0004	0,4264
PM$_{10}$	0,0166	0,2961

The extent of the contribution of air quality to ARI incidence in Pontianak is known through its coefficient of determination (adjusted R^2) as shown in **Table 2**, which is 0.4671. This means that the incidence can be explained by the air quality variables with an effect size of 46.71%. The remaining is contributed by other factors or variables not discussed in this study.

Determination of the influence of each variable can be seen from the p value. If the p value < level of significance (α=0.05), there is a significant influence of these variables. So it can be seen that NO_2, CO, and SO_2 influence the ARI incidence in Pontianak.

Table 2.
Estimation results of multiple linear regression models.

	Coefficient	t value	p value
Intercept	-479,274	- 0,840	0,4042
NO_2	130,505	2,973	0,0043**
CO	2172,618	3,228	0,0020**
O_3	5,881	0,563	0,5754
SO_2	72,937	4,882	$1,04 \times 10^{-5}$***
PM_{10}	- 3,952	- 0,982	0,3303
$R^2 = 0,4671$			
F-statistik $= 10,34$			
p-value $= 3,73 \times 10^{-7}$			

Li et al. (2018) found that the increasing number of ARI among children aged 0-14 years in Heifei was the effect of short-term exposure to air pollution, especially NO_2 as the main air pollutant that affected. This caused an increase the number of hospital visits due to ARI. Humans can produce NO_2 into the air from the use of vehicles and burning charcoal, natural gas, and so on. Hrp's research (2018) also found a relationship between NO_2 and the ARI incidence. NO_2 is four times more toxic than NO gas. The lungs are particularly sensitive to NO_2 gas pollution. Lungs contaminated with NO_2 gas swell so that the patient has difficulty in breathing, which can lead to death. NO_2 gas first affects the mucous membranes, causing the respiratory tract to swell and stimulating cell growth so that the respiratory tract becomes narrowed, triggering the release of cilia and mucous cell layers. This situation prevents microorganisms that enter from being removed from the respiratory tract, which becomes susceptible to infection.

SO_2 in the air is produced by forest fires and transportation fuels. SO_2 remains in the air with a slight concentration of water vapor, but if there is enough water vapor in the air, then a reaction occurs with SO_3 to form H_2SO_4, which affects the mucous membranes of the nose, throat, respiratory tract, and eventually lungs. The primary effect of SOx pollutants on humans is irritation of the respiratory system. SO_2 pollutants are considered harmful to health, especially for older adults and people with chronic respiratory conditions (HRP, 2018).

According to Irawan et al. (2017), a relationship exists between CO exposure and hospital visits due to respiratory problems, with a risk of 1.10 and 1.15 after three days of CO exposure at a concentration of 200 ppb. However, several other studies have suggested that CO concentration is not related to the incidence of ARI. This is possible because the main effect of CO pollutants on health is shifting Hb to COHb. According to PDPI (2019), inhalation of CO has the potential to increase COHb in the blood and can cause headaches, shortness of breath, nausea, and other symptoms. This allows infection through reduced immunity.

This present study found no correlation between O_3 or PM_{10} concentrations and the ARI incidence in Pontianak City. Most researchers conclude that these two pollutants affect ARI incidence. O_3 is a very strong oxidant that can be irritant to the respiratory tract and has lower solubility than SO_2 and NO_2. Therefore, almost all O_3 can penetrate the alveoli, causing symptoms of cough, dry throat, and discomfort in the eyes, chest pain, and headaches. PM_{10} is mostly produced by forest or land burning, transportation activities, and wind-borne dust. PM_{10} in the air that enters the body can be detrimental to the respiratory system. In general, its particulate size of about 5 microns means it can directly enter the lungs and settle in the alveoli. Inhalation of 10-micron matter of PM_{10} can cause irritation of the upper respiratory tract (HRP, 2018).

The non-existent relationship between O_3 or PM_{10} and the ARI incidence in Pontianak City is possibly due to the lack of specific data analyzed. This is because this study used monthly data, where the concentration value was the average for each one-month period. This data condition definitely affected the outcomes, which are still lacking possible specifics. In addition, not all variables that affect ARI are discussed in this study, even though these other variables may be relevant to Pontianak City.

4.3 Effect of the Season on ARI Incidence in Pontianak City

The estimation results of correlation analysis and multiple linear regression models regarding the impact of air quality of NO_2 (µg/m^3), CO (µg/m^3), O_3 (µg/m^3), SO_2 (µg/m^3), and PM_{10} (µg/m^3) in Pontianak on ARI incidence can be seen in **Table 3** and **Table 4.**

Table 3.

Correlation analysis the effect of season.

	Rainy Season		Dry Season	
	p-value	**Correlation Analysis**	**p-value**	**Correlation Analysis**
NO_2	0,0015	0,5894	0,0999	0,2673
CO	0,0441	0,3979	0,0039	0,4515
O_3	0,0055	0,5291	0,0614	0,3023
SO_2	0,0018	0,5815	0,0644	0,2991
PM_{10}	0,0730	0,3574	0,0455	0,3222

Table 4.

Estimation results of multiple linear regression models based on the effect of season.

	Rainy Season			Dry Season			
	Coefficient	**t value**	**p value**	**Coefficient**	**t value**	**p value**	
Intercept	- 1161,409	- 1,674	0,1106	**Intercept**	7212,794	1,729	0,0926
NO2	215,886	3,103	0,0059**	**CO**	2014,311	2,371	0,0234*
CO	1504,961	1,512	0,1471	**PM10**	7,293	1,294	0,2040
O3	- 9,563	- 0,635	0,5328				
SO2	72,288	3,697	0,0015**				
PM10	- 1,526	- 0,308	0,7616				
R2 = 0,6576				R2 = 0,2267			
F-statistic = 9,003				F-statistic = 4,714			
p-value = 9,856 × 10-5				p-value = 0,0072			

The extent of the contribution of air quality effect to ARI incidence in Pontianak is known through its coefficient of determination (adjusted R^2) in **Table 4**, which was 0.6576in the rainy season and 0.2267 in the dry season. This means that the ARI incidence in Pontianak City can be explained by air quality with an effect size of 65,76% in the rainy season and 22,67% in the dry season. The rest is explained by other factors or variables not discussed in this study. This means that air quality is more affected on the ARI incidence during the rainy season than during the dry season. During rainy season, air quality has a dominant effect on ARI incidence Pontianak City. Meanwhile, during the dry season, the influence of other variables not examined in this study is more affected.

As noted by Ernyasih et al. (2018), rainfall can increase the incidence of ARI, because an area becomes cold and humid. The effect of this rainy season is residential density, which affects cross-infection where coughing and sneezing accelerate ARI transmission. Gagarani (2015) stated that the epidemic of ARI, which is often called a seasonal disease, takes place in the fall and winter: around October to March. In a tropical country such as Indonesia, it can take place throughout the year, with a peak in the rainy season. This happens because of the etiology of ARI, such as bacteria or viruses that prefer low humidity and temperature. The incidence of ARI also increases during the change of seasons. This is due to the decrease in body defenses due to changing weather.

4.4 Government Policy in Tackling the Incidence of ARI Disease

Based on the analysis, it was found that the air quality parameters that effected ARI incidence in Pontianak City are NO_2, CO, and SO_2 which these parameters are sourced from the transportation, forest and land fires, and burning waste.

Brugha and Grigg (2014) said that the actions to prevent traffic congestion and reducing emissions (such as zero-emissions vehicles) were an appropriate effort to improve the air quality. The introduction of cleaner indoor fuels and more efficient cook stoves around the world showed promise in reducing deaths from ARI incidence.

Many actions have been taken by the Pontianak City government in tackling forest fires. In terms of prevention, signs forbidding forest fires have been installed (**Fig.7**) in accordance with Law No. 32 of 2009, as well as evacuation route signs (**Fig. 8**) and sign of areas of forest and land fires (**Fig. 9**). The government has also issued a number of policies to increase awareness of haze. Several oxygen houses have been provided in various locations as facilities for use by the community during haze.

Fig. 7. Signs forbidding forest fires.

Fig. 8. Evacuation route signs.

Fig. 9. Sign of areas of forest and land fires.

Poor air quality is also caused by the transportation sector and burning waste. Therefore, it is necessary to affirm the rules regarding mandatory motor vehicle emissions testing as well as the prohibition of waste burning activities. The next government step that needs to be prepared is to add air quality monitoring stations. The limited air quality monitoring, with only one unit in Pontianak City, causes a lack of information on overall air quality. It is feared that this will not be able to provide a representative picture of air quality in Pontianak City. Additional monitoring stations are expected to be installed and accompanied by proper maintenance efforts. Furthermore, air quality monitoring stations are expected to provide an early warning if poor air quality is identified, to reduce the incidence of ARI.

5. CONCLUSIONS

Air quality in Pontianak City has an effect on ARI incidence. The effect size is 46.71%, with the remainder possibly caused by other variables as assessed in this study. Influential pollutants are NO_2, SO_2, and CO, which sourced from the transportation, forest and land fires, and burning waste and can cause infections in the human respiratory tract. The absence of a relationship between O_3 or PM_{10} and ARI incidence in Pontianak may be due to the lack of specificity of the data analyzed. Besides that, air quality effected ARI incidence with an effect size of 65.76% in the rainy season and 22.67% in the dry season. The rest is explained by other factors or variables not discussed in this study. This means that air quality is more affected on the ARI incidence during the rainy season than during the dry season. During rainy season, air quality has a dominant effect on ARI incidence Pontianak City. Meanwhile, during the dry season, the influence of other variables not examined in this study is more affected. So to reduce the incidence of ARI in Pontianak, the action that we can take is by improving the air quality. Many actions have been taken by the Pontianak City government, but it is necessary to affirm the rules so the air quality in Pontianak so it can be prevent the occurrence of poor air quality in Pontianak. Besides that, additional monitoring stations are expected to be installed and accompanied by proper maintenance efforts because only one air quality and monitoring station unit in Pontianak and it can causes a lack of information on overall air quality. Furthermore, air quality monitoring stations are expected to provide an early warning if poor air quality is identified, to reduce the incidence of ARI.

R E F E R E N C E S

Anggraeni, S. N. (2017) *relationship of air quality in home with complaints symptoms of acute respiratory infection in children less than five in marunda flats in north*. Thesis, Universitas Islam Negeri Syarif Hidayatullah, Jakarta.

Aprianto, Y., Nurhasanah. & Sanubary, I. (2018) Particulate Matter (PM10) Prediction for Air Quality Monitoring Using Artificial Neural System with Case Study in Pontianak City. *Positron,* 8 (1), 15-20.

Adriyani, S. (2012) *The relationship between climate factors and chikungunya disease in West Java region in 2002-2010.* Thesis, Universitas Indonesia, Depok.

BPS Kota Pontianak. (2018) *Pontianak City in Figures 2018.* Pontianak Central Statistics Agency, Pontianak.

BPS Kota Pontianak. (2019) *Pontianak City in Figures 2019.* Pontianak Central Statistics Agency, Pontianak.

BPS Kota Pontianak. (2018) *Pontianak City Health Statistics 2017.* Pontianak Central Statistics Agency, Pontianak.

Brugha, R. & Grigg, J. (2014) Urban air pollution and respiratory infections. *Paediatric Respiratory Reviews*. 15(2), 194-199. doi: 10.1016/j.prrv.2014.03.001

Dinas Kesehatan Kota Pontianak. (2018) *Pontianak city health profile in 2017.* Pontianak City Health Office, Pontianak.

Dinayah, K. C. (2014) Air quality, lung function, and respiratory complaints of housewives in affected and unaffected areas of the lapindo mudflow. *Jurnal Kesehatan Lingkungan*, 7 (2), 90-97.

Gagarani, Y. (2015) *Relationship between mother's knowledge level and early management of acute respiratory infection in* . Thesis, Universitas Diponegoro, Semarang.

Haidu, I. – editor (2009) Extremes climatiques: genese, modelisation et impacts. *Geographia Technica*, **4,** Special Issue. 493 pp.

Harahap, M. A. (2018) *Relationship between ambient air quality (O_3, SO_2, NO_2 and PM_{10}) and the incidence of ARI (acute respiratory infection) in Pekanbaru City in 2014. Thesis*, Universitas Sumatera Utara, Medan.

Indonesian Ministry of Health. (2018) *RISKESDAS 2018.* Health Research and Development Agency, Jakarta.

Irawan, A., Sutomo, A. H. & Sukandarrumidi. (2017) Air pollution standards index, meteorological factors, and ARI Occurrence in Pekanbaru. *Journal of Community Medicine and Public Health (Berita Kedokteran Masyarakat)*, 33 (1), 15-32.

Kutner, M. H., Nachtsheim, C. J. & Neter, J. (2004) *Applied Linear Regression Models 4th Ed*, Mc. Graw-Hill Companies Inc, New York.

Li, Y. R., Xiao, C. C., Li, J., Tang, J., Geng, X. Y., Cui, L. J. & Zhai, J. X. (2018) Association between air pollution and upper respiratory tract infection in hospital outpatients Aged 0-14 years in Hefei, China: a time series study. *Public Health*, 156 (92), 92-100.

Hysenaj, M. (2019) Dispersion model prospective of air pollution in Tirana. *Geographia Technica*, **14** (2), 10-19.

PDPI (2019) *Prevention and Management of Health Impacts from Forest Fire Smoke. Universitas Indonesia*, Depok.

FLOOD RISK AREAS SIMULATION USING SWAT AND GUMBEL DISTRIBUTION METHOD IN YANG CATCHMENT, NORTHEAST THAILAND

Haris PRASANCHUM[1]* *, Panuthat SIRISOOK[2], Worapong LOHPAISANKRIT[1]*

ABSTRACT:
Flooding problems have resulted in damage to urban and agricultural areas during the rainy season in the northeast of Thailand. Flood risk assessment at sub-catchment levels and proper explication of risk area can be guidelines for effective protection planning. This study aims to assess flood risk areas in the Yang catchment based on hydro-meteorological data between 2008-2016 by using the SWAT model for analyzing the maximum monthly discharge at each sub-catchment and fitted to the Gumbel distribution in order to evaluate flood risks in return periods of 2, 5, and 10 years. The results indicated that the calibrated the SWAT model can reasonably simulate discharge at the observed stations based on the statistical indicators such as R^2, RE, and E_{ns}. According to the Gumbel distribution methods, the western sub-catchments of the Yang catchment had a high level of flood risks. However, the other in the east sub-catchments were found to have lower levels of flood risks. The methods and results of this study can be useful tools and information for improving an understanding among stakeholders in the affected area in order to reduce damage from flooding in the future.

Key-words: *Yang catchment, discharge, flood risk area, SWAT, Gumbel distribution.*

1. INTRODUCTION

Discharge is the key factor that strongly causes the flood and it is mainly affected by climate and land use changes (Chung et al., 2018). In case that the discharge is much higher than the catchment capacity of rivers or reservoirs and the flow becomes uncontrollable, the excessive volume of the discharge may somehow cause the flood in which the damage levels depends on types of the area, and time period when the flood exists. The fact is that the discharge can be directly estimated at the observed stations that have been situated at many rivers through the past 10 years since the flood could cause a great loss of human's life and properties (Asgharpour & Ajdari, 2011). In order to lessen and prevent the loss as well as to efficiently manage the limited natural resources in the future, the flood frequency and flood-risk areas have been analyzed and detected using several data indexes (Bhagat, 2017) as a tool to directly and indirectly define the conditions of the flood.

Over the last decade, mathematical models have been broadly used to assess the hydrologic processes existing around a catchment for the discharge studies and simulation for medium and small catchments (Haidu & Ivan, 2016; Haidu et al., 2017; Strapazan & Petruţ, 2017). Particularly, SWAT (Soil and Water Assessment Tool) is a semi-distributed model interfaced with ArcGIS that has been popularly implemented since it is able to simulate physical characters of a catchment with a distributed-parameter system following the actual data from the target area and effective calculation procedure (Begou et al., 2016). The model is also able to simulate a site for the discharge assessment from the hydrological data and the data from the observed station and it gives the outcome that is very similar to the actual data.

---

[1]*Faculty of Engineering, Rajamangala University of Technology Isan, Khon Kaen Campus,*

Khon Kaen, 40000, Thailand, **corresponding author haris.pr@rmuti.ac.th; worapong.lo@rmuti.ac.th*

[2]*Regional Irrigation Office 6, Khon Kaen, 40000, Thailand; banana60@gmail.com*

Actually, the discharge data is very necessary for a catchment since it is not only the standard to show the capacity of the catchment for water resource management, but it can be linked to define the flood risk index by analyzing the annually maximum flow rate with a Gumbel frequency distribution method (Győri et al., 2016; Bhagat, 2017). The result from this analysis method can define the severity levels and predict the time period when the flood is coming. This can definitely be one of the methods to decrease the loss after the flood.

In this case, Yang Catchment in the northeast of Thailand, a lot of people have mad use this river especially for agricultural purposes. Unfortunately, the flood has been regularly found around the Yang Catchment through many decades and it has a severe impact on the life quality of the local people in the area. The problem previously mentioned seems to be a negative consequence of the land use and climate changes so that the accurate estimation of the discharge as the source of the flood during the raining season (Ivan et al., 2018) as well as a quick data distribution to reach out all stakeholders will surely facilitate effective water resource management and prevent any problems that might come after the flood in the area. This study hence aims to investigate the maximum discharge with strong impact on the flood using the SWAT model together with a Gumbel frequency distribution method in order to predict and estimate the possibility rate of the flood in the regional river catchments. The result would be presented as spatial map in GIS and it would be able to decrease the impact of the flood on the local agriculture as well as a tool for either water management or lessen any problems coming after the flood in the future.

2. STUDY AREA

Yang Catchment is located at the eastern part of Chi Catchment and most of the area is flat and undulating covering 4,145 km^2. Based on a 10-year climate data from the Thai Meteorological Department (during 2008-2016), the monthly average temperature can be 22.7-29.7 °C. The rainy season typically starts from May to October and the average rainfall is about 1,200 mm per year. There are 2 discharge observed stations found in the area including the E54 and E92 as presented in **Fig. 1(a)**. Most of the discharge will be found from June to May and the average annual discharge is 1,336 million cubic meter (MCM).
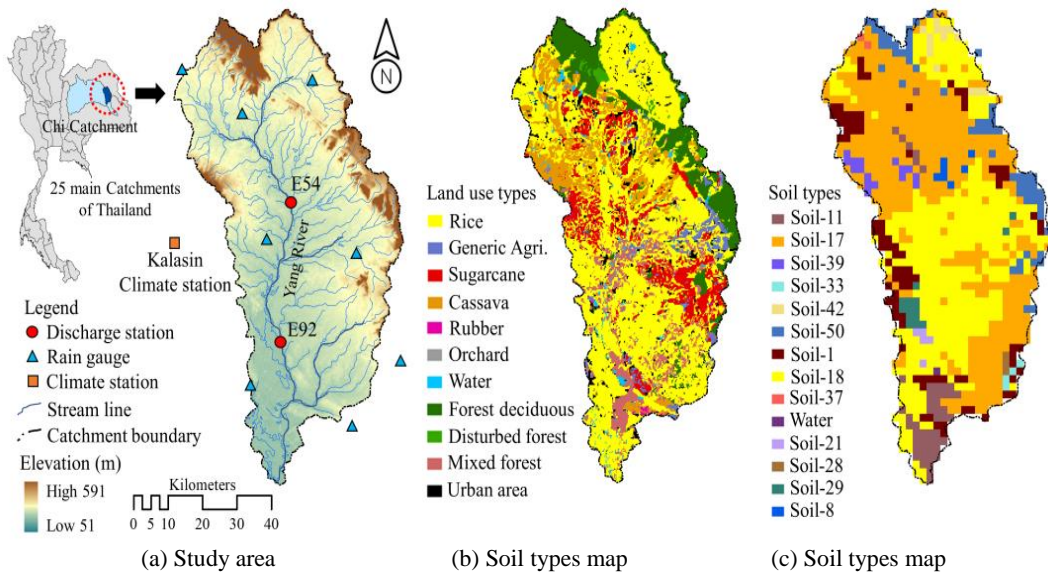
Fig. 1. Study area and spatial data map.

3. METHODOLOGY

3.1. Sub-catchment area and discharge simulations

3.1.1. SWAT model and data collection

The SWAT model (Arnold et al., 1998) is a semi-distributed hydrologic model purposively developed to estimate the hydrological conditions, the discharge form past to present, and predict any situations in the future (Maghsood et al, 2019). The feature of this model is that it can simulate watershed delineation to separate the whole area into sub-catchments (Pereiraa et al., 2016) and create the river route based on the user's need from digital elevation model (DEM) of each sub-catchment created by the model. This allows the user to know the discharge in each sub-catchment which is a great benefit for the spatial data analysis on the discharge from the regional catchments. In term of data calculation, the SWAT model principally considers any hydrological processes using a water balance equation as illustrated in Eq. (1) (Sajikumar & Remya, 2018).

$$SW_t = SW_0 + \sum_{i=1}^{t}\left(R_{day} - Q_{surf} - E_a - W_{seep} - Q_{qw}\right) \tag{1}$$

where, SW_t was final soil water content (mm), SW_0 was initial soil water content (mm), t was time (day), R_{day} was rainfall on day i (mm), Q_{surf} was surface water content on day i (mm), E_a was evapotranspiration rate on day i (mm), W_{seep} was groundwater water content on day i (mm), and Q_{gw} was groundwater return to discharge on day i (mm).

The model requires the input data in order to create Hydrologic Response Units (HRUs) (Ning et al., 2015) and different parameters for the discharge calculation e.g. digital elevation model (DEM), climate and daily rainfall data (from 9 Stations as illustrated in **Fig. 1(a)**), different spatial data, and the discharge data from the observed stations for data calibration on the model's outcome as presented in **Table 1**. Samples of important spatial data were soil types and the land use as presented in **Fig. 1(b)** and **Fig. 1(c)** that the most of soil types consist of 2 types which are Soil-17 (sandy loam to sandy clay loam) and Soil-18 (similar like Soil-17 but increased by increasing in depth). The land contains low to moderate fertility. Regarding the land use, Yang Catchment is mostly used for agriculture or 75% of the area and a regular plant is rice. Meanwhile, 12% of the area is the forest zone and another 3.5% is the local community zone.

Table 1.

Spatial data for input to the SWAT model and for evaluate model accuracy.

Data types	Periods	Scale	Source
Digital Elevation Model (DEM)	2015	30x30 m	Land Development Department
Catchment boundary and river map	2015	1:50,000	
Soil type map	2015	1:50,000	
Land use map	2015	30x30 m	
climate data	2008-2016	Daily	Thai Meteorology Department
Rainfall data (9 Stations)	2008-2016	Daily	
Discharge data from 2 observed stations (E54 and E92)	2008-2016	Daily	Royal Irrigation Department

3.1.2. Model calibration and validation

The model calibration and validation were performed to assess the effectiveness of the outcome derived from the SWAT model (Kumar et al., 2017) to confirm its accuracy compared with the field data (Lin et al., 2015). These methods were done by comparing the discharge from 2 observed stations − E54 and E92 with the calculated result from the SWAT model specifically for the monthly scale.

The calibration period was from 2008 to 2013 (6 years) and the validation period was from 2014 to 2018 (3 years). During this step, the model needed to adjust the hydrological sensitivity parameters (Fukunaga et al., 2015) that might have some impact on the discharge and 7 parameters were mentioned in this study including SOL_AWC, ESCO, ALPHA_BF, SLSUBBSN, GW_DELAY, SURLAG, and CH_N2. Additionally, 3 types of indexes were used for the model assessment consisting of Coefficient of Determination (R^2), Relative Error (RE), and Nash-Suttclife efficiency (E_{ns}) as illustrated in Eq. (2)-(4), respectively.

$$R^2 = \left(\frac{\sum_{i=1}^n (Q_{oi} - \overline{Q})(Q_{si} - \overline{Q_s})}{\sqrt{\sum_{i=1}^n (Q_{oi} - \overline{Q})^2} \sqrt{\sum_{i=1}^n (Q_{si} - \overline{Q})^2}} \right)^2 \tag{2}$$

$$RE = \left(\frac{Q_s - Q_o}{Q_o} \right) \times 100 \tag{3}$$

$$E_{ns} = 1 - \left(\frac{\sum_{i=1}^n (Q_o - Q_s)^2}{\sum_{i=1}^n (Q_o - \overline{Q_s})^2} \right) \tag{4}$$

where i was the data order, n was number of total data, Q_{oi} was the observed data at time i, $\overline{Q}$ was the average of all observed data, Q_{si} was the data from model at time i, and $\overline{Q_s}$ was the average from the model.

3.2. Gumbel frequency distribution method

Gumbel frequency distribution is a method that can be applied to find the extreme value distribution function (Pinherio & Ferari, 2016; Parhi, 2018) in a variety of both hydrological and meteorological works such as the maximum flood or rainfall prediction (Olumide et al., 2013; Ganamala & Kumar, 2017,), etc. This technique is exactly applicable for the area with a short-term maximum discharge (Bhagat, 2017) and, this technique was used in Thailand to statistically study the flood risk at Yang Catchment under the climate changes in the future (Shrestha & Lohpaisankrit, 2017). The equation to analyze the maximum flood in different return periods was depicted in Eq. (5).

$$Q_T = \overline{Q} + K\sigma \tag{5}$$

where Q_T was maximum discharge in return period time T, $\overline{Q}$ was average maximum discharge, K was frequency factor (see Eq. (6)), and σ was standard deviation (see Eq. (7)).

$$K = \frac{Y_T - \overline{Y}_n}{S_n} \tag{6}$$

$$\sigma = \sqrt{\frac{\sum (Q - \overline{Q})^2}{N - 1}} \tag{7}$$

where Y_T was reduced variable as seen in Eq. (8), and S_n was reduced mean and reduced standard deviation respectively depending on the data number of year N, and Q was annual maximum discharge.

$$Y_T = -\left[\ln . \ln . \left(\frac{T}{T-1}\right)\right] \tag{8}$$

3.3. Study procedure and flood risk area mapping

The procedure of the flood frequency analysis and flood-risk area mapping at Yang Catchment was illustrated in **Fig. 3** and the overview of all details were discussed in the sub-section 3.3.1-3.3.4.

3.3.1. Separating the sub-catchments: The sub-catchments were separated during the step of watershed delineation of the SWAT model (Swain et al., 2018) in which each sub-catchment could present the maximum discharge at the desired period and it chose to present the monthly data (the model already passed the calibration and validation method) so the result would be consistent with the discharge verification and calibration between the SWAT model and the observed stations.

3.3.2. Creating a relationship between the discharge and return period: The maximum discharges from each sub-catchment during 2008-2016 (9 years) was used to create a relationship between the flow rate and return period using a Gumbel frequency distribution method (Subyani, 2011). This method was resulted as an equation for the maximum discharge predication at different return periods (2, 5, and 10 years respectively).

3.3.3. Calculating the flood frequency: The maximum discharge derived in the previous sub-section was processed to find the mean score of each sub-catchment as the standard value to define the severity levels of the flood and then the differences between the maximum discharge and the average maximum discharge of every return period were calculated.

3.3.3. Creating the flood-risk area map: The discharge derived from the equations at each different return period from each sub-catchment was converted to a shape file and prepared to put into ArcGIS Model in which the severity levels of the flood were based on the maximum discharge classified into different ranges (100 MCM) and each period was differentiated by the color intensity of each different sub-catchment made by the SWAT model. The result was presented as the spatial map.
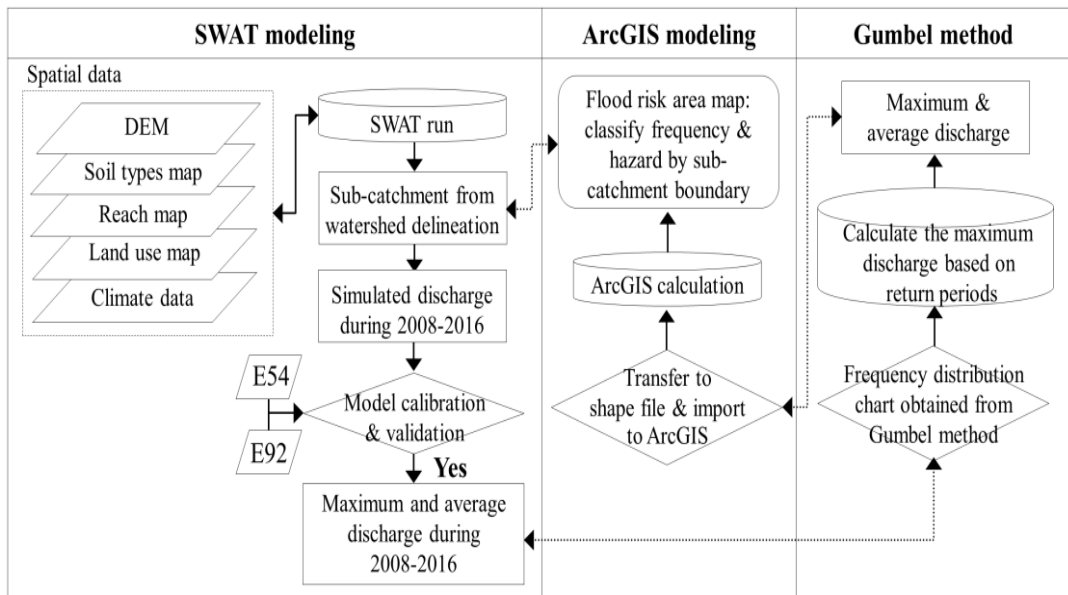
Fig. 3. Study procedure diagram.

4. RESULT AND DISCUSSIONS

4.1. Discharge analysis by SWAT

The watershed delineation of Yang Catchment was resulted as 15 sub-catchments as presented in **Fig. 4(a)** and each of these sub-catchments was analyzed to define and present the discharge of itself. **Table 2** presents the sensitivity parameters after adjusting to make the discharge from E54 and E92 Stations match one another the most. After comparing the discharge derived from the SWAT model with the data from Station E54 during 2008-2016 (9 years), the model demonstrated the annual average of 495.3 MCM which was higher than the result form the observed station where it was 446.1 MCM (RE average = 9.9%). At meantime, when compared with Station E92, the SWAT model showed the annual average of 984.3 MCM that was higher than the result from the observed station where it was 833.3 MCM (RE average = 15.3%). In case of using R^2, the results from both E54 and E92 Stations were 0.86 and 0.91 (on average) respectively. This was similar to E_{ns} where the results from both stations were 0.85 and 0.90 (on average) respectively. However, these results were still at a good rate of accuracy. The goodness of fit of a whole 9 years from E54 and E92 were also illustrated in **Fig. 4(b)**-**(c)**.
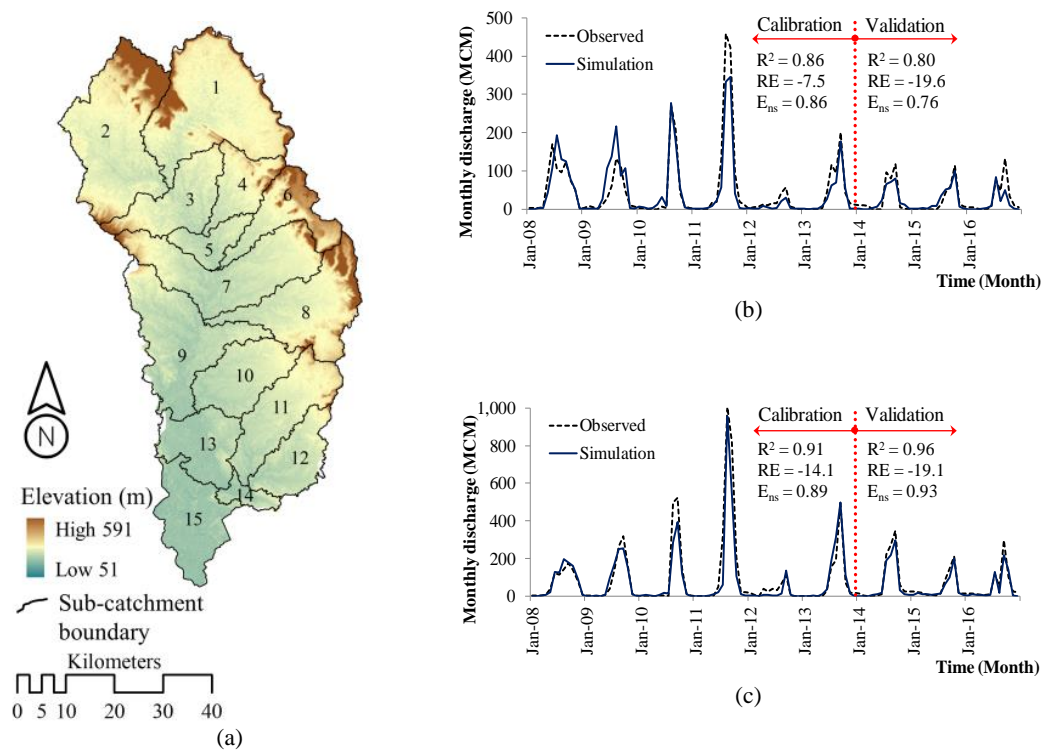
Fig. 4. SWAT simulation results, (a) 15 Sub-catchment in Yang Catchment, and discharge comparison between observed and simulation at (b) E54 and (c) E92.

Fig. 5 presents the monthly discharge of all 15 sub-catchments classified by the SWAT model after passing the verification method. The calculation results indicate the consistency with baseline year discharge from both observed stations. In the year 2008-2010, the value is close to the normal average and in 2011 has increased due to the period of high rainfall. The maximum discharge value will occur in the sub-catchment No.15, which is also the outlet point of the Yang Catchment, (the maximum discharge value was 642 MCM, occurring in 2011). In contrast, the result from 2012-2016 was lower than the average since the rainfall was decreased. After all, the monthly maximum discharges in each year were used to create the equations for Gumbel frequency distribution and flood

frequency chart that was finally derived as the maximum flow rate equation to find the maximum flow rate of each return period.

SWAT final adjusted sensitivity parameters.

No.	Parameter	Description	Range	Before	Final
1	SOL_AWC	Available water capacity	0 - 1	0.14	0.4
2	ESCO	Soil evaporation	0 - 1	0.95	0.85
3	ALPHA_BF	Base flow alpha factor	0 - 1	0.048	0.0001
4	SLSUBBSN	Average slope length	10 - 150	15.42	12.00
5	GW_DELAY	Groundwater delay time	0 - 500	31	30
6	SURLAG	Surface runoff lag coefficient	0.05 - 24	2	1.27
7	CH_N2	Manning's "n" value for the main channel	0 - 0.30	0.014	0.013
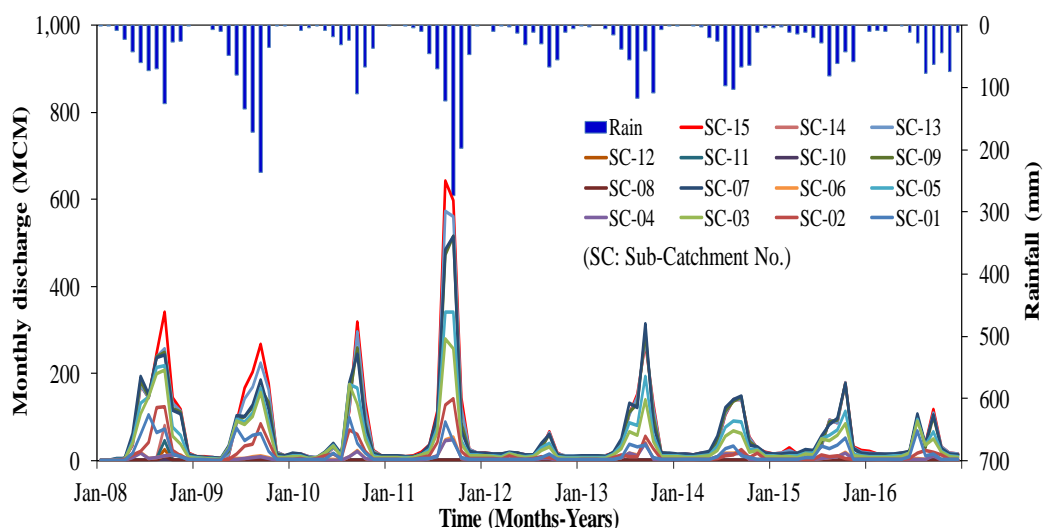
Fig. 5. Monthly discharge of 15 Sub-catchments.

4.2 Maximum discharge by return period

The Gumbel frequency distribution was conducted by finding a relationship between the maximum discharge from each of 15 sub-catchments through a whole 9 years derived from the SWAT model and the results were arranged in a descending order ('y' axis) and the return periods in a logarithmic scale chart ('x' axis). It was finally derived as the equation for the maximum discharge by each return period of all 15 sub-catchments. Particularly, this study considered the return period of 2 years, 5 years, and 10 years respectively (since the data was taken from 9 baseline years for the prediction equation, the return period should not be more than 10 years for accurate result). After all, the maximum discharges of all sub-catchments were presented in **Table 3.**

According to the maximum discharge of 15 sub-catchments derived from the equation in **Table 3**, the maximum discharges were increased following the return period of 2 years, 5 years, and 10 years respectively. Sub-catchment 15 was the one with the highest maximum discharge where the maximum discharges were 216.9, 428.6, and 588.7 MCM sequentially. This was followed by Sub-catchment 13, 7, and 9 where the maximum discharges were decreased one by one. At meantime, Sub-catchment 10, 12, 11, and 14 demonstrated the least discharges ranged from 0.2 MCM (for the 2-year return period) to 49.1 MCM (the 10-year return period) sequentially. Significantly, by comparing the 9-year average maximum discharge of all sub-catchment from the SWAT model (as

presented in a column 'Baseline' in **Table 3**), it was indicated that the results of the 5-year and 10-year return periods were higher than the result from the SWAT model whereas the result from the 2-year return period was slightly lower than the SWAT model's result.

Table 3.

Maximum discharge by the sub-catchment equation in return periods.

Sub-catchment No.	Equations for calculate the maximum discharge	R^2	Maximum discharge by each return period (MCM)			
			Baseline	2 year	5 year	10 year
1	$y = 40.853\ln(x) + 28.336$	0.872	64.3	56.7	94.1	122.4
2	$y = 66.17\ln(x) + 2.9875$	0.934	61.2	48.9	109.5	155.3
3	$y = 105.61\ln(x) + 44.043$	0.967	137.0	117.2	214	287.2
4	$y = 19.04\ln(x) + 4.2243$	0.947	21.0	17.4	34.9	48.1
5	$y = 121.14\ln(x) + 53.064$	0.958	159.7	137	248	332
6	$y = 20.739\ln(x) + 4.9219$	0.953	23.2	19.3	38.3	52.7
7	$y = 183.03\ln(x) + 61.088$	0.959	222.2	188	355.7	482.5
8	$y = 3.9451\ln(x) - 2.1379$	0.617	1.3	0.6	4.21	6.95
9	$y = 183.27\ln(x) + 57.563$	0.954	218.9	184.6	352.5	479.6
10	$y = 1.2196\ln(x) - 0.6635$	0.608	0.4	0.2	1.3	2.1
11	$y = 16.173\ln(x) - 8.8479$	0.563	5.4	2.4	17.2	28.4
12	$y = 8.8445\ln(x) - 4.8101$	0.566	3.0	1.3	9.4	15.6
13	$y = 199.85\ln(x) + 60.247$	0.932	236.1	198.8	381.9	520.4
14	$y = 27.951\ln(x) - 15.293$	0.564	9.3	4.1	29.7	49.1
15	$y = 230.99\ln(x) + 56.812$	0.942	260.1	216.9	428.6	588.7

4.3 Flood-risk area map at Yang Catchment

Fig. 6 presents the map of the flood-risk area in each sub-catchment derived from the spatial data and classified by ArcGIS model. **Fig. 6(a)** shows the maximum discharge through a whole 9 baseline years (2008-2016) from the SWAT model while **Fig. 6(b)-(c)** illustrates the results from the return period of 2, 5, and 10 years. All results were discussed as follows.

4.3.1 2-Year return period: After comparing the regular maximum discharge (9 years) as seen in **Fig. 6(b)**, it was found that Sub-catchment 1, 2, 4, 6, 8, 10, 11, 12, and 14 similarly demonstrated the results in a range from 0-100 MCM which as the same as the regular average. The results from Sub-catchment 3, 5, 7, 9, and 13 were in a range from 101-200 MCM and there were 3 sub-catchments showing lower results than the regular average including Sub-catchment 7, 9, and 13 (regular average was ranged from 201-300 MCM. However, Sub-catchment 15 presented the highest maximum discharge for the 2-year return period that was 216.9 MCM and this was very close to the regular average of 260.1 MCM (16.6% of data difference). Consequently, it was expected that Sub-catchment 15 was most possible to encounter the flood compared to other sub-catchments.

4.3.2 5-year return period: In case of the 5-year return period (see **Fig. 6(c)**), the flood-risk area was expanding from the 2-year return period or from 1 to 7 sub-catchments where the maximum discharges became higher than the regular average including Sub-catchment 2 showing in a range from 101-200 MCM (regular average was from 0-100 MCM), Sub-catchment 3 and 5 showing in a rage of 201-300 MCM (Regular average was from 101-200 MCM), and Sub-catchment 7, 9, and 13 showing in a range of 301-400 MCM (Regular average was from 201 -300 MCM). In addition, Sub-catchment 15 still showed the highest maximum discharge of 428.6 MCM which was 64.8% different from the regular average. Nevertheless, during this return period, there were 8 sub-catchments

showing the results equal to the regular average (from 0-100 MCM) including 1, 4, 6, 8, 10, 11, 12, and 14 sequentially.

4.3.3 10-year return period: Based on the flood-risk distribution map during the 10-year return period (see **Fig. 6(d)**), the most flood-risk area has been expanded to 8 sub-catchments while the maximum discharge was also highly increased 19-52% compared to the regular average. This notably indicated that there were 4 sub-catchments where the maximum discharges had been increased including Sub-catchment 7 and 9, (increased from 301-400 to 401-500 MCM and Sub-catchment 13 and 18 where it became higher than 500 MCM). During this 10-year return period, there still were 7 sub-catchments showing the results equal to the regular average (from 0-100 MCM) including 4, 6, 8, 10, 11, 12, and 14 respectively.
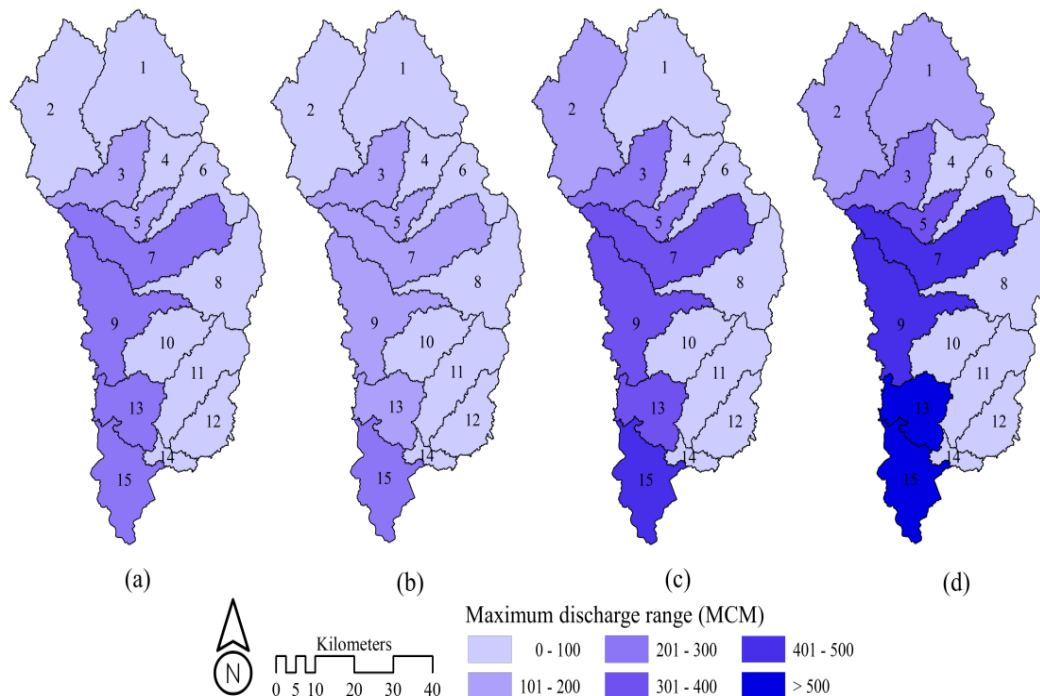
Fig. 6 Maximum discharge in sub-catchment area simulated from Gumbel distribution by each return period compare with the baseline year,)a) Average 9 baseline year,)b) 2-year return period, (c) 5-year return period, and (d) 10-year return period.

5. CONCLUSIONS

In this study, the flood estimation from the maximum discharge at Yang Catchment uses the SWAT model to classy the area into different sub-catchments and estimate the monthly maximum discharge in each year as well as using a Gumbel frequency distribution method to create the flood-frequency equations by the return period of 2 years, 5 years, and 10 years. Then, all of the results were presented as the flood-risk spatial map created by ArcGIS model and it was concluded that the SWAT model was able to classify the target area into 15 sub-catchments by the physical characteristics at each level of land contour. Moreover, it was found that when comparing the discharge estimation during 2008-2016 using the SWAT model with the data from 2 observed stations – E54 and E92, the result was satisfactory that could be affirmed by R^2, RE, and E_{ns} that also allows the user to know the maximum discharge in each sub-catchment from the model.

Creating the flood frequency equation was a process of making the frequency distribution from the monthly maximum discharge in each sub-catchment derived from the SWAT model following

Gumbel's theory. For the results, it was found in the 2-year return period that the maximum discharge was similar to the average maximum discharge (9 years) and it was increasing by years of the return period. Notably in the 10-year return period, the maximum discharge was 19-52% higher than the regular average. Additionally, for flood-risk area simulation in Yang Catchment, the maximum discharge in each return period were presented as the spatial map crated by ArcGIS model that was able to classify the extents and differences of the flood severity and possibility with different shades of colors for different return periods and maximum discharge derived from the equations in each sub-catchment. After considering the flood-risk area from the map, most of the sub-catchments in the southwest (Sub-catchment 7, 9, 13, and 15) has higher possibility of flooding since the maximum discharges there are much higher than the regular average. Furthermore, the physical characteristics there were the lowland with many rivers crossing through, especially Sub-catchment 15 where it is the final outlet to Yang Catchment. On the contrary, the eastern zone has low possibility of flooding since the maximum discharge was similar to the regular average and most of the land is higher than the western zone.

This study is likely a tryout on both hydrological and metrological data that had been completely collected from the target area during 2008-2016 (totally 9 years) where it was used as an initial data. For the accurate result of data analysis, the data prediction in this study was not over 10 years. Hopefully, it was expected that complete data recorded in a longer term (20 – 30 years and more) would provide the equation for maximum discharge estimation with more accurate results from more return periods e.g. 20 years, 50 years, or 100 years (It would probably provide more of the flood frequency map by the increasing return periods). Moreover, the future discharge estimation from different types of climate simulators together with a hydrological model could be another approach to predict the maximum discharge and create the flood-risk area map in the future. Above all, the researcher team hopefully expects that the research methodology and outcomes from this study would provide the useful data and be another channel to facilitate all stakeholders and any organizations within any river catchment areas to understand better about the hydrological processes in order to decrease the loss from the flood as well as be able to manage the sustainable water resources in the future.

ACKNOWLEDGEMENT

R E F E R E N C E S

Arnold, A.G., Srinivasan, R., Muttiah, R.S. & Williams, J.R. (1998) Large area hydrological modeling and assessment pert I: model development. *Journal of American Water Resource Association*, **34**(1), 73-89.

Asgharpour, S.E. & Ajdari, B. (2011) A case study on season floods in Iran, watershed of Ghotour Chai Basin. *Procedia - Social and Behavioral Sciences,* **19**, 556-566.

Begou, J.C., Jomaa S., Benabdallah, S., Bazie, P., Afouda A. & Rode, M. (2016) Multi-site validation of the SWAT model on the Bani Catchment: model performance and predictive uncertainty. *Water*, **8**(178), https://doi.org/10.3390/w8050178.

Bhagat, N. (2017) Flood frequency analysis using Gumbel's distribution method: A case study of lower Mahi Basin, India. *Journal of Water Resources and Ocean Science*, **6**(4), 51-54.

Chung, S., Takeuchi, J., Fujihara, M. & Oeurng, F. (2018) Flood damage assessment on rice crop in the Stung Sen River Basin of Cambodia. *Paddy and Water Environment*, https://doi.org/10.1007/s10333-019-00718-1.

Fukunaga, D.C., Cecílio, R.A., Zanetti, S.S., Oliveira, L.T. & Caiado, M.A.C. (2015) Application of the SWAT hydrologic model to a tropical watershed at Brazil. *Catena,* **125**, 206-213.

Ganamala, K. & Kumar, P.S. (2017) A case study on flood frequency analysis. *International Journal of Civil Engineering and Technology*, **8**(4), 1762-1767.

Győri M-M., Haidu I., & Humbert J., (2016). Deriving the floodplain in rural areas for high exceedance probability having limited data source. *Environmental Engineering and Management Journal*, **15**(8), 1879-1887.

Haidu, I., & Ivan, K. (2016). Évolution du ruissellement et du volume d'eau ruisselé en surface urbaine. Étude de cas : Bordeaux 1984-2014, France. *La Houille Blanche*, **5**, 51-56.

Haidu, I., Batelaan, O., Crăciun, A.I., & Domniţa, M. (2017). GIS module for the estimation of the hillslope torrential peak flow. *Environmental Engineering and Management Journal*, **16**(5), 1137-1144.

Ivan, K., Gagacka, D. & Matecka, P. (2018) Automated tool for the extraction of the surface ponds based on LiDAR data. *Geographia Technica*, **13**(2), 89-96.

Kumar, N., Singh, S.K., Srivastava, P.K. & Narsimlu, B. (2017) SWAT model calibration and uncertainty analysis for streamflow prediction of the Tons River Basin, India, using Sequential Uncertainty Fitting (SUFI-2) algorithm. *Modeling Earth Systems and Environment*, **3**(30), https://doi.org/10.1007/s40808-017-0306-z.

Lin, B.Q., Chen, X., Yao, H., Chen, Y., Liu, M., Gao, L. & James, A. (2015) Analyses of land use change impacts on catchment runoff using different time indicators based on SWAT model. *Ecological Indicators*, **58**, 55-63.

Maghsood, F.F., Moradi, H., Bavani, A.R.M., Panahi, M., Berndtsson, R. & Hashemi, H. (2019) Climate change impact on flood frequency and source area in Northern Iran under CMIP5 scenarios. *Water*, **11**(273), https://doi.org/10.3390/w11020273.

Ning, J., Gao, Z. & Lu, Q. (2015) Runoff simulation using a modified SWAT model with spatially continuous HRUs. *Environmental Earth Sciences*, 74, 5895-5905.

Olumide, B.A., Saidu, M., & Oluwasesan, A. (2013) Evaluation of best fit probability distribution models for the prediction of rainfall and runoff volume (Case study Tagwai Dam, Minna-Nigeria). *International Journal of Engineering and Technology*, **3**(2), 94-98.

Parhi, P.K. (2018) Flood management in Mahanadi Basin using HEC-RAS and Gumbel's extreme value distribution. *Journal of The Institution of Engineers (India): Series A*, **99**(4), 751-755.

Pereiraa, D., dos R., Martinez, M.A., Pruski, F.F., & de Silva, D.D. (2016) Hydrological simulation in a basin of typical tropical climate and soil using the SWAT model part I: Calibration and validation tests. *Journal of Hydrology: Regional Studies*, **7**, 14-37.

Pinheiro, E.C. & Ferrari, S.L.P. (2016) A comparative review of generalizations of the Gumbel extreme value distribution with an application to wind speed data. *Journal of Statistical Computation and Simulation*, **86**(11), 2241-2261.

Sajikumar, N. & Remya, R.S. (2015) Impact of land cover and land use change on runoff characteristics. *Journal of Environmental Management*, **161**, 460-468.

Shrestha, S. & Lohpaisankrit, W. (2017) Flood hazard assessment under climate change scenarios in the Yang River Basin, Thailand. *International Journal of Sustainable Built Environment*, **6**, 285-298.

Strapazan, C. & Petruţ, M. (2017) Application of ArcHydro and HEC-HSM model techniques for runoff simulation in the headwater areas of Covasna Watershed (Romania). *Geographia Technica*, **12**(1), 95-107.

Subyani, A.M. (2011) Hydrologic behavior and flood probability for selected arid basins in Makkah area, western Saudi Arabia. *Arabian Journal of Geosciences*, **4**(5−6), 817-824.

Swain S., Verma M.K., Verma M.K. (2018) Streamflow estimation using SWAT model over Seonath River Basin, Chhattisgarh, India. In: Singh V., Yadav S., Yadava R. (eds) *Hydrologic Modeling. Water Science and Technology Library*, **81**, 659-665.

GEOGRAPHY AND THE IRREGULAR MODERN FORTRESS CITY (GIRONA 18TH AND 19TH CENTURIES)

Ramon RIPOLL[1], Jordi GOMIS [2] , Carlos TURÓN[3] , Miquel-Àngel CHAMORRO[4]

ABSTRACT:
The regular modern fortress city of the seventeenth and eighteenth centuries has been widely studied. However, the irregular modern fortress city, which adapts to the rugged geography of the site, has, to date, been scarcely analysed. In the case of the latter, the irregularities of the terrain force moulding, changing and introducing major changes to common, regular, symmetrical defences. In these cases, geography and construction complement each other unusually, enriching the freer, more functional layout of the bastions, curtain walls and complementary structures. The aim of these changes is both financial and defensive at the same time. The peculiar geography of the traditional city of Girona -Catalonia- is a magnificent example of an irregular defensive approach in modern European history.

Key-words: *Geography, Topography, Fortress City, Urban Geography, Civil Engineering*

1. INTRODUCTION

Analysis of the strategic, geographic and formal uniqueness of the fortress city of Girona in Catalonia demonstrates the adaptation of the rigid, geometric defensive structures of the period to the singularities of the irregular, rugged terrain (Galindo, 1996). The work methodology used is based on the study of the formal and topographic characteristics of the defences of the city of Girona and the high degree of compatibility between them. This research requires reviewing and verifying the extent to which the scientific determinism of the modern era promoted by the science of defence of military engineers, of whom Sebastian le Preste de Vauban is one of the greatest exponents, adapted to the indeterminacy of common sense promoted by traditional customs and master builders. The findings show that defensive functionality (regular typology) was not only compatible with irregular topography, but benefited from these irregularities (morphology of the site).

The analysis highlights how the mathematical principles proposed by Vauban (La Preste de Vauban, 2010) were relaxed to extremes of adaptation to a complex environment in historical, urban, geographical, fluvial etc. terms. In this case the historical data are compared with studies of drawings and diagrams that illustrate this approach. The documentary sources used are the Municipal Archives of Girona, the Girona Historical Archive and the Archive of the Crown of Aragon (AHM, AHG, ACA).

[1, 4] *Universitat de Girona, 61 Maria Aurèlia Capmany Street, 17003-Girona, Spain, ramon.ripoll@udg.edu, mangel.chamorro@udg.edu*

[2, 3] *Universitat Rovira i Virgili, 26 Països Catalans Avenue, 43007-Tarragona, Spain, jordi.gomis@urv.cat, carlos.turon@urv.cat*

It should be recalled that modern fortress cities became widespread in the seventeenth century following the defence theory of military engineers in order to counter the great advances in military attack and siege tactics (Hughes, 1850). Thus, the new modern artillery, characterized by its huge destructive capacity, had to be counteracted with the construction and strengthening of fortresses and cities. Improved war machines forced improving the machines of defence. The machinery was subject to the principles of Vauban, who related the new schemes of attack with new schemes of fortification while military theory scientifically related form, space, time and means. The goal, in both cases, was to reduce the time and the means of any siege or defence, based on better controlling the form or the space.

It is clear that this eminently theoretical approach has its limits and so it is partially true. In this sense, it is widely known that no fortress could achieve unlimited defence; the fortress was therefore a means that, in the worst situation, allowed delaying surrender. These theories were applied to both newly built fortifications and to renovations of old military constructions (Ripoll, 2010). In this case, medieval cities adapted to new defensive strategies: the placing of bastions separated by a perfectly calculated distance, the construction of concentric defensive lines, and the arrangement of curtain walls, moats, palisades, underpasses, and complementary elements. Specific basic principles in the form, but also open to interpretation, that allowed for dual adaptation to the principles of the military treatises of the time and to the geography of the site. In this case it is demonstrated that the scientific, mathematical and military training of military engineers was not a closed, repetitive method but one that enabled creating open defensive typologies according to the topographical and historical circumstances of the site.

In this sense, the small city of Girona, with just 8,000 inhabitants was, militarily speaking, an important city in modern times because of its location on the central communication route in southern Europe between Spain and France (Ripoll, 2001). And it is precisely its strategic situation that forced it in the seventeenth century to adapt to the new military construction systems. Girona's functionality as a fortress city is amply demonstrated by the eight attacks suffered by the city, in the eighteenth century and the first half of the nineteenth century.

Fig. 1. Diagram of the fortifications of the city of Girona in the 18th and 19th centuries
(Drawing by R. Ripoll, private archive, 2018)

These sieges occurred in: 1710 (41 days of war), 1712 (377 days), 1808 (2 days), 1808 (32 days), 1809 (222 days), 1821 (2 days), 1827 (31 days) and 1843 (39 days). In three of them (1711, 1809 and 1843) the city was conquered, while in the rest, the city resisted the attackers. The city of Girona was thus under siege for 746 days over a 150-year period. This accounting does not take into account the pre-war periods when the citizens were forced to work directly preparing defensive constructions and indirectly to pay for these renovations.

Situations are also known in which citizens were required to ready the defences of the city without any fighting taking place. This is the case of the Great War (1793-1795) in which the city of Girona, after carrying out highly costly building repairs, did not join the conflict (Various authors, 2006).

The most difficult times lived by the city of Girona are the sieges of the Napoleonic Wars (1808-1814). Undoubtedly, it was the time when the theoretical approaches of the military ratio between form, space, time and means, discussed above, were tested with excellent results in military terms and exceedingly negative results in social terms (Ripoll, 2005). In this case, the well-arranged city defences allowed resistance that exceeded any conceivable expectation, at the cost, however, of subjecting the population to extreme, inexplicable nutritional, health and psychological situations. The defensive constructions worked better than expected, resisting a siege from 5 May to 10 December 1809 (**Fig. 1**), the population being halved and the civil destruction of homes and urban facilities generalized. Two hundred and thirty-three buildings were demolished, pavements of streets and squares destroyed, and there were a large number of wounded, sick and dead (Various authors, 2008). The human situation worsened with the spread of epidemics due to air and water pollution during the last weeks of the war, according to the descriptions by the French after the occupation of the city (Ripoll, 2009).

2. NATURAL DEFENCES

The transformation of the precarious traditional urban defences, of medieval origin, to the new layout of irregular fortified city with bastions presided over by a regular, independent main fortress, was repeated in most fortified cities in southern Europe throughout the seventeenth century. This approach was executed adapting each city to modern defensive layouts and the topographical characteristics of the site. The case of the city of Girona, and its unique geographical location is of great interest to any scholar of modern defensive strategy. Firstly, we can distinguish two different areas. The upper, rugged part to the east of the city consists of rocky terrain and is characterized by its great defensive vulnerability. In contrast, the part to the west of the city consists of crop land and is characterized by its susceptibility to flooding in times of heavy rain (Various authors, 1992). Due to the limitation of urban space, the mitigation system was also designed as the recreation area (Nusit et al. 2019) named La Devesa.

The special geographical factors that play an important role in the defence of the city are, first, the periodic flooding of the Girona plain, and secondly the especially rocky subsoil of the mountainous area. The flood-experienced people are likely to implement the mitigation measures, to avoid or reduce the damages associated with floods (Odidi et al, 2020).

Concerning the former, the plain area was easily defended, not just by the 8 bastions built in the 17th century, but especially due to its flooding, which hindered the establishment of artillery batteries. For example, in the eighteenth century and the first half of the nineteenth century, 55 different floods were recorded. Flash floods caused the water to reach heights of up to 2 metres in the lower parts of the city (Ripoll et al, 2020). The river that most often broke its banks is the Ter (37 times), followed by the Onyar (33 times), the Galligans (13 times) and finally the Güell (7 times). The rivers that directly caused most damage to the city are the Galligans and the Onyar. These characteristics are very much taken into account by both the military engineers who designed the defences of the city and, above all, by the attacking armies in their approach to laying siege.

The rocky subsoil of the mountainous area is characterized by being formed of highly compact, resistant calcareous nummulitic sedimentary rocks. In military siege strategies on fortresses located in these kinds of mountainous areas, this geological peculiarity made it enormously difficult for the attacking army to dig trenches and passageways in the subsoil, and greatly hindered the advance of siege troops as it forced them to advance on the surface in full view (**Fig. 2**).

Fig. 2. Fortifications of the city of Girona in the 18th and 19th centuries
(Drawing by R. Ripoll, private archive, 2018).

3. DEFENCES CONSTRUCTED

In the seventeenth century, in the mountainous area of Montjuic and Pedreras, 11 fortresses and facilities were built covering an occupied area of 74,855 m2. These fortifications, which are located between 160 and 218 m above sea level, were perfectly arranged, with an average distance between them of 255 m (between 170 and 390 m), allowing creating a protective line of defence in the east of the city (**Table 1**).

During the seventeenth century, in the Girona plain, in the west of the city, attached to the ancient city walls, 8 triangular bastions were built. These bastions covered an average surface area of 5,400 m2 each (between 1,830 and 7,775 m2). For their construction their due arrangement was especially taken into account. They were situated at an average distance of 162 m apart (between 127 and 186 m) and were located in the low areas of the city and therefore at an average height of 68 m above sea level (between 67 and 93 m).

Table 1.
Features of the fortifications of the city of Girona in the 18th and 19th centuries.

	AREA	SURFACE AREA	ELEVATION	DIST A	DIST B
1	"SANT NARCIS" TOWER	3,030	218	250 (2)	650 (4)
2	"SANT MIQUEL" REDOUBT	980	205	250 (1)	430 (5)
3	"CONDESTABLE" FORT	16,800	190	170 (7)	172 (9)
4	"SANT LLUIS" TOWER	3,460	186	390 (5)	650 (1)
5	"MONTJUIC" FORT	23,380	185	241 (12)	390 (4)
6	"CAPUTXINS" FORT	16,155	185	212 (7)	242 (11)
7	"REINA ANNA" FORT	6,725	185	170 (7)	212 (6)
8	"DEL CALVARIO" REDOUBT	1,240	170	335 (3)	319 (10)
9	"DE LA CIUDAD" REDOUBT	1,735	165	172 (3)	303 (13)
10	"DEL CAPITOL" REDOUBT	900	160	319 (8)	306 (3)
11	AMMUNITION DUMP	450	160	179 (7)	242 (6)
12	"SANT JOAN" TOWER	1,710	120	180 (20)	440 (5)
13	"DE LA MERCE" BASTION	6,635	93	186 (14)	303 (9)
14	"SANT FRANCESC" BASTION	6,150	69	186 (13)	152 (15)
15	"SANTA CLARA" BASTION	7,775	68	152 (14)	206 (16)
16	"GOVERNADOR" BASTION	6,855	68	174 (17)	206 (15)
17	"SANTA CRUZ" BASTION	3,475	68	127 (18)	174 (16)
18	"FIGUEROLA" BASTION	5,445	68	127 (17)	168 (19)
19	"RAMENVILLE" LUNETTE	1,830	68	168 (18)	282 (17)
20	"FRANÇA" BASTION	5,260	67	180 (12)	268 (19)
21	"MERCADAL" QUARTER-WEST	151,130	68		
22	CIUTAT VELLA – OLD TOWN	273,800	67-118		
				208.4	305.75
	TOTAL FORTIFICATIONS	**4,010**	**22%**		
	TOTAL CITY	**540,910**	**78%**		
	TOTAL	**544,920**	**100%**		

These defences were organized around an independent primary defence element formed by Montjuic fort, with a surface area of 16,800 m2 (at 185 m above sea level). This central defensive role is reflected in its four-pointed star shape and an additional two points forming outposts located in the most vulnerable spans. This fortress created three defensive lines over the general city area.

The first line was formed by a protective arch consisting of 8 bastions (França, Ramenville, Figuerola, Santa Cruz, Gobernador, Santa Clara, Sant Francesc, and Merced) supplemented by 3 secondary forts in the first foothills (tower of San Juan, "Ciudad" redoubt and "Capítulo" redoubt) (**Fig. 3**). The defensive line protected the west of the city and its north and south flanks.

A second line of protection was the one formed by the straight-line arrangement of the five most important fortifications also organized from the starting point of Montjuic Castle (and completed by the tower of San Luis, Condestable fortress, Queen Anna fort and "dels Caputxins" fort) (**Fig. 4**). This second set of defences was arranged between 170 and 185 m above sea level, displaying great geographical homogeneity both in plan and elevation.

Finally, a third, eminently preventive line of protection was formed by three fortifications ("Sant Narcis" tower, "Sant Miquel" redoubt and the "Calvario" redoubt) and a facility (Ammunition Dump). In this description we have circumvented the more secondary defensive elements such as guardhouses, trenches, etc. scattered around the fortifications.
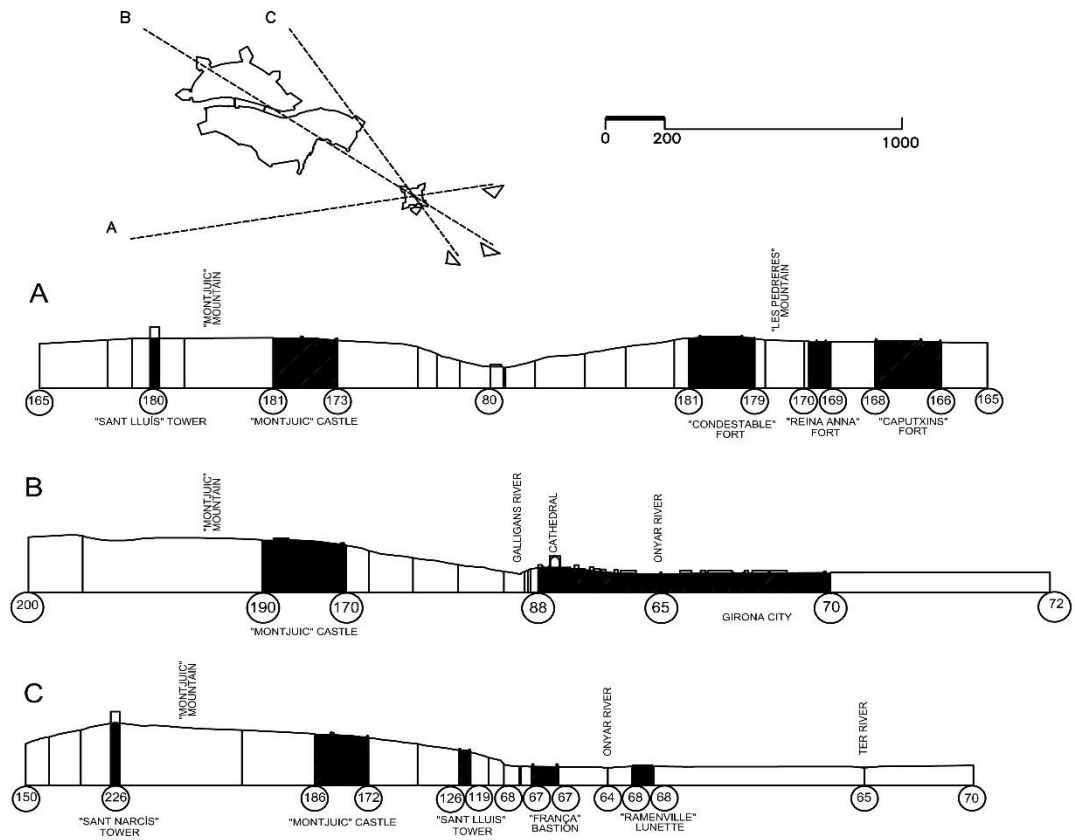
Fig. 3. Sections of the fortifications adapted to the geography of the city of Girona in the 18th and 19th centuries (Drawing by R. Ripoll, private archive, 2018).
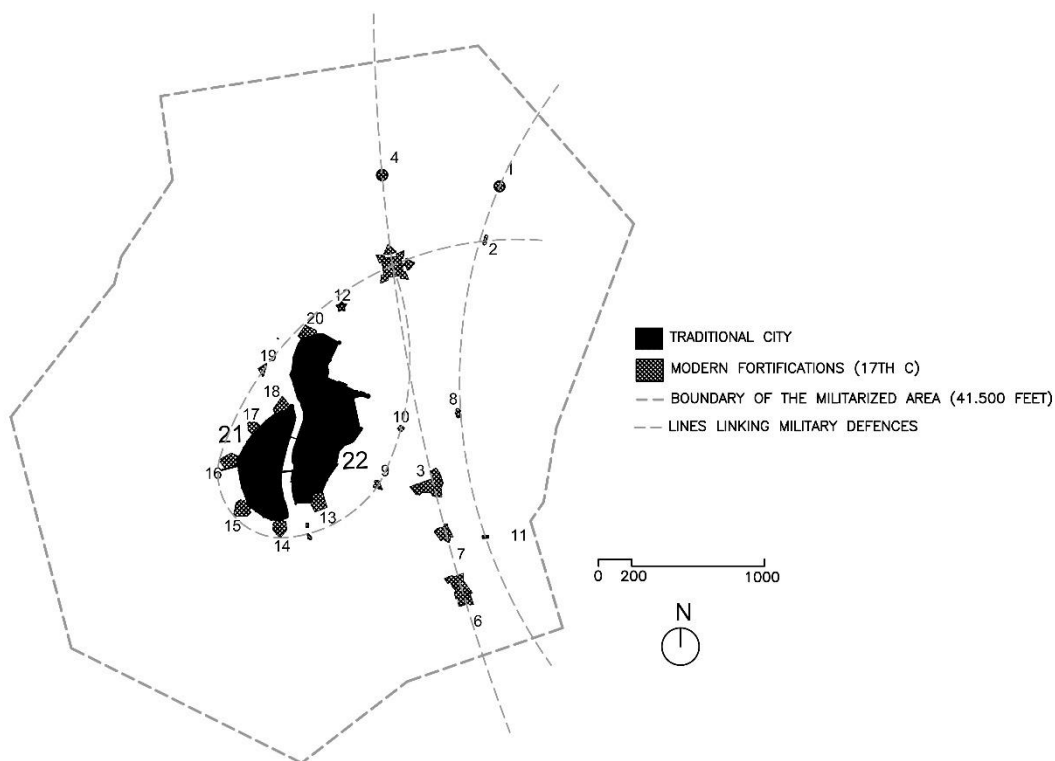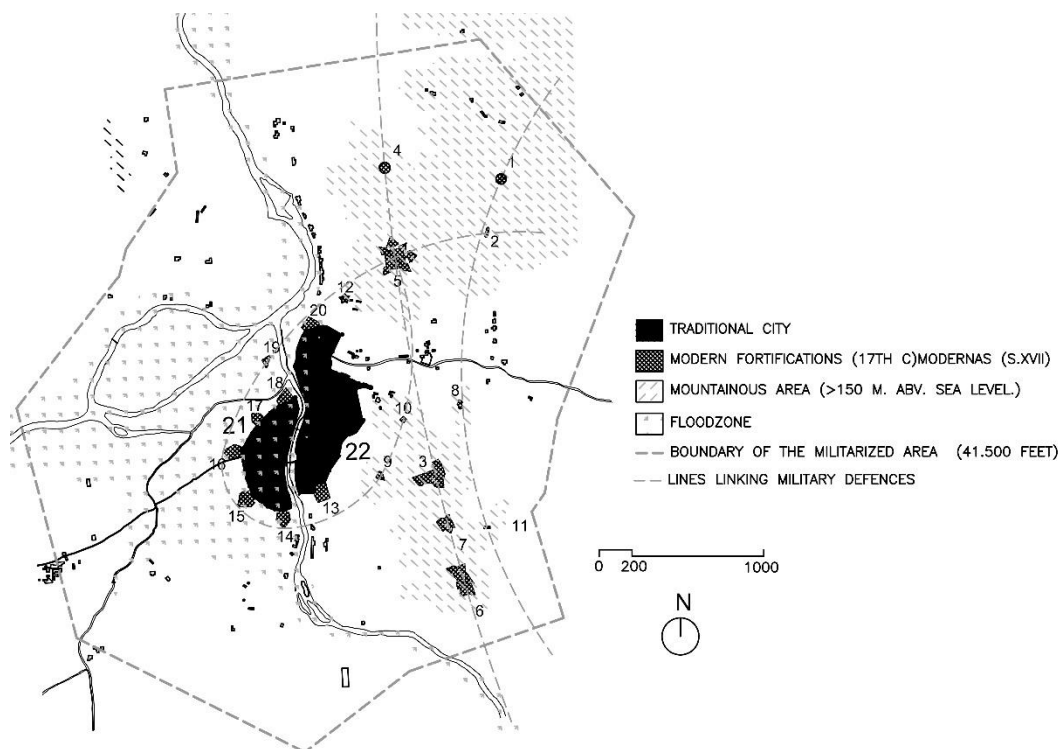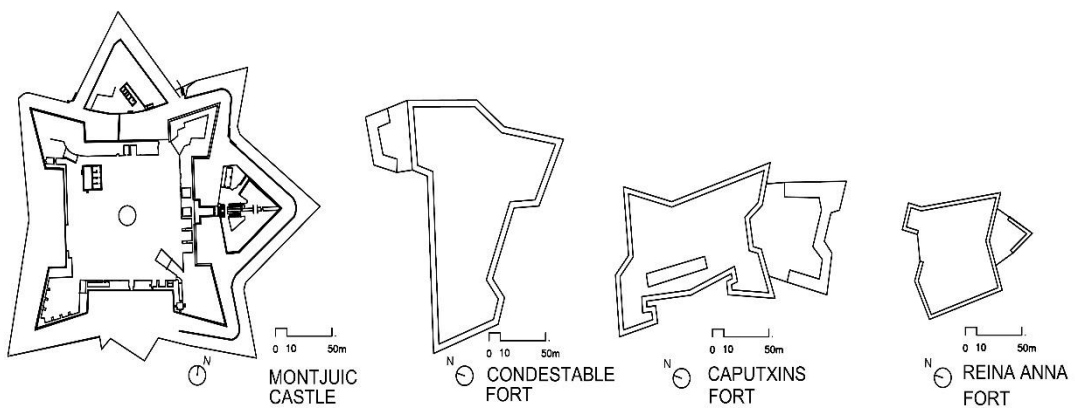

Fig. 4. Form of the isolated fortifications of the city of Girona in the 18th and 19th centuries (Drawing by R. Ripoll, private archive, 2018).

4. CONCLUSIONS

This analysis helps probe more deeply into the adaptation of European defence manuals without breaking away from the fundamental principles that uphold them. After analysing the example of an irregularly shaped fortified European town, it is clear that the excellence of the ratio between form and function does not necessarily require symmetry, regularity and always equal, repetitive models. If it could be demonstrated comprehensively, through the study of a large sample of modern irregular fortifications, it could be stated that the investigations carried out in the twentieth and twenty-first centuries, by modern architecture on the organic form, has its roots in the seventeenth and eighteenth centuries (organic rationalism). In this case the theoretical, methodological and attitudinal similarities would be demonstrated between the best modern military engineers and the most renowned contemporary architects.

REFERENCES

ACA: Archive of the Crown of Aragón.

AHM: Girona Municipal Historical Archive.

AHG: Girona Historical Archive.

Galindo, J.A. (1996). El conocimiento constructivo de los ingenieros militares del siglo XVIII. Un estudio sobre la formalización del saber técnico a través de los tratados de arquitectura miliar. Barcelona: Universidad Politécnica de Catalunya. (Unpublished doctoral thesis)

Hughes, B.P. (1850). Puissance de feu. L'efficacité des armes sur le champ de bataille. Paris : Lausanne.

Le Prestre de Vauban, Sébastien (2010). The new method of fortification, as practised by Monsieur de Vauban, Together with a new treatise of geometry. Gale ECCO, Print Editions.

Nusit, K., Tantanee, S., Subsomboon, K., Leungvichcharoen, S., Yiemwattana, S. (2019). The desing of flood protection along Nan river, Phitsanulok province, Thailand. *Geographia Technica,* **14**(SI), A special Issue On Sustainable Urban Development, 129-137. DOI: 10.21163/GT_2019.141.26

Odini, S., Tantanee, S., Nusit, K., Buranajarukorn, P. (2020). Factors influencing the uptake of flood mitigation measured in Budalangi, Kenya. *Geographia Technica,* **15**(1), 80-90. DOI: 10.21163/GT_2020.151.07

Ripoll, R. (2001). Girona ciutat de pas. La carretera de dins la ciutat a finals del s.XVIII i principis del segle XIX. *Girona. Annals de l'IEG*, **XLII,** 423-434.

Ripoll, R. (2005). L'arquitecte, l'arquitectura i la ciutat. Girona 1760-1835. Barcelona : Publications of Montserrat Abbey.

Ripoll, R. (2009). La volta als Sitges en 43 capitols. Andreu Oller "el primer ciutadà". Girona. *Revista de Girona* **253**, 86-89.

Ripoll, R. (2010). Creixement i servitud militar fora de les muralles de Girona: 1810-1909. Girona. *Annals de l'IEG*. **LI,** 403-424.

Ripoll, R., Gomis, J., Turon, C., Chamorro, M.A. (2020). Urban recreational parkc to offset the flooding of rivers: La Devesa of Girona -Catalonia- (19th Century). *Geographia Technica,* **15**(1), 27-34. DOI: 10.21163/GT_2020.151.03

Various authors, 1992, Atlas Girona ciutat XVII-XX. Girona: COAC.

Various authors. 2006. Història de Girona. Girona: Ateneu d'Acció Cultural.

Various authors. 2008. Girona i la Guerra del Francès (1808-1814). Girona: Girona City Council.

A COMPREHENSIVE GRID-BASED RAINFALL CHARACTERISTICS IN THE CENTRAL PLAIN RIVER BASIN OF THAILAND

Weerayuth PRATOOMCHAI[1] , *Sarintip TANTANEE[2]* , *Chaiwat EKKAWATPANIT[3]*

ABSTRACT:
Eight rainfall indicators were used to analyze the 5 min. × 5 min. grid-based rainfall characteristics in the central plain region of Thailand. The non-parametric statistics called Mann-Kendall test was applied to 32-year (1980-2011) time series data, statically significant (p-value ≤ 0.05) and Kendall's tau correlation maps were considered for informative examination. Annual rainfall showed increasing trend in the upper basin and statically increasing by 35.8% of the whole basin. A number of rainy days (RD) and number of consecutive wet days (CWD) showed increasing by 70.2% and 57.9% of the basin for RD and CWD, respectively, while a number of consecutive dry days (CDD) exhibited decreasing trend over 85.0% of the study area even only 13.8% satisfied at 95% statically significant. The simple daily rainfall intensity (SDRI), heavy rainy days (HRD), max. 1-day, and max. 3-day demonstrated upward trends. The findings suggest that the region is shifting towards wetter condition. The explicit results of rainfall characteristics maps are expected to facilitate and allow various users to make better water resources management and overcome reluctant interpretation rainfall changes/trends for areas lacking of measured data as well as baseline information for climate change study.

Key-words: *Chao Phraya River basin; Mann-Kendall test; rainfall indices; trend analysis.*

1. INTRODUCTION

Rainfall is classified as a stochastic variable in both time and space. Over a last few decades, a number of evidences have been observed that rainfall characteristics are altering by the so called anthropogenic factor. For example, torrential rainfall or consecutive dry spell of rainy days is amplifying globally (Alexander et al, 2006 and IPCC, 2013).

Taking account for climate change inducing extreme rainfall events and disasters, many research articles point out that the global increases in the observed frequency and intensity of extreme rainfall events (e.g., Alexander et al., 2006; Donat et al., 2013; IPCC, 2013). For the global scale, the changes in precipitation extremes were spatially more complex since topography influence. However, on average, there was a trend towards wetter conditions for some precipitation indicators, for example, the intensity, frequency, and duration of extreme precipitation are increasing (Donat et al., 2013). For regional study, an article done by Herath et al. (2018) considering atmospheric temperature in Australia to quantify the properties of extreme rainfall events showing that the Clausius-Clapeyron relation was able to describe the extreme rainfall and daily maximum temperature. A study by Endo et al. (2009) showed that average precipitation intensity of wet days exhibited an increasing trend for many stations in the Southeast Asia. Manton et al. (2001) also pointed out that majority of the analyzed stations across the Southeast Asia showed upward trend in annual rainfall with significant decrease in the number of rainy days. Rainfall, especially an extreme event, has some links and influence on people's perception and their concerns (Pratoomchai et al, 2015).

[1]*Department of Civil Engineering, Faculty of Engineering, King Mongkut's University of Technology North Bangkok, Bangkok, Thailand, weerayuth.p@eng.kmutnb.ac.th*

[2] *Department of Civil Engineering, Faculty of Engineering, Naresuan University, Phitsanulok, Thailand, sarintipt@nu.ac.th*

[3] *Department of Civil Engineering, Faculty of Engineering, King Mongkut's University of Technology Thonburi, Bangkok, Thailand, chaiwat.ekk@kmutt.ac.th*

The latest report, Global Risks Reports, by the World Economic Forum (2018) points out that extreme weather events, natural disasters, and failure of climate change mitigation and adaptation are three out of the top five global risks in terms of livelihood and influence on global economic growth.

In Thailand, a few studies have been done on rainfall and temperature extreme indicators, but those results were classified as station-based studies (Limjirakan et al, 2010; Limsakul et al, 2010; Limsakul and Singhruck, 2016). An assessment will be more useful and applicable if high station density was used and transformed a analyzed result to a map (King et al, 2013). To fulfil this knowledge gap, this paper was carried out in order to analyze and construct the spatial distribution of rainfall patterns and trends in the Chao Phraya River basin.

2. STUDY AREA

Chao Phraya River basin (CPRB) is located in the central plain region of Thailand as shown in **Fig. 1** (a). It covers for 157,284 km^2. This area is home for approximately 34 million people or 51.7% of the country population and that shared for 73% of the overall country GDP because it includes Bangkok, the capital city. The region can separate into upper basin which consists of the Ping, Wang, Yom, and Nan Rivers and lower part has three tributaries, i.e., the Sakaekrang, Pasak, and Chao Phraya Rivers. Flooding is a major dilemma problem in this area (GISTDA, 2018; Nusit et al, 2019). Based on satellite imaged data which were analyzed by the Geo-Informatics and Space Technology Development Agency or GISTDA (2018), approximately 1,500-25,560 km^2 of the CPRB were classified as annual flood inundations over the period 2005 to 2016. Major driving factor associates to this problem is torrential rainfall that will predominate the basin during May to October (rainy season). In addition, rainfall in this region varies greatly by season as a result of complex interaction among the climate circulation in the Indo-Pacific region together with orographic conditions (e.g., Misra and DiNapoli, 2014; Takahashi and Yusunari, 2006).

(a)   (b)   (c)
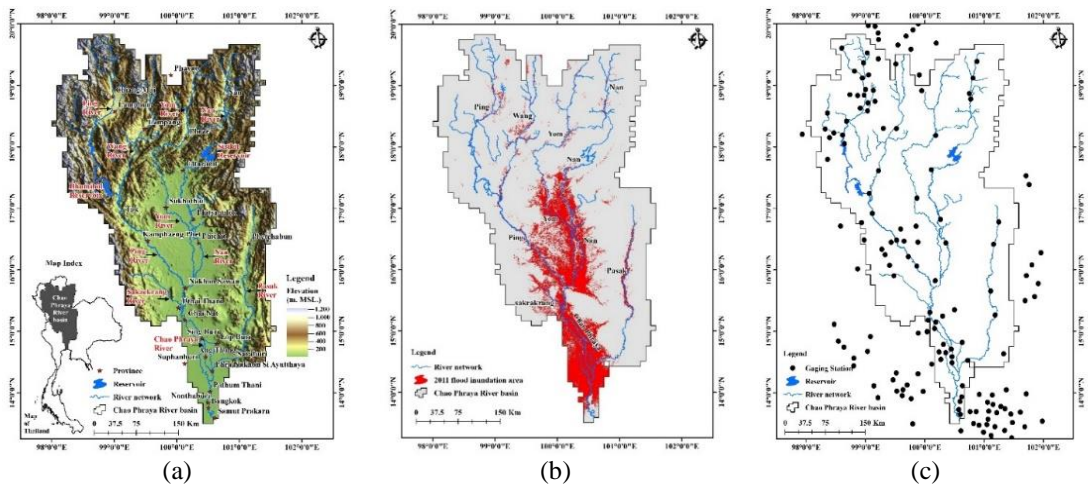
Fig. 1 Chao Phraya River basin in Thailand: (a) upper part of the basin is mountainous range while the central and lower parts are flood plain areas, (b) 2011-flood inundation area, and (c) IMPAC-T gaging stations used.

The CPRB is also considered as a climate change hotspot of Thailand. 2011 flood event was recorded as the extremely historical flood disaster. As shown in the shading area of **Fig. 1** (b), the lower Yom and Nan Rivers and lower part of the basin including northern parts of Bangkok were flooded for almost 2 to 4 months. Thus, this region has been selected as the study area to improve understanding of spatial distribution of rainfall characteristics.

3. METHODOLOGY

A non-parametric test called Mann-Kendall test, which is a practical and famous tool for examining whether statically significant trend of hydro-meteorological time-series data (Helsel and Hirch, 2002; Haidu and Magyari-Sáska, 2009; Pravalie, 2014), was applied for this study.

Kendall's tau (τ) correlation is an index to measures the strength of the monotonic relationship (directions) in time-series data (Kendall, 1975). Tau is a rank-based procedure and is therefore resistant to the effect of a small number of unusual values. It is well-suited for variables which exhibit skewness, e.g., rainfall, around the general relationship. The strength of the evidence whether statistically significant exist is presented by p-value. Typically, in hydro-climatology trend test, if p-value $\leq$ 0.05 or at 95% confidence level it is presumed that statistically significant exist in the examination data.

In this study, the Kendall Family of Trend Tests (Helsel et al, 2006), the Fortran source code, which was developed by the U.S. Geological Survey, was modified to the grid-based rainfall. To figure out grid-based rainfall characteristics in the CPRB, eight indicators as listed in **Table 1** were examined. Mostly, they are based on the recommendation by World Meteorological Organization-Commission for Climatology (WMO-CCI)/World Climate Research Program (WCRP)/Climate Variability and Predictability (CLIVAR) project's Expert Team on Climate Change Detection Indices (ETCCDI) (Zhang et al, 2011).

Table 1.

Rainfall indicators used in the study.

No	Indicator name	Definition	Unit
1	Annual rainfall	Annual total rainfall	mm
2	Number of rainy days	Annual count of days when rainfall $\geq$ 1 mm	Days
3	Number of consecutive wet days	Annual maximum number of consecutive days with rainfall $\geq$ 1 mm	Days
4	Number of consecutive dry days	Annual maximum number of consecutive days with rainfall $<$ 1 mm	Days
5	Simple daily rainfall intensity	Annual total rainfall divided by number of rainy days	mm day^{-1}
6	Number of heavy rainy days	Annual count of days when rainfall $\geq$ 20 mm	Days
7	Max. 1-day rainfall	Annual maximum 1-day rainfall	mm
8	Max. 3-day rainfall	Annual maximum consecutive 3-day rainfall	mm

4. FORCING DATASET

This study we used the 5 min. × 5 min. (approximately 9.3 km. × 9.3 km.) grid-based data that was an outcome of the Integrated study on Hydro-Meteorological Prediction and Adaptation to Climate Change in Thailand (IMPAC-T Project). Several achievements of the project were published on the Hydrological Research Letters (Special Collection 2) which is available on http://www.hrljournal.org/special-collections/special-collection-2. There are two datasets called K10 and T12 under the project archive (Kotsuki et al., 2014). Both of them are 5 min. × 5 min. horizontal resolution which were created from measured gaging stations (**Fig. 1** (c)). The K10 comprises of 7 climate dataset, i.e., rainfall, surface temperature, wind speed, specific humidity, long-wave and short-wave radiations, and atmospheric pressure while the T12 is only rainfall data. However, T12 is covered a 32-year historical data from 1980 to 2011 whereas the K10 is extended in 1981-2004 (24 years). Therefore, T12 data was used for this study since the main objective was only focused on rainfall.

5. RESULTS AND DISCUSSION

The entire area of the region was divided by grid size of 5 min. × 5 min. horizontal resolution into 1,925 grids in total. A simple percentage was used to show a quantitative examination or general trend of the study. Three types of spatial distribution maps, i.e., 32-year average value, Kendall′s tau correlation, and p-value, were created for all indicators. Results and discussion were made as follows:

5.1 Annual Rainfall

Generally, average annual rainfall in the area over the period 1981-2011 (32 years) was varied between 871-1,608 mm (1,169 mm using area-averaged over the entire basin) as shown in **Fig. 2** (a). It was clearly seen that areas along the Yom and Nan Rivers were received more rainfall (1,200-1,400 mm) if compared to other tributary areas. Based on the isohyetal rainfall, approximately 1,000-1,100 mm were found over the Ping and Wang sub-basins except the upper Ping River that received higher amount of 1,300-1,500 mm. Meanwhile, the lower part of the CPRB except Bangkok and her vicinity areas was gained precipitated water approximately 900 mm, on average. For the capital city and surrounding regions, which are located by the Gulf of Thailand, were subjected to rain water of 1,200-1,400 mm.
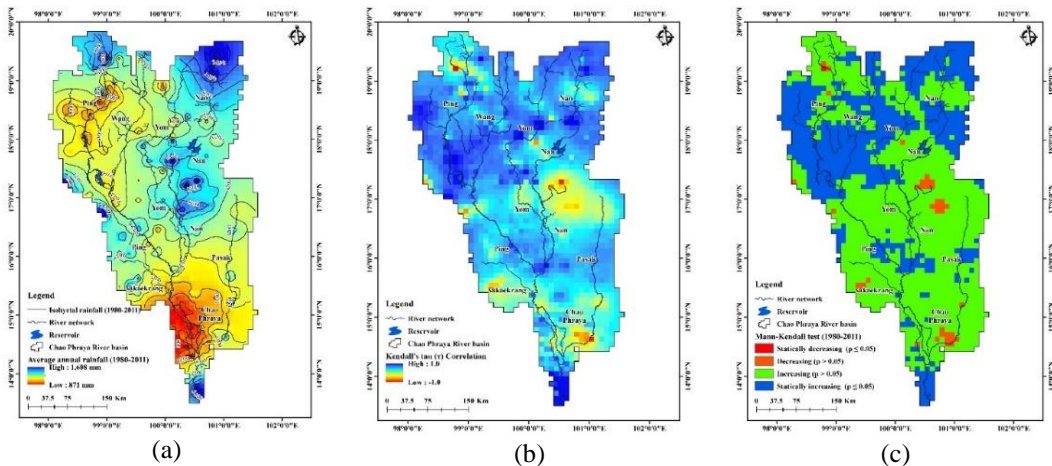
Fig. 2 Spatial distribution of the average annual rainfall (a), Kendall's tau (b), and Mann-Kendall statically test (c).

Based on the area-averaged, rainy season rainfall was 1,020 mm (ranged between 761-1,378 mm on average) which was considered for 87.2% of the average annual rainfall. Based on the findings, it was noteworthy that 1,858 grids (96.5% of the whole basin) showed increasing trend.

Fig. 2 (b and c) show the examination of spatial distribution of Kendall′s tau and statistically significant test (p-value). The findings indicated that annual and rainy season rainfall generally showed in upward trend. And they were strongly increasing in the upper areas of the basin. 35.8% and 38.0% of the basin areas were statically increasing in annual and rainy season, respectively. However, there was a few percentage of the total area subjected to decreasing trend. Another point to note on this finding is the areas long the Ping and Wang Rivers normally receiving less rainfall are being got more annual rainfall progressively and statically. Using the area-averaged, a general trend of annual rainfall linear regression was increase by 6.8 mm year^{-1} or 68 mm decade^{-1}. The quantitative figures from our analysis could provide detail information at regional assessment.

5.2 Number of Rainy Days

A number of rainy days (RD) are a day that measured rainfall ≥ 1 mm. In the study area, there were approximately 71-190 days, on average, in RD distributed over the basin annually. More wet days in mountainous region and relatively low in the low-lying areas along the rivers especially in the Chao Phraya River plain (**Fig. 3** (a)). Based on the Kendall′s tau and p-value (**Fig. 3** (b and c)), 1,352 grids (70.2% of the total area) showed increasing trend and 543 grids out of the RD increasing grids were statically significant. Whereas about 29.8% of the basin showed decreasing in RD and statically significant by with 89 grids or only 4.6% of the whole CPRB.

Overall, RD tended to increase by 0.44-day year^{-1} with the fluctuation between + 4.54 (increasing) and – 2.50-day year^{-1} (decreasing). This finding is not agreed with Limsakul and Singhruck (2016) that found a general trend in decreasing of RD by 0.99-day decade^{-1}. Although there is mixed spatial distribution pattern (upward or downward) on RD; however, it can be noted that an area on the left by the middle Nan River is relatively wetter region than the others. In contrast, over the upper-end of the Nan River the RD showed declining trend with statically significant and was agree with Manton (2001).

(a)   (b)   (c)
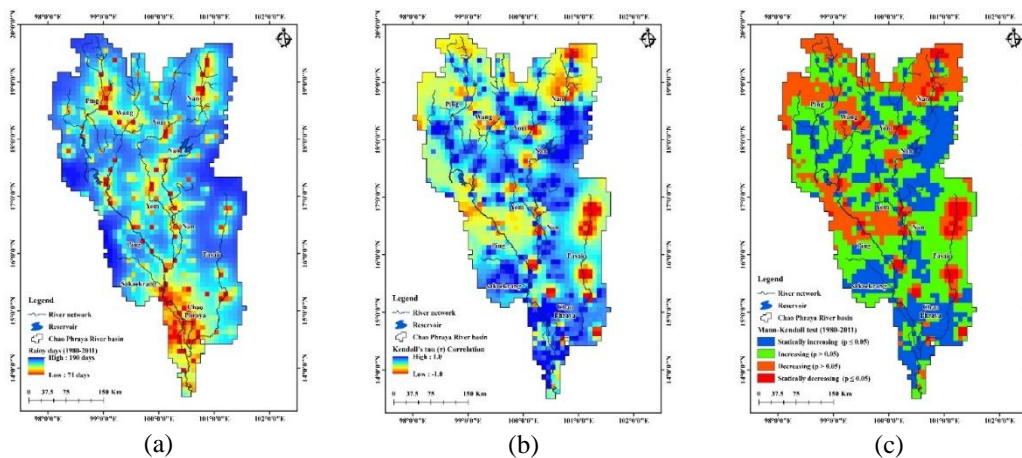
Fig. 3 Spatial distribution of the average number of rainy days (a), Kendall's tau (b),
and Mann-Kendall statically test (c).

5.3 Number of Consecutive Wet Days

The average of Number of Consecutive Wet Days (CWD) was varied between 7 to 64 days over the study period. It is quite scatter spatial distribution from place to place. Relatively low CWD in low land areas that lie along river valleys particularly by the Chao Phraya River plain, whereas the watershed divide which is a mountainous range, CWD are relatively high. The spatial distribution of Kendall′s tau correlation of CWD revealing that the low land areas lie along the rivers are subjected to increase in CWD. In addition, the regions that corresponding to positive Kendall′s tau (increasing in the CWD in the time series) with statically significant were about 418 grids or 21.7% of the basin. On the other hand, the upper areas in the Pasak, Nan, Yom, Wang, and Ping Rivers were corresponding to decreasing trend in CWD. Overall, 811 (126) grids or 42.7% (6.5%) of the CPRB show negative trend (statically significant) in CWD. The rate of change of the trend analysis showed that CWD ranged +1.49 (increasing) to -1.22-day year^{-1} (decreasing) with the basin-wide averaged of 0.08-day year^{-1}. This grid-based examination of CWD in the study show a contrast finding by Limsakul and Singhruck (2016) that show a 0.027-day year^{-1} (based on 41 stations) downward trend in CWD across Thailand.

5.4 Number of Consecutive Dry Days

Consecutive dry days (CDD), was also included in the study. Basically, the consecutive no rainfall days or dry days (rainfall < 1 mm) were ranged 40-84 days (almost 3 months for the maximum) distributed over the entire basin. The longest prevailing dry areas were located in the upper parts of the Ping, Wang, and Yom Rivers.

On the other hand, The Nan, lower Ping and Yom, and lower CPRB areas were relatively short duration in CDD. However, the areas subjected to long duration in CDD were reducing. This signal was interpreted from Kendall′s tau and p-value. Overall, the linear regression of CDD was descending by -0.33-day year^{-1}. In the big picture, it was clearly to note that CDD was trending to decrease. 1,635 grids or approximately 85.0% of the total basin area showed CDD decreasing although only 267 grids were satisfied with 95% confidence level.

5.5 Simple Daily Rainfall Intensity

Simple daily rainfall intensity (SDRI) is the total annual rainfall divided by the annual number of rainy days. In general, the analysis revealed that SDRI was approximately 6 to 18 mm day^{-1}. Furthermore, the intensity which was less than 10 mm day^{-1} were accounted for 1,838 grids (95.5% of the CPRB) as illustrated in **Fig. 4** (a). Considering of the general trend of annual rainfall, RD, and SDRI altogether implied that the basin tends to wetter condition but rainfall intensity less than a 10 mm day^{-1} was predominating in the basin. The Kendall′s tau and statically test are showed in **Fig. 4** (b) **and Fig. 4** (c) indicating that SDRI exhibited increasing trend. About 77.5% (1,493 grids) of the basin were increasing trend and 628 grids out of 1,493 grids increasing with 95% confidence level. However, there were some regions, especially in the Lower CPRB (floodplain area), showed decreasing in SDRI. Approximately 157 grids from the entire basin were categorized in statically significant deceasing.

Based on the trend analysis, overall signal of SDRI was slightly increasing by 0.02 mm day^{-1} year^{-1} over the study period. The rate of change of the SDRI from our result is relatively closed to the previous study (0.17 mm day^{-1} decade^{-1}) by Limsakul and Singhruck (2016). In fact, there is no monotonic SDRI trend in the complex topography and large basin, our analysis showed that the fluctuation of SDRI across the CPRB were +0.33 and -0.70-mm day^{-1} year^{-1} for the maximum and minimum of SDRI, respectively. For example, the observations of mountainous rainfall in the upper Ping River are increasing with significant signal (Kuraji et al, 2009).

(a)　　　　　　　　　(b)　　　　　　　　　(c)
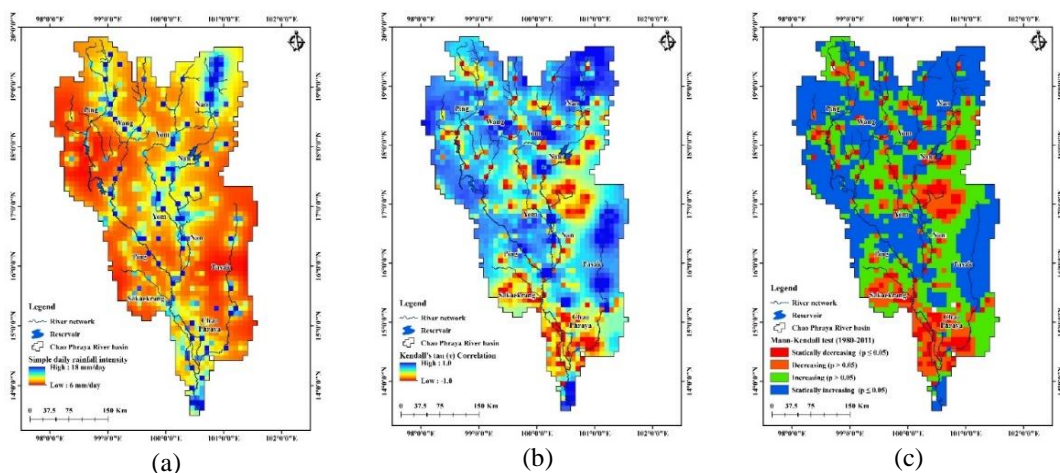
Fig. 4 Spatial distribution of the simple daily rainfall intensity (a), Kendall's tau (b), and Mann-Kendall statically test (c).

5.6 Number of Heavy Rainy Days

A day that receives rainfall greater or equal 20 mm is classified as a heavy rainy day (HRD). In the study area, HRD exhibited between 4 to 26 days and relatively high in the upper Nan River. In general, a number of HRD over the study period were increased by 1,554 grids (80.7% of the study area) with 36.3% (699 grids) of the CPRB showed statically significant increasing. However, there were some areas subjected to decrease in HRD and only a few percentage (4% of the basin) showed statically significant decreasing. HRD is one factor relating to a degree of rainfall inducing natural disaster. The regression analysis showed that HRD was increasing by 0.11 day year^{-1}, on average, with the fluctuation range of $\pm$ 0.67 day year^{-1}. Based on the findings, Upper Nan River sub-basin is the region that likely to be risky because there tends to increasing in rainfall amount, SDRI, and HRD while decreasing in RD, CWD and CDD. Combination of the mentioned factors imply that the area might face with extreme rainfall.

5.7 Maximum 1-Day and 3-Day Rainfall

Fig. 5 and **Fig. 6** show the spatial distribution of maximum 1-day and 3-day rainfall, respectively. The Kendall′s tau and classification of p-value are also presented. 32-year average of 3-day rainfall ranged between 66-230 mm.

| (a) | (b) | (c) |
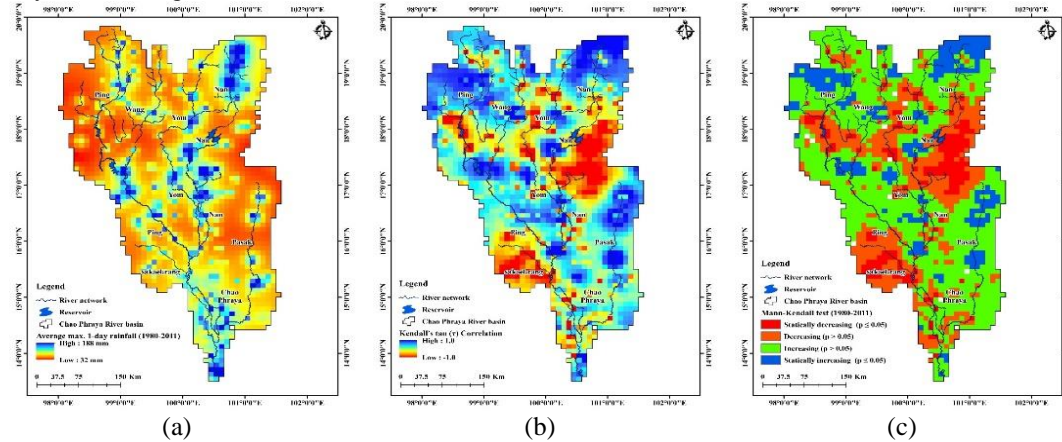
Fig. 5 Spatial distribution of the maximum 1-day rainfall (a), Kendall's tau (b), and Mann-Kendall statically test (c).

| (a) | (b) | (c) |
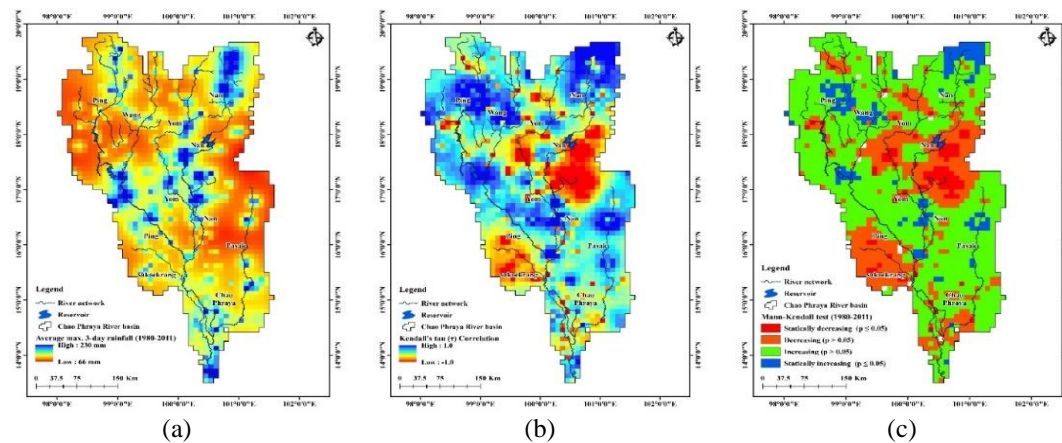
Fig. 6 Spatial distribution of the maximum 3-day rainfall (a), Kendall's tau (b), and Mann-Kendall statically test (c).

It was clear from the figures that grids locations near by rivers, particularly upper Nan River, showed more pronounced value of maximum rainfall. Majority of the whole basin subjected to an increase of both max. 1-day and max. 3-day. These were interpreted from positive sign of the Kendall′s tau maps. Approximately 1,240 grids (64.4% of the basin) and 1,331 grids (or 69.1% of the basin) were exhibited of increasing max. 1-day and max. 3-day, respectively. If considered in terms of statically increasing or decreasing, there were not much different in the directions. 248 (174) and 134 (91) grids or 12.8% (9.0%) and 7.0% (4.7%) of the entire basin satisfied with 95% confidence level of increasing (decreasing) for the max. 1-day and max. 3-day, respectively.

6. CONCLUSIONS

This study focuses on spatial distribution and trends of rainfall characteristics using daily grid-based rainfall. The Mann-Kendall test was used to identify the CPRB's rainfall characteristics for eight indicators as summarized in **Table 2**. The table shows percentage of the areas that subjected to increase/decrease for two categories, increasing (overall trend) and statically increasing (satisfy at 95% confidence level). In short, the basin trends towards wetter condition especially over the upper sub-basins (the Ping, Wang, and Nan sub-basins). 97.9% (35.8%) of the CPRB were subjected to the increase (statically significant) of annual rainfall with the rate of 6.8 mm year^{-1}. Increasing of the RD and CWD and decreasing of CDD for 70.2%, 57.3%, and 84.9%, respectively, pointed out the likelihood wetter condition in this region. For the SDRI, max. 1-day, and max. 3-day indicators showed upward trend and also predominated majority areas of the basin.

We would note that this was the first time for grid-based examination on rainfall characteristics over the most important area in Thailand. Various spatial distribution maps for the 32-year average and statically test provide the base values, probabilistic trends, and practical information towards rainfall monitoring as well as the baseline data for climate change study. This local assessment will provide a clearer perspective of rainfall characteristics and beneficial to various users as well as a decision-making stage associated with water resources engineering and disaster mitigation in the study area.

Table 2.

Summary of the rainfall characteristics in the study area.

Rainfall indicators	Trends (% of the basin area)				Trends/Changes year^{-1}		
	Increasing		Decreasing		Max.	Min.	Area averaged
	Overall	Statically significant	Overall	Statically significant			
Annual rainfall (mm)	97.9	35.8	2.1	n/a	21.6	- 9.22	6.8
Number of rainy rays (Days)	70.2	28.2	29.8	4.6	4.54	- 2.50	0.44
Number of consecutive wet days (Days)	57.3	35.6	42.7	6.5	1.49	- 1.22	0.08
Number of consecutive dry days (Days)	15.1	n/a	84.9	13.8	0.55	- 1.92	- 0.33
Simple daily rainfall intensity (mm day^{-1})	77.5	44.9	22.5	8.1	0.33	- 0.70	0.02
Number of heavy rainy days (Days)	80.7	36.3	19.3	4	0.67	- 0.67	0.11
Max. 1-day rainfall (mm)	64.4	12.8	35.6	9	1.66	- 2.97	0.08
Max. 3-day rainfall (mm)	69.1	6.9	30.9	4.7	2.17	- 3.18	0.18

Acknowledgements

R E F E R E N C E S

Alexander, L.V., Zhang, X., Peterson, T.C., Caesar, J., Gleason, B., Klein Tank, A.M.G., Haylock, M., Collins, D., Trewin, B., Rahimzadeh, F., Tagipour, A., Rupa Kumar, K., Revadekar, J., Griffiths, G., Vincent, L., Stephenson, D.B., Burn, J., Aguilar, E., Brunet, M., Taylor, M., New, M., Zhai, P., Rusticucci, M., Vazquez-Aguirre, J.L. (2006) Global observed changes in daily climate extremes of temperature and precipitation. *J. Geophys. Res*., **111**, D05109

Donat, M.G., Alexander, L.V., Yang, H., Durre, I., Vose, R., Dunn, R.J.H., Willett, K.M., Aguilar, E., Brunet, M., Caesar, J., Hewitson, B., Jack, C., Klein Tank, A.M.G., Kruger, A.C., Marengo, J., Peterson, T.C., Renom, M., Oria Rojas, C., Rusticucci, M., Salinger, J., Elrayah, A.S., Sekele, S.S., Srivastava, A.K., Trewin, B., Villarroel, C., Vincent, L.A., Zhai, P., Zhang, X., Kitching, S. (2013) Updated analyses of temperature and precipitation extreme indices since the beginning of the twentieth century: the HadEX2 dataset. *J. Geophys. Res.,* **118**, 2098–2118

Endo, N., Matsumoto, J., Lwin, T. (2009) Trends in precipitation extremes over Southeast Asia. *SOLA*, **5**, 168–171 doi: http://dx.doi.org/10.2151/sola.2009-043.

GISTDA, (2018) Thailand Flood Monitoring System, Geo-Informatics and Space Technology Development Agency (Available online http://flood.gistda.or.th/ (accessed 1 March 2018)).

Haidu, I., Magyari-Sáska Zs., (2009) Animated Sequential Trend Signal Detection in Finite Samples. *Information Technology Interfaces, IEEE Publication,* Catalog Number CFP 09498-PRT, pp.249-254. ISSN 1330-1012., DOI 10.1109/ITI.2009.5196088

Helsel, D.R., Hirsch, R.M. (2002) Statistical methods in water resources: U.S. Geological Survey Techniques of Water-Resources Investigations. 524 pp.

Helsel, D.R., Mueller, D.K., Slack, J.R. (2006) Computer program for the Kendall family of trend tests: U.S. Geological Survey Scientific Investigations Report 2005–5275, 4 p.

Herath, S.M., Sarukkalige, R., Nguyen, V.T. (2018) Evaluation of empirical relationships between extreme rainfall and daily maximum temperature in Australia. *J. Hydrol.,* **556**, 1171-1181

IPCC. (2013) Climate Change 2013: The Physical Science Basis. Contribution of Working Group I to the Fifth Assessment Report of the Intergovernmental Panel on Climate Change. IPCC: Cambridge, UK.

Kendall, M. G. (1975) Rank Correlation Methods 4th ed, Charles Griff, London.

King, A.D., Alexander, L.V., Donat, M.G. (2013) The efficacy of using gridded data to examine extreme rainfall characteristics: a case study for Australia. *Int. J. Climatol.*, **33**, 2376–2387.

Kotsuki, S., Tanaka, K., Watanabe, S. (2014) Projected hydrological changes and their consistency under future climate change in the Chao Phraya River basin using multi-model and multi-scenario of CMIP5 dataset. *Hydrolo. Res. Lett.,* **8**, 27-32.

Kuraji, K., Mei, G., Kowit, P. (2009) Inter-annual and spatial variation of altitudinal increase in rainfall over Mount Inthanon and Mae Chaem watershed, Northern Thailand. *Hydrolo. Res. Lett.,* **3**, 18-21.

Limjirakan, S., Limsakul, A., Sriburi, T. (2010) Trends in temperature and rainfall extremes in Bangkok Metropolitan area. *J. Environ. Res*., **32**, 31–48.

Limsakul, A., Limjirakan, S., Sriburi, T. (2010) Observed changes in daily rainfall extremes along Thailand's coastal zone. *J. Environ. Res*., **32**, 49–68.

Limsakul, A., Singhruck, P. (2016) Long-term trends and variability of total and extreme precipitation in Thailand. *Atmospheric Res*., **169**, 301-317

Manton, M.J., Della-Marta, P.M., Haylock, M.R., Hennessy, K.J., Nicholls, N., Chambers, L.E., Collins, D.A., Daw, G., Finet, A., Gunawan, D., Inape, K., Isobe, H., Kestin, T.S., Lefale, P., Leyu, C.H., Lwin, T., Maitrepierre, L., Ouprasitwong, N., Page, C.M., Pahalad, J,, Plummer, N., Salinger, M.J., Suppiah, R., Tran, V.L., Trewin, B., Tibig, I., Yee, D. (2001) Trends in extreme daily rainfall and temperature in Southeast Asia and the South Pacific: 1961–1998. *Int. J. Climatol*. 21: 269–284

Misra, V., DiNapoli, S. (2014) The variability of the Southeast Asian summer monsoon. *Int. J. Climatol*. 34, 893–901

Nusit, K., Tantanee, S., Subsomboon, K., Leungvichcharoen, S., Yiemwattana, S. (2019) The design of flood protection along Nan River, Phitsanulok province, Thailand. *Geographia Technica*, 14, Special Issue 2019, pp. 129-137

Pravalie, R. (2014) Analysis of temperature, precipitation and potential evapotranspiration trends in southern Ol tenia in the context of climate change. *Geographia Technica*, 9(2), 68-84

Pratoomchai, W., Kazama, S., Manandhar, S., Ekkawatpanit, C., Saphaokham, S., Komori, D., Tongduang, J. (2015) Sharing of people's perceptions of past and future hydro-meteorological changes in the groundwater use area. *Water Resour Manage*. 29: 3807-3821

Takahashi, H.G., Yasunari, T. (2006) Climatological monsoon break in rainfall over Indochina singularity in the seasonal march of the Asian summer monsoon. *J. Clim*. 19, 1545–1556.

Yue, S., Pilon, P., Cavadias, G. (2002) Power of the Mann–Kendall and Spearman's rho tests for detecting monotonic trends in hydrological series. *J. Hydrol*, 254-271

The World Bank. (2012) Thai Flood 2011: Rapid Assessment for resilient recovery and reconstruction planning. https://www.gfdrr.org/thaifloods2012.

World Economic Forum. (2018) The global risks report 2018, 13th ed. 80 pp (Available on http://wef.ch/risks2018).

Zhang, X., Alexander, L.V., Hegerl, G.C., Klein-Tank, A., Peterson, T.C., Trewin, B., Zwiers, F.W. (2011) Indices for monitoring changes in extremes based on daily temperature and precipitation data. *WIREs Clim Change* 2: 851–870

PRELIMINARY ANALYSIS OF FLOODS INDUCED BY URBAN DEVELOPMENT IN YOGYAKARTA CITY, INDONESIA

Slamet SUPRAYOGI[1] , Reviana LATIFAH[1] and Muh Aris MARFAI[1]*

ABSTRACT:
The growing population size in the City of Yogyakarta increases the need for settlement and supporting facilities, which consequently expands land-use conversion from previously vacant, productive, and conservative lands to built-up areas. Meanwhile, extensive development means wider impervious surface and gradually narrowing recharge areas, increasing the potential for flooding. This study aimed to analyze the land-use change in the last fourteen years and its relation to runoff coefficients, the maximum discharges occurring with the return periods of 2, 5, 10, and 25 years, and the inundated areas in each return period. The flood inundation was modelled using HEC-RAS. The results showed, in particular, the expansion of the settlement area during the period of 2004-2017. However, such change did not significantly alter the runoff coefficient and, by proxy, the maximum flood discharge. Spatially, the flood scenarios showed overflows from the upper and middle segments of the river.

Key-words: urban, flood, HEC-RAS, Indonesia

1. INTRODUCTION

The rising number of populations in Indonesia is a major fundamental issue. A high population in urban area can cause new problems, among others, increased needs for settlement. Requiring more spaces for living, human initiates conversion of land utilization from non-residential to settlement areas. In urban development, urbanization (urban feature expansion) is also a cause of land-use conversion (Kodoatie & Sugianto, 2002). Changes in land functions shrink the number of productive and conservative zones, such as forests and plantations. Decrease in land cover in the form of forest can affect the rise or fall of the discharge value, which in turn affects the extent of inundating water (Dasanto et al, 2014).

Expansion of built-up area and city development broadens the open and impervious surface. As a result, rain falling to the ground transforms into runoff and increases the proportion of surface runoff in the total amount of runoff. The rainfall is an important weather factor because it can increase the quantity of peak flow (Karaoui et al, 2016). The ground no longer has layers that can retain rainwater but immediately turning it into runoff instead. In the case when flow velocity exceeds the infiltration rate, water can neither be absorbed nor appropriately stored (Hadisusanto, 2011). The sprawl of built-up land is proportionally followed by a decrease in the rain catchment area, resulting in a higher potential of flooding. Land-use conversion significantly contributes to the increase in flood quantity and quality (Kodoatie & Sugianto, 2002).

In the last ten years, the City of Yogyakarta has experienced quite rapid development. It is followed by the accelerated growth of infrastructure (new road networks) (Prayitno, 2018), to support the needs of facilities in the city. This growth expands to the surrounding regions and forms an agglomeration, referred to as the Yogyakarta Urban Agglomeration Area. The increasing density of infrastructures like roads that connect the centers of activities indicates that Yogyakarta is currently developing as the core and point of development according to the spatial concept (Buletin Tata Ruang, 2008). With roads reaching more regions, economic activities multiply as more and more population mobility around their centers is accommodated. An indicator of population mobility is a rise in the population size of Yogyakarta, i.e., around 400,000 inhabitants (BPS Kota Yogyakarta, 2018).

One characteristic of urban physical development is more extensive built-up areas. The growth of the City of Yogyakarta has led to changes in the structure of spatial use. Villages on the outskirts of the city, i.e., Sleman and Bantul Regencies, that provide spaces for shelter have now transformed

into urban areas (Johnston, 1981; Giyarsih & Marfai, 2018). Obstacles in developing regions include uncontrolled Building Permit (IMB) that causes constructions to fail to correspond to the principle of water conservation. Multi-story buildings and impervious surfaces in urban areas decrease the chance of rainwater to infiltrate into the soils and, instead, change most of it into surface runoff and even floods. In addition, the lack of ability to manage urban development accompanied by increased climate variability can also be a trigger for flooding (Alvarez & Resosudarmo, 2019).

Floods occur not only within the city where roads are submerged but also on the banks of the river as well as on floodplain event on the rural area (Gyori et al. 2016). Riverbanks are used for settlements and other types of constructions that involve soil hardening, reducing the capacity of the river to store water and can causing flood (Idham 2018). Drastic human activity can also cause drainage patterns to change (Xie et al, 2017) and decrease the capacity of river channel and river water quality (Suprayogi et al, 2019). Then, water flows faster even when its discharge is unchanged because the cross-section of the river segment narrows. The combination of accelerated flow and exceeded capacity increases the likeliness of intensified erosion on riverbanks. When erosion with faster river flow occurs continuously, buildings on the riverbanks are more prone to collapse.

The state of the art of GIS technology has grown (Goodchild, 2009), and continue to gain important recognition from disaster practitioners and academic researchers. GIS has also been widely used for geographic analysis of flood (Fujiki & Renand, 2018), for spatio-temporal analysis (Ivan, 2015), to support design and planning on flood protection (Nusi et al. 2019; Al Dianty et al. 2020), and to produce modifications together with other application to visualize flood (Marfai & Sekaranom, 2015; Tomaszewski, 2015). One of the applications that uses GIS to visualize the results of flood modelling is HEC-RAS. This application is widely used for flood inundation analysis in urban area (Marfai, 2003; Silva et al, 2014; Beretta et al, 2018; Kim et al. 2020)

HEC-RAS is developed for the application of floodplain management and studies that evaluate flood inundation, and it can assess changes in the profiles of riverwater and channel (US Army Coprs of Engineers, 2010a). This application helps to create models and examine hydrological problems and watershed-related issues, specifically floods (US Army Corps of Engineers, 1987). Integrated with the Geographic Information System (GIS) software, it assists users in explaining data spatially. This study aimed to analyze (1) land use in the last fourteen years and its relation to runoff coefficient, (2) the maximum flood discharges occurring with the return periods of 2, 5, 10, and 25 years, and (3) the area of flood inundation for each return period.

2. METHODS

2.1. Research area

This research was carried out in Winongo Watershed, which administratively includes seven districts, namely Turi, Pakem, Sleman, Ngaglik, Mlati, Gamping, and Tegalrejo. As for the flood inundation scenario, it used a segment of the Winongo River that traverse five districts in the City of Yogyakarta, which are Tegalrejo, Jetis, Gedongtengah, Wirobrajan, and Ngampil. This research area id presented in **Fig. 1.** This river segment was selected because it is located in an urban area with the rapid growth of urban housing. Meanwhile, the drainage system is natural, i.e., rivers and tributaries. Rivers are the primary system that receives rainwater and wastewater from secondary and tertiary channels, triggering flood problems in the study area, particularly overflows to urban settlements and roads.

2.2. Material and equipment

The study employed field observations for spatial analysis, and the required data were as follows: Quickbird imagery for land cover analysis on a detailed scale, the Indonesian Topographic Maps (RBI), land use map, soil map, time-series rain data, and drainage network map. Meanwhile, the tools and instruments used were GPS, Abney levels, measuring tapes, ranging rods, digital cameras, personal computers, and stationery, as well as distometer and uncrewed aerial vehicles to create DEM.
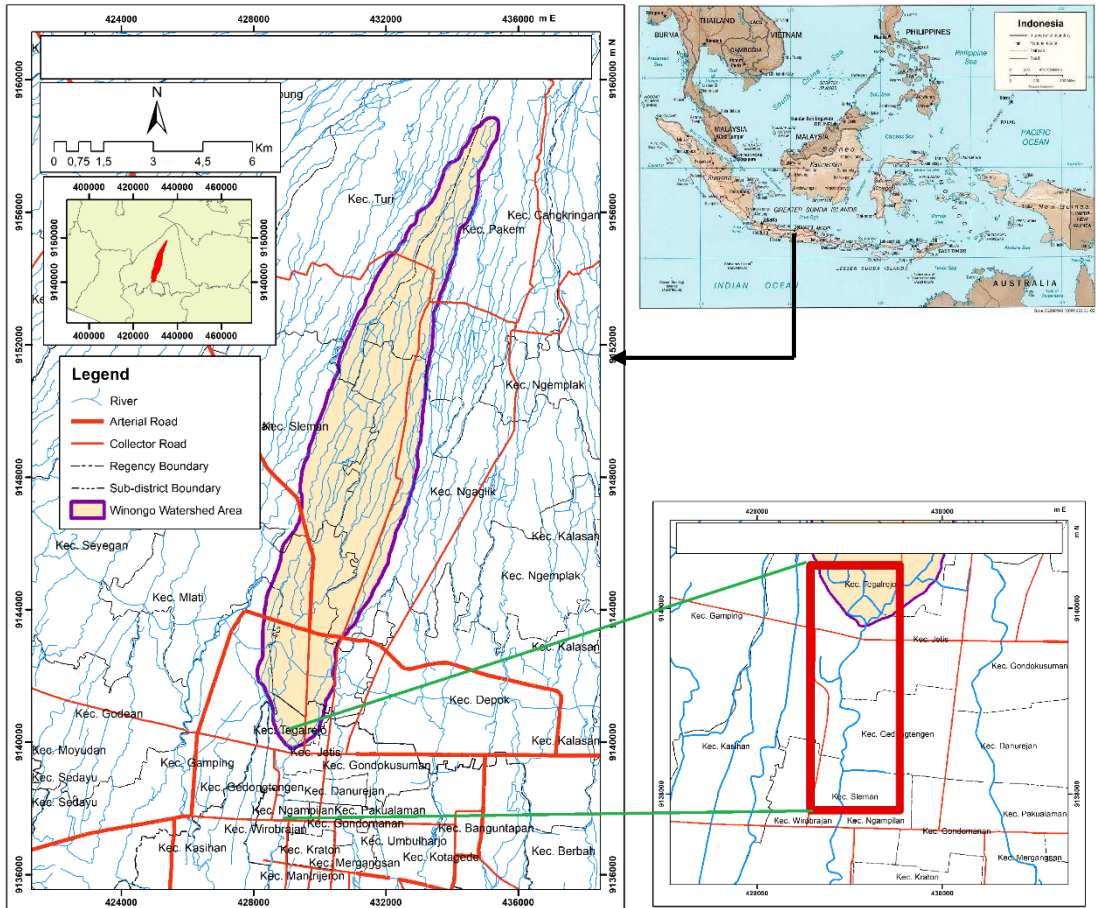
Fig. 1. The map of research area

2.3. Procedure

Flood inundation scenario or modelling was created in HEC-RAS and ArcGIS software using riverflow data, river geometry, and Manning's roughness coefficient as the parameters (US Army Corps of Engineers, 2010b). However, due to limited data on river flow, the rational method was used to estimate the maximum discharge (flood peak) (Kusumastuti et al, 2019). Spatially, the river geometry was obtained through mathematical calculations on DEM derived from elevation data. The Manning's coefficient of roughness was determined at each cross-section on each channel (Arcement and Schneider, 1989), namely the left overbank, main channel, and right overbank. The modelled or simulated flood inundations were displayed in ArcGIS software to identify the location and distribution of flooding spatially.

- *Maximum discharge calculation*

The rational method is widely used to calculate peak flow (Chin, 2019). The formula used to estimate the maximum discharge was that of the rational method, which is:

$$Q = 0,278 \, C \, I \, A \tag{1}$$

Notes:

Q : the peak discharge of surface runoff (m^3/s)

C : runoff coefficient (dimensionless)

A : area of drainage basin (Km^2)

I : rainfall intensity (mm/hour)

The runoff coefficient (C) was based on the Cook's method (Miller, 1984) i.e., by calculating the weight of the overlaid layers of land use, soil, relief (slope gradient), and surface storage. In this study, the surface storage was computed by the flow density approach. As for the rainfall intensity, it was estimated using the formula $I = \frac{P24}{24}(\frac{24}{Tc})^{\frac{2}{3}}$ where P24 is 24-hour rainfall (mm) and Tc is the time of concentration (in hour, based on the Kirpich's method) (Suripin, 2002). Rainfall was estimated from predicting recurrent maximum precipitation for the return periods of 2, 5, 10, and 25 years in the Rainbow software. From this rainfall data, the maximum discharge for each return period was derived.

- *River geometry data*

The geometric features of a river can be spatially described in HEC-GeoRAS, which shows river network and elevation data in the TIN format. There are four geometric components, namely stream centerlines, bank lines, flow path centerlines, and XS Cross Section. Stream centerlines were used as a reference for creating bank lines, flow path centerlines, and XS Cross Section. XS Cross Section, a line traversing the river flow, was used to determine the condition of the river cross-sections produced in the TIN extraction process. The geometric components of the river are presented in **Fig. 2.**
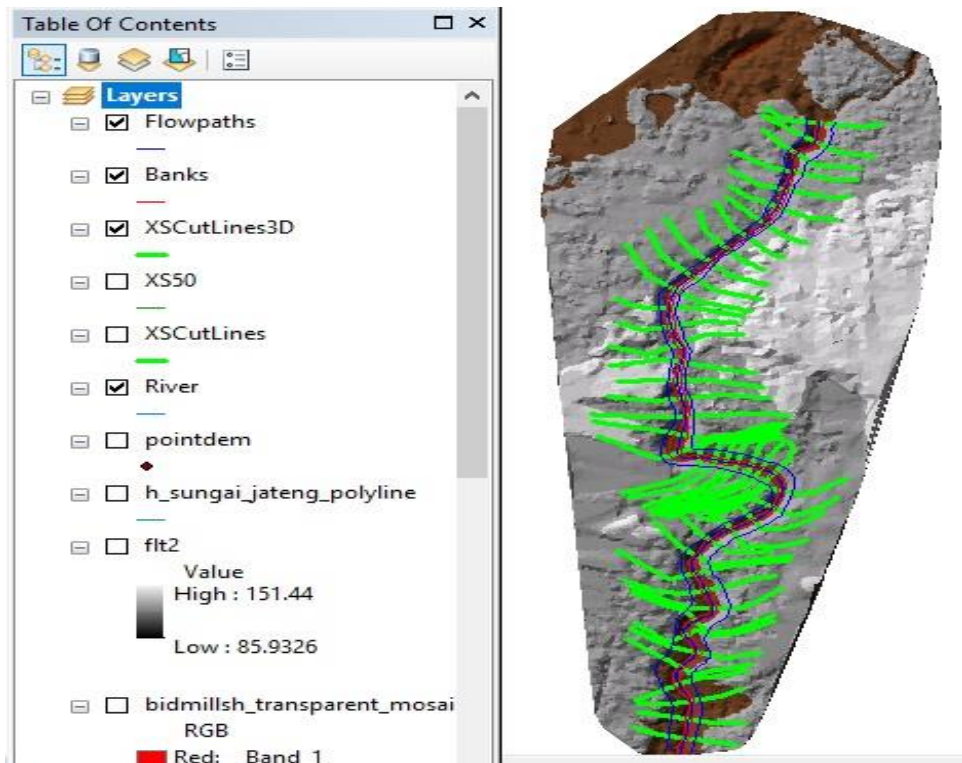
Fig. 2. The visual description of river geometry in HEC-GeoRAS

(*Source: US Army Coprs of Engineers, 2010a*)

3. RESULTS AND DISCUSSION

3.1. Physical Condition

The soil in the study area is composed of volcanic deposits, deposits of clay, clay-sand, sand, and gravel, and dacitic tuffs. Based on the spatial distribution, clay and sand deposits are dominant. In terms of responses to rainwater, a more porous soil absorbs higher rainwater volume. Therefore, compared with clay, sandy soils absorb water faster and store a more significant amount of water.

Flow velocity is influenced by the slope and roughness of the surface (frictions) on which water flows (Govers et al. 2000). Topography (slope) plays a role in modifying the speed and volume of river flow. Higher slope gradient reduces the capacity of soil to absorb rainwater and, instead, it transforms more portions of it into surface runoff that accumulates in the river body. In the study area, the slope ranged between 0.0097-10.26% with high slope gradients identified in Turi and Pakem Districts; then, it gradually flattened from the middle to the lower part of the watershed.

Winongo Watershed is mainly used for irrigated rice fields and settlements. The study found land-use conversions between the year 2004 and 2017. The increased residential areas in the City of Yogyakarta is attributable to educational activities, which are believed to have triggered urbanization and urban development (Rachmawati et al, 2004). A higher density of settlement means a broader impervious surface that contributes to transforming more proportion of rainfall into surface runoff. This is consistent with previous research, that urban areas will affect the infiltration process. The waterproof surfaces will worsen the runoff process because the dynamics of the infiltration process area disrupted (McGrane, 2016). The land-use change in Winongo Watershed is presented in **Table 1**. Spatially, the densely populated residential areas in the downstream, i.e., close to the city, had significantly expanded in 2017. The 2004 and 2017 land use maps are illustrated in **Fig. 3.**

Table 1.

The land utilization of Winongo Watershed in 2004 and 2017

Land use	Area (Km^2)			
	2004	**%**	**2017**	**%**
Shrubs	0.11	0.26	0.109	0.26
Building	0.04	0.10	0.254	0.60
Plantation	2.05	4.81	2.379	5.58
Settlement	12.47	29.22	15.239	35.72
Grass	0.34	0.80	0.337	0.79
Rice field	26.73	62.65	23.391	54.83
Dry agricultural land	0.93	2.17	0.829	1.94
Industrial area	-	0	0.123	0.29
Total	42.661	100.00	42.661	100.00

Land use with increased areas included buildings, plantations, settlements, and industrial zones. These four types of land use are closely related to human activities. Expansion of buildings, residential areas, and industrial estates is an effort to improve urban facilities due to urban development. Meanwhile, a decrease in vacant land covered by shrublands and grass, as well as irrigated rice fields and dry agricultural lands with productive soils, confirms that the land-use conversion in Winongo Watershed is oriented to built-up areas. Moreover, abandoned spacefaring of many factors attracting developers to build houses in the city (Suradi & Bakti, 2004).
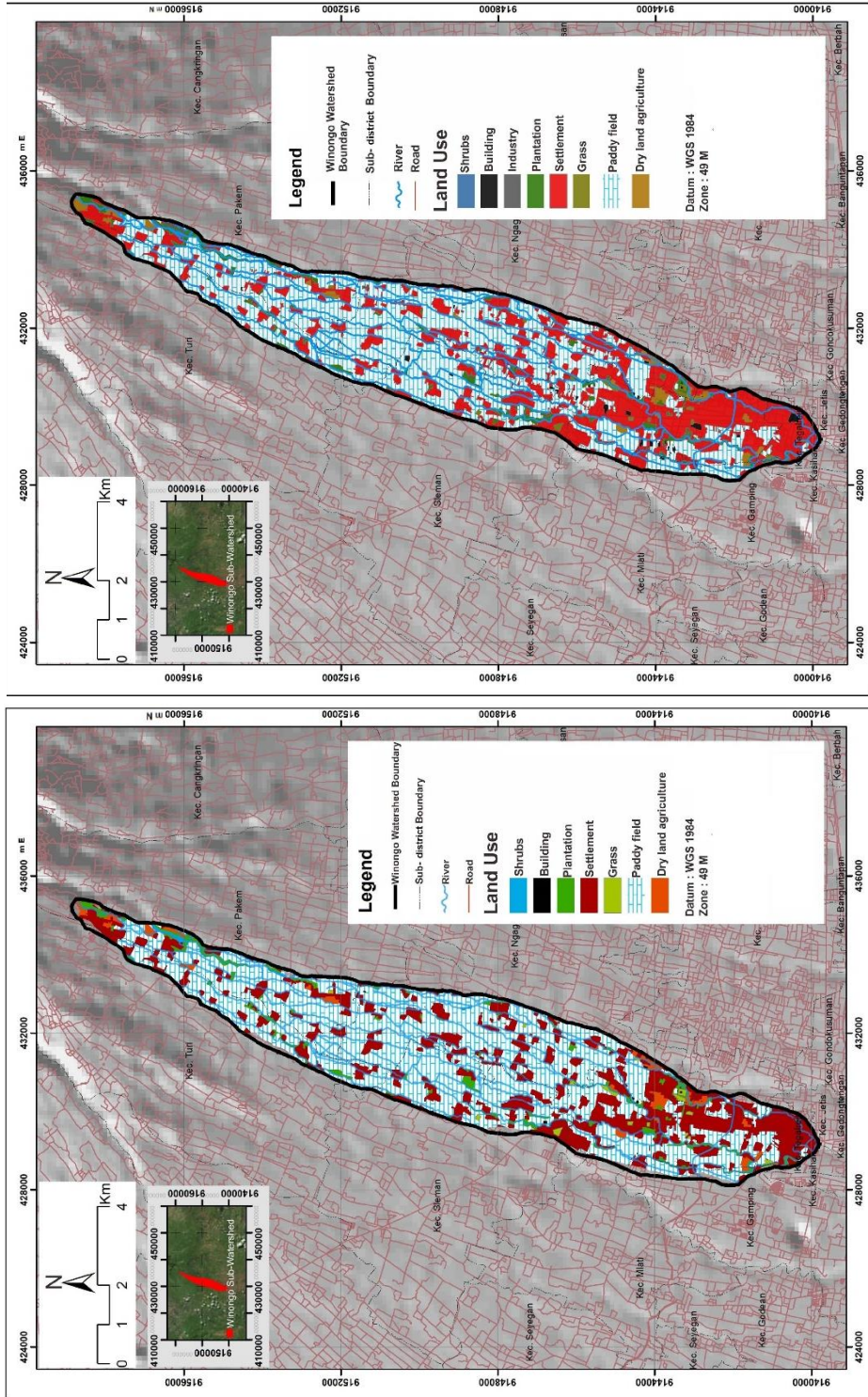
Fig. 3. The land use of Winongo Watershed in 2004 (left) and 2017 (right)

Recurrent rainfall was estimated using 15-year series of rain data at five weather stations, namely Angin-Angin, Beran, Gemawang, Kemput, and Prumpun. The software calculation resulted in rainfall

data with the return periods of 2, 5, 10, 25, and 50 years. Afterward, Intensity Duration Curve Frequency (IDF) was developed to obtain rainfall intensity based on time of concentration, as presented in **Fig. 4.**
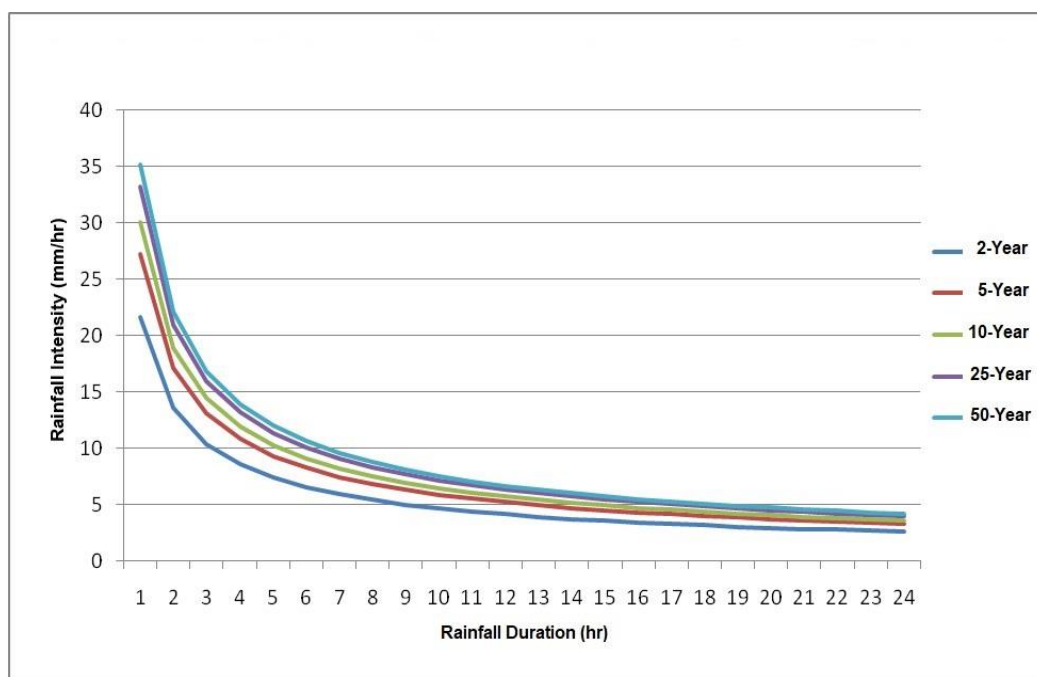
Fig. 4. Rainfall intensity-duration-frequency curves based on time of concentration.

3.2. Runoff coefficient

The runoff coefficient shows the ratio of surface runoff to rainfall, with values ranging from 0 to 1. A smaller coefficient (approaching 0) indicates that an area stores a portion of rainwater falling to it, whereas a larger one (closer to 1) shows that an area has less ability to store rainwater properly and tends to transform it into runoffs. Cook's methodconfirmed that the land-use conversion from the year 2004 to 2017 did not change the runoff coefficient drastically. The runoff coefficients in both years were similar, i.e., the weighted average in 2004 was 0.64 and slightly increased to 0.652 in 2017.

3.3. Maximum flood discharge

The maximum flood discharge calculated by the Rational method is presented in **Table 2.** The characteristics of a watershed are relatively static, except for land use that tends to be dynamic. Therefore, parameter C (runoff coefficient) in 2004 was different from the one in 2017, and it represents how land use has changed in fourteen years. Meanwhile, the rainfall intensity and area of drainage basin incorporated in the calculation were unchanged. High rainfall intensity and concomitant extreme runoff can lead to flooding in urban areas (Jha et al. 2012). The rainfall intensities of Winongo Watershed for each return period were as follows: 16.5 mm/hour for the 2-year return period, 20.8 mm/hour for 5-year, 23.0 mm/hour for 10-year, and 25.3 mm/hour for 25-year. This watershed covers an area of 42.66 Km2.

The estimation of maximum flood discharge (in m³/sec) in 2004 and 2017

Return Period (Year)	2004				2017			
	C	I	A	Q	C	I	A	Q
2	0.640	16.5	42.66	127.3	0.652	16.5	42.66	127.9
5	0.640	20.8	42.66	157.9	0.652	20.8	42.66	160.5
10	0.640	23.0	42.66	174.6	0.652	23.0	42.66	177.6
25	0.640	25.3	42.66	192.0	0.652	25.3	42.66	195.7

From 2004 to 2017, changes in land use did not significantly affect the maximum flood discharge for the 2-year return period, with a difference of merely 0.6 m³/s. However, for the 5-, 10-, and 25-year return periods, the differences were noticeable, i.e., 2.6 m³/s, 3.0 m³/s, and 3.7 m³/s, respectively. The longer the recurrence intervals, the higher the maximum discharge and the more extensive the flood inundation are.

3.4. Flood inundation analysis

The stream centerlines generated from HEC-GeoRAS were 2.12 km in length. Referring to Marfai (2003), this study concluded that there were two types of channel surfaces. Since meandering channels with clear water were dominant in Winongo River, its Manning's coefficient of roughness was n=0.04. Also, the presence of dams and buildings on both right and left floodplains categorized the coefficient of roughness at n=0.013. The terrain along the river varied, and there were even river segments with terraced cliffs and crags.

The modeling using elevation data,as derived from aerial photographs, produced an acceptable accuracy, with recommended minor corrections on points of elevation that were distorted due to the high densities of vegetation and built-up land in the study area. The HEC-GeoRAS modeling generated a pattern of flood inundation scenarios that were similar for each return period and runoff coefficient in 2004 and 2017. In general, the eight models (four return periods each in 2004 and 2017) showed that several river segments could not accommodate the maximum discharge and, therefore, caused overflows. Spatially, these segments are located in the upper and middle parts of the river. Settlements and buildings were land utilizations that regularly suffered losses due to flood inundation for the return periods of 2, 5, and 10 years because these forms of human occupation were built close to the river, particularly on the riverbanks. Meanwhile, for the 25-year return period, the area of inundation was broader and even reached several cemeteries.

Compared to the year 2004, the simulated floods in 2017 inundated a more extensive area but with less noticeable change. This condition was caused by the conversion of land use in the last fourteen years, which likely led to increased runoff coefficient and, subsequently, maximum discharge. The inundated area for the 2-year return period was 7,131.1 m² in 2004 and expanded to 7,178.1 m² in 2017.For the 5-year return period, the modeled maximum discharge inundated 7,461.7 m² land in 2004 and broadened to 7,498.8 m² in 2017. As for the return period of 10 years, the inundated area increased from 7,977.8 m² in 2004 to 8,017.8 m² in 2017. The same case applies to the maximum discharge with a 25-year return period, which inundated 8,649.7 m² in 2004 and up to 8,844.4 m² in 2017. The spatial distributions of flood inundation based on land use in 2004 and 2017 are presented in **Fig. 5, 6, 7 and 8** each for maximum flood discharge with the return period of 2, 5, 10, and 25 years.
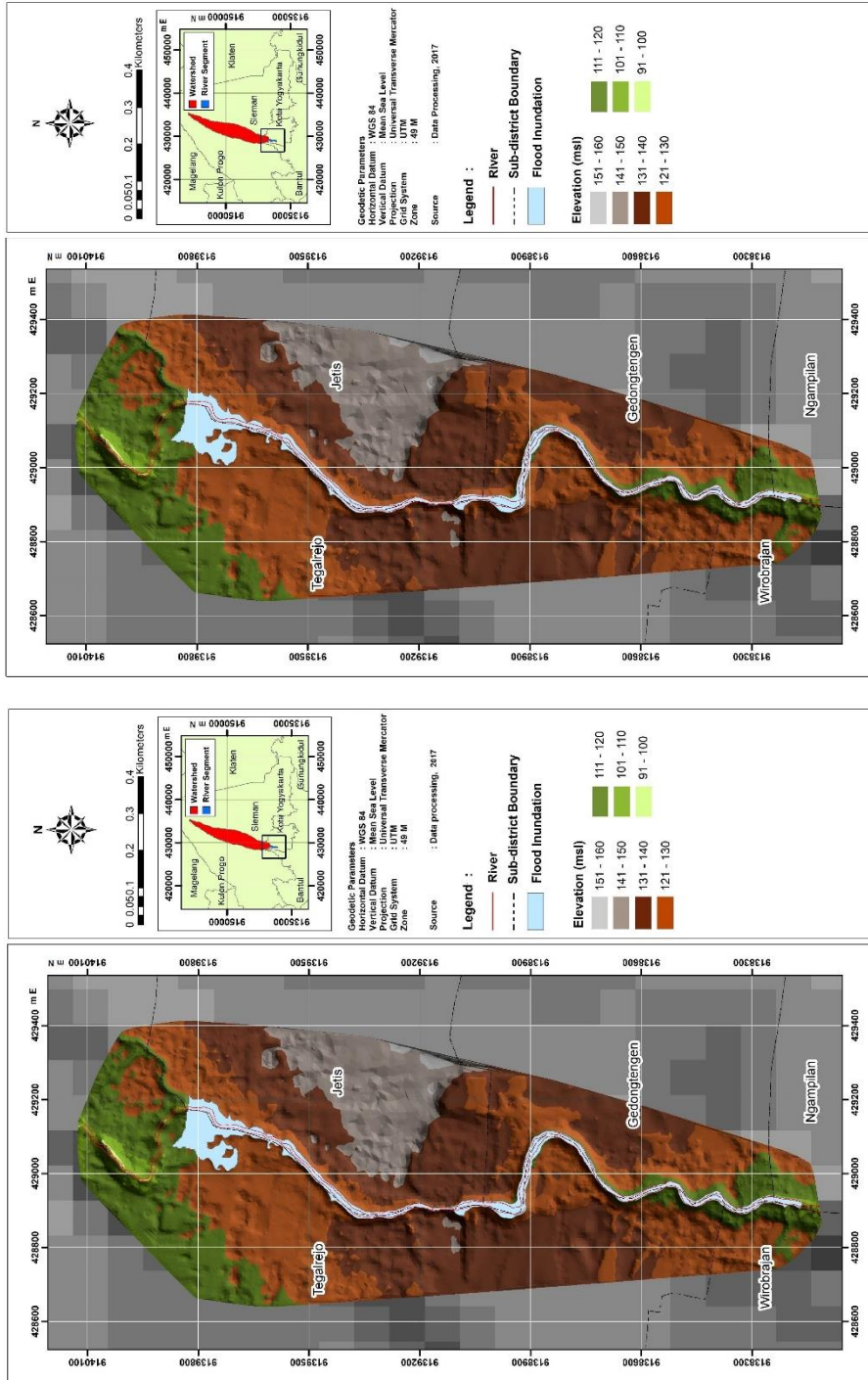
Fig. 5. Flood inundation map due to maximum discharge with 2-year return period based on the land use condition in 2004 (left) and 2017 (right)
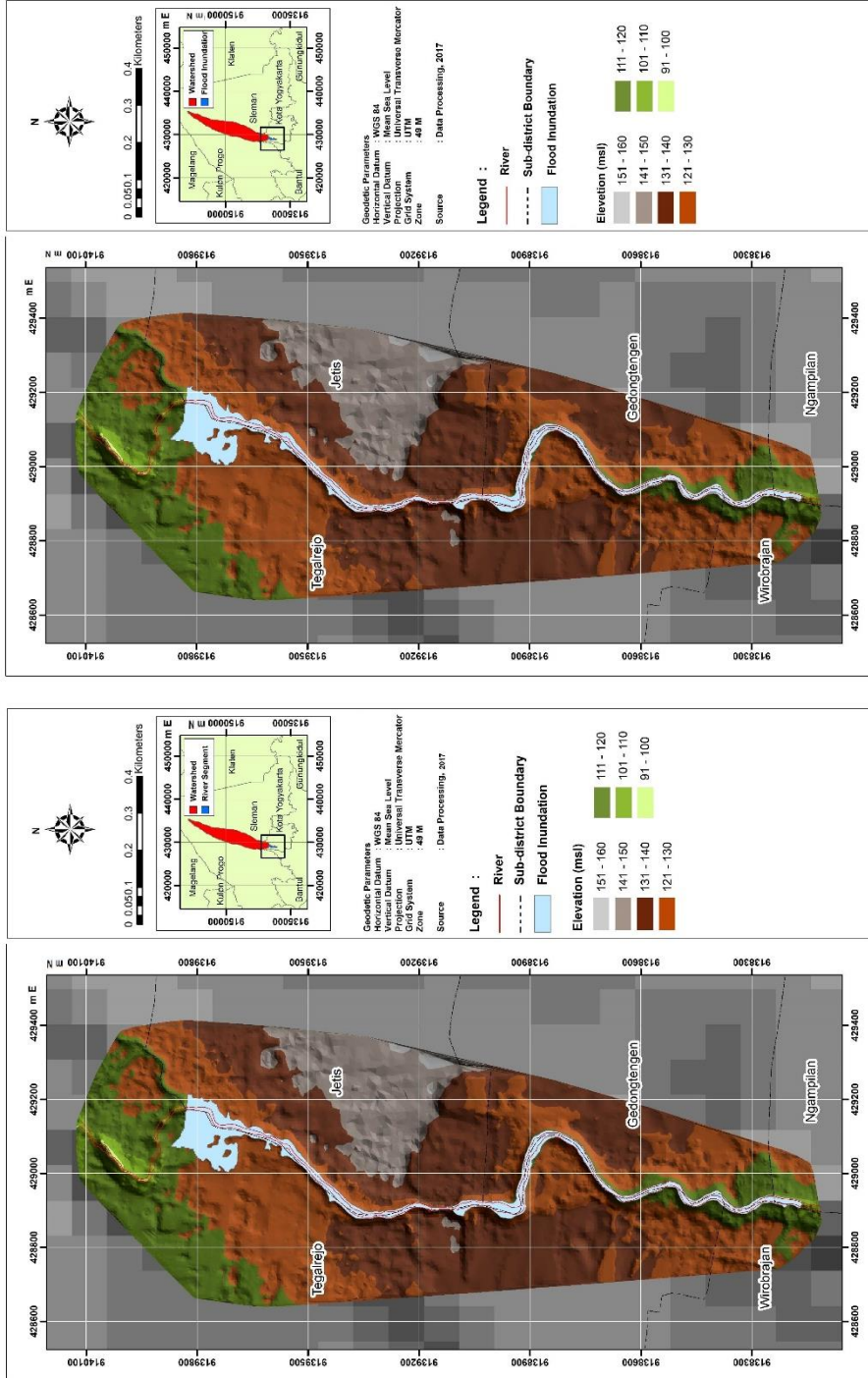
Fig. 6. Flood inundation map due to maximum discharge with 5-year return period based on the land use condition in 2004 (left) and 2017 (right)
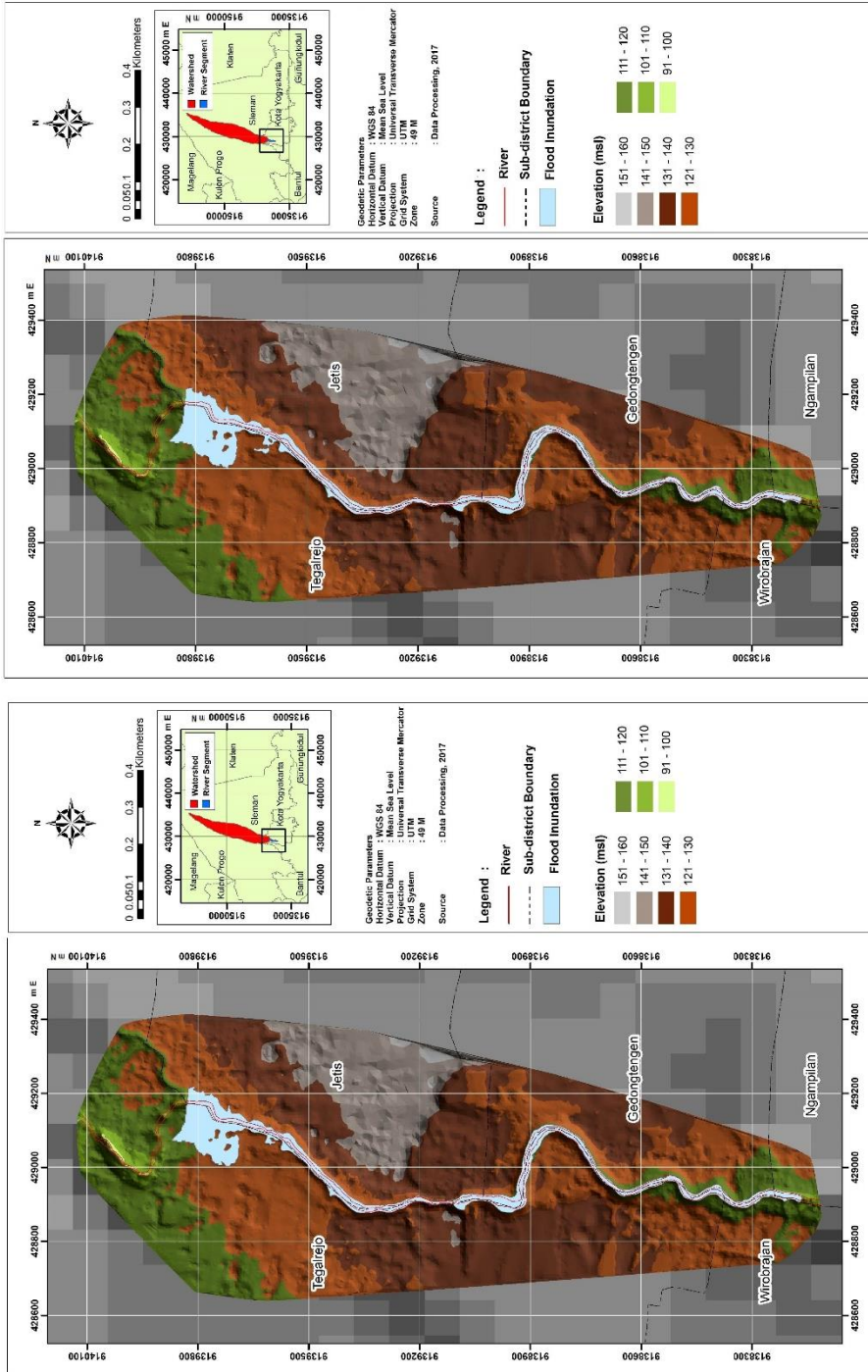
Fig. 7. Flood inundation map due to maximum discharge with 10-year return period based on the land use condition in 2004 (left) and 2017 (right)
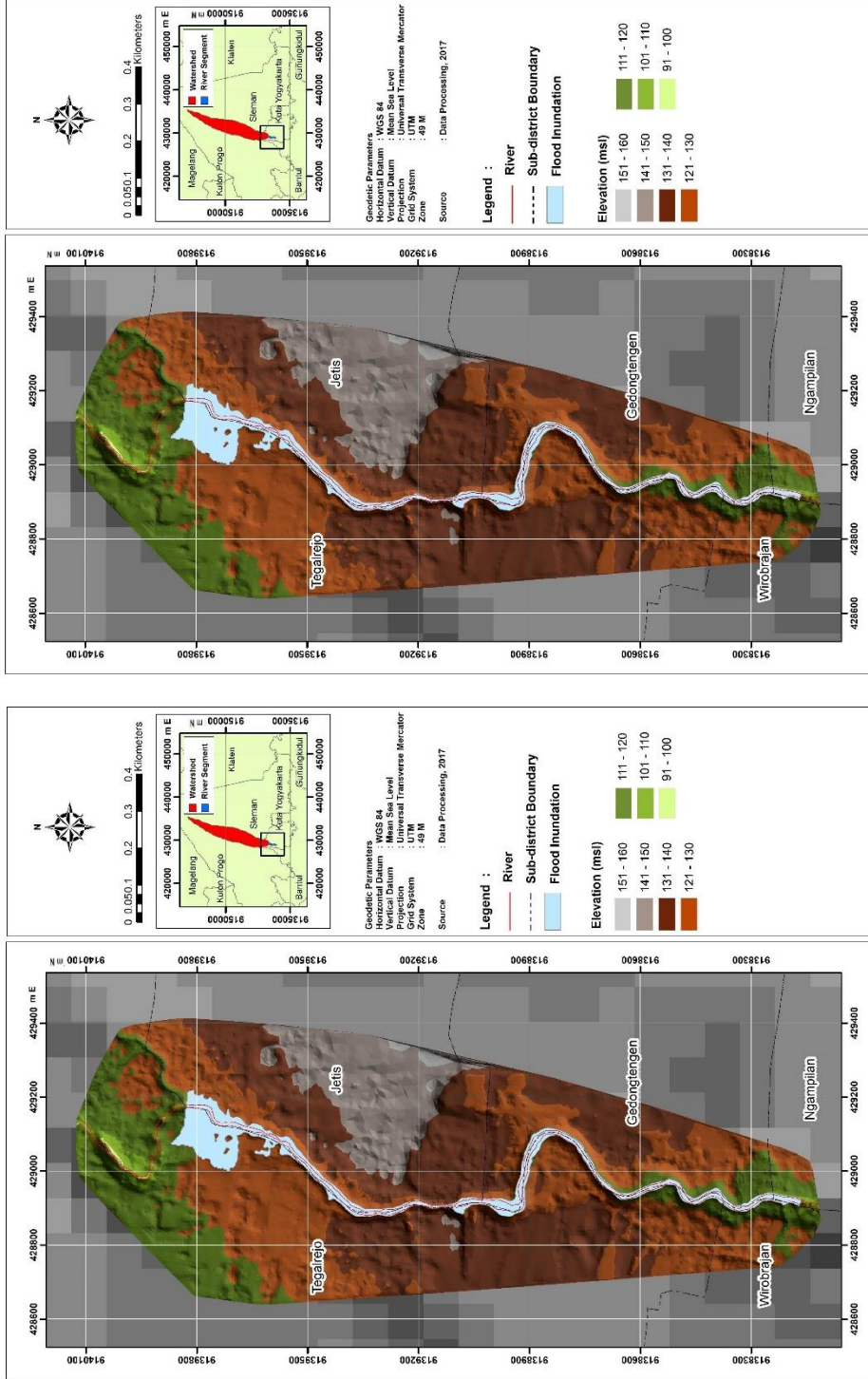
Fig. 8. Flood inundation map due to maximum discharge with 25-year return period based on the land use condition in 2004 (left) and 2017 (right)

4.   CONCLUSION

Land-use conversion, as seen in the last fourteen years from 2004 to 2017, is the consequence of urban development in Winongo Watershed. It causes an increase in built-up areas (i.e., settlements, buildings, industrial zone) and a decrease in vacant land (i.e., shrubs, grass) and productive land (i.e., irrigated rice fields and dry agricultural land). As a result, the runoff coefficients changed from 0.64 in 2004 to 0.652 in 2017. Although insignificant, such difference has led to varying changes in maximum river flow discharge. In 2014, the maximum discharge with a 2-year return period was 127.3 m^3/s and slightly increased to 127.9 m^3/s in 2017. However, for the 5-, 10-, and 25-year return periods, there were noticeable rises in maximum discharge. The model for a 5-year return period showed an increase from 157.9 m^3/s (in 2004) to 160.5 m^3/s (in 2017). For the 10-year return period, the maximum discharge rose from 174.6 m^3/s (in 2004) to 177.6 m^3/s (in 2017), and for the 25-year return period, it also increased from 192.0 m^3/s (in 2004) to 195.7 m^3/s (in 2017). Furthermore, the areas of flood inundation for each return period (2, 5, 10, and 25 years) were respectively: 7,131.1 m^2 (2004) and 7,178.1 m^2 (2017); 7,461.7 m^2 (in 2004) and 7,498.8 m^2 (in 2017); 7,977.8 m^2 (in 2004) and 8,017.8 m^2 (in 2017); 8,649.7 m^2 (in 2004) and 8,844.4 m^2 (in 2017). As preliminary, this analysis shown that spatially, the overflows and floods have been identified in the upper and middle segments of the Winongo River. More elaborative research including the governance in disaster management is necessary to be done in the near future.

R E F E R E N C E S

Alvarez, J. A. C. & Resosudarmo, B. P. (2019) The cost of floods in developing countries' megacities: a hedonic price analysis of the Jakarta housing market, Indonesia. *Environmental Economis and Policy Studies,* 21, 555-577.

Al Dianty M., Arbaningrum, R., Putuhena, F.J. (2020) The linkage of effect climate change for determining design flood of Tenggang river. *Geographia Technica,* 15, Special Issue, 3-12. DOI:10.21163/GT_2020.151.17

Arcement, G. J. & Schneider, V.R. (1989) *Guide for Selecting Manning's Roughness Coefficients for Natural Channel and Flood Pains* Available from: https://pubs.usgs.gov/wsp/2339/report.pdf [Accessed 14th November 2019].

Beretta, R., Ravazzani, G., Maiorano, C. & Mancini, M. (2018) Simulating the Influence of Buildings on Flood Inundation in Urban Areas. *Journal of Geosciences MDPI,* 8 (77).

Booker, A. S. (2006) Modeling the 100-Year Flood Using GIS: A Flood Analysis in the Avon Park Watershed. *Graduate Theses and Dissertations*, University of South Florida.

BPS Kota Yogyakarta (2018) *Kota Yogyakarta dalam Angka 2018*. Yogyakarta: BPS Kota Yogyakarta.

Buletin Tata Ruang (2008) *Kawasan Aglomerasi Perkotaan YOGYAKARTA dan Trans Jogya*.

Chin, D. A. (2019) Estimating Peak Runoff Rates Using the Rational Method. *Journal of Irrigation and Drainage Engineering,* 145.

Dasanto, B. D., Pramudya, B., Boer & Suharnoto, Y. (2014) Effects of Forest Cover Change on Flood Characteristics in the Upper Citarum Watershed. *Jurnal Manajemen Hutan Tropika (JMHT),* 10 (3), 141-149.

Fujiki, K., Renard F. (2018) A geographic analysis of post-disaster social impacts on a municipal scale – a case study of a potential major flood in the Paris region (France). *Geographia Technica,* 13 (2), 31-51. DOI : 10.21163/GT_2018.132.03

Giyarsih, S.R. & Marfai, M.A. (2017) The perception of stakeholders on regional transformation on the outskirts of Yogyakarta City, Indonesia. *Geojournal*, 83(5), 83-91

Goodchild, M. F. (2009) Geographic information systems and science: today and tomorrow. *Journal Annals of GIS,* 15.

Govers, G., Takken, I. & Helming, K. (2000) Soil roughness and overland flow. *Agronomie, EDP Sciences,* 20 (2), 131-146.

Győri, M. M., Haidu, I., & Humbert, J. (2016). Deriving the floodplain in rural areas for high exceedance Probability Having limited data source. *Environmental Engineering and Management Journal,* 15, 1879-1887. DOI:10.30638/eemj.2016.201.

Hadisusanto, N. (2011) *Aplikasi Hidrologi*. Yogyakarta: Yogya Mediautama.

Idham, N. C. (2018) Riverbank Settlement and Humanitarian Architecture, The Case of Mangunwijaya's Dwellings and 25 Years After, Code River, Yogyakarta, Indonesia. *Journal of Architecture and Urbanism,* 42 (2), 177-187.

Ivan, K. (2015). The spatio-temporal analysis of impervious surfaces in Cluj-Napoca, Romania. *Geographia Technica,* 10 (2), 50-58.

Jha, A. K., Bloch, R. & Lamond, J. (2012) *Kota dan Banjir, Panduan Pengelolaan Terintegrasi untuk Resiko Banjir Perkotaan di Abad 21*. Washington: The World Bank.

Johnston, R. J. (1981) *The Dictionary of Human Geography*. London: Basil Backwell Publisher Limited

Karaoui, I., Arioua, A., and Idrisi A E A (2016) Flood Inundation Mapping of Risk Zones in the Future Flood Events in Alfet River-Oued Al Abid Watershed-Using GIS Techniques and HEC-RAS Model. *ATINER'S Conference Paper Series*, No: ERT2016-2111

Kim, V., Tantanee, S., Suparta, W. (2020) GIS-based flood hazard mapping using HEC-RAS model: a case study of lower Mekong river, Cambodia. *Geographia Technica,* 15 (1), 16-26. DOI: 10.21163/GT_2020.151.02

Kodoatie, R. J. & Sugiyanto (2002) *BANJIR: Beberapa Penyebab dan Metode Pengendaliannya dalam Perspektif Lingkungan*. Yogyakarta: Pustaka Pelajar.

Kusumastuti, C., Sudjarwo, P., Christhie, M. & Krisna, T. (2019) Intensity-Duration-Frequency (IDF) Curve and the Most Suitable Method to Determine Flood Peak Discharge in Upper Werba Sub-Watershed. *Civil Engineering Dimension Journal,* 21 (2), 70-75.

Marfai, M. A. (2003) Pemodelan Banjir pada Kali Banjir Kanal Barat. *Forum Geografi,* 17 (1), 39-50.

Marfai, M. A. & Sekaranom, A. B. (2012) SIG dan aplikasinya untuk analisis bahaya banjir. *Proc. Seminar penginderaan jauh & SIG*, 292-300. UMS press. issn:978-979-636-137-3

McGrane, S.J. (2016) Impacts of urbanisation on hydrological and water quality dynamics, and urban water management: a review. *Hydrological Sciences Journal,* 61 (13), 2295-2311.

Meng, X., Zhang, M., Wen, J., Du, S., Xu, H., Wang, L. & Yang, Y. (2019) A Simple GIS-Based Model for Urban Rainstorm Inundation Simulation. *Journal of Sustainability MDPI,* 11.

Miller, S. (1994) *Handbook for Agrohydrology*. Chatam, UK: Natural Reasources Institute Available from: http://www.nzdl.org/ [Accessed 14th November 2019].

Nusit, K., Tantanee, S., Subsomboon, K., Leungvichcharoen, S., Yiemwattana, S. (2019) The design of flood protection along Nan river, Phitsanulok Province, Thailand. *Geographia Technica,* 15, Special Issue, 129-137. DOI: 10.21163/GT_2019.141.26

Prayitno, B. (2018) Co-habitation Space: A Model for Urban Informal Settlement Consolidation for the Heritage City of Yogyakarta, Indonesia. *Journal of Asian Architecture and Building Engineering,* 16 (3), 527-534.

Rachmawati, R., Rijanta, R., Subanu & Leksono, P. (2004) Peranan Kampus sebagai Pemicu Urbanisasi Spasial di Pinggiran Kota Yogyakarta. *Majalah Geografi Indonesia,* 18 (1), 45-46.

Samanta, S., Pal, D. K. & Palsamanta, B. (2017) Flood susceptibility analysis through remote sensing, GIS and frequency ratio model. *Journal of Applied Water Science,* 8 (66).

Silva, F.V., Bonuma, N.B. & Uda, P.K. (2014) Flood Mapping in Urban Area Using HEC-RAS Model Supported by GIS. *6th International Conference n Flood Management, Sao Paulo Brazil* Available from: https://pdfs.semanticscholar.org/d841/024eab916629c07efd988bcb5093d265ecfa.pdf [Accessed 14th November 2019].

Suprayogi, S., Marfai, M. A., Cahyadi, A., Latifah, R. & Fatchurohman, H. (2019) Analyzing the characteristics of domestic wastes in Belik river, Yogyakarta. *Asean Journal on Science and Technology for Development*, 36 (3), 97–102

Suradi & Bakti, S. (2004) Efisiensi Pemanfaatan Lahan Perkotaan melalui Pengembangan Pengisian di Yogyakarta. *Jurnal Manusia dan Lingkungan,* 11 (1).

Suripin (2002) *Pelestarian Sumberdaya Tanah dan Air*. Yogyakarta: ANDI.

Tomaszewski, B., Judex, M., Szarsynski, J., Radestock, C. & Wirkus, L. (2015) Geographic Information Systems for Disaster Response: A Review. *Journal of Homeland Security& Emergency Management,* !2 (3).

US Army Corps of Engineers (1987) *The Hydrologic Engineering Center's Activities in Watershed Modeling* Available from: https://www.hec.usace.army.mil/publications/TechnicalPapers/TP-116.pdf [Accessed 14th November 2019].

US Army Corps of Engineers (2010a) *HEC-RAS: River Analysis System. Applications Guide Book* Available from: https://www.hec.usace.army.mil [Accessed 6th November 2019].

US Army Corps of Engineers (2010b) *HEC-RAS: River Analysis System. User's Manual* Available from: https://www.hec.usace.army.mil/ [Accessed 6th November 2019].

Xie, Y., Bie, Q. & He, C. (2017) Human settlement andchanges in the distribution of river systems in the Minqin Basin over the past 2000 years in Nothwest China. *Journal of Ecosystem Health and Sustainability,* 3.

DOWNSCALING BUDYKO EQUATION FOR MONTHLY ACTUAL EVAPOTRANSPIRATION ESTIMATION OVER THE EMILIA-ROMAGNA REGION

Mărgărit-Mircea NISTOR[1,2] iD *, Federico CERVI[3]* iD

ABSTRACT:
This paper presents a modified Budyko equation (Budyko DOWNSCALED) for assessing actual evapotranspiration (AET0). The approach is tested by using 100 controlled and homogeneous meteorological stations located in the Emilia-Romagna region from North of Italy. A period of 55 years, from 1961-1990 and 1991-2015, was analyzed as long-term datasets of monthly values of precipitations, maximum and minimum temperatures. These data have allowed AET0 to be computed both at the yearly and the monthly scale with the Budyko ORIGINAL and Budyko DOWNSCALED formula, respectively. Results of both methods have been compared at the yearly scale, demonstrating that the Budyko DOWNSCALED approach almost correctly reproduces the annual AET0 values (R^2 equal to 0.77 and 0.73 for 1990s and 2015s, respectively) even if slightly underestimated (by 119 mm for 1990s and by 136 mm for 2015s). Further, monthly AET0 values were aggregated over a baseline period (between 1961 and 1990: 1990s) and a recent period (between 1991 and 2015: 2015s). In both baseline and recent periods, AET0 is higher in the summer months (May to September), while it is almost nil in winter season (January, February, and December). Monthly values of AET0 did not increase over the recent period as a result of increased temperatures. Further, this study contributes to the future management of water resources in the region.

Key-words: *climate data, evapotranspiration, Budyko approach, Emilia-Romagna.*

1. INTRODUCTION

Climate (here meant as the long-term averages of meteorological variables across a specific area) is the main driver of the surface water and groundwater resource renewal worldwide. Long-term changes in the amount of solid (snow) and liquid precipitations occurring at the soil surface may alter the recharge of surface water and groundwater. Evapotranspiration processes are influenced by several meteorological variables such as precipitations, humidity, wind and temperature. As a result, changes in the long-term trends of the above-mentioned variables lead to different precipitation quotas that return to the atmosphere by means of plant transpiration (Nistor et al., 2018).

Among the others, the Budyko formula is widely used to obtain estimates of the annual actual evapotranspiration (AET0). In this study, we use a 55-year long dataset (1961-2015) from 100 controlled and homogeneous meteorological stations located in the Emilia-Romagna region (northern Italy), an area in which clayshales widely outcrop and soil moisture changes in the upper part of the soil (to be intended as a thin weathered cover above the non-permeable materials) are somehow reduced. Moreover, several authors have already highlighted a precipitation reduction in the last century (Pavan et al., 2008; Pavanelli & Capra, 2014; Nistor & Mîndrescu, 2019; Haidu & Nistor, 2019). The latter became more intense starting from the 1990s (Tomozeiu et al., 2002; Pavan et al., 2008; Antolini et al., 2016) and has mainly affected the winter and spring seasons (Tomei et al., 2010). Moreover, from 1961 to 2010 the Emilia-Romagna region experienced an increase in the mean annual

---

[1]*1Nanyang Technological University, School of Civil and Environmental Engineering, Singapore*
[2]*Department of Hydrogeology, Earth research Company, Cluj-Napoca, Romania, renddel@yahoo.com;*
[3]*Scientific High School Aldo Moro, Reggio Emilia, Italy, fd.cervi@gmail.com.*

temperatures up to 0.5°C/decade for the period 1961−2010. Recently, Du et al. (2016) made a first attempt to adapt the Budyko formula to a monthly time-scale in an arid environment.

The main objective of this work is thus to test a Budyko DOWNSCALED formula for assessing AET0 at a monthly scale. The results of this work are promising as they confirm the reliability of this approach even under unsteady-state of the soil moisture. Annual AET0 obtained by both Budyko ORIGINAL and Budyko DOWNSCALED formulas are compared in order to check the reliability of the new tested method. For the sake of convenience, the former dataset is split into a reference period 1961−1990 (1990s) and a recent period 1991−2015 (2015s).

Fig. 1. Location of the Emilia-Romagna region on a map of Italy.

2. STUDY AREA

The Emilia-Romagna region is located in the northern Italy and is between 43°44′ and 45°08′ latitude North and between 9°11′ and 12°45′ longitude East (**Fig. 1**). The altitudes range from below 0 m in Po Plain to 2165 mm in Mt. Cimone.

The monthly precipitation varies from 37 mm to 211 mm (monthly average for 1961-1990), with higher values the South-Western part of theregion and lower values on the North-Eastern part (**Fig. 2**). The recent period (1991-2015) indicates a monthly precipitation range from 34 mm to 309 mm (**Fig. 3**). In both the 1990s and 2015s periods, July experienced the most arid month with a large territory with values below 50 mm. During the 1990s, the mean annual temperature varied from 6.1 °C to 13.6 °C, while during the 2015s, the mean annual temperature varied from 7.1 °C to 15 °C.

The climatic characteristics of the region are closely related to the relief unit arrangements: northern Apennines mountains in South, South-West, and West, hilly areas in the central, West, and South-East parts, and Po Plain in the East, North, and North-West, and North-central parts of the region.

Fig. 2. Spatial distribution of monthly precipitation (PP) in the Emilia-Romagna region related to the 1990s. Background image source: Esri, Garmin, GEBCO, NOAA NGDC, and other contributors.

Fig. 3. Spatial distribution of monthly precipitation (PP) in the Emilia-Romagna region related to the 2015s. Background image source: Esri, Garmin, GEBCO, NOAA NGDC, and other contributors.

3. DATA AND METHODS

3.1. Climate data

Three datasets of maximum and minimum monthly temperature and precipitation were used in this study. The climate data represent historical monthly records from 1961 to 2015. The datasets have been made freely available by Arpa Emilia-Romagna environmental agency (ARPA-EMR, 2019). In detail, these monthly datasets derived from the observed measurements of 100 meteorological stations uniformly distributed over the region. Antolini et al. (2016, 2017) have already verified the temporal homogeneity, synchronicity and consistency of these 100 meteorological stations.

It should be noted that the Budyko ORIGINAL approach results into the annual AET0.

3.2. Evapotranpiration calculation

3.2.1. Monthly Potential Evapotranspiration (ET0)

We decided to assess the monthly Potential Evapotranspiration (ET0) by using Thornthwaite method (1948) (Eq. (1)). This method assesses evapotranspiration by using the only the mean monthly temperature data. Even it has been used since the mid-20th century, this approach is still recognized as being appropriate for long-term studies requiring evapotranspiration estimates (Baltas, 2007; Čenčur Curk et al., 2014) and is suitable for climate and hydrological studies at a spatial scale (Zhao et al., 2013; Cheval et al., 2017).

The formula is expressed as follows:

$$ET_0 = 16bi(\frac{10T_i}{I})^\alpha \quad \text{[mm/month]} \tag{1}$$

where:

ET_0	-potential evapotranspiration;
bi	-radiation parameter for specific latitude (Table 1);
T_i	-monthly air temperature;
I	-annual heat index (see Eq. 2);
α	-complex function of heat index (see Eq. 3)

$$I = \sum_{i=1}^{12} \left(\frac{T_i}{5}\right)^{1.514} \tag{2}$$

where: T_i = monthly air temperature

$$\alpha = 6.75 \times 10^{-7} I^3 - 7.71 \times 10^{-5} I^2 + 1.7912 \times 10^{-2} I + 0.49239 \tag{3}$$

where: I = annual heat index

3.2.2. Budyko ORIGINAL for annual Actual Evapotranspiration (AET0)

The Actual Evapotranspiration (AET0) is defined as the quantity of water that is actually removed from the soil due to the processes of both evaporation from water surfaces and transpiration from plants. The Budyko approach (1974) (Eq. (4)) requires ET0 and total annual precipitation PP and it return the annual AET0. This method is widely used worldwide for water balance assessment at the annual scale (Gerrits et al., 2009; Greve et al., 2016; Fathi et al., 2019).

$$\frac{AET0}{PP} = [\left(\varphi\tan\frac{1}{\varphi}\right)(1 - \exp^{-\varphi})]^{0.5} \tag{4}$$

where:

AET0	-actual evapotranspiration [mm]
PP	-total annual precipitation [mm]
Φ	-annual aridity index (Eq. (5))

$$\varphi = \frac{ET0}{PP} \tag{5}$$

3.2.3. Budyko DOWNSCALED for monthly AET0m

The procedure for Budyko DOWNSCALED approach (Eq. (6)) consists of using monthly variables instead of yearly ones. At this stage, the monthly precipitation (PPm) and monthly (ET0m) were used to carry out the monthly aridity index (Φm). Further, the Budyko formula was modified to calculate the monthly AET0m. The latter can be calculated as follows:

$$\frac{AET0\,m}{PP\,m} = [\left(\varphi\,m\,\tan\frac{1}{\varphi m}\right)(1 - \exp^{-\varphi}m)]^{0.5} \tag{6}$$

where:

AET0m	-monthly actual evapotranspiration [mm]
PPm	-monthly precipitation [mm]
Φm	-monthly aridity index (Eq. (7))

$$\varphi\,m = \frac{ET0\,m}{PP\,m} \tag{7}$$

Thus, the effective annual AET0 is downscaled to the monthly temporal scale.

3.3. Validation of the Budyko DOWNSCALED approach for AET0m estimates

In order to validate our results, we compared in an x-y plot the mean annual AET0 obtained by Budyko ORIGINAL with the mean annual AET0 calculated by aggregating the AETm from the Budyko DOWNSCALED method. In detail, the mean annual AET0 (i.e., the annual actual evapotranspiration obtained as a unique mean value for both baseline and recent periods) has been obtained at each of the 100 meteorological stations by using Budyko (x-value) and Budyko DOWNSCALED (y-value). Then, a straight-line y=ax+b was fitted to the data by using the Ordinary Least Squares (OLS) method and regression was forced through 0 (i.e., a null value of AET0 calculated with Budyko must correspond to a null value of AET0 estimated with Budyko DOWNSCALED). OLS regression assumes the x values are fixed and finds the line which minimizes the squared errors in the y values (Davis, 2001). By using the OLS method, we assume that x values have very little error associated with them, i.e. we consider as correct actual evapotranspiration data those obtained by using the Budyko ORIGINAL. Goodness of fits are reported in form of correlation coefficient (R^2).

4. RESULTS AND DISCUSSIONS

4.1. Validation of the Budyko DOWNSCALED approach for AET0m estimates

The annual AET0 from Budyko ORIGINAL and Budyko DOWNSCALED approaches have been compared by means of the OLS regression. Tests were carried out for both baseline (1990s) and recent (2015s) periods and evidenced that annual AET0 from Budyko ORIGINAL and Budyko DOWNSCALED were always correlated with similar goodness of fits (R^2=0.77 for 1990s, **Fig. 4**; R^2 = 0.73 for 2015s, **Fig. 5**). Equations characterizing the regression lines are also similar (y=0.78x for 1990s and y=0.76x for 2015s) and indicates that Budyko DOWNSCALED slightly underestimated the annual AET0 values as calculated by the Budyko ORIGINAL approach.
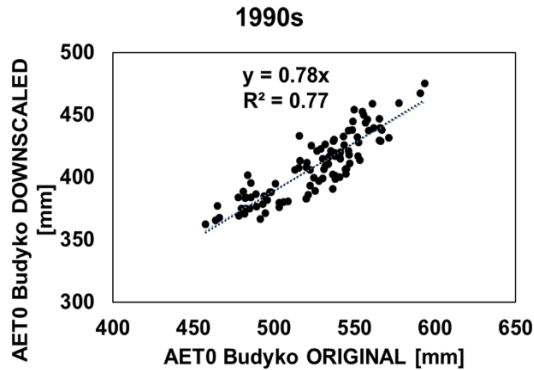
1990s

Fig. 4. Statistical analysis of annual AET0 values between the Budyko ORIGINAL and Budyko DOWNSCALED for the 1990s.
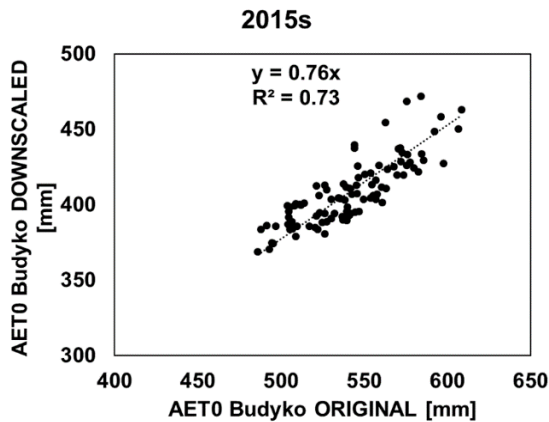
2015s

Fig. 5. Statistical analysis of annual AET0 values between the Budyko ORIGINAL and Budyko DOWNSCALED for the 2015s.

4.2. Evaluation and mapping of monthly AET0m

The variation of monthly actual evapotranspiration AET0m is related to the monthly ET0m and monthly precipitation PPm. As expected, AET0m values as calculated by the whole dataset of meteorological stations are almost lower than the corresponding ET0m for both baseline (1990s) and recent (the 2015s) periods. No remarkable changes can be evidenced between baseline and recent periods if we exclude the summer months of July and August, when the 2015s were characterized by lower values of this parameter. In particular, and for the 1990s period, the Budyko DOWNSCALED method allowed us to calculate values of monthly AET0m between 0.7 mm (January) mm to 68 mm (August). Spatial analysis indicates that higher values were found in the central part of the Northern Apennines, while the lowest values were detected in the northern part of the region (lowlands; **Fig. 6**). During the 2015s, the monthly AET0m varied from 2.2 mm (January) to 68 mm (June). Being controlled by the temperatures, the highest AET0m values were identified in the lowland areas while the lower ones along the main watershed divide of the northern Apennines (**Fig. 7**).

For both the 1990s and the 2015s periods, the lowest values (below 10 mm) of AET0m were found in the winter (December, January, February). During the months of March, April, May, September, October, and November, the AET0m variation showed values between 10 mm and about 60 mm for both periods.
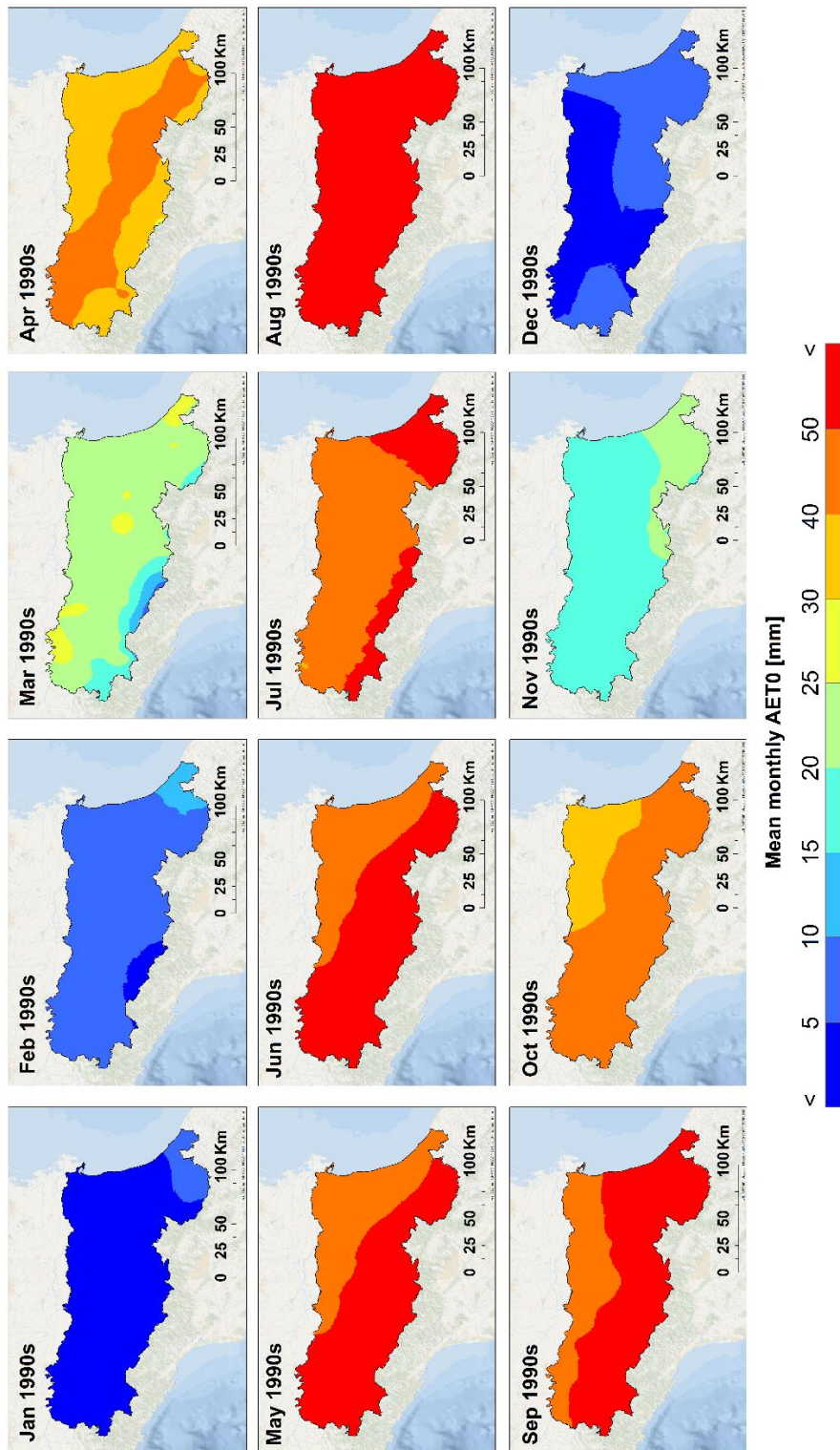
Fig. 6. Spatial distribution of monthly actual evapotranspiration (AET0) in the Emilia-Romagna region related to the 1990s. Background image source: Esri, Garmin, GEBCO, NOAA NGDC, and other contributors.
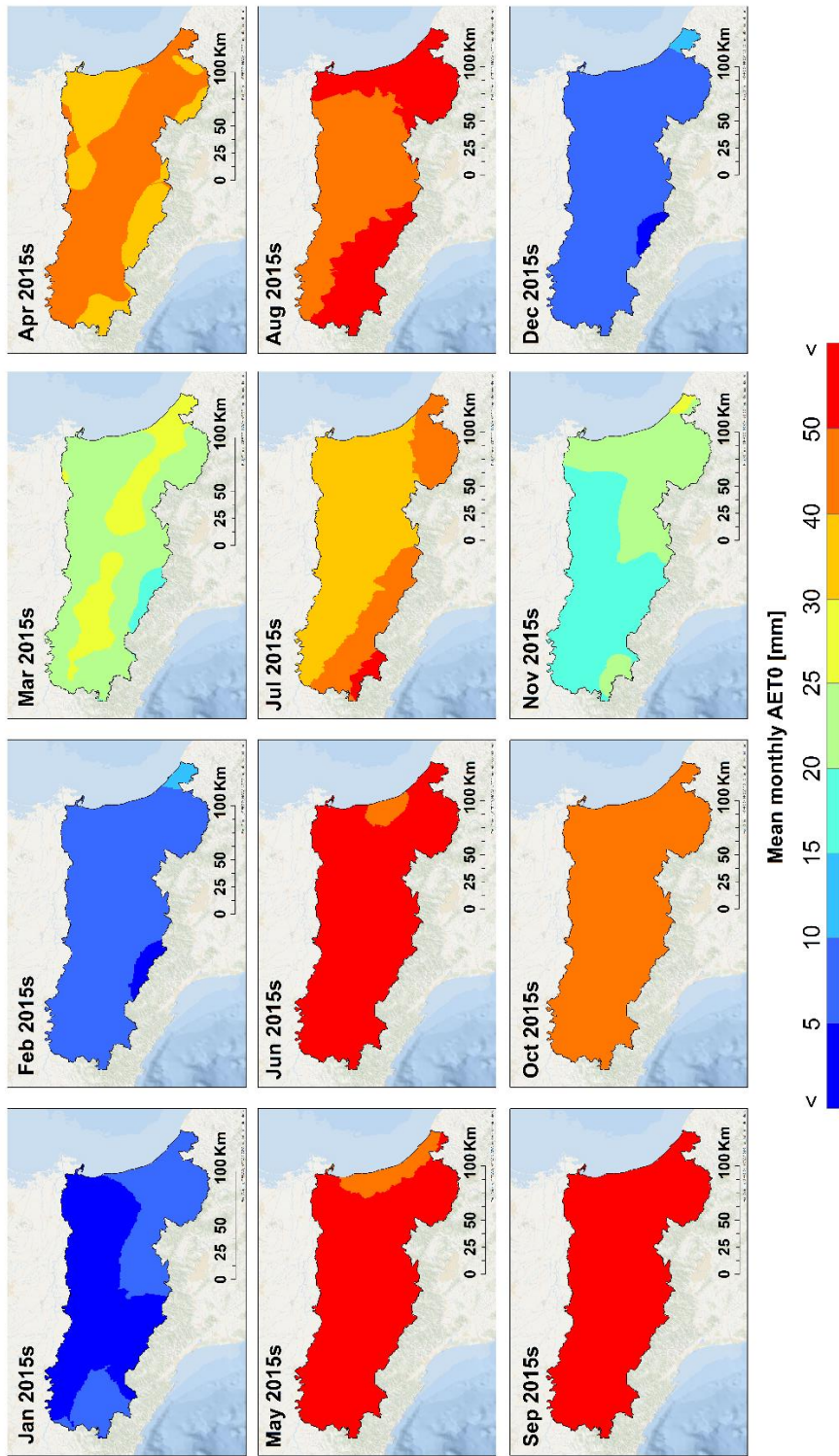
Fig. 7. Spatial distribution of monthly actual evapotranspiration (AET0) in the Emilia-Romagna region related to the 2015s. Background image source: Esri, Garmin, GEBCO, NOAA NGDC, and other contributors.

4.3. Mapping of the annual AET0

During the 1990s, the variation of annual AET0 carried out by Budyko ORIGINAL shows values between 458 mm to 589 mm and by Budyko DOWNSCALED (as sum of the 12 months) the values of annual AET0 vary from 362 mm to 470 mm. During 2015s, Budyko ORIGINAL indicates values between 485 m to 606 mm for annual AET0, while Budyko DOWNSCALED (as sum of the 12 months) indicates values between 369 mm to 470 mm. For both analyzed periods, the higher values of annual AET0 were depicted in the Northern Apennines and the lower values in the Po Plain. Interestingly, the area with high annual AET0 increased in the 2015s under Budyko ORIGINAL approach, while under Budyko DOWNSCALED, the pattern of the annual AET0 remained almost the same (**Fig. 8**).
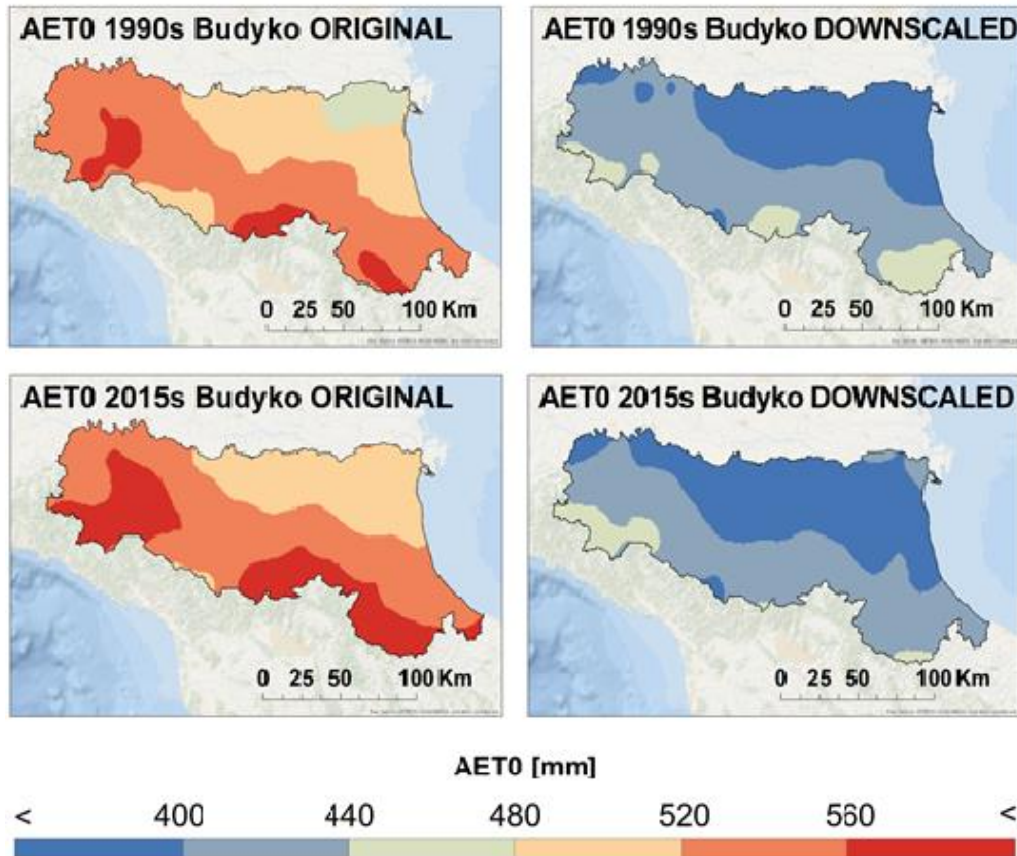
Fig. 8. Spatial distribution of annual AET0 in the Emilia-Romagna region. Background image source: Esri, Garmin, GEBCO, NOAA NGDC, and other contributors.

5. DISCUSSION

Goodness of fits by the regression lines between yearly actual evapotranspiration AET0 obtained by original and downscaled methods demonstrate that the results are correlated both in the case of the 1990s (R^2=0.77) and the 2015s (R^2=0.73). Regression lines slopes are similar (0.78 and 0.76, respectively) and evidenced that Budyko DOWNSCALED slightly underestimated the yearly actual evapotranspiration as compared with the Budyko ORIGINAL.

This fact is probably related to the non-perfect compliance with the assumption of steady-state in case of the Budyko DOWNSCALED approach; this means that by passing from month to month the

soil moisture varies and therefore the system is in a non-stationary state (unsteady state). Nonetheless, it should be noted that the underestimates are somehow reduced (about 20%) and similar for both baseline and recent periods, a value which makes it possible to state that the estimates of the monthly parameters are suitable for the comparison of different time-periods.

From the results, it was observed that the annual AET0 carried out by Budyko ORIGINAL indicates higher values than Budyko DOWNSCALED. The difference is about 120 mm respective 130 mm (i.e. 470 mm vs. 606 mm) for the maxima while for the minima, the difference is about 100 mm (i.e. 362 mm vs. 458 mm). These differences are influenced by the monthly precipitation and evapotranspiration regime. Budyko DOWNSCALED performs the cumulated annual AET0in good agreement with the Budyko ORIGINAL. However, the annual AET0 carried out using Budyko DOWNSCALED is lower than AET0 carried out by Budyko ORIGINAL. There are two reasons for the sub-estimation of Budyko DOWNSCALED. First, the sub-estimation of the Budyko DOWNSCALED in comparison to the Budyko ORIGINAL are due to the lower values of the aridity index (ET0/PP) in winter months. In that situation, the aridity index is influenced by low mean monthly temperatures, especially in the mountain stations. Secondly, the precipitation amount in the summer season is too low to be subtracted for the AET0. This indicates that in the months with high temperatures and high ET0, the monthly AET0 by Budyko DOWNSCALED remains low because of a lack of water from precipitation. This effect is not accounted for in the annual AET0 calculation by Budyko ORIGINAL. Du et al. (2016) observed that the local precipitation influences the overall application of Budyko at the local scale. Mianabadi et al. (2017) mentioned that the Budyko curves expressed in the Gerrits (2009) model are sensitive to the number of rain days and months especially for the higher precipitation rates.

6. CONCLUSIONS

The current study demonstrates the usefulness of the Budyko DOWNSCALED approach to estimate the mean monthly values of actual evapotranspiration (AET0m) by exploiting long time series of monthly temperature and precipitation datasets from a temperate area. We have used datasets from 100 meteorological stations spread over the Emilia-Romagna region and consisting of monthly data of temperatures and precipitations from 1961 to 2015. Time-series have been split into two time periods (baseline 1990s and recent 2015s) allowing for a comparison of the yearly averaged actual evapotranspiration values as obtained with the original and downscaled methods. The results highlight that averaged annual AET0 from both methods are strongly correlated (R^2 equal to 0.78 and 0.73, respectively) even if those from Budyko DOWNSCALED are slightly underestimated (about 20%). Although the Budyko DOWNSCALED slightly underestimates the final AET0 values, similar values of underestimation between the 1990s and the 2015s confirm the suitability for the comparison of AET0m from different periods.

The increase of the AET0 in the Emilia-Romagna region over the recent period (2015s) influences the recharge of rivers and aquifers both in the mountains and the plain. The results carried out here and the original maps could be useful instruments for the plan risk and water resources management in the region.

R E F E R E N C E S

Antolini, G., Auteri, L., Pavan, V., Tomei, F., Tomozeiu, F. & Marletto, V. (2016) A daily high-resolution gridded climatic data set for Emilia-Romagna, Italy, during 1961-2010. *International Journal of Climatology,* 36, 1970−1986.

Antolini G. et al. (2017) Atlante Climatico dell'Emilia-Romagna 1961-2015. Casma Tipolito, Bologna, Italy.

ARPAE-EMR, 2019. Regional agency for environmental protection in Emilia-Romagna Region:Analisi climatica giornaliera 1961-2015. Last access on September 2019, https://www.arpae.it/dettaglio_documento.asp?id=6147&idlivello=1528.

Baltas, E. (2007) Spatial distribution of climatic indices in northern Greece. *Meteorological Applications,* 14, 69−78.

Budyko, M.I. (1974) Climate and Life. Academic Press, New York, USA, p. 508.

Čenčur Curk, B., Cheval, S., Vrhovnik, P., Verbovšek, T., Herrnegger, M., Nachtnebel, H.P., Marjanović, P., Siegel, H., Gerhardt, E., Hochbichler, E., Koeck, R., Kuschnig, G., Senoner, T., Wesemann, J., Hochleitner, M., Žvab Rožič, P., Brenčič, M., Zupančič, N., Bračič Železnik, B., Perger, L., Tahy, A., Tornay, E.B., Simonffy, Z., Bogardi, I., Crăciunescu, A., Bilea, I.C., Vică, P., Onuțu, I., Panaitescu, C., Constandache, C., Bilanici, A., Dumitrescu, A., Baciu, M., Breza, T., Marin, L., Draghici, C., Stoica, C., Bobeva, A., Trichkov, L., Pandeva, D., Spiridonov, V., Ilcheva, I., Nikolova, K., Balabanova, S., Soupilas, A., Thomas, S., Zambetoglou, K., Papatolios, K., Michailidis, S., Michalopoloy, C., Vafeiadis, M., Marcaccio, M., Errigo, D., Ferri, D., Zinoni, F., Corsini, A., Ronchetti, F., Nistor, M.M., Borgatti, L., Cervi, F., Petronici, F., Dimkić, D., Matić, B., Pejović, D., Lukić, V., Stefanović, M., Durić, D., Marjanović, M., Milovanović, M., Boreli-Zdravković, D., Mitrović, G., Milenković, N., Stevanović, Z., & Milanović, S. (2014) CC-WARE Mitigating Vulnerability of Water Resources under Climate Change. WP3 - Vulnerability of Water Resources in SEE, Report Version 5. URL: http://www.ccware.eu/output-documentation/output-wp3.html.

Cheval, S., Dumitrescu, A. & Barsan, M.V. (2017) Variability of the aridity in the South-Eastern Europe over 1961−2050. *Catena,* 151, 74−86.

Du, C., Sun, F., Yu, J., Liu, X. & Chen, Y. (2016) New interpretation of the role of water balance in an extended Budyko hypothesis in arid regions. *Hydrol. Earth Syst. Sci.,* 20, 393−409.

Fathi, M. M., Awadallah, A. G., Abdelbaki, A. M. & Haggag, M. (2019) A new Budyko framework extension using time series SARIMAX model. *Journal of Hydrology,* 570, 827−838.

Gerrits, A. M. J., Savenije, H. H. G., Veling, E. J. M. & Pfister, L. (2009) Analytical derivation of the Budyko curve based on rainfall characteristics and a simple evaporation model. *Water Resources Research,* 45(W04403): 1−15, DOI: 10.1029/2008WR007308.

Greve, P., Gudmundsson, L., Orlowsky, B. & Seneviratne, S. I. (2016) A two-parameter Budyko function to represent conditions under which evapotranspiration exceeds precipitation. *Hydrol. Earth Syst. Sci.,* 20: 2195−2205.

Haidu, I. & Nistor, M.M. 2019. Long-term effect of climate change on groundwater recharge in the Grand Est region, France. *Meteorological Applications,* doi: 10.1002/met.1796.

Mianabadi, A., Coenders−Gerrits, M., Shirazi, P., Ghahraman, B. and Alizadeh, A. (2019) A simple global Budyko model to partition evaporation into interception and transpiration. *Hydrol. Earth Syst. Sci. Discuss.*, https://doi.org/10.5194/hess-2017-306.

Nistor, M. M., Man, T. C., Benzaghta, M.A., Vaasu, N. N., Dezsi, S., Kizza, R. (2018) Land cover and temperature implications for the seasonal evapotranspiration in Europe. *Geographia Technica,* 13 (1), 85-108.

Nistor, M. M. & Mîndrescu, M. (2019) Climate change effect on groundwater resources in Emilia-Romagna region: An improved assessment through NISTOR-CEGW method. *Quaternary International*, 504, 214-228.

Pavan, V., Tomozeiu, R., Cacciamani, C. & Di Lorenzo, M. (2008) Daily precipitation observations over Emilia-Romagna: mean values and extremes. *International Journal of Climatology,* 28 (15), 2065−2079.

Pavanelli, D. & Capra, A. (2014) Climate change and human impacts on hydroclimatic variability in the Reno river catchment, Northern Italy. *CLEAN-Soil Air Water*, 42 (5), 1−11.

Thornthwaite, C.W. (1948) An approach toward a rational classification of climate. *Geographical Review,* 38, 55−94.

Tomei, F., Antolini, G., Tomozeiu, R., Pavan, V., Villani, G. & Marletto, V. (2010) Analysis of precipitation in Emilia-Romagna (Italy) and impacts of climate change scenarios, in Proceedings of Statistics in Hydrology Working Group (STAHYWG) International Workshop, pp. 23−25, Taormina, Italy, May 2010.

Tomozeiu, R., Lazzeri, M. & Cacciamani, C. (2002) Precipitation fluctuations during the winter season from 1960 to 1995 over Emilia-Romagna, Italy. *Theoretical and Applied Climatology,* 72 (3-4), 221−229.

Zhao, L., Xia, J., Xu, C., Wang, Z, Sobkowiak, L. & Long, C. (2013) Evapotranspiration estimation methods in hydrological models. *Journal of Geographical Sciences,* 23 (2), 359−369.

GEO-BASED VISUAL NETWORK ANALYSIS OF EXPORT AND IMPORT PATTERNS IN INTERNATIONAL WHEAT TRADE

Tamás T. SIKOS [1] , Aigul MEIRMANOVA[2]

ABSTRACT:
The aim of this paper is to describe worldwide export and import patterns in wheat trade and investigate their interconnections. The analysis uses Gephi techniques, including Geo layout and Fruchterman-Reingold algorithms. The research reveals the most important objectives of the wheat network by identifying and quantifying exporters and importers, subnetworks and flow pathways by calculating the centrality, network and clustering metrics. The results of the network analysis of the global wheat trade system highlight the scale-free character of the world's wheat supply system.

Key-words: *International wheat trade, GVNA, Gephi analysis, Geo layout and Fruchterman-Reingold algorithms.*

1. INTRODUCTION

What do a chapati, a matza, a bagel, an English muffin or a knäckebröd have in common? The answer is wheat, which is the main source of our staple food and it consists one-fifth of the calories and protein consumed globally. Climate change can affect agriculture in various ways. The crop yields as the wheat is susceptible to climate changes and most countries are less equipped to deal with the impact of heat stress, droughts, storms on their crops. Most exporter countries of wheat which are located in the Earth's southern hemisphere such as Australia, Argentina, India may face a reduction in wheat harvests of between 6% and 23% by 2050 (Wood, 2019). The projected deficiency of the world's wheat consume could be filled up by countries of the Earth's northern hemisphere by broadening their output and expanding crop harvests. As climate change warms the planet, unstable weather patterns and shifting seasons are disrupting the way of crops cultivation. The top wheat exporters such as Russia, the United States, Canada, France, Germany, Ukraine, Romania, Poland and other countries also may face disease, pests and weeds which may cause by frequent and rising temperatures.

The complexity of the international wheat trade necessitates the application of network analysis. The web of the international trade relations in wheat is considered as a network. The nodes of the network are the different countries, while the trade flows of wheat form the edges of the network in order to describe the presence of an import-export trade relations between geographic subnetworks or countries. This approach is widely used in studies of international trade (Chaney, 2014). There is a growing significance of network-based approaches to food system analysis and food safety-based analysis of supply systems in particular (Pinior et al., 2015; Hueston & McLeod, 2012; McDowell, 2017). Network- based approach has been recently applied in empirical studies of international trade (Li et al., 2003; Kastelle et al., 2005; Serrano et al., 2007; Bhattacharya et al., 2007). In the present paper it is important to describe the relationships and interdependence of the geographic subnetworks, also the countries included in the given subnetworks. The different dimensions of connectivity can be designated applying complex network indices that measure the number and the density of the trading relationships, the level of clustering (bilateral or multilateral trade), their dispersion or concentration, the centrality for a given node (country).

_____

[1]*University of Miskolc, Institute of Management Sciences, 3515 Miskolc, Hungary, sikos.t.tamas@uni-miskolc.hu; National University of Public Service, sikos.t.tamas@uni-nke.hu*
[2]*University of Miskolc, Institute of Management Sciences, 3515 Miskolc, Hungary, aygulmeyr@mail.ru*

The trade-network studies has been profoundly deeply manipulated by the so-called "world system" theories, i.e. the notion that one can distinguish between core and peripheral countries. Thus, the structural analysis of the network is an indispensable condition for the completeness and universality of the network approach. The structure of interactions in the network is the object of research in areas such as theory graphs, the theory of random networks, the theory of the "tight world", the theory of scale-free networks.

Climate change including warming, drought and heat stress is highly likely to impact agricultural yields and, thereby, the proliferation of wheat availability. Due to the trade plays a key role in reallocating wheat production, addressing wheat security issues requires understanding the structure of trade networks. Graph theory is a network science modelling approach that studies the graphs made by the nodes and edges identified as relevant for describing a system. It defines metrics to capture the topology of empirical networks and tackle complex patterns of change. The topology in graph theory describes the arrangement of nodes and edges in networks, and gives important information on the pattern of nodes connectivity. Here, we study the world wheat trade network based on the BACI International Trade database and use the countries as nodes and the mass of international wheat flows as edges.

In the framework of this research we intend to test the following objectives through Gephi methods:

- No. 1: The international network of wheat can be characterized by a small number of central countries and a high number of peripheral countries. No. 1_a: The central countries are linked in a densely-connected core, while the majority of participant countries are relatively atomized around the periphery of the network. No. 1_b: The peripheral countries which are unable to cultivate and provide wheat to other countries due to its unsuitable weather and climate conditions, despite of this the peripheral countries export wheat to other countries;
- No. 2: A small number of countries which are located in one geographic subnetwork sell more than a big number of countries which are located in other geographic subnetworks with suitable conditions of weather for wheat cultivation. No. 2_a: Therefore, there are countries that both do not export and do not import wheat being outliers in the network graph. No. 2_b: The top importer of wheat is located in Asian or African subnetwork with a big population.

In the introduction section, we outlined two research objectives. Next, we present an overview of methodological issues related to the analysis of inter-country trade patterns and the nature of analyzing network data. Particular attention was paid to weighted network data and the corresponding centrality measures. This is followed by an overview of key results related to three types of weighted centrality measures, results from visual inspection of the network, and the optimal solution from weighted generalized modeling. The article concludes with a discussion of results and their implications; particularly with regard to export-import patterns of geographic subnetworks.

2. DATA USED AND METHODS

The heuristic value of network visualizations was first discovered in the second period of the 20th century in the early school of social network analysis or SNA (Wasserman & Faust, 1994). Jacob Moreno, founder of such approach, accurately stated that "the expression of an individual position can be better visualized through a sociogram than through a sociometric equation" (Moreno, 1953). Moreno and his disciples set the standards for the visualization of networks (Freeman, 2009). The analysis of social networks gained significant popularity in communication research, economics, geography, computer science, organizational and developmental research. GVNA or geo-based visual network analysis is the data visualization subsystem of the SNA and it is an important component of high-quality data mining systems, especially those focused on processing large volumes of information. Three main characteristics of data visualization tools are: the nature of the data; visualization methods and samples through which data can be represented; possibilities of interaction with visual images and methods for better data analysis. The visualization data tools can work with

the following types of data: one-dimensional data such as one-dimensional arrays, time series; two-dimensional data such as points of two-dimensional graphs, geographical coordinates; algorithms and programs such as information flows, debugging operations, etc.

The data used in the present article retrieved originally from the United Nations Statistical Division, but cleaned by BACI International Trade research and expertise teams using methodology of harmonization (BACI International Trade database, 2019). The dataset represents countries that exporting and importing wheat around the world in 2018-2019. The top exporters of wheat are Russia, the United States, Canada, Australia and France, whereas the top importers are Egypt, Indonesia, Algeria, Italy and Japan.

Gephi software was used as a tool to visualize and spatialize different network graphs due to its flexibility and multi-task architecture that brings new possibilities to work with complex datasets and produce valuable visual results (Jacomy et al., 2014). Gephi can represent graphs through various layouts such as ARF layout, Circular layout, Concentric layout, DAG layout, Dual Circle layout, Force Atlas layout, Fruchterman-Reingold layout, Geo layout, Hiveplot layout, Isometric layout, Layered layout, Maps of countries layout, Multipartile layout, Network Splitter 3D layout, OpenOrd layout, Radial Axis layout, Yifan Hu layout, Yifan Hu proportional layout (Cherven, 2015). Moreover, the abovementioned layout algorithms can be classified among themselves. The Geo layout, Maps of Countries layout, Isometric layout, Network Splitter 3D layout, Fruchterman-Reingold layout and other geo-based network layouts are categorized as Geographic layouts. The network data of the present article has a geographic component, such as longitude and latitude of each country, Geo layout and Fruchterman-Reingold layout algorithms were used to display geo-based network of the worldwide wheat trade flow.

The micro-analytical level is one of key constituent elements of *Geo-based Visual Network Analysis* which is used to evaluate node centrality (degree, closeness, betweenness), network measures (eccentricity, graph density, average path length), clustering measures (modularity). In **Table 1** the graph $G = (V, L)$ represents the group of dyadic connections among the vertices (nodes). The dimension of the graph is $V = (1, ..., 94)$, where $N = 94$ is the overall amount of countries included in the analysis (De Benedictis & Tajoli, 2011). The link dimension of the graph is $L = (1,…,1041)$, where $M = 1041$ is the overall number of existing links. The links (i.e. edges) are directed, routing from the exporter country, i, to the importer country, j, and $L_{ij} \in \{0,1\}$. The binary information defines the existence, 1, and non-existence, 0, of a trade link. By adding W and P the graph will be transformed into the network: $N = (G (V, L); W; P)$, where W comprises all characteristics of the links, P comprises all characteristics of the nodes (e.g. attributes, geographical coordinates). The trade network is generally distinguished by solid heterogeneity. The 1041 existing edges in 2018-2019 conform to a density of the network of 0.119 (i.e the proportion of the number of existing connections to the total number of maximum connections possible), showing 12% of nodes are connected with one another.

Table 1.

Overview of graph statistics of the graph

No. Countries	94
No. Links	1041
Graph density	0.119
Centrality measures:	
In-degree centrality	36
Out-degree centality	58
Closeness centralization	1
Betweenness centralization	0.12679
Network measures:	
Eccentricity	6
Average path length	2.397
Clustering measures:	
Modularity	0.222

This is neither an exceptionally high number, nor could it be considered very low.

Centrality statistics provide the framework to compare the roles played by various nodes within a single network and the centrality measures help to define aggregate patterns within the graph. Centrality measures are categorized into three main groups: a) degree centrality, that measures how a node is connected to other nodes; b) closeness centrality, that measures how easily a node can be reached by other nodes; c) betweenness centrality, describing how important a node is in terms of connecting other nodes (Jackson, 2010). Centrality statistics is an appropriate tool in analyzing wheat trade data.

In a given network there are two measures of degree centrality: in-degree centrality, measuring the number of edges pointing to ego, and out-degree centrality, measuring the number of edges going from ego. The out-degree is the total number of countries toward which country *i* is exporting;

$$C_{Dout} = \frac{\sum_{j \neq i}^{N} L_{ij}}{(N-1)} \tag{1}$$

whereas in-degree is the total number of countries from which country *i* is importing:

$$C_{Din} = \frac{\sum_{j \neq i}^{N} L_{ji}}{(N-1)} \tag{2}$$

The given dataset in the present article has an *in-degree centrality* of 36% and an *out-degree centrality* of 58%. The importing countries are receiving edges 36% of the countries in the network, while is sending edges to 58% of them. One of the most commonly used global centrality measures is the closeness centrality. It is a measure of how close (in terms of topological distance) a node is with respect to all other nodes. The shortest path between country *i* and country *j* is called the geodesic distance between *i* and *j*:

$$C_C = \frac{(N-1)}{\sum_{j \neq i}^{N} D_{ij}} \tag{3}$$

The *closeness centrality* is equal to $C_c = 1$, which indicates there are no far-flung outliers lying at a great distance from the hub of the graph. All countries are on average 1 topological step away from all other countries in the network. The betweenness centralization is the variation in the betweenness centrality of vertices divided by the maximum variation in betweenness centrality scores possible in a network of the same size.

The *betweenness centrality* is equal to $C_b = 0.12679$, which indicates showing the strength of the economic links between countries in the network. The *eccentricity* is tightly related to diameter for each vertex within the network. Every vertex in the network have a value equal to 6, indicating how many nodes match the criteria. *Average path length* can provide insight into the general structure and connectedness of a network. Average path length measure is 2.397 which is below the eccentricity indicator showing that the network is efficient, and information can easily flow across the graph.

Modularity was used for graphs as one of the measures of the network. The modularity is used for network partition into clusters and for disclosure of community structure (Dedić & Stanier, 2017). The *Modularity* statistic places individual nodes into an aggregated group or cluster based on shared characteristics. Output for this function is simply an integer value starting at 0.222.

3. RESULTS AND DISCUSSIONS

Fruchterman-Reingold algorithm had been applied in order to generate a more precise map of the given dataset, pushing the most connected nodes away from each other whereas flattening the nodes that are connected to the hubs in clusters around them. The geographical coordinates of research locations with latitudinal, longitudinal and attribute values were imported into the Gephi, the overall quantity of the nodes were 94 and appropriate edges were 1041 in the network graph. The various communities in a network have distinct characteristics such as node degree, centrality, betweenness etc. A numerous real-world problem may be indicated as the structured feature by applying graphs.

Each node corresponds to a country and each edge performs an export-import relationship between countries. The colored nodes represent wheat exporters around the world (**Fig. 1**). The present geo-based network displays a clear pattern of a core of interconnected countries where shown as categorized clusters of countries which supply wheat around the world.

NODES			EDGES	
▇ very low	(63.83%)		▇ very low	(46.4%)
▇ medium	(14.89%)		▇ low	(22.38%)
▇ low	(10.64%)		▇ high	(15.56%)
▇ very high	(5.32%)		▇ medium	(14.12%)
▇ high	(5.32%)		▇ very high	(1.54%)
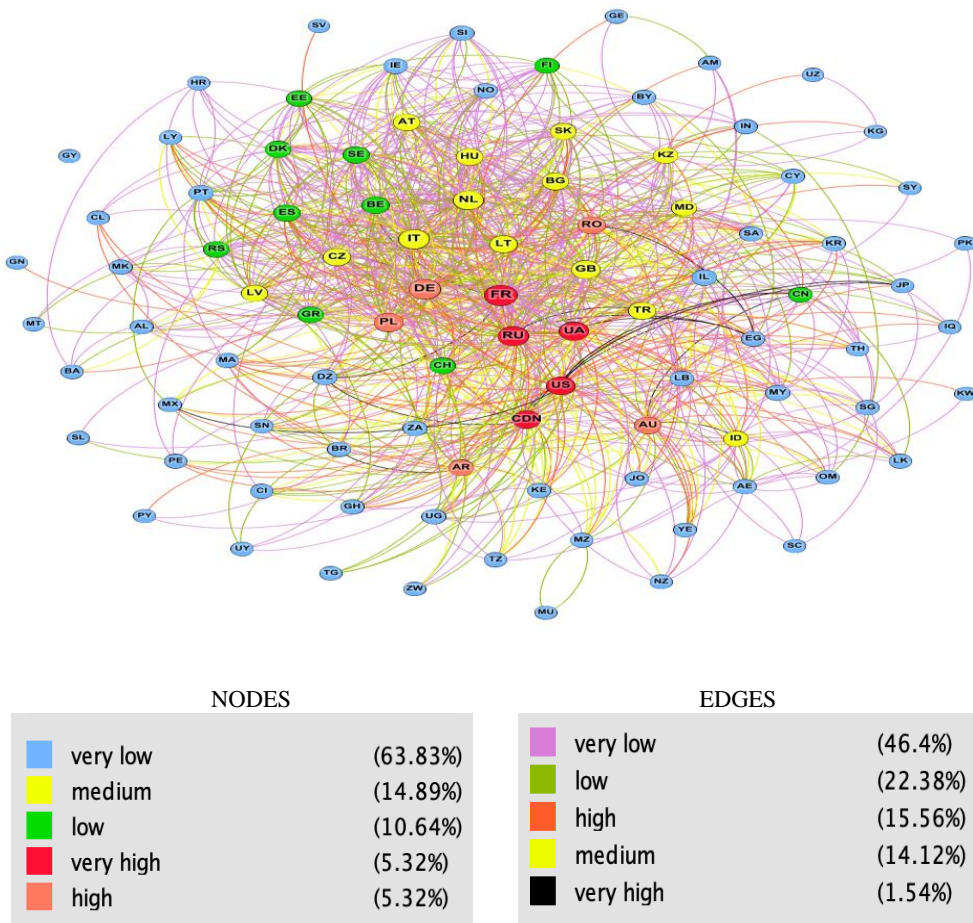
Fig. 1. The worldwide wheat exporters by Fruchterman-Reingold algorithm, 2018-2019.

The wheat exporter-countries are classified by attributes which are identified by to how many countries they export wheat to. The categorization is identified by red colored nodes – to very high amount of countries export to (5.32%), orange colored nodes – to high amount of countries export to (5.32%), yellow colored nodes – to medium amount of countries export to (14.89%), green colored

nodes – to low amount of countries export to (10.64%), blue colored nodes – to very low amount of countries export to (63.83%). Each node performs wheat exporter country which leads to identify 'hub' supplier countries and to categorize exporters in order to highlight the largest players in the market **(Fig. 1)**. The majority of countries are rather peripheral, but some countries play a central role in wheat trade flows. The identification of local centres and the most important trade flows is critical to determine the most vulnerable parts of the network (Ślusarczyk, 2017).

Clustering methods will do this through specialized algorithms that interpret network patterns into distinct groupings (clusters) of similar nodes (Cherven, 2015). Clustering of the network graph by nodes according to the sizing and coloring options, therefore beforementioned options were created according to the categories to which they belong to. The same approach can be applied using node size to scale values according to their degree level (David & Tukey, 1977). The size of vertices is proportional to the number of countries where exporters send wheat to: a large circle indicate that the corresponding country is among the main partner for a large number of importing countries. A typical approach is to have scaled coloring based on a measurable attribute, with orange and red colored nodes corresponds to a high and very high number of countries they export wheat to. The network graph represents how the wheat trade network is polarized around the United States of America, Canada, Russia, Ukraine, France, Australia, Argentina, Poland, Germany, Romania, acting as the trajectory of the wheat trade system.

A typical approach is to have scaled coloring based on a measurable attribute, with yellow and green colored nodes corresponds to a medium and low number of countries they export wheat to. The centrality of such countries as India, the United Kingdom, Latvia, Lithuania, Kazakhstan, Turkey, Moldova, Bulgaria, Italy, the Netherlands, Hungary, Czech Republic, Slovakia, Austria, China, Switzerland, Belgium, Serbia, Greece, Spain, Sweden, Estonia, Finland and Denmark are evident and these countries have a supportive position in the wheat trade system. Other countries represented in blue colored nodes are peripheral countries in the network graph, indicating that the international network of wheat can be characterized by a small number of central countries and a high number of peripheral countries. This means that the central countries are interconnected in a densely-linked core, while the majority of peripheral countries are relatively atomized around the circumference of the network. As a summary it can be stated that Fruchterman-Reingold layout algorithm determines the hubs and peripheral states of the international wheat trade network, which can be considered by a scale-free network. In Barabási's and Bonabeau's (2003) view, a scale-free network can be characterized by a relatively low number of nodes, which have a high number of connections to other nodes. The results have supported Objectives No. 1, 1_a due to the international trade in wheat can be designated by a few hubs, around which there are numerous peripheral countries.

A typical approach is to have scaled coloring based on a measurable attribute with blue colored nodes corresponds to a very low number of countries they export wheat to. Some peripheral countries as el Salvador, the Seychelles, Sri Lanka, Kuwait, Singapore, Oman, Thailand, Jordan, Yemen, Japan, Iraq, Syria, Senegal, Israel, South Korea, Cyprus, Bosnia and Herzegovina, Macedonia, Croatia, Malta, Libya, Guinea, Kyrgyzstan, Uzbekistan, Guyana, Zimbabwe, Uruguay, Sierra Leone, Mauritius, Mozambique, Tanzania, Ghana, Kenya, Togo etc. are unable to provide wheat to other countries due to its weather and climate conditions that is unsuitable for cultivation wheat. Despite of this the abovementioned countries export wheat to other countries, supporting Objective No. 1_b.

Geo layout algorithm was applied in order to spatialize a full geo-based network of wheat trade flow. Nodes repulse each other like charged particles, while edges attract their nodes, such as springs. These forces create a movement that converges to a balanced state (Jacomy et al., 2014). The network represented the separate countries as the nodes in a directed spatial network, based on the geographic coordinates (latitude/longitude) for each country. Edges between node pairs were weighted by the value of wheat exports (US$) transferred between each origin and destination country in 2018-2019 (**Fig.2**). The categorization is identified by black colored edges – exporter send wheat to importer in very high value between $330M - $3B (consists of 1.54%), orange colored edges – exporter send wheat to importer in high value between $30M - $330M (consists of 15.56%), yellow colored edges – exporter send wheat to importer in medium value between $9M - $30M (consists of 14.12%), green

colored edges – exporter send wheat to importer in low value between \$1M - \$9M (consists of 22.38%), purple colored edges – exporter send wheat to importer in very low value between \$1K - \$1M (consists of 46.4%).

NODES			EDGES		
	very low	(63.83%)		very low	(46.4%)
	medium	(14.89%)		low	(22.38%)
	low	(10.64%)		high	(15.56%)
	very high	(5.32%)		medium	(14.12%)
	high	(5.32%)		very high	(1.54%)
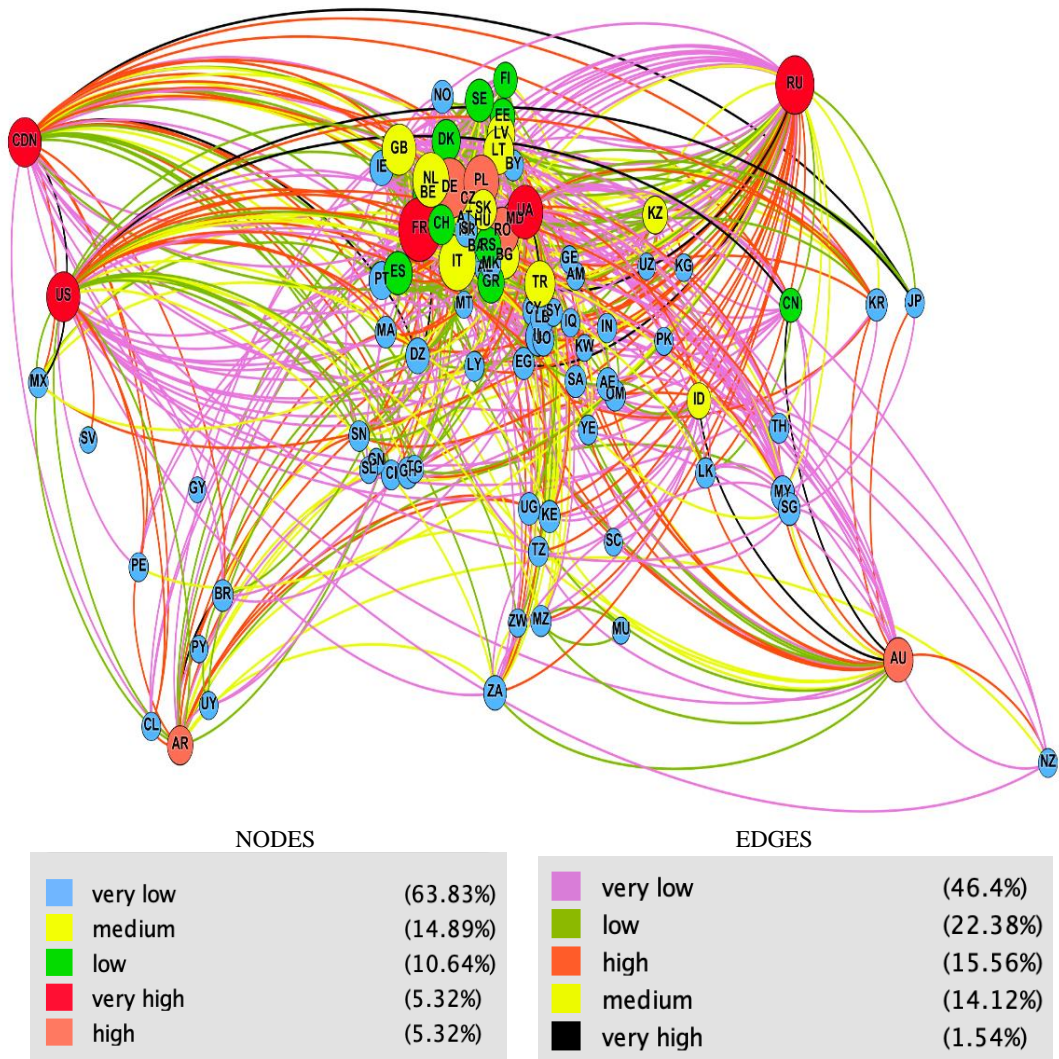
Fig. 2. Graphical representation of the world trade flow of wheat ((1) the number of nodes is proportional to the number of outflows, (2) the number of edges is proportional to the amount of the export value).

Classifications by geographical sub-networks is not only identify the main trends of the worldwide trade flow, but also analyze, compare continents with each other. But any classification is useful only when it is possible to identify clear criteria, classification features that enable us unambiguously evaluate certain phenomena. International trade export in wheat considered as geographically segmented, with the major role played by European sub-network (export value is \$22.7B), while the North American sub-network with its main players such as Canada, the United States are located in a decentralized position (export value is \$11.4B) (**Fig.2**). The third hub is Oceanic sub-network (export value is \$4.88B) supporting Objective No. 2 which claims that one geographic sub-network export more than other sub-network with more countries with suitable conditions of weather for cultivating wheat in comparison with the South American sub-network (export value is

$2.71B), the Asian sub-network (export value is $900M), the African sub-network (export value is $33.2M) from **Fig.2**.

There are inward and outward flows between countries, based on the network shown in **Fig.2** we notice that:

• Some edges between countries do not exist, due to some countries such as Mongolia, Afghanistan, Colombia, Venezuela, Ecuador, Mauritania, Mali, Chad, Sudan, Angola, Mozambique etc. do not export wheat to other countries and Turkmenistan, Chad, Namibia, Botswana, Laos do not import wheat. Therefore, there are countries Turkmenistan, Chad, Namibia, Botswana, Laos both do not export and do not import wheat being outliers in the network graph supporting Objective No. 2_a which claims that there are number of countries do not export and do not import;

• The top importers of wheat around the world in the African sub-network are Egypt (import share 9.8%) and Algeria (import share 4%), in the Asian sub-network are Indonesia (import share 6.1%) and Japan (import share 3.3%), in the South American sub-network is Brazil (import share 2.5%), in the North American sub-network is Mexico (import share 2.5%); in the European sub-network is Italy (import share 3.6%), supporting Objective No. 2_b which claims that the top importer located in Africa or in Asia with big population.

4.   CONCLUSION

We examined a number of issues related to the international wheat trade system applying the tools of Network Analysis. The world wheat trade network is represented graphically and analytically through the indices describing the network's properties, such as in-degree centrality, out-degree centrality, closeness centralization, betweenness centralization, eccentricity, average path length and modularity. The analysis shows a role of countries in shaping the wheat trade network. This approach has relevant implications in demonstrating some valuable insights about the group of wheat exporters and importers around the world: what are the subgroups it consists of, who are the most influential players, what are the peripheral players and outliers, etc. The results of a network analysis of the global wheat trade system highlight the scale-free character of the world's wheat supply system. This information is important for the organizations of international trade control systems during temperature changes and when some countries are less equipped to deal with the impact of heat stress on their crops.

R E F E R E N C E S

Baci International Trade Database (2019). – Available from https://oec.world/en/profile/hs92/1001/. [Accessed December 2019].

Barabási, A. & Bonabeau, E. (2003) Scale-free networks. *Scientific American,* 288 (5), 50-59.

Bhattacharya, K., Mukherjee, G., Saramaki, J., Kaski, K. & Manna, S. (2007) The International Trade Network: Weighted Network Analsys and Modeling. *Journal of Statistical Mechanics: Theory and Experiment*, 2008 (02), 2002.

Chaney, T. (2014) The network structure of international trade. American Economic Review, 104 (11), 3600-3634.

Cherven, K. (2015) *Mastering Gephi Network Visualization*, Packt Publishing Ltd., Birmingham.

David, F.N & Tukey, J. W. (1977) Exploratory Data Analysis. *Biometrics*, 33 (4), 768.

Dedić, N. & Stanier, C. (2017) Towards Differentiating Business Intelligence, Big Data, Data Analytics and Knowledge Discovery. *Lecture Notes in Business Information Processing*, 114–122.

De Benedictis L. & Tajoli L. (2011) The World Trade Network. *The World Economy*, 34 (8), 1417-1454.

Freeman, Linton C. (2009) Methods of Social Network Visualization. *Encyclopedia of Complexity and Systems Science*, 1-17.

Hueston, W. & McLeod, A. (2012) *Overview of the global food system: Changes over time/space and lessons for future food safety. Improving Food Safety through a One Health Approach,* National Academies Press, Washington.

Jacomy, M., Venturini, T., Heymann, S. & Bastian, M. (2014) Continuous Graph Layout Algorithm for Handy Network Visualization Designed for the Gephi Software. *PLoS ONE*, 9 (6), e98679.

Jackson, M. (2010) *Social and Economic Networks*, Princeton University Press, New Jersey.

Kastelle, T., Steen, J. & Liesch, P. (2005) Measurig globalisation: an evolutionary economic approach to tracking the evolution of international trade. Paper presented at *the DRUID Summer Conference on Knowledge, Innovation and Competitiveness: Dynamycs of Firms, Networks, Regions and Institutions*.

Li, X., Jin, Y. Y., & Chen, G. (2003) Complexity and synchronization of the World trade Web. *Physica A: Statistical Mechanics and its Applications*, 328, 287-296.

Moreno, J. (1953) *Who Shall Survive? Foundations of sociometry, group psychotherapy and psychodrama*, Beacon House Inc., New York.

McDowell, T. C. (2017) The complexity of the international food industry. *International Journal of Society Systems Science,* 9 (1), 1-28.

Pinior, B., Conraths, F.J., Petersen, B. & Selhorst, T. (2015) Decision support for risks managers in the case of deliberate food contamination: the dairy industry as an example. *Omega,* 53(1), 41-48.

Serrano, A., Boguna, M., & Vespignani, A. (2007) Patterns of dominant flows in the world trade web. *Journal of Economic Interaction and Coordination*, 2, 111-124.

Ślusarczyk, B. (2017) Prospects for the shared services centers development in Poland in the context of human resources availability. *Polish Journal of Management Studies*, 15(1), 218-231.

Wasserman, S. & Faust, K. (1994) *Social Network Analysis: Methods and Applications: Methods and Applications*, University Press, Cambridge.

Wood, J. (2019) *These 5 foods are under threat from climate change.* [Online] Available from https://www.weforum.org/agenda/2019/08/these-5-foods-are-under-threat-from-climate-change/. [Accessed January 2020].

LAND USE/COVER CHANGE IN DINEVAR RURAL AREA OF WEST IRAN DURING 2000-2018 AND ITS PREDICTION FOR 2024 AND 2030

Mohammad MALEKI[1] 🆔 *, John Lodewijk VAN GENDEREN[2]* 🆔 *,*
Seyed Mohammad TAVAKKOLI-SABOUR[1], Samira Sadat SALEH[1], Ehsan BABAEE[1]

ABSTRACT:
Land use change, monitoring and predicting the future land use is often demanded by decision makers. Many land use change models have been developed aiming at the accurate prediction of land use changes. This study is aimed at mapping land use changes during past years and predicting the future trends in the rural environment of the Dinevar region to support local decision makers. For this research, we used the archive of Landsat satellite images of 2000, 2006, 2012 and 2018 to investigate the land-use changes in and initial pre-processes such as geometrical correction, radiometric correction. PCA was utilised to reduce the bands and multi-spectral images were fused with panchromatic band using Gram-Schmidt method to increase spatial separation. Four land uses of agriculture, rocky lands, pasture and bare soil were extracted through maximum likelihood method and predictions are made using CA-Markov chain. Land use for 2018 was predicted and the results were compared with the field observations, to evaluate the validity of the prediction method. Finally, the prediction was conducted for 2024 and 2030 land use. The highest extent of changes in the study period (2000-2030) was related to the change from pasture to bare soil with 1689 hectares. Based on the results, 0.7499% of changes were occurred between 2000 and 2006, 0.8562% between 2000 and 2012, and remaining 15% from 2012 to 2018. It indicates that the highest rate of changes in the area occurred within 2000-2006, while stagnation occurred in the period of 2006 to 2012. These changes increased during the last 5-years due to the promotion of rural life. The results show that human activity and lifestyle changes have caused many changes in LULC in the area. Based on the results of this paper, many aspects of rural, agricultural, natural hazard, natural resources and even social studies can be understood in the study Reasons of land use changes are discussed at the end.

Key-words: *Lands use, predicting the changes, Ca-Markov, Dinevar Rural area.*

1. INTRODUCTION

Land use/cover (LULC) and its environmental effects have become the most debatable subject since 1990s and is considered as one of the major subjects of studying the global changes (Anderson et al.2017; Feddema et al., 2005; Luo et al, 2003; Liu, 1992; Wang et al, 2006). It has been figured out that the factors such as changing the land use and cutting the trees are very complicated (Golnow & Lakes, 2014). "Land use/cover change detection can identify potential environmental events associated with rapid urbanisation, forest conversion, and agricultural expansion" (Zurqani et al., 2018; Drummond and Loveland, 2010; Agaton et al., 2016). The life in arid rural areas and limited natural resources cause poverty and may impact the overall living system of the people. The techniques of discovering changes using multi-temporal satellite imaging data helps to understand the dynamics of landscape such as desertification and land degradation which are considered as worldwide problems affecting soils, vegetation and the livelihoods of rural populations (Padonou et al., 2017; D'Odorico et al., 2013; Gao and Liu, 2010, Zhang et al.,2012). LULC are two different terms where, LC represents the physical characters of land surface such as spatial distribution of vegetation, water and other spatial features which are created merely by human residences (Dimyati et al, 1996). On the other hand, LU argues how the land is being exploited for human use and residence, e.g. the role of land for economic uses (Rawat & Kumar, 2015). The changes of LU/LC

---

[1] *Kharazmi University, Department of Remote Sensing & GIS, Tehran-Iran, malekimohamad14@gmail.com,*
tavakkoli.khu.ac@yahoo.com, samiras.salehi1989@gmail.com, ehsanb86@gmail.com
[2] *University of Twente, Department of Remote Sensing & GIS, Netherlands, genderen@alumni.itc.nl*

are rapid and comprehensive procedures. Human activities in changing the land is absolutely significant through changing LULC (Liu et al, 2005; Tian et al, 2014; Liu and Tian, 2010; Hurtt et al, 2006; 2005b). Land cover data documents how much of a region is covered by forests, wetlands, impervious surfaces, agriculture, and other land and water types. Water types include wetlands or open water. Land use shows how people use the landscape – whether for development, conservation, or mixed uses. The different types of land cover can be managed or used quite differently (NOAA, 2019). Research studies aimed at integrating socio-economic and geo-bio-physical factors are increasingly being used in order to improve ourunderstanding of the causes and effects of land-use change and to support sustainable landscape development (Mottet et al, 2006). Identifying changes in land surface objects can provide valuable information for specialists in geometrics, crisis management, urban management, agriculture and forestry (Janalipour and Taleai, 2017).

Studies have shown that converting pastures to agricultural fields leads to the change in microbiological and biochemical properties of soil such as soil degradation etc. (Hajiabbasi et al, 2007; Aleagha et al, 2011). However, excessive exploitation of renewable natural resources (pastures) and the habitat supplying the needs of human population have had degrading effects on these important environmental resources. Such trend reduces the efficiency of these resources and threatens the human's life (Karimi and Karami Dehkordi, 2015; Hadeel, 2009). GIS provides a flexible environment for collecting, storing, displaying and analysing digital data necessary for change detection which has been used successfully in many developed and developing countries (Amade et al., 2018; Liping et al., 2018; Reis, 2008; Khan et al., 2016; Zeleke & Hurni, 2001). Some studies have been conducted about seizing the land, changing the land use as well as converting the pastures to agriculture lands. (Wetzel, 2012; Wetzel, 2012; Hove & Gwiza, 2015; Van der Sluis et al, 2017; You et al, 2015, Butt et al, 2009; Hajiabbasi et al, 2007; Aleagha et al, 2011 and Karimi and Karami Dehkordi, 2015). Keeping in mind the importance of land use and changes, the aim of this study is to investigate the extent of rural land use manipulation over the years 2000-2015430 using Remote Sensing Data and Geographic Information Systems (GIS) as well as its prediction for 2020 and 2025 years for Dinevar rural area in western Iran.

1.1. Study Area

Dinevar rural area is located in the central part of Dinevar section located in Kermanshah Province in the West of Iran. Dinevar Rural Area is located within geographical longitude of E47˚21' to E47˚36' and latitude of N34˚31' to N34˚41' (**Fig. 1**).
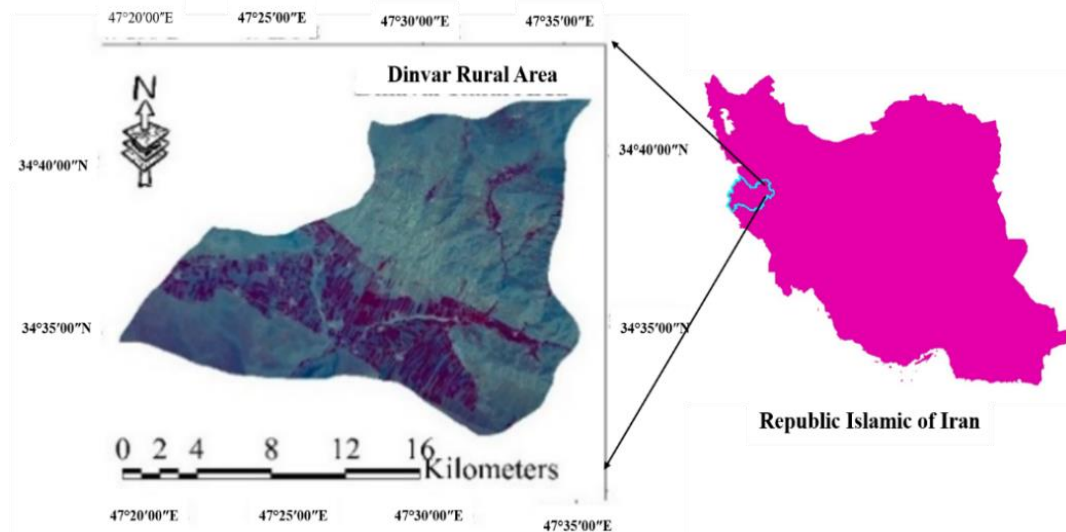
Fig. 1. The Location of Study Area in Iran.

The extent of study area is 34,313 hectares. According to the statistics of 2013, this area contains 44 inhabited villages and 9201 residential population while major activities of the residents in this area include cultivation and pastoralism. Most of lands are cultivated as dry farming. The oldest settlement in the region dates back to 9800 BC and is formed on a hill known as Sheikhi Abad near an adjacent river (Sadidi et al., 2016).

2. METHODOLOGY

2.1. Data

Landsat images of four time-points: 2000, 2006, 2012 and 2018 were used in this study. The goal is to detect the changes between four classes of land such as Agriculture, Pasture, bare Soil and Rocky Land. Considering the circumstances in the study area, the best time for imaging is late May to early June, since agricultural fields are still vegetated and not harvested at this period whereas pastures are almost dried out. Therefore, agricultural fields can be best separated from pastures and rocky lands during this time. **Table 1** shows images used in this study. The images downloaded from archive of Earth-explorer site.

Table 1.

Images used.

Resolution	the exact date	the path/row	scene per year
30 M	05-JUN-00	Path: 167 / Row: 36	1
30 M	06-JUN-600	Path: 167 / Row: 36	1
30 M	06-JUN-002	Path: 167 / Row: 36	1
30 M	15-JUN-008	Path: 167 / Row: 36	1

2.2. Pre-processing and processing

After providing the raw images, the primary pre-processing such as geometric and radiometric corrections were applied to prepare the images. Using Dark Object Subtraction, the atmospheric changes were applied on TM, ETM+ and OLI images. Principle Component Analysis (PCA) is one of the techniques that reduces the correlation on the cost of number of bands (Amini, 2009 and Rasouli, 2008). Therefore, PCA was used in this study to reduce the number of bands and to decorrelate the data. Multi-spectral images were fused to the single panchromatic band, in order to enhance spatial resolution using Gram-Schmidt technique (Jawak and Luis, 2013). The first components of a PCA contain the most information of the initial data. **Fig. 2** shows an example of scree plot of eigenvalues vs. component number. The expected information is reduced with the component number which indicates an inverse correlation between component number and information content. The steep trend of the eigenvalues indicates the fast reduction of information with increasing component number. A threshold should be set in order to select the components containing the most information.
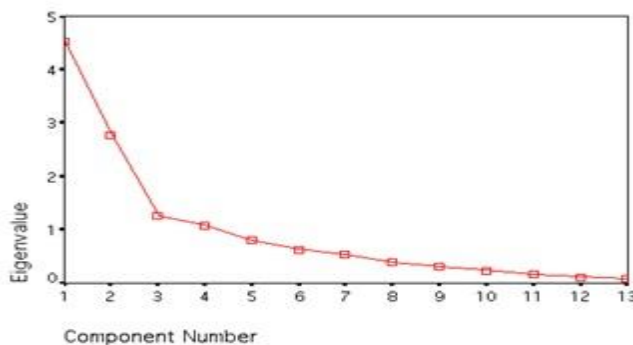
Fig. 2. Scree Plot. Eigenvalue vs. component number (janda.org, 2018).

2.3. Classification and predict changes

Additional data sources like topography maps, field surveys, and google earth data were also used in this study. Strategy sampling using this classification, additional old data and images visual interpretation. The satellite images were classified by nearest neighbour classifier (Because usually a land use / cover is more than the area of a Landsat pixel method of sample collection was stratified random. Accuracy of results were evaluated based on error matrices and Kappa statistics. Finally, a map of LULC changes during 2000-2018 was provided. In order to predict the changes, CA-Markov technique was used. The changes were first predicted for 20188 in order to examine the reliability of techniques using available ground truth of 2015. The LULC predictions were made for years 2024 and 2030, then the user changes compared to year 2000 were identified. Markov models can be integrated with cellular automata models (a.k.a. Markov-CA models), and such models have been used to model and predict land use change at different scales (Guan et al., 2011; Weng, 2002; Ye & Bai, 2008). The Markov-CA approach used in the current study is considered a spatial transition model as it combines the stochastic spatial Markov techniques with the stochastic spatial cellular automata method (Eastman, 2009). It has the advantage of predicting two-way transitions among the available LULC classes, in contrast to the Geomood technique that only predicts one-way loss/gain from one class to another (Pontius & Malanson, 2005; Halmy et al, 2015). For the preparation of LULC maps used of ENVI software and for predict map use of Idrisi software. **Table 2** shows size of reference samples for classification. **Fig. 3** shows the flowchart of the methodology.

Table 2.

Size of reference samples.

		Year			
		2000	**2006**	**2012**	**2018**
LULC	**Agriculture**	1846	1546	2037	2565
	Pasture	569	723	719	547
	bare Soil	632	654	665	421
	Rocky lands	419	614	514	373
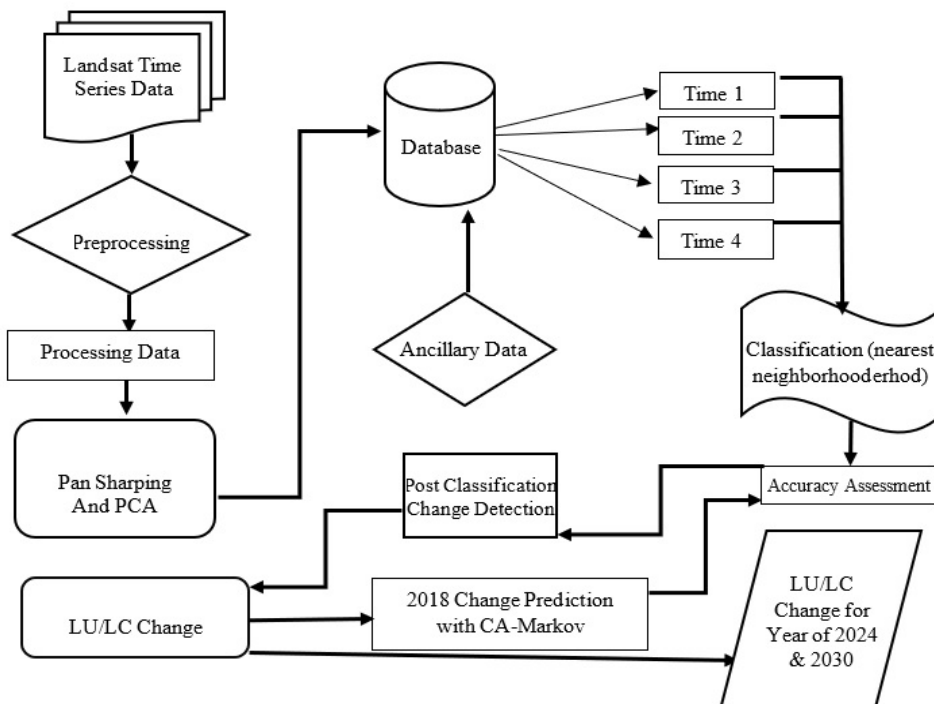
Fig. 3. The flowchart of methodology.

Fig. 4 shows the PCA of TM and ETM+ data (right) and OLI (left). On the basis of the figure, it is clear that the longer we depart from the original component, give the less useful new information. This helps us to identify the principal components and extract the most information from the fewer number of image analysis. While **Fig. 5** represents Scatter Plot of the images that facilitates the selection of features. **Fig. 5** shows the correlation of image bands.
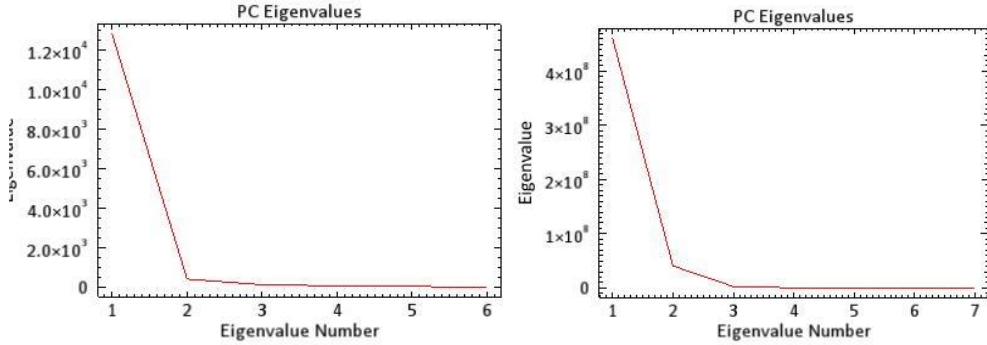
Fig. 4. Samples of Applying PCA on TM and ETM+ Data (left side) and OLI (right Side).
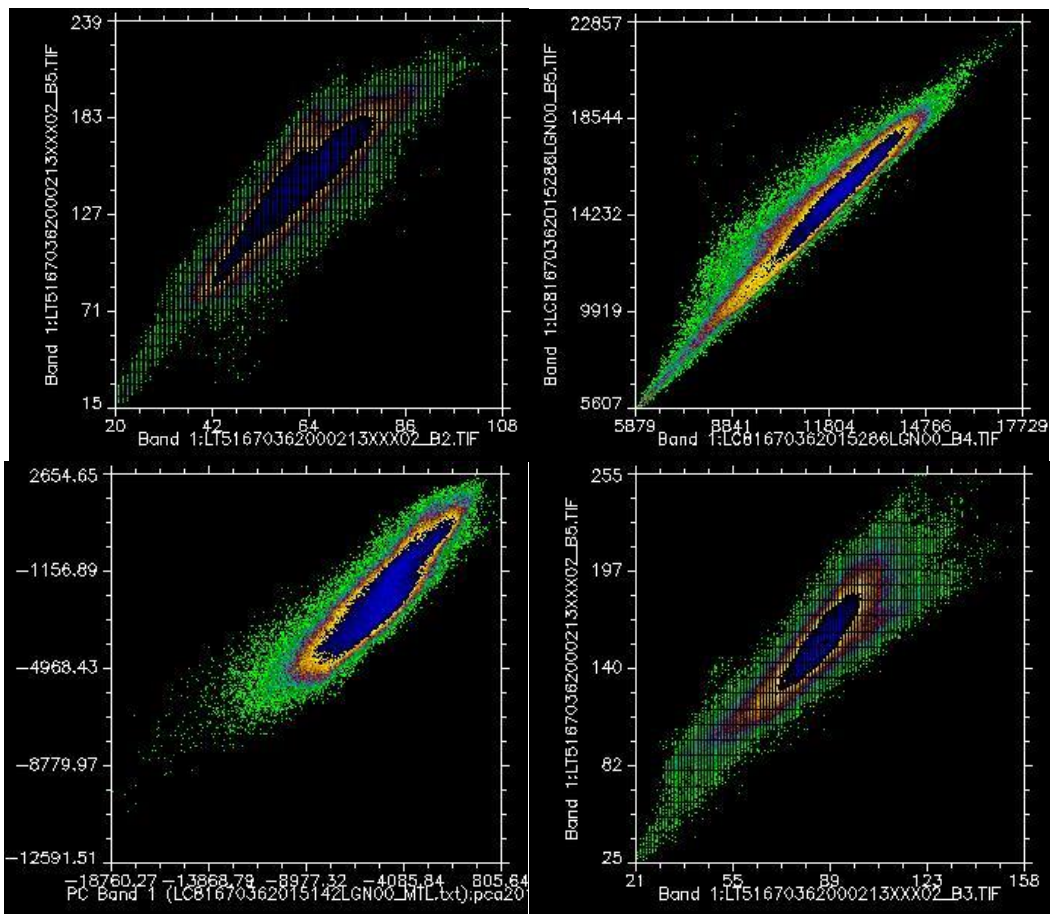
Fig. 5. Scatter Plot of Used Images in this Study.

3. RESULTS

The statistical accuracy assessments of the classifications of produced maps are provided in **Table 3**. Based on the table, it is clear that a proper classification of LULC has been made in different periods.

Table 3.

The accuracy assessment of the produced maps.

Years	Class	Completeness (%)	Overall Accuracy	Kappa Coefficient
2000	Agriculture	94.37		
	Pasture	84.31	89.55	81.31
	bare Soil	85.26		
	Rocky lands	94.26		
2006	Agriculture	93.73		
	Pasture	89.92	89.50	81.30
	bare Soil	88.64		
	Rocky lands	85.69		
2012	Agriculture	90.33		
	Pasture	92.43	90.15	86.07
	bare Soil	90.38		
	Rocky lands	87.47		
2018	Agriculture	91.61		
	Pasture	91.45	87.7	81.09
	bare Soil	79.63		
	Rocky lands	88.12		

The resulted land use maps of 2000 and 2018 are respectively shown in **Fig. 6** and **Fig. 7**. Using these maps, the changes in land use have been obtained for an 18 years period (The beginning and end of the course are the images in the study).
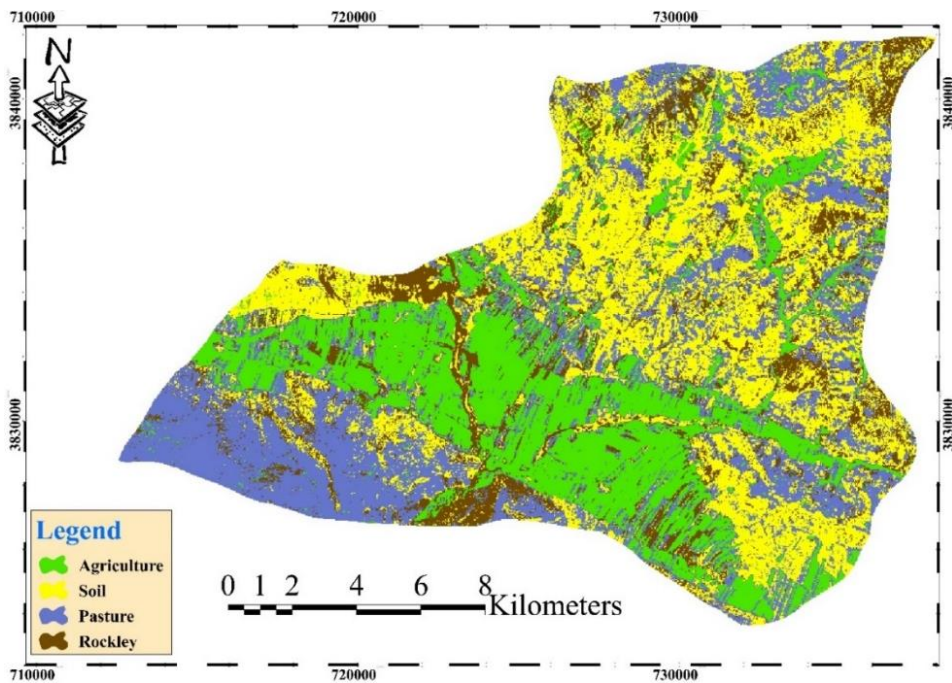
Fig. 6. Dinevar Land Use 2000.
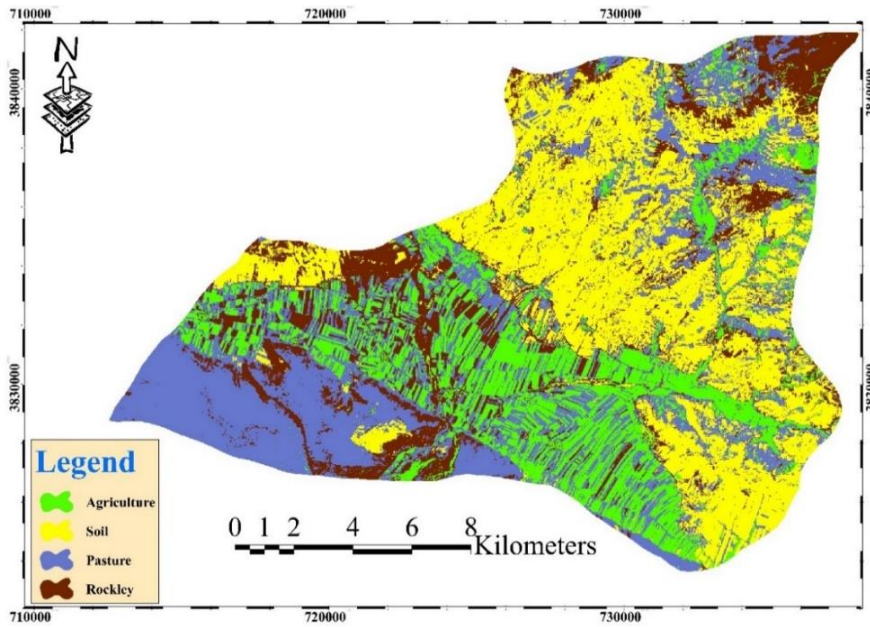
Fig. 7. Dinevar Land Use 2018.

The map of changes for 2018 compared to 2000 is represented in **Fig. 8**. 13 classes including no change and the changes of agriculture to the pasture, agriculture to bare soil, agriculture to rocky, pasture to agriculture, pasture to bare soil, pasture to rocky lands, bare soil to agriculture, bare soil to rocky lands, bare soil to pasture, rocky lands to agriculture, rocky lands to pasture and rocky lands to bare soil are shown in this map.
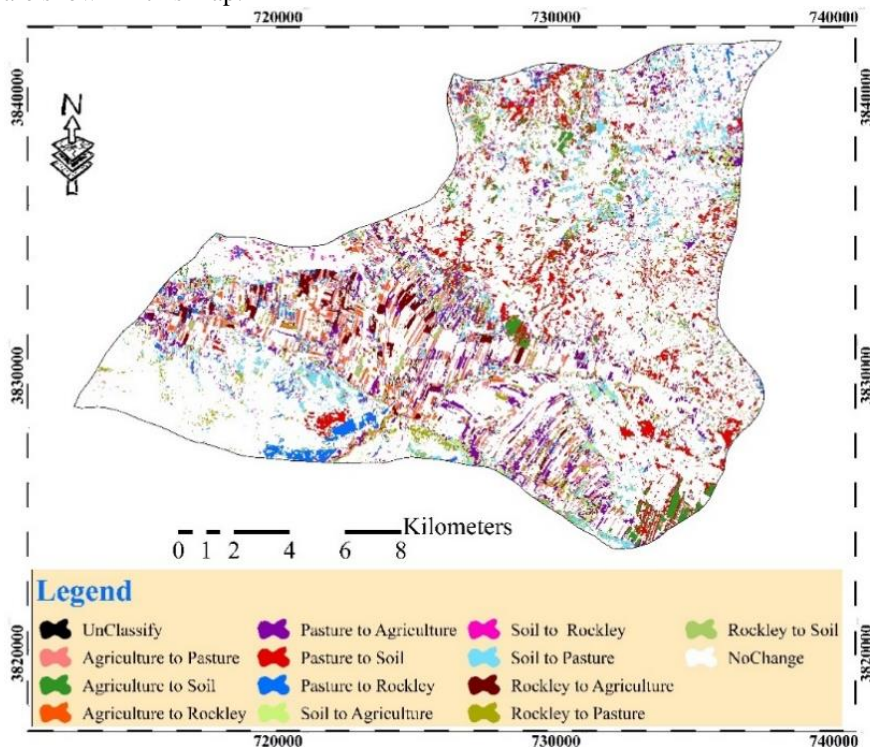
Fig. 8. Land Use Changes During 2000-2018.

The predicted land use changes for 2018 using CA-Markov is provided as **Fig. 9**. **Fig. 10** shows the prediction for 2024 based on the former trends. Also **Fig. 11** shows LULC Changes for Year 2030, based on Year 2000 LULC Map.
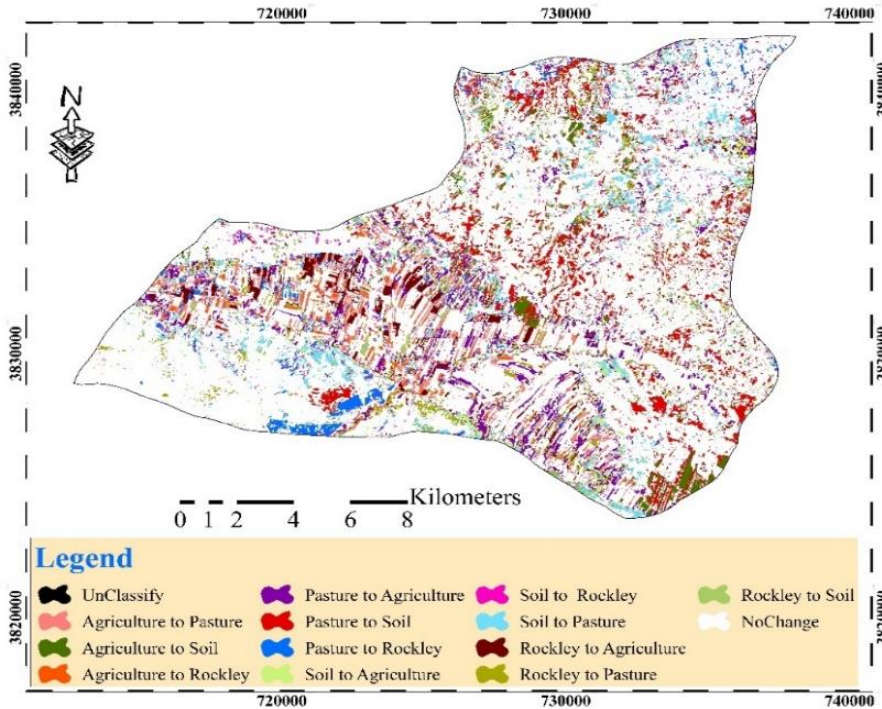
Fig. 9. Predicted Changes and Land Use Conversions During 2000-2018.
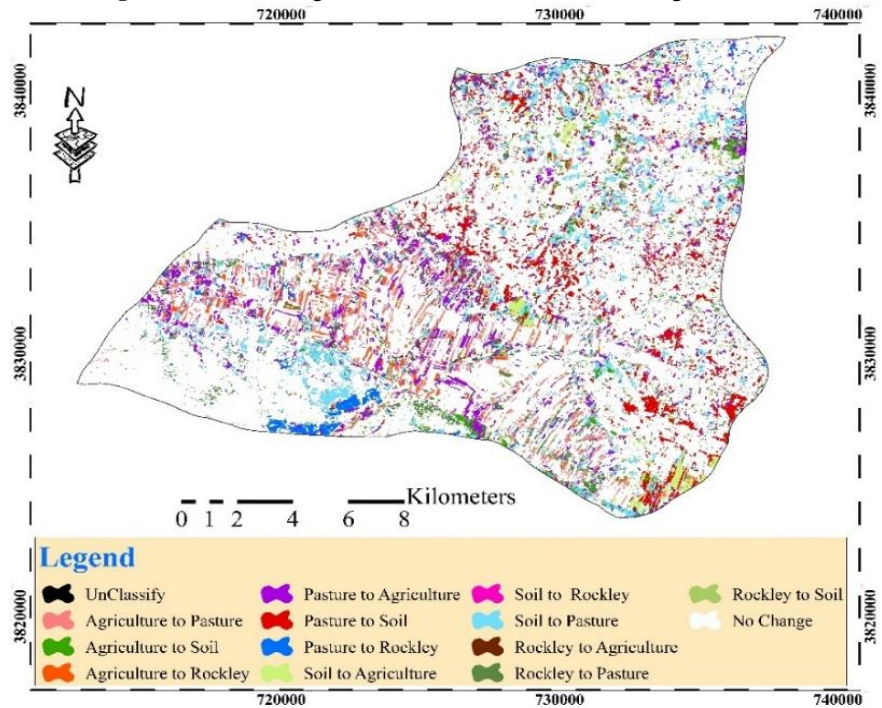
Fig. 10. Predicted Map of Land Use Changes During 2000-2024.
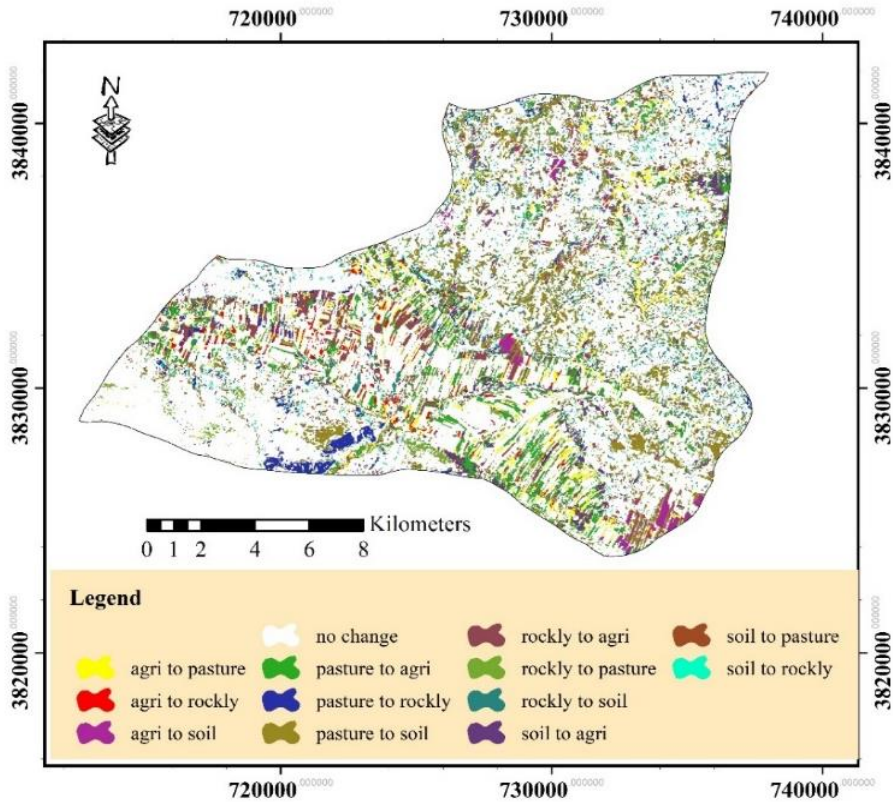
Fig. 11. Predicted Map of Land Use Changes During 2000-2030.

Fig. 12 shows the rate of land use changes during four periods; 2000-2006, 2000-2012, 2000-2018 and predicted 2000-2024 and 2000-2030. The rate of converting agriculture to bare soil, pasture to rocky and rocky to pasture during 2000-2024 will be less in comparison with 2000-2018.
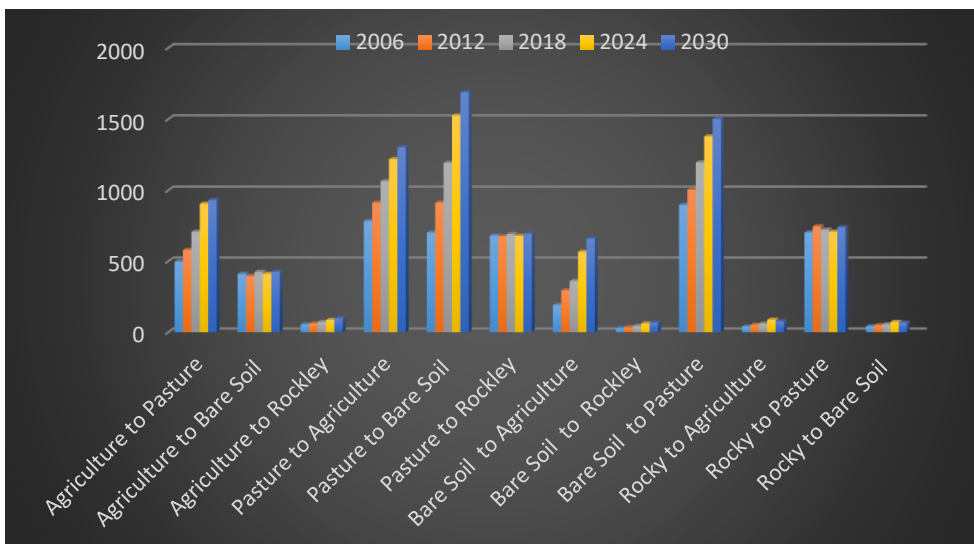
Fig. 12. Extent of land use changes in different periods (hectares).

4. DISCUSSION

It should be considered that it is impossible to achieve 100% accuracy in the results and the results might include an error rate. One of the main sources of error is the annual period of selection. In addition, it is not always possible to provide satellite data at the same date in all selected years. Hamed et. al investigated land use change predictions under two different conditions (sanctioned or not sanctioned) in the Iraq's Kurdistan and concluded that the environment will be led to stability and homogeneity, if the region is not sanctioned during the next 6 years. Halmy et. al (2015) showed that land use changes and urbanization will extend mainly towards the west and north.

Results showed that a high classification accuracy could be achieved via CA-Markov which can predict changes in 2018. Moreover, the evaluation of land use in 2024 was not possible which might also create a minimal error in maps. Most obvious trend of the changes is the conversion of pasture to farmlands and degradation to bare land. Land use change has become a fundamental factor in environmental change and has become a global threat. Reviewing these changes through satellite imagery and predicting these changes can help planners. According to the results of this paper, the trend of degradation and change in environment and LULC between years 2000 to 2006 is greater than any other period. The highest gradient of change was for changing pasture land cover to soil bare, indicating the destruction of rangelands. On the other hand, the second gradient of change was related to the conversion of bare soil to grassland, which indicates the restoration of rangelands in some places.

5. CONCLUSION

According to Alimohammadi et al (2010), Markov chain has great capability to predict land use changes. They found that the change from agriculture to settlement has been the most observed changes and this trend is going to continue in the future. Prediction of changes is often conducted aiming at evaluation of land use change consequences (Alimohammadi et. al 2010), whereas the most studies have been unconcerned about the cause of changes. This study is concerned not only about the usual issues of other studies, but also about the causes of land use changes, which may help the decision makers to prevent the disadvantages of changes.

Following change reasons have been identified in this research with respect to each type of land use change:

- Pasture to agriculture: it happens due to the demand of profit and food production. Some fallow fields may be classified as pasture and are considered as a change from pasture to agriculture or vice versa (for example in the image of 2000, it has been shown as pasture and in other periods they were turned to agricultural land)
- Pasture to bare Soil: due to high density of livestock and excessive exploitation of pasture, especially near water sources and around villages.
- Pasture to Rockley land: excessive exploitation of rocky pastures and shortage in water supply.
- Agriculture to pasture: stopping the cultivation and leaving fields unused due to infertility, water shortage or immigration of the owners (sometimes evacuating the residences) or fallowing the fields allowing pasture plants to grow.
- Agriculture to bare Soil: fallowing the land through cultivation of some products like peas. In this case, more than a half of land is exposed as bare soil and the product grows sparsely which may cause a misclassification as bare soil.
- Agriculture to Rocky land: soil degradation and erosion may force farmers to leave rocky fields and stop the cultivation.
- Bare Soil to agriculture: planting the lands which were fallow previously or planting very weak or those pastures which were not cultivated previously.
- bare Soil to pasture: growing pasture plants in the lands with bare soil cover where less amount of livestock is present

- Bare Soil to Rocky land: this might be because of erosion or exploitation and brick factories in the region which have reached to the beneath layers by soil extraction.
- Rocky land to agriculture: cultivating rocky lands which is common in mountainous and poor villages
- Rocky land to pasture: low exploitation of mountain lands, due to the reduction in number of people working as traditional animal farmers which bare lead mountains to recover the vegetation and regenerate the pastures.
- Rocky land to bare Soil: there is some sand factories in the selected region, in which rocky lands can be converted to bare soil as a result of covering rocks with deposited bare soil.

R E F E R E N C E S

Agaton, M., Setiawan, Y. and Effendi, H., 2016. Land use/land cover change detection in an urban watershed: a case study of upper Citarum Watershed, West Java Province, Indonesia. *Procedia Environmental Sciences*, *33*, pp.654-660.

Alimohammadi, Abbas, Mousivand, Alijafar and Shayegan, siavash., 2010. Predicting the LU/LC changes of land surface using satellite images and Markov chain, planning and space alignment, period 14, number 3, pp. 117-130. (In Farsi).

Amade, N., Painho, M. and Oliveira, T., 2018. Geographic information technology usage in developing countries–A case study in Mozambique. *Geo-spatial Information Science*, *21*(4), pp.331-345.

Amini, Jalal (2009). Computer processing of remote assessment images (translated by: M. Mizer), Tehran University publication, Tehran, Iran, P650. (In Farsi).

Anderson, K., Ryan, B., Sonntag, W., Kavvada, A. and Friedl, L., 2017. Earth observation in service of the 2030 Agenda for Sustainable Development. *Geo-spatial Information Science*, *20*(2), pp.77-96.

Beheshti-aleagha, Ali; Raeisi, Faez; and Golchin, Ahmad., 2011. The effect of land use changes from pasture to farm on the microbiological and biochemical indicators of soil, the journal of water and soil, vol. 25, number 3, pp 548-562. In Farsi.

Butt, A., Shabbir, R., Ahmad, S.S. and Aziz, N., 2015. Land use change mapping and analysis using Remote Sensing and GIS: A case study of Simly watershed, Islamabad, Pakistan. *The Egyptian Journal of Remote Sensing and Space Science*, *18*(2), pp.251-259.

D'Odorico, P., Bhattachan, A., Davis, K.F., Ravi, S. and Runyan, C.W., 2013. Global desertification: drivers and feedbacks. *Advances in water resources*, *51*, pp.326-344.

Dimyati, M.U.H., Mizuno, K., Kobayashi, S. and Kitamura, T., 1996. An analysis of land use/cover change in Indonesia. *International Journal of Remote Sensing*, *17*(5), pp.931-944.

Drummond, M.A. and Loveland, T.R., 2010. Land-use pressure and a transition to forest-cover loss in the eastern United States. *BioScience*, *60*(4), pp.286-298.

Eastman, J.R., 2009. IDRISI guide to GIS and image processing Accessed in IDRISI Selva 17 (pp. 182e185). *Worcester, MA: Clark University*.

Falcucci, A., Maiorano, L. and Boitani, L., 2007. Changes in land-use/land-cover patterns in Italy and their implications for biodiversity conservation. *Landscape ecology*, *22*(4), pp.617-631.

Fang, S., Yan, J., Che, M., Zhu, Y., Liu, Z., Pei, H., Zhang, H., Xu, G. and Lin, X., 2013. Climate change and the ecological responses in Xinjiang, China: Model simulations and data analyses. *Quaternary International*, *311*, pp.108-116.

Fatemi, Sayyed-Bagher., Rezaei, Yosef., 2012. Principles of Remote Sensing. Azadeh Publishing. Pp 296. (In Farsi).

Feddema, J.J., Oleson, K.W., Bonan, G.B., Mearns, L.O., Buja, L.E., Meehl, G.A. and Washington, W.M., 2005. The importance of land-cover change in simulating future climates. *Science*, *310*(5754), pp.1674-1678.

Gao, J. and Liu, Y., 2010. Determination of land degradation causes in Tongyu County, Northeast China via land cover change detection. *International Journal of Applied Earth Observation and Geoinformation*, *12*(1), pp.9-16.

Gollnow, F. and Lakes, T., 2014. Policy change, land use, and agriculture: The case of soy production and cattle ranching in Brazil, 2001–2012. Applied Geography, 55, pp.203-211.

Guan, D., Li, H., Inohae, T., Su, W., Nagaie, T. and Hokao, K., 2011. Modeling urban land use change by the integration of cellular automaton and Markov model. *Ecological Modelling*, *222*(20-22), pp.3761-3772.

Hadeel, A., Jabbar, M. and Chen, X., 2009. Application of remote sensing and GIS to the study of land use/cover change and urbanization expansion in Basrah province, southern Iraq. *Geo-spatial Information Science*, *12*(2), pp.135-141.

Hajiabbasi, Mohammadali, Besharatpour, Asghar and Melali, Ahmadreza., 2007. The effect of converting the pastures to agriculture lands on physical and chemical characteristics of soils of south and southwest of Isfahan, agricultural sciences and techniques, number 42, pp 525-534 (In Farsi).

Halmy, M.W.A., Gessler, P.E., Hicke, J.A. and Salem, B.B., 2015. Land use/land cover change detection and prediction in the north-western coastal desert of Egypt using Markov-CA. *Applied Geography*, *63*, pp.101-112.

Hamad, R., Balzter, H. and Kolo, K., 2018. Predicting land use/land cover changes using a CA-Markov model under two different scenarios. *Sustainability*, *10*(10), p.3421.

Hove, M. and Gwiza, A., 2012. The fast track land reform programme and food insecurity: A case of Zimbabwe from 1992 to the present. *American International Journal of Contemporary Research*, *2*(8), pp.282-293.

Hurtt, G.C., Frolking, S., Fearon, M.G., Moore, B., Shevliakova, E., Malyshev, S., Pacala, S.W. and Houghton, R.A., 2006. The underpinnings of land-use history: Three centuries of global gridded land-use transitions, wood-harvest activity, and resulting secondary lands. *Global Change Biology*, *12*(7), pp.1208-1229.

Janalipour, M. and Taleai, M., 2017. Building change detection after earthquake using multi-criteria decision analysis based on extracted information from high spatial resolution satellite images. *International journal of remote sensing*, *38*(1), pp.82-99.

Jawak, S.D. and Luis, A.J., 2013. A comprehensive evaluation of PAN-sharpening algorithms coupled with resampling methods for image synthesis of very high resolution remotely sensed satellite data. *Advances in Remote Sensing*, *2*, pp.332-344

Karimi, Kobra; Karami Dehkordi, Esmaeil., 2015. Exploiting the pastures and the necessity of diversifying the livelihood of rural families, case study: MAhanshan Town, rural research, period 6, number 2. PP 342-368 (In Farsi).

Kaveh, Neda; Ebrahimi Atalloh., 2013. Predicting the LU/LC changes through CA-Markov model (case study: Aghbolagh river). Remote assessment and the system of geographical information in natural resources, period 2, number 4: pp 41-51(In Farsi).

Khan, S., Qasim, S. and Ambreen, R., 2016. Spatio-temporal analysis of landuse/landcover change of district pishin using satellite imagery and GIS. *Journal of Geographic Information System*, *8*(3), pp.361-368.

Liping, C., Yujun, S. and Saeed, S., 2018. Monitoring and predicting land use and land cover changes using remote sensing and GIS techniques—A case study of a hilly area, Jiangle, China. *PloS one*, *13*(7).

Liu, J., Liu, M., Tian, H., Zhuang, D., Zhang, Z., Zhang, W., Tang, X. and Deng, X., 2005a. Spatial and temporal patterns of China's cropland during 1990–2000: an analysis based on Landsat TM data. *Remote sensing of Environment*, *98*(4), pp.442-456.

Liu, J., Tian, H., Liu, M., Zhuang, D., Melillo, J.M. and Zhang, Z., 2005b. China's changing landscape during the 1990s: Large-scale land transformations estimated with satellite data. *Geophysical Research Letters*, *32*(2).

Liu, M. and Tian, H., 2010. China's land cover and land use change from 1700 to 2005: Estimations from high-resolution satellite data and historical archives. *Global Biogeochemical Cycles*, *24*(3).

Luo, G., Zhou, C. and Chen, X., 2003. Process of land use/land cover change in the oasis of arid region. *ACTA GEOGRAPHICA SINICA-CHINESE EDITION-*, *58*(1), pp.63-72.

Mottet, Anne, Sylvie Ladet, Nathalie Coqué, and Annick Gibon. "Agricultural land-use change and its drivers in mountain landscapes: A case study in the Pyrenees." *Agriculture, ecosystems & environment* 114, no. 2-4 (2006): 296-310.

Padonou, E.A., Lykke, A.M., Bachmann, Y., Idohou, R. and Sinsin, B., 2017. Mapping changes in land use/land cover and prediction of future extension of bowé in Benin, West Africa. *Land Use Policy*, *69*, pp.85-92.

Pontius, G.R. and Malanson, J., 2005. Comparison of the structure and accuracy of two land change models. *International Journal of Geographical Information Science*, *19*(2), pp.243-265.

Rasouli, Aliakbar., 2008. The principles of applied remote assessment emphasizing on the process of satellite images, Tabriz University Publication, Tabriz, Iran, p806. (In Farsi).

Rawat, J.S. and Kumar, M., 2015. Monitoring land use/cover change using remote sensing and GIS techniques: a case study of Hawalbagh block, district Almora, Uttarakhand, India. Egypt J Remote Sens Space Sci 18 (1): 77–84.

Reis, S., 2008. Analyzing land use/land cover changes using remote sensing and GIS in Rize, North-East Turkey. *Sensors*, *8*(10), pp.6188-6202.

Sadidi, J., Maleki, M., Rahmati, M. and TAVAKKOLI, S.M., 2016. Investigating the Role of Faults in the Establishment and Survival of Settlements using Remote Sensing and Geographic Information System (GIS). The Case of Sahneh County in Iran. *Journal of Settlements and Spatial Planning*, *7*(2), pp.201-206.

Song, X.P., Huang, C. and Townshend, J.R., 2017. Improving global land cover characterization through data fusion. *Geo-spatial information science*, *20*(2), pp.141-150.

Tian, H., Banger, K., Bo, T. and Dadhwal, V.K., 2014. History of land use in India during 1880–2010: Large-scale land transformations reconstructed from satellite data and historical archives. *Global and Planetary Change*, *121*, pp.78-88.

Tracewski, L., Bastin, L. and Fonte, C.C., 2017. Repurposing a deep learning network to filter and classify volunteered photographs for land cover and land use characterization. *Geo-spatial information science*, *20*(3), pp.252-268.

van der Sluis, T., Pedroli, B., Kristensen, S.B., Cosor, G.L. and Pavlis, E., 2016. Changing land use intensity in Europe–Recent processes in selected case studies. *Land Use Policy*, *57*, pp.777-785.

Wang, X.Z., Zheng, Y.H. and Li, S., 2006. Analysis of land use and landscape pattern change in west of Hainan Island. *Journal of Desert Research*, *26*(3), pp.409-414.

Wang, Y., Chen, Y., Ding, J. and Fang, G., 2015. Land-use conversion and its attribution in the Kaidu–Kongqi River Basin, China. *Quaternary international*, *380*, pp.216-223.

Weng, Q., 2002. Land use change analysis in the Zhujiang Delta of China using satellite remote sensing, GIS and stochastic modelling. *Journal of environmental management*, *64*(3), pp.273-284.

Wetzel, C., 2009. Theorizing Native American land seizure: An analysis of tactical changes in the late twentieth century. *Social Movement Studies*, *8*(1), pp.17-34.

Wetzel, C., 2012. Envisioning land seizure: Diachronic representations of the occupation of Alcatraz Island. *American Behavioral Scientist*, *56*(2), pp.151-171.

Ye, B., & Bai, Z., 2008. Simulating land use/cover changes of Nenjiang County based on CA-Markov model. International Federation for Information Processing PublicationsIFIP, 258, 321e330.

You, W., Ji, Z., Wu, L., Deng, X., Huang, D., Chen, B. and He, D., 2017. Modeling changes in land use patterns and ecosystem services to explore a potential solution for meeting the management needs of a heritage site at the landscape level. *Ecological Indicators*, *73*, pp.68-78.

Zeleke, G. and Hurni, H., 2001. Implications of land use and land cover dynamics for mountain resource degradation in the Northwestern Ethiopian highlands. *Mountain research and development*, *21*(2), pp.184-191.

Zhang, F., Tashpolat, T., Kung, H.T. and Ding, J., 2010. The change of land use/cover and characteristics of landscape pattern in arid areas oasis: an application in Jinghe, Xinjiang. *Geo-spatial Information Science*, *13*(3), pp.174-185.

Zhao, W., Yan, L. and Zhang, Y., 2018. Geometric-constrained multi-view image matching method based on semi-global optimization. *Geo-spatial information science*, *21*(2), pp.115-126.

Zurqani, H.A., Post, C.J., Mikhailova, E.A., Schlautman, M.A. and Sharp, J.L., 2018. Geospatial analysis of land use change in the Savannah River Basin using Google Earth Engine. *International journal of applied earth observation and geoinformation*, *69*, pp.175-185.

http://www.janda.org/workshop/factor%20analysis/SPSS%20run/SPSS08.htm accessed on 23.12.2018

https://oceanservice.noaa.gov/facts/lclu.html acsses on 13.10.2019.

DIVE RESORT MAPPING AND NETWORK ANALYSIS: WATER RESOURCES MANAGEMENT IN PEMUTERAN COASTAL AREA, BALI - INDONESIA

Muh Aris MARFAI[1,] , Benarifo AHMADA[1], Bachtiar MUTAQIN[1,2] , Rainey WINDAYATI[1]*

ABSTRACT:
As the world's best tourist destination in 2017 according to the world's largest travel site, Trip Advisor, Bali offers several tourism activities, including scuba diving. One of the famous dive sites is in the north of Bali, specifically Pemuteran Village. As a result, tourism activities contributed to water shortages in 2009 and 2013, partly because they used up to 65% of the available water supply. This study sought to determine water use and management by the dive resorts in Pemuteran Village and analyze their work connections in supporting tourism business activities, particularly those related to scuba diving. The technical approach used in this research, namely the integration of the mapping and network analysis to measure the water management in the local context, is considered as the appropriate method where the human geographical interview and survey meets with the technical geography of network analysis and mapping. Interviews with dive resort owners and managers in July 2019 produced information on 1) annual water use, 2) efforts and policies related to water use management, and 3) cooperation between dive resorts in Pemuteran Village as an attempt to create sustainable tourism. The results showed that all dive resorts in the village used 30,202,375 liters of water per year and that each of them had internally implemented several strategies to conserve more water. However, based on the technical approach of the Gephi program, the sociogram of the network is currently shown the weak collaboration or agreement between dive resorts on this front, which potentially threatens the sustainability of tourism in Pemuteran Village and affects the income of the local people.

Key-words: Tourism, Water use, Social network, Scarcity, Bali, Indonesia.

1. INTRODUCTION

Indonesia is one of the largest archipelagic countries in the world, with a water area of 6,315,222 km^2 and coasts stretching along 99,093 km (Mutaqin, 2017). This condition makes Indonesia had numerous tourist destinations as well as attract numerous tourists, including more than 16 million foreigners, to explore those places (Indonesian Ministry of Tourism and Creative Economy, 2020). Tourism activities in Indonesia began in the New Order era (1966-1998), and it is among the highest growing sectors in Indonesia (Agustan and Kausar, 2019). Since 2017, Bali, an island in Indonesia, has become the world's best tourist destination according to TripAdvisor, the world's largest travel site (Lewis & Lewis, 2009; TripAdvisor, 2018; Mutaqin et al., 2020). According to Statistics Indonesia, in 2018, I Gusti Ngurah Rai International Airport in Denpasar, Bali, is the most visited gateway by international tourists arriving in Indonesia.

One of the favorite dive sites in Bali is Menjangan Island, part of the West Bali National Park (TNBB) (Ernawati, 2011). In the national park area, lodging activities or hotel constructions are prohibited. As a result, Pemuteran Village, situated 18 km or 1 hour by speedboat from the national park (**Fig. 1**), has been developed into a lodging center or resorts for tourists planning to visit Menjangan Island. Pemuteran Village is geographically located at the coordinates 8°13'00" - 8°07'30"S and 114°40'30" - 114°37'00" E and has an area of 32.86 km^2 (**see Fig. 1**).

[1]*Universitas Gadjah Mada, Faculty of Geography, Coastal and Watershed Research Group, 55281 Yogyakarta, Indonesia, arismarfai@ugm.ac.id , benarifo.ahmada@mail.ugm.ac.id, mutaqin@ugm.ac.id , rainey.windayati@mail.ugm.ac.id*

[2]*Université Paris 1 Panthéon Sorbonne, Laboratoire de Géographie Physique UMR 8591, 92190 Paris, France, mutaqin@ugm.ac.id*
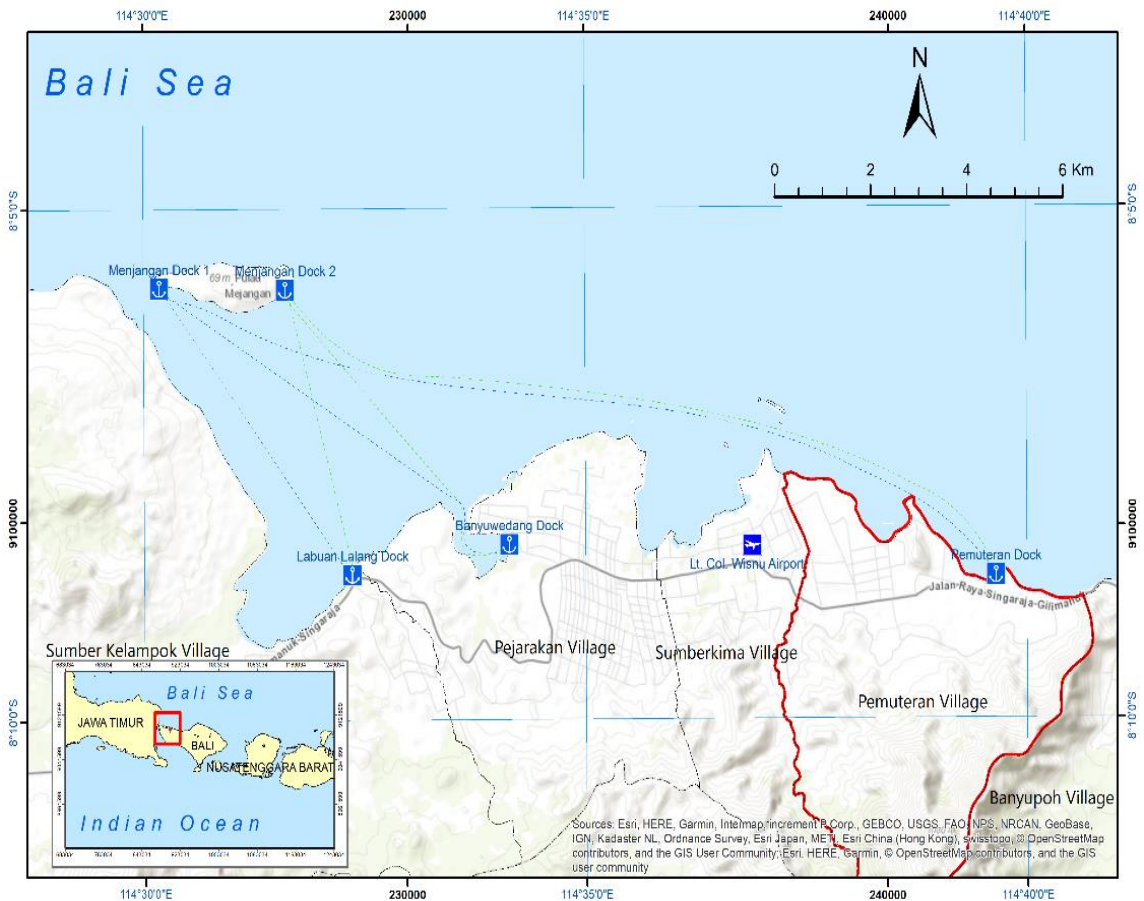
Fig. 1. Map of the locations of Pemuteran Village and Menjangan Island.

In 2017, there were 44 hotels in this village, with 1,158 people engaging in tourism to accommodate 27,018 tourists (Statistics Indonesia, 2018). Aside from Pemuteran Beach, tourists can cross Labuhan Lalang in Sumber Klampok Village to reach Menjangan Island in 25-45 minutes.

Water resources are a vital asset in the tourism industry and tourism activities that have long been part of the culture of Bali abstract nearly 65% of groundwater supplies (Gössling et al., 2012; Picard, 1996; Cole, 2012). Consequently, the industry can be less environmentally friendly as it potentially leads to water shortages (Dwianika et al., 2020), as occurred in Pemuteran Village in 2009 and 2013. In Bali, the philosophy of Tri Hita Karana perceives water as a symbol of harmony between humans and nature (Sunarta & As-syakur, 2015; Windia & Dewi, 2011). This study explores the water use and management strategies adopted by every dive resort in Pemuteran Village and compares this information with the strategic directives issued by the Agency for the Assessment and Application of Technology (BPPT).

In order to understand the water use and management strategy, every dive resort is mapped and exploited in the network analysis. This approach is considered as technical geography, by mapping and analyzing of the geographical object to support the current and future spatial decision-making processes aimed at preserving the sustainable development of earth (Ormeling 2009). This technical approach by the integration of the conventional mapping of the social/human geographical object and network analysis (a technical geographic method) represents a significant advance in knowledge. Dive resorts are hotels or places of lodging that provide marine tourism services, including scuba

diving. Due to their ubiquity in the village, understanding their role in local water resource conservation is imperative.

This study also reveals how dive resorts collaborate to organize marine tourism in the village. To measure the intensiveness of the collaboration of dive resorts, the sociogram from the Gephi program has been utilized in this research. It offers information on whether the collaboration is limited to business matters such as cooperation under the pretext of sharing costs, news, knowledge, and skills, or it extends to collective water resource management (Jesus & Franco, 2016; Krželj-Čolović et al., 2016).

2. METHODS

This study collected four types of data: (1) the amount of water used by dive resorts in Pemuteran annually, (2) the strategies adopted by each dive resort in Pemuteran to manage its water resources, (3) networks between dive resorts to maintain their activities, and (4) the respondent's view of the water crisis in Bali, especially in Pemuteran. Also, it used two criteria for dive resorts. First, the dive resorts are defined as lodging businesses that provide scuba diving experiences for their guests who have or have not been certified by diving affiliates such as PADI, SSI, and SDI. Second, if a resort or homestay has permanent cooperation with a dive center, then it is excluded from this research. By combining these criteria with a snowball sampling technique, this study obtained ten (10) dive resorts for the object of analysis.

The required data were collected by structured interviews using a questionnaire and began with an observation phase to find suitable dive resorts. After two days of observation at the end of June, the next step was an interview for the next ten days and a census of the dive resorts in Pemuteran Village according to the predefined criteria. Structured interviews with key informants, owners, managers, or front desk employees aimed to acquire information on the identity of the dive resort and its total water consumption per year. Identity and water needs were approached using several factors, namely: 1) monthly water bills, 2) the number of guests per year, 3) the number of employees working at the dive resort, and 4) facilities and services (i.e., swimming pools, fish ponds, laundry services, spa, and swimming pools to clean diving equipment like masks, snorkels, fins, wetsuits, and scuba sets). If the dive resort did not keep any groundwater bills, then total water consumption was estimated from the number of guests and employees and through questions on the frequency of lawn watering and room cleaning.

Based on the assumption of water consumption per capita, the number of guests was multiplied by 250 L/day (SNI, 2005), while the number of employees was multiplied by 30 L for the entire working hours (Gössling et al., 2015). The interviews also identified the strategies that the dive resorts adopted to manage water resources and the type of networks and connections they established with each other. These data included the current and future models of cooperation to sustain the business circumstances in Pemuteran and, at the same time, preserve the environment.

Afterward, data on water usage of each dive resort were summed. Meanwhile, details on strategies to reduce water consumption were analyzed descriptively and compared with water-saving efforts that had been established in other regions (literature reviews). Finally, information on dive resort cooperation was transformed into visual illustrations. Adequate and appropriate visual presentation of the geographical object is crucial to give an understanding of the entire spatial analysis and connectivity of the object studied (Haidu, 2016; Ruda, 2016; Bobková and Holešinská, 2017). Visual illustration has been done by utilizing a technical approach using the Gephi program. Gephi is an open-source computer program that helps researchers to uncover designs and patterns, highlight exceptions instinctively, and tells stories with their data. Gephi combines built-in functionalities and adaptable engineering to visualize, analyze, and manipulate all sorts of networks and their data properties (Bastian et al., 2009; Jacomy et al., 2014).

Gephi program, in combination with the spatial analysis, is beneficial and considered as an innovative way to do the analysis of the geographical phenomenon and to measure the intensiveness of the collaboration among actors in the study area. This presentation was integrated with spatial data,

i.e., coordinate points, to produce a comprehensive map containing water consumption and dive resort networks in Pemuteran Village.

The technical character is reflected on the point coordinate mapping through survey and interview as well as on the appropriate and adequate presentation of network analysis by sociogram and Gephi program.

3. RESULTS AND DISCUSSIONS

In the illustration on water usage and dive resort's collaborative networks, the ten dive resorts were represented by numbers, from 1 to 10, to preserve anonymity.

3.1. Total water usage

The overall water usage by the dive resorts in Pemuteran Village was 30,202,375 L/year. This figure was obtained through interviews with dive resort managers and owners. Only three of the ten dive resorts kept proof of paid monthly well water bills. As for the other seven dive resorts, the water consumption rate was approached from water use per capita (guests and employees), facilities and maintenance, cleanliness, and irrigation. The amount of water consumption is presented in **Table 1.**

Table 1.
Total groundwater use by the dive resorts in Pemuteran, Bali.

Dive Resorts	Groundwater consumption (L/year)
1	159,000
2	511,345
3	567,357
4	573,237
5	1.149,524
6	1,438,000
7	2,068,000
8	2,349,494
9	10,494,418
10	10,892,000
Total	**30,202,375**

Compared with other dive resorts, the ones in Pemuteran Village used a smaller amount of water in 2019 (30,202,375 L/year). For instance, Resort A in Langkawi and Resort B in Miri withdraw up to 63,875,000 L and 118,625,000 L of water per year (Tang, 2012). These resorts have 117 and 220 rooms, respectively, which are more than the dive resorts in Pemuteran. The number of rooms is directly proportional to the number of potential guests and the amount of water these guests need. In Pemuteran Village, Dive Resort 9 had the highest number of rooms, namely 80, and the annual water consumption was 10,494,418 L. The total water usage of all dive resorts in the study area is still lower than hotels or resorts that do not offer diving services, such as in Malaysia (182,500,000 L/year), Makassar (259,875,072 L/year), and Zanzibar (316,765,250 L/year) (Gössling, 2001; Tang, 2012; Ridwan, 2012). Other than the number of rooms and visitors, differences in water requirements depend on the resort or hotel facilities, e.g., swimming pools, laundry services, cleaning and floor maintenance (i.e., mopping), fish ponds, plant maintenance, place of worship, and food preparation activities in the restaurant (i.e., dishwashing and cooking). Furthermore, seasons and the size and type of resort also determine the water demand (Chan et al., 2009).

3.2. Water-saving strategy in the dive resorts

Dive resorts are a form of business that combines diving tourism with a place of lodging. Despite the high precipitation rate in Indonesia, it is only natural for each lodging business entity to implement

a water-saving strategy to sustain water availability for domestic use and, consequently, preserve the supply and demand flow of the guests visiting Pemuteran Village (Becken, 2014).

Besides, water conservation is covered in the Sustainable Development Goals, Goal 6: Clean water and sanitation, issued by the United Nations (UN) in early 2016 (https://www.un.org/sustainabledevelopment/). The results showed that seven out of the ten dive resorts had implemented efforts to conserve groundwater use, while the other three did not have clear water-saving strategies.

For the respondents, be it employees, managers, or hotel owners, water-saving means reducing not only groundwater bills but also electricity expenses. The water pipelines managed by the regional government-owned water company, PDAM, does not reach Pemuteran Village; therefore, the dive resorts, as well as other homestays, have to use electric pumps to extract water from bore wells. The withdrawal of a higher amount of water requires a higher voltage for the pump to work. Dive Resorts 5 and 9 have official licenses from PADI, an international diving affiliate, as PADI five-star dive resorts. Also, Dive Resort 5 has been named as one of the 16 best eco-resorts in the Asia Pacific by Scuba Diver magazine because it has a recycling system for wastewater from baths.

Based on the interview with a respondent from Dive Resort 5, the wastewater from bathing flows from each room in this resort to the recycling system and is reused to water the plants. With this design, the wastewater recycling system is similar to that of Frangipani Langkawi Resort and Spa in Malaysia (Kasim et al., 2014). Frangipani recycles by discharging treated wastewater to the wetland, and this process is assisted by planting aquatic plants in this ecosystem. Dive Resort 5 does not use aquatic plants to recycle wastewater, but it relies on a liquid waste-treating machine used by the Agency for the Assessment and Application of Technology (BPPT) (Yudo, 2018). It also sorts towels, linens, and pillowcases for the guests by choosing only ones with thin material that requires less time and water for washing and drying. This strategy has not been exposed in previous studies and is thereby a new and simple innovation.

Only five dive resorts provide a swimming pool for their guests, namely Dive Resorts 1, 2, 4, 8, and 9. The first four claimed to have never changed the water in the swimming pool since it was first operated. However, instead, they added chemicals such as Poly Aluminum Chloride (PAC), Soda Ash, and Copper Sulphate to maintain the quality of the swimming pool water. The five dive resorts have also installed water recycling equipment for the swimming pools. This water-saving method for the swimming pool is also found in the resorts in Thessaloniki, Greece, that use chemicals (Cl) as a disinfectant and water re-installation equipment to keep the pool water clean (Marinopoulos and Katsifarakis, 2017). Furthermore, Dive Resorts 2, 3, 4, and 9 have built fish ponds on their properties to improve their decoration, and three of them have installed water purification equipment to drain water from the fish ponds every 1-2 months. At the same time, Dive Resort 6 has constructed some infiltration wells around the property to conserve water. This application follows the water-saving strategy adopted by the BPPT building (Yudo, 2018), which aims to accommodate overland flow or surface runoff in case of heavy rain and, therefore, decrease groundwater exploitation.

Most dive resorts have a technical water-saving strategy. Some have different ways of conserving drinking water, but this is not necessarily followed by an increase in groundwater use by the dive resorts. For instance, instead of providing water in disposable bottles, these resorts serve drinking water in a gallon. According to the respondent, bottled water is a waste of water because, habitually, many people do not drink the entire content. When no longer needed, the bottle is thrown away with the remaining water in it. If calculated cumulatively, there will be much water wasted from this type of package. Meanwhile, water gallons will not be replaced until they are empty, and the used ones can be refilled. Aside from adding up the volume of plastic waste, bottled water is believed to increase the company's operating budget. For these reasons, the dive resorts choose to provide water gallons as part of their amenities. A key informant from Dive Resort 8 admitted that the resort was committed to the plastic reduction movement. **Table 2** summarizes the identified strategies and efforts of each dive resort to reduce groundwater exploitation.

Interviews with 14 respondents found out their opinion on water scarcity in Bali, including water deficit in 2009 and 2013 (Sunarta and As-Syakur, 2015) (**Fig. 2**). Respondents who were residents of

the Buleleng Regency were mostly unaware that the regency and the entire Bali were experiencing water crises.

In contrast, respondents who were foreign nationals claimed that they knew about these adverse events because their curiosity about the local condition before arriving in Bali to work at the dive resorts had led them to this information and the fact that the tourism industry used up to 65% of the available water in Bali.

Table 2.

The water-saving strategies adopted by the dive resorts in Pemuteran, Bali.

No	Strategies	Number of Users	Dive Resorts
1	Applying recycling technology for toilet wastewater and reusing the treated water for the plants	1	5
2	Adding chemical ingredients and equipment to clear the swimming pool water	4	1, 2, 4, 8
3	Installing a water purifier for the fish ponds	1	2
4	Constructing infiltration wells	1	6
5	Providing water in gallons instead of plastic bottles	1	8
6	Using sprinklers to water the plants	4	5, 7, 8, 9
7	Reusing the wastewater from dive-gear washing to water the plants	2	4, 3
8	Using household appliances made of thin materials	1	5

About 69% of the respondents reported no difficulty in accessing water, while the other 31% claimed that access to clean and fresh water had been challenging. For Dive Resort 7, clean water was difficult to access, and the deep wells often completely dried despite their 15m depth. This situation is potential because the dive resort is not located in a shallow groundwater zone. Besides, Dive Resort 7 is located on the west and adjacent to Sumberkima Village. Based on the interview results, this location suffered water shortages even though the local government, through the water company PDAM, had facilitated the residents of Sumberkima Village with access to clean water.

In general, the respondents showed awareness and positive attitude toward the water problem in Pemuteran and, under this circumstance, had applied various attempts to save water. The government can use this finding as a reference to promote water conservation programs. Most importantly, all respondents expressed their willingness to support these plans should the government decide to actualize them. Public opinion of the criticality of water in Pemuteran Village is presented in **Table 3**.

Fig. 2. Water balance diagram of Bali Province.
(*Source: Sunarta and As-Syakur, 2015*).

The response of informants to the water scarcity issue in Pemuteran, Bali (in %).

No	Questions	Yes	No
1	Do you know that Bali is projected to suffer water shortages?	46%	54%
2	Do you know that Buleleng Regency is experiencing water shortages?	15%	85%
3	Do you encounter difficulties in accessing water?	31%	69%
4	Do you care about the water problems in Pemuteran Village?	100%	0%
5	Have you tried any strategies to save water?	100%	0%
6	Do you know that the tourism industry uses up to 65% of available water in Bali?	69%	31%
7	Are you willing to support any efforts that the government and community perform to save water?	100%	0%

3.3. Network analysis between dive resorts

The network established among the dive resorts was analyzed using a sociogram, which was created in Gephi application with ten nodes (dive resorts) and ten edges. Here the sociogram is considered as a useful method to understand the network of collaboration among the actors. The sociogram is a result of the technical approach in the analysis of the Gephi program. The size of each node is the amount of water consumption per year, while the color represents the presence or absence of water-saving strategies adopted by the dive resort. The edge is a line that connects the nodes, depicting the collaboration between the dive resorts. There are two types of edges, namely the blue line with arrows for cooperation in coral reef protection called Pemuteran Environmental Trust (PET) and the black line for operational activities. Dive Resort 5 initiated PET by inviting all diving enthusiasts and nearly all dive resorts and dive centers in the village. According to the respondent representing Dive Resort 5, many parties have participated in PET activities. Aside from private resorts, several dive resorts that are still under development (only about two years old) are not included in the PET network. An example includes Dive Resort 6, which is a private one that partners with the dive center in Denpasar and, therefore, only accepts guests from it. Based on the statement of respondents from Dive Resort 9—which is one of the Pemuteran Local Dive Center (PLDC) groups, PET activities take place every week with a rotating work system. For example, Dive Resort A is in charge of carrying out PET activities in the first week, and Dive Resort B is responsible for the second week, then Dive Center A in the next week, and so on. The sociogram is shown in **Fig. 3** and is placed over the map of the study area in **Fig. 4**.

Fig. 3. The sociogram of the dive resorts in Pemuteran, Bali. The availability of water-saving strategies is shown in green and red colors. Node's size is based on annual water use.

Operational activities seek to maintain a healthy ecosystem for business competition and a place for communication between dive resorts and dive centers, which are represented by divemasters employed at one of the companies or working odd jobs (freelance dive masters). The conversation merely takes place in an online group chat via WhatsApp application. It mostly discusses requests on a divemaster or dive instructor and equipment and boat sharing to reduce the operational costs of a marine tour to Menjangan Island or the dive sites around Pemuteran and Sumberkima. Several respondents mentioned that a few years ago, there was a price agreement in dive tourism service between the companies to prevent damages to the market price (i.e., below price floors or above price ceiling) and interference to the business competition atmosphere. However, several individuals denied this agreement, which indirectly caused it to cease. Until now, there has been no attempt to bring the companies together to discuss the issue.
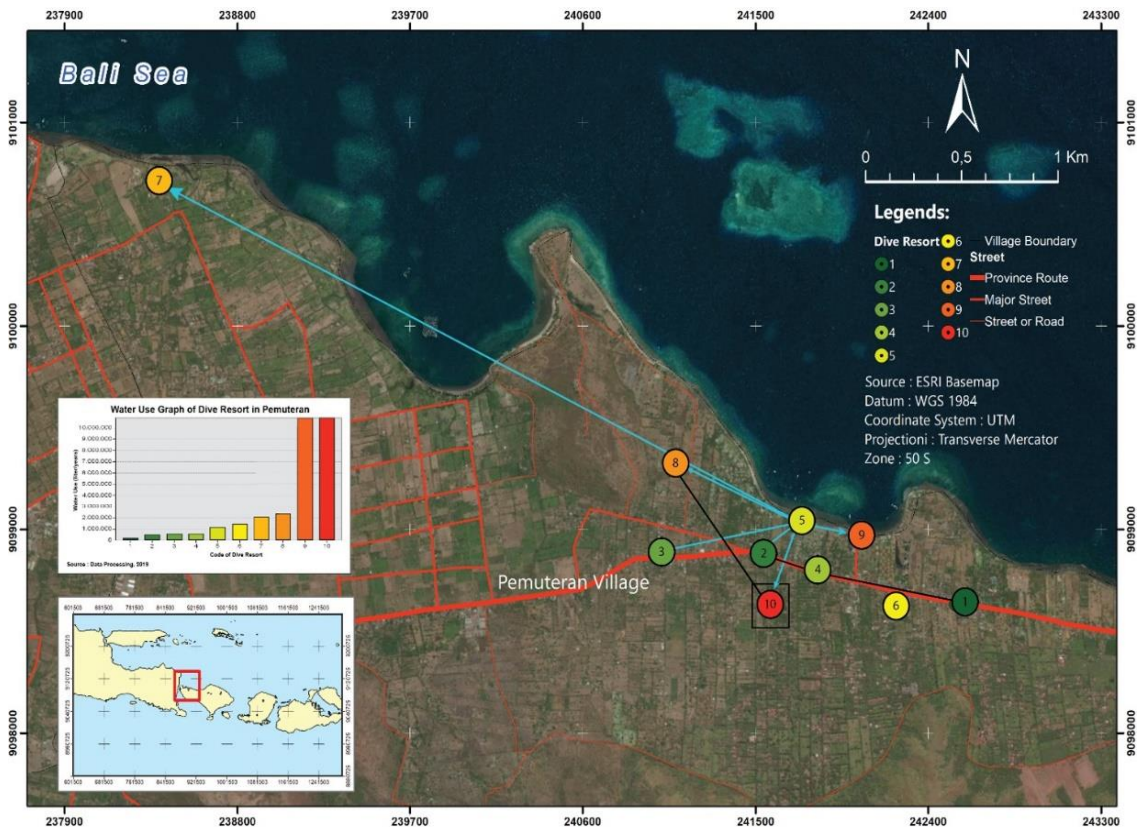
Fig. 4. The sociogram map of the dive resorts in Pemuteran, Bali.

Every dive resort has its connections in operational aspects that stem from personal kinship, intercompany working contracts, and geographical proximity. The black lines or edges illustrate the statement of each respondent on intercompany connections. This connection reflects the cooperation among the dive resorts in several situations: (1) lack of equipment, requiring the company to rent one from other dive resorts, (2) unavailable divemaster/instructor at the dive resort for the marine tour, forcing the company to rent one from another dive resort, and (3) the number of guests do not meet the operational costs for the tour, requiring the company to coordinate with other dive resorts, share a boat, and entrust their guests at an agreed price. These connections only illustrate ones among dive resorts, but not between dive resort, dive center, and other dive shops.

The work connections depicted in **Fig. 4** are not as complicated as the ones developing on Gili Trawangan Island. Parteleow and Nelson (2020) include the work connections between the dive center and dive shops, resulting in a significantly higher number of nodes and edges. In 1992, a dive center was established on Gili Trawangan, and this year marks the beginning of the dive tourism on the island, which is eight years older than the first official dive tourism activity in Pemuteran Village (2000). In contrast to Parteleow and Nelson (2020), this study highlights the work connections among the dive resorts, providing more enriched information.

4. CONCLUSIONS

All dive resorts in Pemuteran Village need 30,202,375 liters of water per year to provide the best services to their guests. In response to potential water scarcity in Bali, each dive resort manages water by implementing specific strategies to conserve more groundwater. Although there is no mutual agreement or specific regulation from the government of Pemuteran Village, each business actor behind the dive resorts is aware of the importance of minimizing groundwater consumption and even willing to help and support the government in its efforts to save water.

The work connections among the dive resorts in Pemuteran Village are divided into two types of partnerships, namely operational cooperation and collaboration in marine ecosystem conservation. This work is considered as a preliminary project utilizing more interviews and secondary data. However, for future work, a statistical approach and method should be used to reveal the quantitative analysis and to understand the detailed connectivity in every dive resort.

R E F E R E N C E S

Agustan, A. and Kausar, D.R.K. (2019). Towards a Framework for Disaster Risk Reduction in Indonesia's Urban Tourism Industry Based on Spatial Information. *Geographia Technica*, 14 (Special Issue), 32-38. http://doi.org/10.21163/GT_2019.141.16.

Bastian, M., Heymann, S., Jacomy, M. (2009). *Gephi: an open source software for exploring and manipulating networks*. International AAAI Conference on Weblogs and Social Media, May 17-20, San Jose, California, North America.

Becken, S. (2014). Water equity - Contrasting tourism water use with that of the local community. *Water Resources and Industry*, 7–8, 9–22. https://doi.org/10.1016/j.wri.2014.09.002.

Bobková, M. and Holešinská, A. (2017). Networking in a Destination from the Perspective of Virtual Relationships and their Spatial Dimension. *Geographia Technica*, 12 (2), 10-19. http://doi.org/10.21163/GT_2017.122.02.

Chan, W., Wong, K., & Lo, J. (2009). Hong Kong hotels' sewage: Environmental cost and saving technique. *Journal of Hospitality and Tourism Research*, 33 (3), 329–346. https://doi.org/10.1177/1096348009338525.

Cole, S. (2012). A political ecology of water equity and tourism. A Case Study From Bali. *Annals of Tourism Research*, 39 (2), 1221–1241. https://doi.org/10.1016/j.annals.2012.01.003.

Dwianika, A., Murwaningsari, E., Suparta W. (2020). Analysis of Water Awareness, Accountability, and Governance to Improve Sustainability of Firm's Performance in Urban Areas. *Geographia Technica*, 15 (1), 35-42. http://doi.org/10.21163/GT_2020.151.04.

Ernawati, N.M. (2011). Pengaruh Pariwisata Terhadap Kehidupan Sosial Budaya Pesisir Di Kawasan Taman Nasional Bali Barat Dan Taman Wisata Pulau Menjangan. *Sabda*, 6 (April), Pp. 69–74.

Gössling, S. (2001). The consequences of tourism for sustainable water use on a tropical island: Zanzibar, Tanzania. *Journal of Environmental Management*, 61 (2), 179–191. https://doi.org/10.1006/jema.2000.0403.

Gössling, S., Peeters, P., Hall, C.M., Ceron, J.P., Dubois, G., Lehmann, L.V., and Scott, D. (2012). Tourism and water use: Supply, demand, and security. An international review. *Tourism Management*, 33 (1), 1–15. https://doi.org/10.1016/j.tourman.2011.03.015.

Gössling, S., Hall, C.M., and Scott, D. (2015). *Tourism and Water*. Channel View Publications. 190p.

Haidu, I. (2016). What is Technical Geography. *Geographia Technica*, 11 (1), 1-5. http://doi.org/10.21163/GT_2016.111.01.

Indonesian Ministry of Tourism and Creative Economy. (2020). *Kunjungan Bulanan Wisatawan Mancanegara 2019 vs. 2018*. https://www.kemenparekraf.go.id/post/data-kunjungan-wisatawan-mancanegara-bulanan-tahun-2019. Accessed on 16 March 2020.

Jacomy, M, Venturini, T, Heymann, S, Bastian, M. (2014). ForceAtlas2, a Continuous Graph Layout Algorithm for Handy Network Visualization Designed for the Gephi Software. *PLoS ONE* 9 (6): e98679. https://doi.org/10.1371/journal.pone.0098679.

Jesus, C., & Franco, M. (2016). Cooperation networks in tourism: A study of hotels and rural tourism establishments in an inland region of Portugal. *Journal of Hospitality and Tourism Management,* 29, 165–175. https://doi.org/10.1016/j.jhtm.2016.07.005.

Kasim, A., Gursoy, D., Okumus, F., & Wong, A. (2014). The importance of water management in hotels: a framework for sustainability through innovation, *Journal of Sustainable Tourism*, 22 (7), 1090-1107. https://doi.org/10.1080/09669582.2013.873444.

Krželj-Čolović, Z., Vrdoljak Raguž, I., Beran, I.M. (2016) Strategic Networking in Hospitality Industry. In: Vrdoljak Raguž I., Podrug N., Jelenc L. (eds) *Neostrategic Management*. Contributions to Management Science. Springer, Cham. https://doi.org/10.1007/978-3-319-18185-1_3.

Lewis, J., & Lewis, B. (2009). *Bali's silent crisis: Desire, tragedy, and transition*. Lanham, USA: Lexington Books. 252p.

Marinopoulos, I.S., & Katsifarakis, K.L. (2017). Optimization of Energy and Water Management of Swimming Pools. A case study in Thessaloniki, Greece. *Procedia Environmental Sciences*, 38, 773–780. https://doi.org/10.1016/j.proenv.2017.03.161.

Mutaqin, B.W. (2017). Shoreline changes analysis in Kuwaru coastal area, Yogyakarta, Indonesia: An application of the digital shoreline analysis system (DSAS). *International Journal of Sustainable Development and Planning*, 12 (7), 1203–1214. https://doi.org/10.2495/SDP-V12-N7-1203-1214.

Mutaqin B.W., Marfai M.A., Helmi M., Rindarjono M.G., Windayati R., Sunarto. (2020). Spatio-temporal Mapping of Ecotourism Activities in Buleleng Conservation Zone: A Methodological Review, *IOP Conf. Ser.: Earth Environ. Sci*. 451 012095. https://doi.org/10.1088/1755-1315/451/1/012095.

Ormeling, F. (2009). Technical Geography: Core Concepts in the Mapping Sciences. In Sala, M. (ed.) *Geography – Volume II*. EOLSS Publications, pp. 211-231.

Partelow, S., & Nelson, K. (2020). Social networks, collective action and the evolution of governance for sustainable tourism on the Gili Islands, Indonesia. *Marine Policy*. 112. https://doi.org/10.1016/j.marpol.2018.08.004.

Picard, M. (1996). *Bali: Cultural tourism and touristic culture*. Singapore: Archipelago Press. 231p.

Ridwan, A. (2014). *Studi Analisis Kebutuhan Air Sektor Nondomestik Kategori Hotel Di Wilayah Kecamatan Ujung Pandang.* Bachelor Thesis. Universitas Hasanuddin, Makassar.

Ruda, A. (2016). Exploring Tourism Possibilities using GIS-Based Spatial Association Methods. *Geographia Technica*, 11 (2), 87-101. http://doi.org/10.21163/GT_2016.112.09.

SNI. (2005). *Tata Cara Perencanaan Sistem Plambing: SNI 03-7065-2005*. Badan Standardisasi Nasional Indonesia. 23p.

Statistics Indonesia. (2018). *Statistik Indonesia: Statistical Yearbook of Indonesia 2018*. BPS - Statistics Indonesia. 762p.

Sunarta, I.N., & As-Syakur, A.R. (2015). Study on the Development of Water Crisis in Bali Island in 2009 and 2013. *E-Journal of Tourism*, 2 (1), 33–42. https://doi.org/https://doi.org/10.24922/eot.v2i1.19441.

Tang, F.E. (2012). A Study of Water Consumption in Two Malaysian Resorts, World Academy of Science, Engineering and Technology, *International Journal of Environmental and Ecological Engineering*. 6 (8), 506–511.

Tripadvisor. (2019, February 20). *Top 25 des destinations–Asie*. Retrieved from https://www.tripadvisor.fr/.

Windia, W., & Dewi, R.K. (2011). *Analisis Bisnis Berlandaskan Tri Hita Karana*. Denpasar: Udayana University Press. 142p.

Yudo, S. (2018). Upaya Penghematan Air Bersih di Gedung Perkantoran Water Saving Efforts in Offices Building Case Study: Water Saving in BPPT Office Building. *Jurnal Teknologi Lingkungan*, 19 (1), 97–106.

NATURAL GEOGRAPHY AND DISPERSE URBAN DEVELOPMENT. RESIDENTIAL DEVELOPMENTS ON MOUNT MONTJUÏC IN BARCELONA IN THE NINETEENTH CENTURY

Jordi GOMIS [1] , *Ramon RIPOLL* [2], *Carlos TURÓN* [3] , *Miquel-Àngel CHAMORRO* [4]

ABSTRACT:
With regard to the nineteenth century, planned extension projects have been widely studied whereas semi-planned urban development plans have been researched rather more vaguely. The number of instances, situations and solutions of this latter type of disperse urban development, and its notable impact on current times, is the reason behind this research into twelve semi-planned residential developments on Mount Montjuïc in Barcelona between 1864 and 1868. They are examples of suburban settlements that represented a new way of hybrid living between the city and the countryside and, therefore, an attempt to come halfway between regular, repetitive urban planning and the natural, irregular, free reality forced by the underlying topography. This research article provides material for reflection on the history of urban planning linked to the natural environment, and above all on the contemporary origin of a new relationship between predictable (reversible) urban planning and the unpredictable (irreversible) natural geography in the definition of the suburban landscape.

Key-words: Geography, City Planning, Topography, Landscape.

1. INTRODUCTION

In the city of Barcelona, as in many other European cities that underwent great industrial development in the nineteenth century, there are many examples of urban growth bordering between regular planning and irregular spontaneity. Of interest in this regard are areas of expansion that interrupt regularity due to pre-existing features that persist over time and have been studied in depth (González, 2008) or consolidated irregular alignments quite unlike the repetitive grid (Sica, 1981). During this period, also interesting is the growth of peripheral settlements of Barcelona (Sarrià, Horta, Sant Gervasi, Sant Martí de Provençals, les Corts, Sants, etc.) characterized by their planning and spontaneity (Serra, 1995); a peripheral ring defined by partially repetitive planning and imperfect continuity (Solà-Morales, 1993). Such examples can be described as disperse planning that enables the emergence of both singular social forms and genuine cultural spaces (Solà-Morales, 1993). Such situations result from the advantages and disadvantages of urban planning that is sometimes a consequence, and others in advance of the events it seeks to control (Benevolo, 1992).

The aim of this study is to examine the concept of disperse urban planning which is on the border between planning and spontaneity, especially due to its direct implications on a social level directly solving problems of housing migratory movements that took place during the 19th century. Culturally, highlighting society's great ability to adapt to the most varied processes of urban development (García, 2016) and especially at the level of the individual and collective imaginary, identifying the

---

[1, 3] *Universitat Rovira i Virgili, Av. Països Catalans 26, 43007-Tarragona, Spain,*
  jordi.gomis@urv.cat, carlos.turon@urv.cat

[2, 4] *Universitat de Girona, C/Maria Aurèlia Capmany 61, 17003-Girona, Spain,*
ramon.ripoll@udg.edu, mangel.chamorro@udg.edu

roots shared with the geographic location. The result is the emergence of a partial urban design, a combination of the rational model and the organic model or between determinate urban planning and the indeterminate "collage" (Julián, 1988). A kind of heterodox growth that over the years, as has been shown, is increasingly recognized, accepted and valued as an alternative to more orthodox, rigid, regular and radical growth due to being totally planned "a priori" (Rowe et al., 1998). These examples are more open and interesting for the study of their rich, complex urban meanings (Choay, 1965), and of the growing importance of geography as a method of analysis between city and countryside (Cassassas, 1977). Also, of the interrelated, and not simply juxtaposed uses, which interact continuously through space and time (Capell, 2001). Forms of growth that enable the emergence and renewal of unlimited geographical and urban meanings (De Castro, 1997).

In the case of the city of Barcelona, during the second half of the nineteenth century, the population quadrupled in sixty years (from 183,787 inhabitants in 1857 to 710,337 inhabitants in 1920). It is interesting to note that some of these people, though few, occupied the urban periphery of the Eixample (Cerdà, 1968) district with new, different settlement patterns. From all of these diverse and relatively interesting examples, we have selected actions based on more regular typological proposals located in places of natural, rather irregular geography. They are the initiatives of private developers, which gained the acceptance of the owners of the land (or vice-versa), and obtained the approval of the military authorities to build within the militarized zone of Mount Montjuïc. Thus, a hypothesis is posed, based on the rise, already in the nineteenth century, of a kind of disperse growth of small urban districts in the middle of the countryside that entails a different relationship between architecture (repetitive types), planning (organization of spaces) and geography (human occupation of natural habitats). With regard to our methodology, field data were obtained from building permits in the archives of military engineers of the General Archive of the Crown of Aragón (ACA). Each application consists of the report, the justification, location and plot plans, as well as the layout, section and front elevation of the dwellings. Our working method is based on comparing this theoretical information with the actual geographical features, such as topography, the road network and the cadastral properties of Mount Montjuïc at the time. The aim is to investigate how disperse planning proposes a way of life between the regularized functionality of architectural typologies and, at the same time, the rational morphology of planning with the irregularities and naturalness of rural geography. In all likelihood, the creation of these fragmented districts does not involve situations of social disunity, segregation or deactivation, quite the opposite. So, one should consider that these examples, like so many other similar ones throughout Europe during this period, represent clear attempts to anticipate the new geographical, social and cultural relationship between countryside and city, which was, as we all know, to develop significantly in the twentieth century.

2. HISTORICAL BACKGROUND

It should be recalled that Mount Montjuïc in Barcelona, as a strategic military area and of social control over the city, the port and the plain of Barcelona, is dominated by the Castle. A modern fortress, built according to the principles of geometry, mathematics and defence of Sébastien Le Prestre de Vauban, which at the same time, in the eighteenth and nineteenth centuries, delimited a military security zone of 1,500 varas (equivalent to 1,253 m) from all is surroundings. It should also be said that this military protection zone was privately owned but subject to rigorous military servitude. This rule allowed only the use of the land without any building intervention, unless special permission was given, such as for quarrying, the building of retaining walls or the construction of buildings for very well justified reasons. In the latter case, the buildings had to be on just a single level and made of easily demolishable materials, should the military so rule. This forced buildings of less than 3.5 m in height with walls 14 cm thick or less, and structural pillars no greater than 56 cm across. Thus, a special geographical ring was created that was defined by both military/defensive standards and by the natural/agricultural customs and residential-manufacturing activities.

Regarding building permits, residential-manufacturing activities specifically accounted for 220 licences granted between 1740 and 1913. Initially, the granting of permits for exploitation and

construction was scarce and as the years went by, it increased in number and importance. It can also be seen that the period with the greatest number of permits validated comes above all during the second half of the nineteenth century and particularly during the 1860s. It should also be noted that residential permits are most numerous, accounting for 50% of the total (109 permits) including those for the building of single-family dwellings houses (52 permits), groups of two and five dwellings (24 permits), and clusters of more than five dwellings (23 permits). Thus, the construction of a total of 784 dwellings was granted (**Table 1**). Of these, 12 examples of one-off developments were selected (between 6 and 87 houses). This was performed using criteria of diversity and clarity of the information presented and especially their location.

Table 1.
Building permits for Mount Montjuïc in Barcelona (1740-1930).

	BUILDING PERMIT	TOTAL PERMITS	<1850	1851-1860	1861-1870	1871-1880	1881-1890	1891-1900	>1900	TOTAL DWELLINGS	FIRST DATA	LAST DATA
1	VARIOUS	71	9	8	16	4	8	7	19	/	1740	1913
2	SINGLE FAMILY	52	/	4	19	10	/	17	2	52	1851	1908
3	MULTI-FAMILY (2 to 5 dwellings)	24	1	1	19	2	/	1	/	69	1849	1891
4	MULTI-FAMILY (>5 dwellings)	23	/	/	23	/	/	/	/	513	1864	1867
5	ROUNDABOUTS	17	/	/	/	/	5	2	10	150	1884	1905
6	TILING	14	/	2	9	3	/	/	/	/	1856	1880
7	FACTORY	7	1	2	4	/	/	/	/	/	1858	1877
8	HOUSE	4	/	/	2	1	/	1	/	/	1864	1899
9	LIVESTOCK PENS	4	1	/	3	/	/	/	/	/	1830	1868
10	QUARRY	3	/	/	/	/	1	1	1	/	1880	1902
11	PLOTS	1	/	/	/	1	/	/	/	/	1877	1877
	TOTAL	**220**	**12**	**17**	**95**	**21**	**14**	**29**	**32**	**784**		

In all these permits, a strict protocol is followed:
- Request for the building permit: The owner of the property or developer requests building permission from the Queen by means of a written report and plans to a scale of 1/200 and 1/100 (measured in meters and others also in meters and spans).
- Report by the military engineers: The chief engineer drafts a report following military regulations and a map of the exact location of the building work on the mount to a scale of 1/10,000 (measured in meters).
- Granting by the military governor: The military governor justifies the suitability or not of granting a building permit in accordance with military regulations.
- Monitoring of the works: The military engineers ensure compliance with the permit granted.

This information allows deducing the following general aspects. First, the technical requirements of the engineers that force the private owners to render clear, accurate plans. Their authorship, though not reflected in these drawings, evidently corresponds to master builders and architects given their preciseness in defining the property, the geomatization of space, the layout of the houses, the careful style of the facades, etc. Secondly, the profitability of these developments means that their goal is to make financial profit from the rural land that was predominantly not used by its owners. Therefore, the persons applying for permission are always the most entrepreneurial proprietors of Mount Montjuïc. And, thirdly and finally, the high architectural functionality of the developments aims to meet the needs of the real estate market for townhouses, such as hygiene, sanitation, good internal organization, the large size of the outdoor patio, and so forth. Thus, sanitation and functionality are equally important and totally complementary features. Of these developments carried out during this period, twelve have been studied whose features and location were considered particularly characteristic (**Fig. 1**).
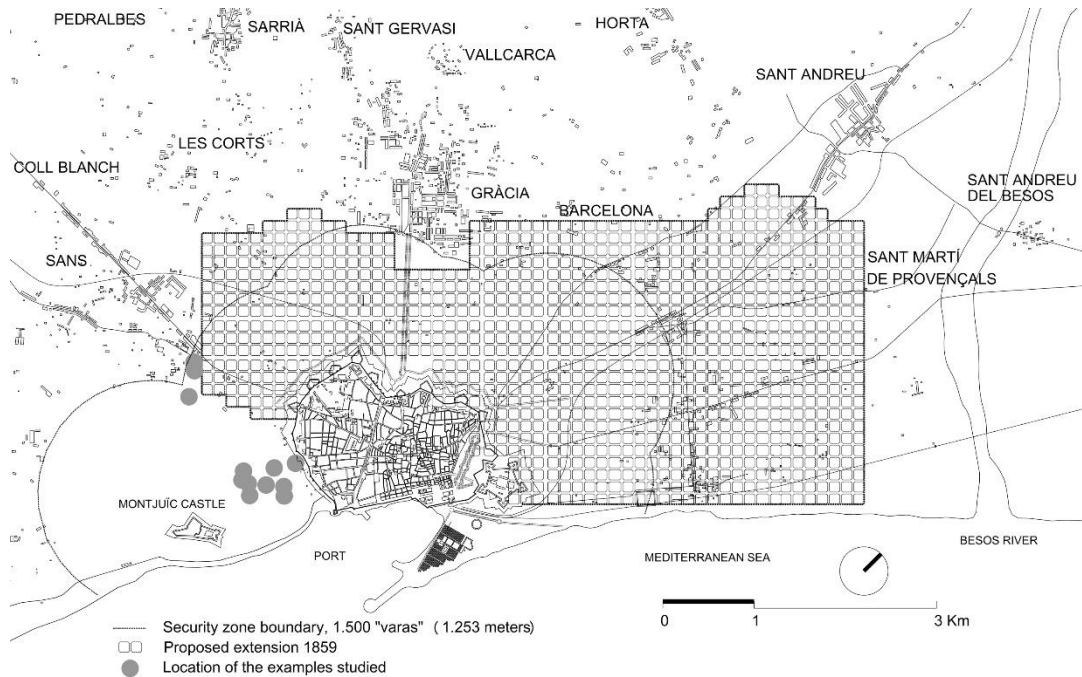
Fig 1. Location map of the 12 developments of Mount Montjuïc of Barcelona (1864-1867).
(Drawing by R. Ripoll, private archive, 2019)

3. SITE TOPOGRAPHY AND GEOGRAPHY

The study of the topography of Mount Montjuïc in Barcelona reveals that it is at an elevation of approximately 174 m higher than the city of Barcelona at its highest point (+184 m above sea level) compared to the city flatlands (+10 m above sea level). This relatively large difference in altitude gives rise to different gradients according to the aspects of the mount. The steepest slopes are located on the eastern aspect facing the sea (from 30 to 200%), normal slopes are located on the north, or city-facing slope (15 to 24%), while the gentlest gradients are found facing the west and south in the direction of the inland plains (5 to 22%). This results in a rugged geography with sporadic natural crags (in the area of the port and the sea) and artificial cuts caused by quarries and torrents of water (from the Trobada and dels Jueus fountains, etc.). Such diversified geography that connects the city by road and tracks with small fields of crops (Beltran orchards, scarcely productive crops, etc.) and the various private properties. The result is an austere, heterogeneous and fragmented topography (**Fig. 2**). An analysis of the ownership structure (according to the cadastre of 1851) allows us to observe a very important property division. Let us recall that a proprietor can own at the same time one or several cadastral units, which, in turn, can be joined or separated by short or long distances. However, this study demonstrates the advantages of owning a rural property in Mount Montjuïc due to its proximity to the city of Barcelona, while its negative aspects include the limitations of its rugged geography (steep, rocky area) and especially the burden of military jurisdiction (limited uses and buildings). Furthermore, the surface area of each of the average-sized properties is of around 10,000 m2 (specifically between 8,000 and 12,000 m2). The smaller properties cover an area of approximately 2,000 m2 (properties of less than 1,800 m2 are scarce), and the largest properties are approximately 20,000 m2 (properties of over 30,000 m2 are scarce). Their perimeters range from rectangular to irregular trapezoidal in shape. In most of the dwellings studied (examples 1 to 8) the cadastral unit of the property generally coincides with the developed unit. However, in the most important interventions (examples 9 to 12) it can be deduced that the size of the developed unit requires the union of several cadastral units.
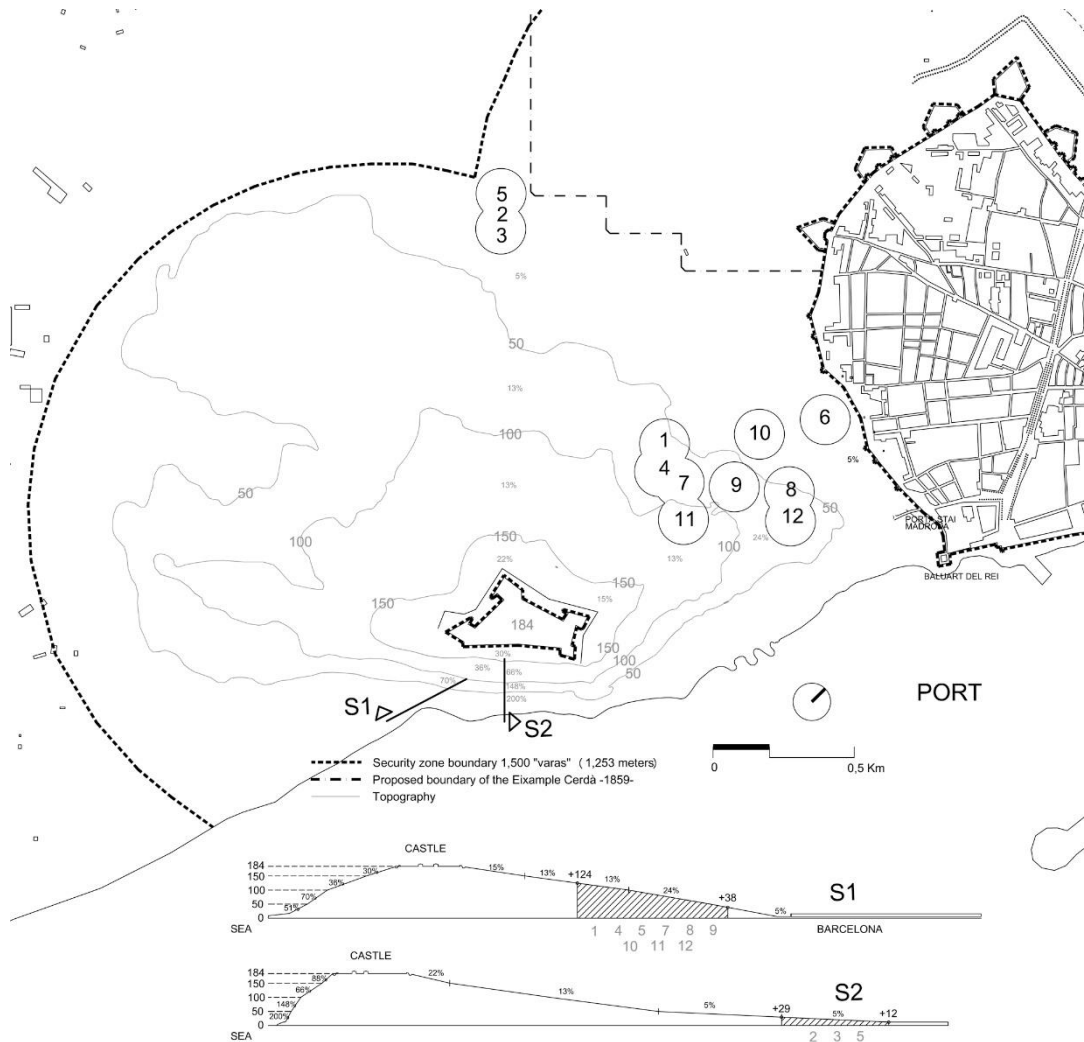
Fig 2. Topographic study of Mount Montjuïc concerning the settlements studied (1-12).
(Drawing by R. Ripoll, private archive, 2019)

The adaptation of the proposed developments is seen to be carried out topographically- and cadastrally-speaking on two different levels. An initial adaptation arises from the preservation of the original irregular property boundary and, therefore, the implementation of compensation mechanisms with neighbouring properties to realign the perimeters and adapt them to the regular delimitation lines of the proposed planning are not observed (**Fig. 3**). These cadastral irregularities, despite representing an objective loss of land use, introduces a morphological uniqueness and richness. Pre-existing perimeters that may be conceptualized as urban accidents, functionally negative, but positive in terms of landscape, with a direct impact when defining both the streets and open spaces and the arrangement of the plots. This involves a second aspect of adaptation that directly relates the forms of urban planning with the forms of the landscape. Without doubt, this morphological adaptation requires seeking the places with the gentlest gradients both in the intermediate developments as far as the number of dwellings is concerned (examples 6 to 8) and in the larger housing estates (examples 9 to 12).
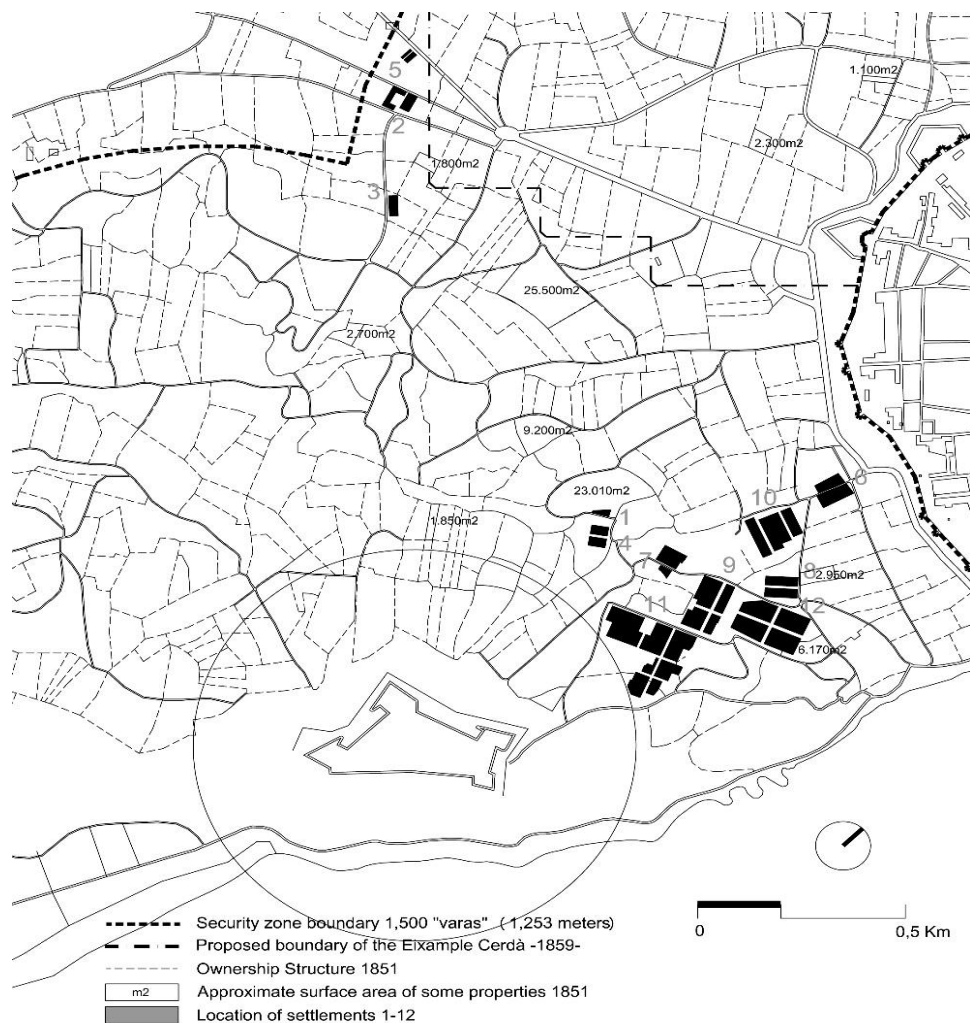
Fig 3. Cadastral study of Mount Montjuïc concerning the settlements studied (1-12).
(Drawing by R. Ripoll, private archive, 2019)

4. MORPHOLOGY AND INTEGRATION IN THE LANDSCAPE

The first thing noticed is the little time required for the granting of the permits for the studied works (between 1864 and 1868). This relatively short period, in the case of the examples studied, led to the construction of 466 single-family houses in little time. This resulted in both typological systematization (similar types) and constructive rationalization (traditional construction). This influenced the creation of single-family houses set in a row, usually formed by a structural bay with cross ventilation and arranged in most cases with the street on one side and the courtyard or garden on the other. Such architectural typology requires the creation of rectangular parcels ranging from 28 m2 (example 5) to 288 m2 (example 12). This in turn imposed the arrangement of facades of a width of between 4.4 m (example 5) and 6 m (examples 7, 9 and 12). The other urban parameters are characteristic of low-density single-family dwellings (occupation fluctuates around 60%, the floor area ratio of 0.6 m2/m2, and height is less than 3 m).

It should be noted that the key feature of these dwellings is their autonomy of services, such as their individual toilet (commonly located at the exit of the rear courtyard), the drinking water well (also mainly found in the courtyard), the sink, tank or pond for watering (always located beside the well), and finally the enclosed patio/garden (located behind the house) (**Table 2**).

Table 2.

Urban parameters of the types of architecture.

	NUMBER OF DWELLINGS	YEAR	OWNER	LOCATION	DISTANCE MONTJUIC CASTLE	LAND AREA (m2)	PARCELS TOTAL SURFACE AREA (m2)	TOTAL SURFACE AREA TRANSFERRED TO COUNCIL (m2)	TRANSFER (%)	STREET WIDTH (m)	PARCEL SURFACE AREA (m2)	FACADE WIDTH (m)	REGULATORY HEIGHT (m)	OCUPANCY (%)	BUILDABLE DEPTH (m)	ACA / ENGINEERS collection
1	6	1865	VALLCORBA, Pau	Cami Creu de Molers	3rd zone	533	77-120	0	0	/	77-120	6.3 to 10	3,5	67 to 85	6 to 15	file 53/13
2	22	1865	BONAFONT, Esteve	Carrer Princesa	1390	2661	133	769	29	/	133	5,6	3,5	48	13	file 57
3	11	1864	BONAFONT, Joan	3rd zone of the Castle	3rd zone	1155	105	0	0	/	105	5	3	45	9	file 57
4	16	1865	VALLCORBA, Pau	Cami Creu de Molers	3rd zone	2508	134	0	0	8	134	5,6	3,5	68	16	file 53/13
5	21	1864	GASET, Miquel	Hostafrancs district	1450	826	28	171	21	4	28	4,4	3	100	6,1	file 20
6	27	1867	VILA, Domenec	Hortes d'en Bertran	1150	4789	126 to 263	352	7	5	126 to 263	5,6	3,5	33 to 57	12,5	file 55
7	24	1868	RACIONERO, Joan	Camí de la Font Trobada	870	4083	132	1399	34	9	132	6	3,15	52	11,5	file 40/9
8	30	1866	VALLCORBA Pau	Camí de la Font Trobada	850	4383	125	635	15	8,2	125	5,2	3,5	69	16,2	file 53
9	62	1867	RACIONERO, Joan	Camí de la Font Trobada	810	13186	120	4520	34	10	120	6	3,15	59	11,5	file 42/23
10	64	1866	CARIBAL, Joan and Josep	3rd zone of the Castle	800	11464	144	1785	16	8	144	5,8	3,1	55	13,5	file 20/11
11	87	1867	CARIBAL, Joan and Josep	Camí de la Font Trobada	800	16859	139	3304	20	10	139	5,8	3,1	49	12	file 18/14
12	96	1867	PADROL, Francesc	3rd zone of the Castle	810	28522	144 to 288	9343	33	8	144 to 288	6	3,1	25 to 50	12	file 34/4
	466															

This approach involves a strong link between the dwelling and the natural environment and its main elements (sun, air, water and vegetation). This relationship is especially realized through the street, relatively well-proportioned by the height of the buildings, with widths ranging from 4 m (example 5), 8 m (examples 4, 7, 8, 10 and 12) and up to 10 m (examples 9 and 11); as well as through spacious courtyards of more than 50 m2 (examples 3, 6, 7, 9, 10, 11 and 12).

The study of the integration of urban planning and landscape was performed using the relationship between: situation, morphology, natural geography and disperse development of each of the examples. A relational study that enables verifying the high level of regional implementation (before and after construction), that measures visually the integration of planning proposals with the reality of the landscape (**Fig. 4**). A clear comparative picture that enables drawing conclusions, despite being partial and limited, between disperse urban development (with a strong social component) and the fragmented landscape (with a strong natural component) near Mount Montjuïc in Barcelona during this period.

Fig 4. Examples of disperse urban development and its relationship between urban morphology and natural geography (1-6). (Drawings by R. Ripoll, private archive, 2019).
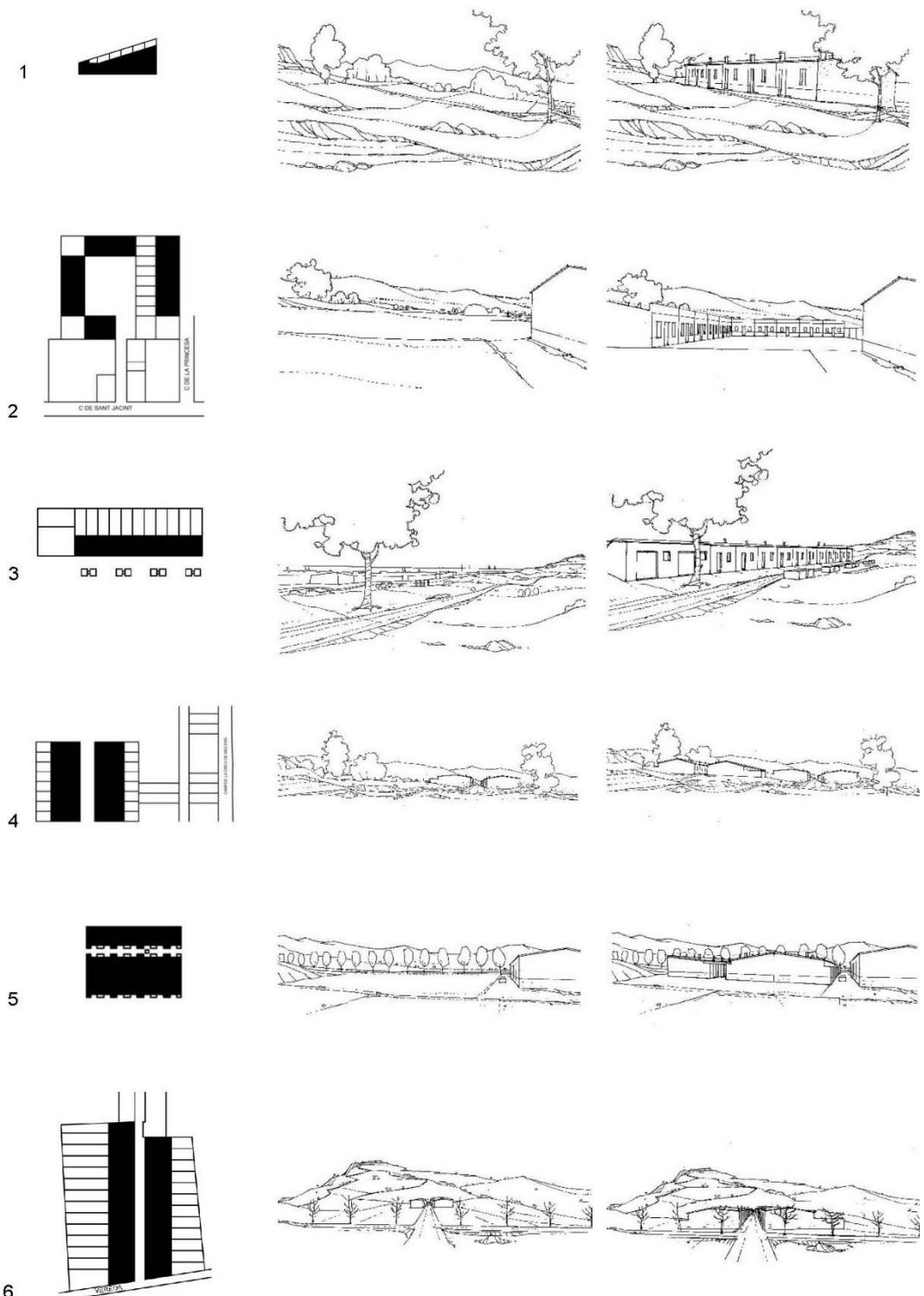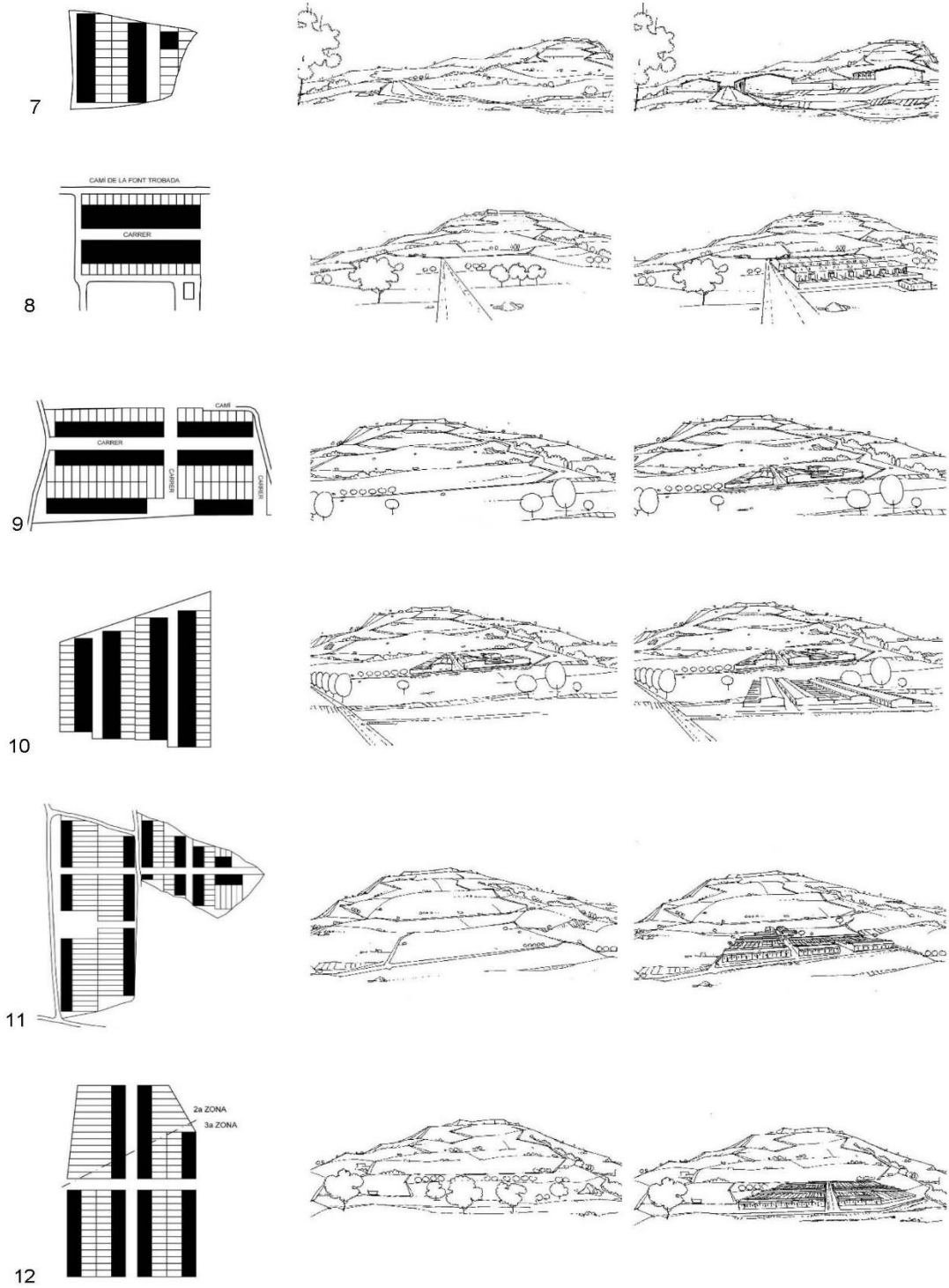
Fig 4. Examples of disperse urban development and its relationship between urban morphology and natural geography (7-12). (Drawings by R. Ripoll, private archive, 2019).

5. CONCLUSIONS

Following the analysis conducted according to the documentation provided, the clear social and cultural potential of disperse urban planning can be deduced, provided that it establishes a close relationship with the natural geography. This hypothesis has been verified in the topographical and geographical adaptation between the different residential groups studied (urban development projects) and Mount Montjuïc (natural environment). The result is not so much a series of marginal suburban developments with respect to the city, but rather a set of small-sized residential centres, integrated into the privileged natural landscape (humanizing), enjoying good views (raised), constant ventilation (dry), and suitable orientation (sunny). Also evident is the complementarity of this duality (city and countryside) which started to be investigated and defined, with all kinds of attempts, during the second half of the nineteenth century, involving projects of the industrial city that intensively bring families to the rural environment. Such projects in other eras were reserved for the rich, becoming increasingly accessible to citizens in general and to factory workers in particular (factories and workshops of the port of Barcelona and the "Poble Sec" district).

We certainly know that the theorizing of the garden city was carried out at the end of the nineteenth century in the project of the town of Letchworth, in the county of Hertfordshire, England, work of the architect Ebenezer Howard (1850-1928), taking place mainly during the twentieth century (Bosma et al., 1997). But it is also true that it arose thanks to multiple antecedents, throughout the second half of the nineteenth century, which are essential for establishing the proposed new relationship between urban and rural geography. Such a background consists of a series of developments of houses linked with the landscape, like the ones in our study, that are essential to begin to popularize some of the benefits of joining the city and the countryside, both in the social imaginary (popular imagery) and in the management of new ways of living in the contemporary world (achievable utopias).

R E F E R E N C E S

ACA: Archive of the Crown of Aragón. Engineers collection. Barcelona: Files 3 to 57.

Benevolo, L. (1977). Diseño de la ciudad 5. El arte y la ciudad contemporánea. Barcelona: Editorial Gustavo Gili.

Bosma, K., Hellinga, H. (1997) Mastering the City: North-European City Planning 1900- 2000. Rotterdam: NAi Publications

Cassassas, Ll. (1977). Barcelona i l'espai català. Barcelona: Editorial Curial.

De Castro, C. (1997). Geografia en la vida cotidiana. De los mapas cognitivos al prejuicio regional. Barcelona: Ediciones del Serbal.

Capell, H. (2001). Dibujar el mundo. Borges, la Ciudad y la geografia del siglo XXI. Barcelona: Ediciones del Serbal.

Cerdà, I. (1968). Teoria general de la urbanización. Reforma y ensanche de Barcelona. Barcelona: Ediciones Ariel i Editorial Vicens Vives.

Choay, F. (1976). El urbanismo. Utopias y realidades. Barcelona: Editorial Lumen.

García Vázquez. C. (2016). Teorias e historia de la ciudad contemporània. Barcelona: Editorial Gustavo Gili.

González Moreno-Navarro, A. (2008). El camp d'en Grassot, família i territori. Barcelona: Editorial Costa llibreter

Julián, I. (1988). L'urbanisme a Barcelona entre dues exposicions (1888-1929). Barcelona: Els llibres de la frontera.

Rowe, C., Koetter, F. (1998). Ciudad collage. Barcelona: Editorial Gustavo Gili.

Solà-Morales, M. (1994). Les formes de creixement urbà. Barcelona: Edicions UPC.

Serra, E. (1995). Geometria i projecte del sòl als orígens de la Barcelona moderna. La vila de Gràcia. Barcelona: Edicions UPC.

Sica, P. (1970). La imagen de la Ciudad. De Esparta a Las Vegas. Barcelona: Editorial Gustavo Gili.

ASSESSMENT OF THE IMPACT OF INDUSTRIAL DEVELOPMENT AT THE COAST OF LÉVRIER BAY THROUGH THE SPATIO-TEMPORAL STUDY OF METALLIC CONTAMINANTS (CD, PB, CU, ZN AND HG) IN SURFACE SEDIMENTS

M'Beirika AHMED SALEM CHEIKH[1,3], Mohamed Salem EL MAHMOUD-HAMED[2], Día MAMADOU[3] , Harouna TOUNKARA[2], Mohamed El Housseine LEGRAA[3], Mohamed RAMDANI[4] and Zeinebou SIDOUMOU[1]

ABSTRACT:
Lévrier Bay is located at the northern Atlantic Mauritanian coast, between 19 ° 20'N and 20 ° 40'N and between the coast and 17 ° 20W in the vicinity of Cap Blanc peninsula. This work aims at contributing to the assessment the impact of industrial development in the Lévrier Bay through the study of the toxicity and the spatio-temporal distribution of trace metals (Cd, Pb, Cu, Zn and Hg) in surface sediments, during the four hydrological seasons. The trace metal concentrations of the sediments are generally heterogeneous and vary according to the metal analyzed and the sampling site according to the order Zn> Cu>Pb> Cd>Hg. In fact, the present work shows higher average concentrations of metals studied in surface sediments than those found for the same metallic elements in previous recent studies at Lévrier Bay, which may be due to anthropogenic pressure in these areas. , especially since the different sites of the Bay are deprived of any sanitation system. In addition, the levels of these metals in the sediments of Lévrier Bay are below the international standards recommended for the toxicity assessment of sediments.

Key-words: Sediment, Trace metals, Industries, Seasons, Lévrier Bay

1. INTRODUCTION

The fisheries sector is one of the pillars of Mauritania's economy and the main activities related to this sector are located in the Lévrier Bay. The Lévrier Bay is located at the northern Atlantic Mauritanian coast, between 19 ° 20'N and 20 ° 40'N and between the coast and 17 ° 20W in the vicinity of Cap Blanc peninsula. (Fig.1).In addition, this area includes two natural sites of great ecological importance, notably the Cap Blanc satellite reserve, classified as World Heritage (recognized for its role in protecting the last viable colony of Mediterranean monk seals) and the Baie de l'Etoile, site recognized by IUCN and candidate to be classified Marine Protected Area (IUCN, 2008). This area is characterized by four hydrological seasons. They have been identified in the context of studies carried out in Mauritanian marine waters (Dubrovin et al.1991; Wagne et al.2011; Wagne et al.2013), namely, the cold season (January to May) and the hot season (August to October). These are interspersed by two inter-seasons, hot-cold (from June to July) and cold- hot (from November to December).

[1]*Department of Biology, Faculty of Science and Technology, UR / EBIOME, University of Nouakchott AL Aasriya, Mauritania mbksalem1@yahoo.fr, mintsidoumou@yahoo.fr*
[2]*National Office for Sanitary Inspection of Fisheries and Aquaculture Products (ONISPA), Mauritania imouh84@yahoo.fr, h_tounkara@yahoo.fr*
[3]*Mauritanian Institute for Oceanographic and Fisheries Research (IMROP), madou.mr@gmail.com, legraahoussein@yahoo.fr, mbksalem1@yahoo.fr*
[4]*Institut Scientifique Rabat, Université Mohamed V Agdal, Avenue Ibn Batouta, Maroc, ramdanimed@gmail.com*

The Lévrier bay is under heavy human pressure because of the economic activities. Indeed, the installation of fishing companies such as fishmeal and fish oil factories which represent 32 factories in more than 70 establishments for processing fishery products intended for human consumption (WebgateEU2019). These pressures are, among other things, at the origin of several types of industrial discharges at sea, such as 2,388 active canoes (IMROP 2019), the presence of four main ports (fishing, trade, mineral and petroleum), in addition to domestic discharges are all potential sources of chemical pollution (Dartige and OuldDedah1996;Belin and Le Gal2005). These various urban and industrial wastes are directly dumped into the marine environment in the absence of any sanitation system. In addition, Zamel et al. 2010 have shown that 75,632 m3 of wastewater are discharged daily into the bay, including 3 m3 of oily water and 51,755 tons of solid discharge which constitute a major source of pollution, harmful to the bay environment. In the aquatic and coastal environment, numerous studies have shown that trace metals are used to reveal the level of anthropogenic influence, because they are persistent, toxic and have a tendency to bioaccumulate that which constitutes a risk for biotas and ecosystems (USEPA 2002; Memet 2011; Diop et al. 2012; Liang et al.2013).

In Mauritania, numerous studies on the state of contamination of the Atlantic coasts of Nouadhibou (Lévrier Bay) by trace metals in biological tissues have been carried out, notably in bivalve filter molluscs (Sidoumouet al.1992; Dardige2006; Wagneet al.2013; M'Hamada et al.2014; Legraa et al.2019). For the first time a study using the sediment matrix over two seasons only (cold season and hot season) during 32 months from January 2013 to October 2016 (Legraa et al.2019) has been conducted. For the sake of contributing to the evaluation of the impact of industrial development at the level of the Lévrier Bay, the present study was conducted, to assess the toxicity and the spatio-temporal distribution during the four hydrological seasons in the surface sediment matrix. To give a better visibility of the space-time distribution, we will compare our results with those found by authors cited above.

2. MATERIALS AND METHODS

2.1. Sampling

Depending on the nature of the industrial activities, eight sites (discharge points) were chosen according to the nature of the discharges from the source of pollution, at the Lévrier Bay (**Fig. 1**). The different sampling sites were subject to seasonal monitoring and the characteristics of the sampled sites are as follows:

• Bountiya (hereafter BONT): area of agglomeration of fishmeal and fish oil production factories, which generate several types of discharges such as: waste water, organic matter, solid discharges and cooling water, etc.

• Port Artisanal (hereafter EPBR): home port and landing of canoes and coastal vessels intended for artisanal fishing generating the main discharges which may contain oils, fuel, detergents, waste water (untreated) and solid waste.

• Centrale électrique [fr] (Powerplant, hereafter CE): main thermal power station, which supplies electricity to the Nouadhibou city including the discharge of hot and contaminated water.

• Port minéralier [fr] (Mineral port, hereafter PM): main port for loading iron ore.

• SNIM 1 (Port minéralier = Mineral port): tidal balancing area near the mining port

• SNIM2 (Port minéralier = Mineral port): tidal balancing area near the mining port further offshore.

• Cap Blanc coast (hereafter CBC): witness sites (absence of industries).

• Cap Blanc large (hereafter CBL): the tip of Cap Blanc, which is a tidal balancing area.

We carried out 3 sampling sat each site and per hydrological season during the period from June 2016 to December 2017. The offshore sediment sampling was carried out on board of a research boat (Amrigue), using an Eckman type grab whose jaws close automatically, thus collecting the substrate (sediment), over an area of 1,225 m². In the coastal area, the sediments were collected on a canoe

board, using an Eckman type grab over an area of 0,225 m², however, at the sampling sites located on the coast (intertidal area), surface sediments were collected using a PVC cover with 66 mm in diameter and 50 cm in length over a depth of 5 cm.
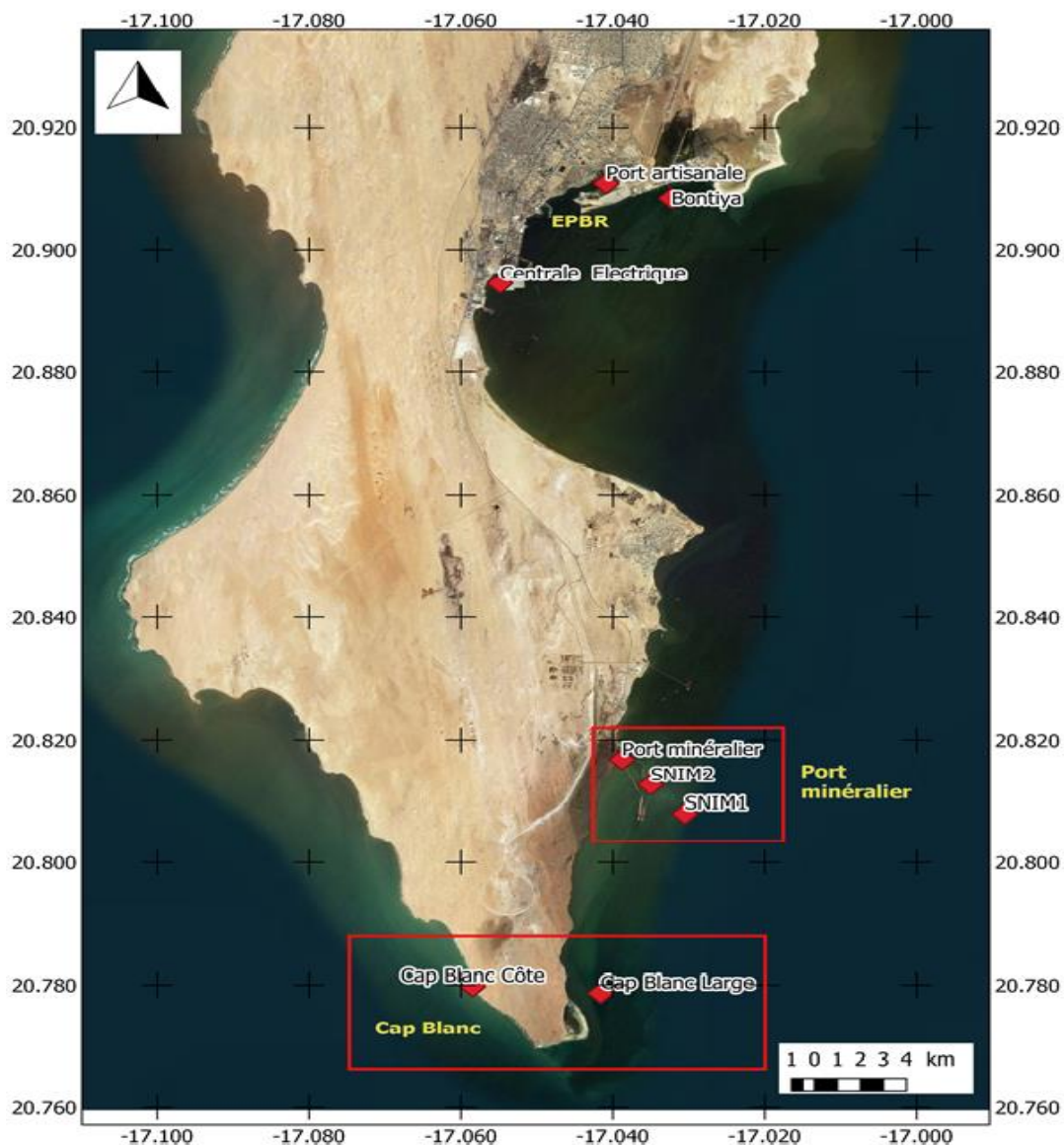
Fig.1. Location of the study area and sampling sites.

2.2. Sample preparation and analytical procedure

Samples of 0.5 g were digested by duplicate, then, were placed in microwave closed-vessels with a mixture (6:2) of ultra-pure nitric acid 67% and hydrogen peroxide 30% at room temperature for one hour and then extracted by microwave. Digestion conditions applied in the microwave system were as follows: 3 min at 250 W, 5 min at 650 W, 22 min at 500 W, 5 min at 0 W and vent. The digested samples were diluted to 50 mL with deionized water (Milli-Q quality).

The analysis of Pb, Zn, Cu and Cd were conducted using an atomic absorption spectrometer with furnace graphite (LOD of 0.046 for Pb and 0.004 µg·g-1 for other elements), according to the ISO 15586:2003. Hg was analyzed using Direct Mercury Analyzer (LOD=0.003µg/g), according to the method "MA.207–Hg 2.0, (Centre d'expertise en analyse environnementale du Québec).

The potential presence of trace metals in the chemicals that were used during the digestion was determined. Blanks were run simultaneously in each batch analysis to authenticate the analytical quality. All of the glassware and plastics were soaked overnight in 10% (v/v) nitric acid, rinsed with distilled and deionized water and dried before being used. The potential presence of trace metals in the chemicals that were used during the digestion was determined. Blanks were run simultaneously in each batch analysis to authenticate the analytical quality. All of the glassware and plastics were soaked overnight in 10% (v/v) nitric acid, rinsed with distilled and deionized water and dried before being used.

Samples were mineralized by nitric acid (67%) mixed with hydrogen peroxide (30%) and then the extraction was carried out using an Anton- Paar microwave model Multiwave-3000.

Atomic Absorption Spectrometer (AAS, Perkin Elmer AAnalyst 800) and Direct Hg Analyzer (DMA-80, Millstone) equipment was used to analyze the trace metals. The certified standard reference material for sediment samples (BCR 146R) was used, it shows recoveries varied from 93% to 113% of certified values (**Table** 1).

Table 1.

Measured and certified values of metal concentrations (mg/kg).

	Cd	**Pb**	**Cu**	**Zn**	**Hg**
n	4	4	4	4	4
Measured value	18	569,7	966,7	2839,3	7,6
certificate value	18 ± 0.5	609±14	838±16	3060±60	93
Recovery (%)	102	94	116	93	90,5

2.4. Statistical analysis

All data were imported and statistically processed in the SPAD software (version. 5) and Excel 2016. The trace metal concentrations in the sediments were compared at the different sites in the study area and during the hydrological seasons (Spatio-temporal distribution). The study of variations of intra-site and inter-site, trace metals as well as the correlations study between trace metals (PCA) were carried out.

3. RESULTS AND DISCUSSION

The results obtained relate to the variations in trace metals concentrations (Cd, Pb, Cu, Zn and Hg) in the surface sediments of the sampling sites exposed to different industrial and urban discharges and then the results found are presented in **Table 2**.

Cadmium (Cd) variations were found for the lowest value at 0.00 mg / kg at the CE, while the largest value (0.58 mg / kg) was recorded at the CBL offshore. In addition, the average minimum and maximum concentrations recorded for Cd are respectively: (0.04 ± 0.014 mg / kg and 0.265 ± 0.078 mg / kg) at CE and EPBR. The important significant variations of Cd concentrations (0.04 to 0.58 mg / kg; 0.07 to 0.42 mg / kg; 0.03 to 0.39 mg / kg and 0.14 to 0.38 mg / kg) by site are recorded, respectively, at CBL, EPBR, PM and BONT. While the lowest variations of Cd concentrations (0.00 to 0.07 mg / kg and SNIM1 0.08 to 0.2 mg / kg) were found in the CE site, we note nevertheless the absence of variation of the Cd concentration values at the SNIM2.

Concentrations of trace metals (mean ± Standard deviation: mg/kg) in sediments for the studied sites.

Sites	Cd	Pb	Cu	Zn	Hg
EPBR	0,265±0,078	5,7±2,924	11,284±4,903	47,245±16,835	0,008
CE	0,04±0,014	2,125±0,880	4,434±1,028	9,185±1,939	0
BONT	0,225±0,053	1,017±0,393	3,337±1,319	15,445±6,906	0,001
PM	0,142±0,084	1,722±0,719	11±3,214	5,137±2,072	0
CBC	0,11±0,054	0,555±0,306	6,505±4,760	5,105±0,995	0
SNIM1	0,137±0,030	1,135±0,401	4,862±1,180	15,035±4,131	0
CBL	0,202±0,126	0,647±0,294	4,317±3,400	5,85±1,774	0
SNIM2	0,147±0,012	0,637±0,126	2,775±0,745	8,397±3,869	0

According to Bowen (1966) the concentration in natural seawater is around 0.1µg/l and comes mainly from petrochemical or metallurgical industrial activities (Odin1995). Our results for Cd contain a maximum average concentration (0.265 ± 0.07 mg/kg), these results are very close to those in the sediments of Dakar coast (0.270 mg / kg) reported by Diop et al. 2014. But the maximum average value Cd concentration (0,130±0,070) found by Legraa et al. (2019) at Etoile bay which is part of the Lévrier bay, could lead us to say that the Cd comes from a source of pollution such as the deposit of industrial and anthropogenic discharges and the current discharge in the EPBR.

Although other sources of the Cd are not excluded, such as the permanent presence of upwelling in the Cap Blanc area, the results found by (Kaimoussi et al.2000) in the coastal marine sediments of the Atlantic coast of the region of EL Jadida in Morocco (0.75 mg/kg) and those reported by (Belabed et al.2013) in the sediments of the Gulf of Annaba in Algeria displayed Cadmium contents (0.02 to 2.2 mg/kg).

The lowest Pb concentration was found at the CE (0.00 mg/kg), while at the EPBR the Pb displayed its highest value (12.11 mg/kg). Yet the mean minimum and maximum Pb concentrations (0.555 ± 0.306 mg/kg to 5.7 ± 2.924 mg/kg) are recorded respectively at the CBL and at EPBR. The highest concentrations of Pb (0.00 to 12.11 mg/kg; 0.00 to 4.11 mg/kg and 0.00 to 3.10 mg/kg) are respectively recorded at (EPBR, CE and PM), while the lowest concentration (0.00 to 0.82 mg/kg) were found at SNIM2. The high concentrations of Pb can be mainly due to the port activity through the wide use of lead in fishermen's nets and the high fuel consumption by motor boats as well as the nature of the hull paints of the different boats. Lead concentrations in sediments are not high compared to the threshold for unpolluted sediments which is 30 mg/Kg (OSPAR, 1997).

The lowest Copper (Cu) concentration (0.09 mg/kg) was found at CBL, while the highest most concentration (24.40 mg/kg) was recorded at the EPBR. In addition, the average concentrations of Cu (2.775 ± 0.745 mg/kg and 11.284 ± 4.903 mg/kg) were recorded respectively at SNIM2 and the EPBR site. The significant variations in Cu concentrations (3.52 to 24.40 mg/kg; 0.80 to 20.74 mg/kg; 3.70 to 19.15 mg/kg; 1.03 to 6.70 mg/kg and 2.74 to 6.99 mg kg) were recorded respectively at EPBR, CBC, PM, CE, BONT and SNIM1. The average concentration of Cu (11.284 ± 4.903 and 11 ± 3.214 mg/kg) were respectively recorded at EPBR and PM, indeed, Cu is considered like an urban pollutant (Pichardetal. 2005), then, these high concentrations can be explained by a high contribution of industrial discharges and urban domestic waste from Nouadhibou city without any sanitation system.

The variations in Zinc (Zn) found for the lowest values at 0.00 mg/kg at the BONT site and SNIM2, while the most important value at 77.2 mg/kg was recorded at the EPBR level. In addition, the average concentrations Minimum and Maximum recorded for Zinc are respectively 5.105 ± 0.995 mg/kg in the two sites (CBC and SNIM2) and 47.245 ± 16.835 mg/kg in the EPBR. Although, the average maximum metal concentrations of Zn at BONT and EPBR do not exceed the guideline values of surface sediments toxicity, they remain higher than those at (CE, PM, SNIM and CB) sites, which can be explained by the pressure due to artisanal canoes and coastal boats at EPBR area and the

regrouping of fishmeal and fish oil production factories in the BONT area. In fact, these two zones are deprived of any drainage system, in addition to the weak currentology in the Lévrier bay.

The high concentration of Zn was recorded at EPBR while the lowest concentration was fond at BONT and SNIM2. In addition, the minimum and maximum average Zn concentrations (4.72 to 77.2 mg/kg; 00.0 to 30.20 mg/kg; 2.87 to 21, 30 mg/kg; 0.00 to 16.30 mg/kg; 4.72 to 13.2 mg/kg; 0.52 to 10.6 mg/kg) were recorded respectively at the EPBR, BONT, SNIM2, EC and PM.

In the present study, all mercury (Hg) concentrations are below the detection limit (<0.0058) for all sites and during all seasons with the exception of EPBR and BONT during the cold season and the inter hot cold season. The maximum value was recorded at EPBR (0.03 mg/kg), however this value remains below the standard of 0.5 mg/kg set by the OSPAR convention (1997) for sediments contaminated by Hg. Lead, coper and Zinc levels in Lévrier Bay are the highest in Mauritania coast. The increase of trace metals concentration in levier Bay environment is caused by the demographic and industry development in Nouadhibou city, which is became a free zone and it known a proliferation of fish industry (**Table 3**).

Table 3.

Comparison of the results of this study with other results from the littoral zone of Mauritania (mg/kg).

Site	Cd	Pb	Cu	Zn	Hg	Coordinates	References
EPBR	0,265±0,078	5,7±2,924	11,284±4,903	47,245±16,83	0,008± 00	20° 54' 38.8"N. 17° 02'27.1"W	Present study
CE	0,04±0,014	2,125±0,880	4,434±1,028	9,185±1,939	0	20° 53' 40.0"N. 17° 03'17.4"W	
BONT	0,225±0,053	1,017±0,393	3,337±1,319	15,445±6,906	0,001± 00	20° 54' 30.1"N. 17° 01'56.2"W	
PM	0,142±0,084	1,722±0,719	11±3,214	5,137±2,072	0	20° 49' 00.5"N. 17° 02'19.6"W	
CBC	0,11±0,054	0,555±0,306	6,505±4,760	5,105±0,995	0	20° 46' 47.2"N. 17° 03'30.4"W	
SNIM1	0,137±0,030	1,135±0,401	4,862±1,180	15,035±4,131	0	20° 48' 28.8"N. 17° 01'49.8"W	
CBL	0,202±0,126	0,647±0,294	4,317±3,400	5,85±1,774	0	20 46. 722 N. 17 02.496W	
SNIM2	0,147±0,012	0,637±0,126	2,775±0,745	8,397±3,869		20° 48' 45.5"N. 17° 02'06.0"W	
COMECA	0,090±0,018	1,671±0,534	0,084±0,003	1.349±0,011	0,016 ±0,002	20° 50' 24.7'' N. 17° 02' 03.6'' W	Legraa & al,2019
Etoile Bay	0,130±0,070	1,000±0,400	0,590±0,007	1,283±0,04	0,017 ±0,002	21° 02' 19.2'' N. 17° 01' 36.8'' W	
Cap Blanc	0,076±0,021	0,251±0,111	0,573±0.083	1,900±0,620	0,020 ±0,002	20° 46' 47.58" N. 17° 03' 30.24" W	
IMROP	0,082±0,012	0,805±0,028	0,352±0,008	1.219±0.424	0,019 ±0,002	20° 51' 26.2'' N. 17° 01' 52.0'' W	
Iwik	2,03±0,32	0,40±0,09	nd	nd	0,02 ±0,002	19° 53' 02.7'' N, 16° 17' 32.8'' W	S.Bilal, Thesis 2014
Mamghar	1,96±0,36	0,33±0.6	nd	nd	0,02 ±0,002	19° 52' 03.3'' N, 16° 17' 43.2'' W	

Comparing the concentrations of Cd (0.04 to 0.265 mg/kg) recorded in the present work with those found (0.076 to 0.130 mg/kg) by Legraa et al. (2019), we found that the cadmium level in Lévrier Bay are increased in recent years. Meanwhile, the cadmium level in Lévrier Bay is less than in Iwik and Mamghar (2.03 and 1.96 respectively. Bilal 2014) at Banc d'Arguin region. The important variation of cadmium level could be linked to the permanent presence of upwelling in this area. However, mercury concentration in Lévrier Bay was low in ours samples. The considerable variation between ours finding and others previous studies. in Mauritania coast (Legraa et al. 2019; Bilal 2014) can probably be linked to the sampling points that differ in this study compared to previous works.

3.1. Relationship between the trace metals

Figure 2 shows a relatively high positive correlation between Zn and Pb and moderate correlation between zinc, lead and copper, then these correlations indicate a possible common source of the elements from industrial and/or urban activities as well as comparable behavior in the sediment. The percentage of the eigenvalues relative to the variables Zn, Cu and Pb are well projected on Axis1, because it 66.25% of information. However, Cd is well represented on Axis 2 and constitutes 18,12% of information; the source of which can be attributed to other origins.
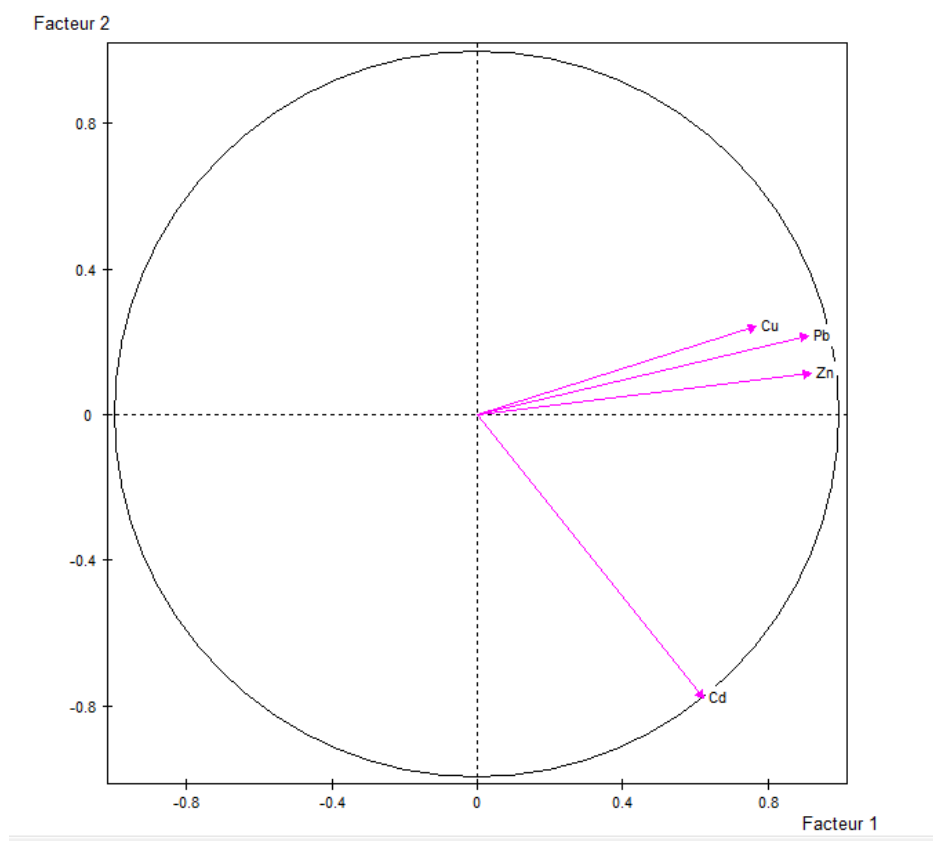

Fig. 2. PCA between the variables (trace metals: Zn, Pb, Cu and Cd)
in the surface sediments of the Lévrier Bay

3. 2. Seasonal variations

The ANOVA test showed the absence of significant ($P > 0, 5$) seasonal variations in the metallic elements analyzed in the sediments at all the sites studied (**Table 4**).

ANOVA analysis of variance of the elements studied (ZN, Pb, Cu et Cd)

Metal	Cd	Pb	Cu	Zn
P. value seasons	0,219	0,076	0,217	0,123

Although the ANOVA applied between metallic elements, sites and seasons did not give rise to a significant season effect because this statistical analysis used the cumulative average concentrations; nevertheless, in all the sites studied, zinc displayed in hot season its highest contents of all the elements analyzed and its lowest values in cold season (**Fig. 3**). For the other elements, the highest values were also encountered in the hot season and the lowest values of the metals analyzed were recorded in the cold season for all studied sites, with the exception of Cd, which had its highest content in the cold –hot season. The high concentrations of Zn observed at PM during the cold season may be due to intensive ore shipping activities during this period.
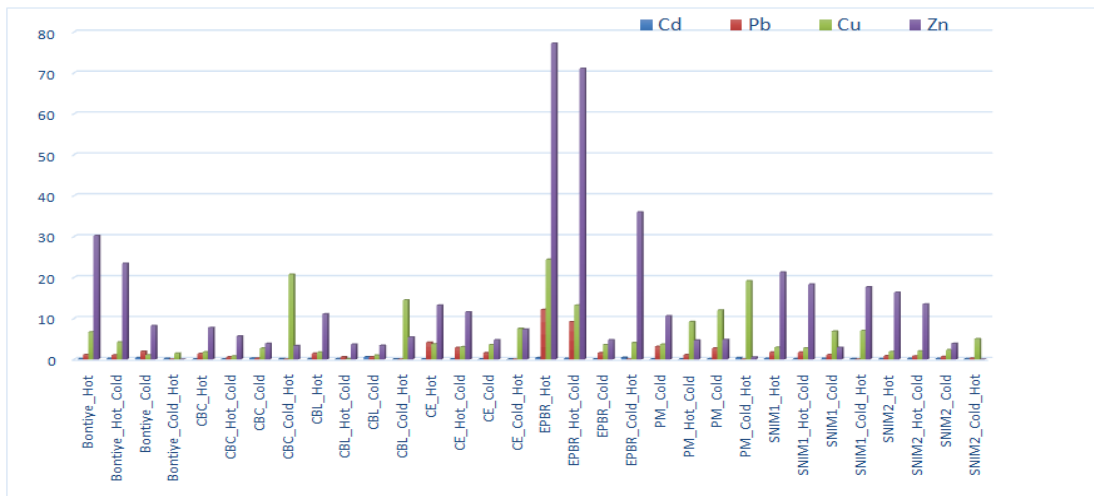
Fig. 3. Variations in trace metals by site and by season.

3.3. Comparison with previous studies carried out on the Mauritanian coast

For comparison, the concentrations found for Pb, Cu and Zn in the sampling sites of the present study remain higher than those found by other authors in previous studies carried out on the Mauritanian coast for the same elements (Legraa et al, 2019 ; Bilal, 2014).This may be due to the absence of industries and infrastructures at the sites sampled in previous studies, unlike those in this work, the sediments of which were collected in areas close to industries that could be sources of elements cited. Moreover, the concentrations of Cd recorded in the present work are similar to those found in the works carried out on the Mauritanian coast, with the exception of certain high contents of this element encountered in Iwik and Mamghar (Banc d'Arguin), which could be linked to the permanent presence of upwelling in this area.

3.4. Comparison with international standards

Spain and France are among the various countries' signatories to the Oslo Convention for the Guide values proposed for trace metals (Alzieu et al. 1999). Environment Canada (CCME, 1999), whose ELP is the concentration above which harmful effects are expected to occur frequently and the ISOGS is a quality guideline value. The comparison between the average concentrations of trace metals in this study and those proposed by the international standards relating to the toxicity of metals in surface sediments showed that all the values recorded for trace metals in all the sites of the present work are less than those recommended by these standards (**Table 5**).

Table 5.
Comparison of the average concentration values of the present study with the proposed guideline values for trace metals (mg / kg) in certain countries which are signatories to the Oslo Convention. (Alzieu et al. 1999) and with international standards

	Standard				Present study							
	Spain	France	Canada environment (CCME, 1999)		EPBR	CE	BONT	PM	CBC	SNIM1	CBL	SNIM2
			PEL	ISOGS								
Cd	1 to 5	0,2-2,4	4,2	0,7	0,265±0,078	0,04±0,014	0,225±0,053	0,142±0,084	0,11±0,054	0,137±0,030	0,202±0,126	0,147±0,012
Pb	120-600	20-40	112	30,2	5,7±2,924	2,125±0,880	1,017±0,393	1,722±0,719	0,555±0,306	1,135±0,401	0,647±0,294	0,637±0,126
Cu	100-400	26-36	108	18,7	11,284±4,903	4,434±1,028	3,337±1,319	11±3,214	6,505±4,760	4,862±1,180	4,317±3,400	2,775±0,745
Zn	500-3000	140-200	271	124	47,245±16,835	9,185±1,939	15,445±6,906	5,137±2,072	5,105±0,995	15,035±4,131	5,85±1,774	8,397±3,869

4. CONCLUSION

The five metals (Zn, Cu, Pb, Cd and Hg) were detected in our samples and their concentrations in sediment were generally heterogeneous and vary according to the metal analyzed and the sampling site, where Zn showed the high value recorded among all metallic elements, according to the order Zn > Cu >Pb> Cd >Hg.

The metallic elements analyzed displayed significant seasonal variations for certain studied sites; however, the use of ANOVA did not show any seasonal effect.

Indeed, the present work shows high average concentrations of the metals studied in the surface sediments than those found for the same metallic elements in recent previous studies at the Lévrier Bay, which due to the absence of important sources in metals at the sampled sites in previous work.

Furthermore, the average concentrations of the metals studied in this work are all below the average values of the international standard guideline relating to the toxicity of surface sediments. However, the high concentrations of metals at the EPBR and BONT sites compared to those found for the same elements at the other sampling sites could be explained, on the one hand, by the increased presence of artisanal canoes and coastal vessels at EPBR level (home port), and by the presence of all fishmeal and fish oil production plants at BONT on the other hand, which discharges may be the source having contributed to the elevation of the trace metals at these two spaces.

R E F E R E N C E S

Alzieu, C. (Ed.) (1999). Dragages et environnement marin : état des connaissances. *IFREMER*: Plouzané, France, 223 p.

Belin, C. & Le Gal D. (2005). Mission pour l'évaluation du réseau de surveillance sanitaire du milieu marin en Mauritanie et pour l'expertise du système d'analyse des toxines mis en place par l'IMROP. *Rapport, IFREMER*, 38 p.

Bilal, S. (2014). Contribution à l'étude de la qualité des eaux du Banc d'Arguin (Mauritanie) : Dosage des métaux lourds chez le Mollusques (Anadara Senilis), le Poissons Tilapia (Sarotherodon melanotheron) et dans le Sédiment. Thèse de Doctorat. Faculté des Sciences de Kénitra. Université Ben TOFAIL,Maroc, 160p

Bowen, H.J.M. (1966). Trace Elements in Biochemistry. *Academic Press, London*, 241 p.

Dartige, A.Y. (2006). Teneur en métaux lourds (Cadmium, Zinc, Fer et Cuivre) de la moule *Perna perna* prélevée dans la Baie du Lévrier (Mauritanie). *Thèse, Univ. Libre de Bruxelles* (VUB), 120 p.

Dartige, A.Y., & Ould Dedah, S. (1996). Etat des connaissances sur la pollution marine en Mauritanie. *Proceedings of the INOC Workshop*, 7p.

Diop, C., Dewaele, D., Diop M et al. (2014). Assessment of contamination, distribution and chemical speciation of trace metals in water column in the Dakar coast and the Saint Louis estuary from Senegal, west Africa. *Mar Pollut Bull* 86:539–546.

Diop, C., Dewaele, D., Toure, A & al. (2012). Study of sediment contamination by trace metals at waste water discharge points in Dakar (Senegal). *J. Water Sci*. 25 (3), 277–285.

Dubrovin B., Mahfoudh, M., &Dedah, S. (1991). La ZEE Mauritanienne et son environnement géographique et hydroclimatique. *Bulletin CNROP*, 23, 227p.

Fraga, F. (1973). Oceanografia química de la región de afloramiento del noroeste de Africa .*1. Resultados Expediciones Científicasdel Buque Oceanográfico Cornide de Saavedra 2* : 13-52.

IMROP. *(2019).* Institut Mauritanien de Recherches Océanographiqueset des Pêches ; *Rapport de synthèse du Neuvième édition du groupe de travail* : "Aménagement des ressources halieutiques et gestion de la biodiversité au service du développement durable » .9 p.

Kaimoussi, A., Chafik, A., Mouzdahir, A., & Bakkas, S. (2000). Les métaux lourds dans les sédiments superficiels de la cote littorale de la région d'El Jadida et de l'estuaire d'Oum R'bia (MAROC). *bull. Inst. Natn. Scien. Tech. Mer de Salammbô*, vol. 27.

Legraa, M. H., Erraoui, H., Dartige, A. Y., et al. (2019). Assessment of metallic contamination of the northen Atlantic coast of Mauritania (Coastal fringe "Lévrier Bay"), using *Perna perna*. International *Journal of Civil Engineering and Technology (IJCIET).* Volume 10, Issue, pp. 782-795.

Legraa, M. H., Mohamed Saleck, A., Dartige, A. Y., et al. (2019). Assessment of metal contamination in coastal sediments of the Lévrier Bay area, Atlantic Ocean, Mauritania. *GeographiaTechnica*, Vol. 14, Issue 1, pp 65 to 81.

Liang, C.P., Liu, C.W., Jang, C.S., Wang, S.W., Lee, J.J., (2011). Assessing and managing the health risk due to ingestion of inorganic arsenic from fish and shellfish farmed in black foot disease areas for general Taiwanese. *J. Hazard. Mater*. 186, 622–628.

M'Hamada M., Ould Mohamed Cheikh M., Dartige A., Erraioui H, (2011). Etat de la contamination des côtes atlantiques de Nouadhibou par les métaux lourds (Mauritanie). *Conférence Méditerranéenne Côtière et Maritime*. EDITION 2, Tanger, Maroc.

Manriquez, M., Fraga, F. (1982). The distribution of water masses in the upwelling region off Northwest Africa in November. *Rapp. P.-v. Réun. Cons. int. Explor. Mer*, 180. P. 39-47.

Memet, V. (2011). Assessment of heavy metal contamination in sediments of the Tigris River (Turkey) using pollution indices and multivariate statistical techniques. *Journal of Hazardous Materials*. 195, 355–364.

Odin, M. (1995). Transferts des dérives du mercure et du cadmium entre les sédiments ou la colonne d'eau et les larves d'Hexageniarigida (Ephéméroptères), en fonction des conditions expérimentales (température, photopériode, pH et nature du sédiment). *Doc. Univ. Bordeaux* I .273 p.

Organisations Liste par pays (Mauritania) :
https://webgate.ec.europa.eu/sanco/traces/output/non_eu_listsPerCountry_fr.htm.

Ould Dedah, S. (1993). Wind, surface water temperature, surface salinity and pollution in the area of the Banc d'Arguin, Mauritania. *Hydrobiologia* 258, 9–19 -

Pichard, A., Bisson, M., Houeix, N., & al. (2005). Fiche de données toxicologiques et environnementales des substances chimiques. *INERIS*. Cuivre et ses dérivés.66P.

Sidoumou, Z., Romeo, M., Gnassia-Barelli, M., Nguyen, P., Caruba, R. (1992). Détermination de la qualité des eaux du littoral mauritanien par la mesure des métaux traces chez les mollusques Donax rugosus et Venus verrucosa*. Hydroécol. Appl., Tome 4, Vol 2,* pp 33-41.

UICN/BRAO (2008). Evaluation de l'efficacité de la gestion des Aires protégées : parcs et réserves de Mauritanie.

USEPA. (2002). Methods for Measuring the Acute Toxicity of Effluents and Receiving Waters to Freshwater and Marine Organisms. fifth ed. U.S. Environmental Protection Agency, Office of Water, Washington.

Wagne M.M., Dartige A., Sefrioui S., Zamel M.L., Tounkara H. & Bah M.L., 2013. Utilisation de la moule *Perna perna* en biosurveillance du cadmium et du plomb dans les eaux de la baie du Lévrier, Mauritanie. *Journal des Sciences Halieutique et Aquatique* 7:287-295.

Wagne, M. M., Brahim, H. O., Dartige, A., & Séfrioui, S. (2011). Contribution à l'étude du phytoplancton potentiellement nuisible de la baie du Lévrier (Mauritanie). *Bulletin de l'Institut Scientifique, Rabat, section Sciences de la Vie, n°33(2)*, p. 31-41.

Zamel, M. L et al. (2010). Suivi de la qualité du milieu marin et identification des sources de pollution des côtes mauritaniennes (Baie du Lévrier et le Sud du Cap Blanc).*Tunisian Journal of Medicinal Plants and Natural Product, pp30-36*

THE ATMOSPHERIC DYNAMIC EXTREME OF TROPICAL AS AN ANALYSIS OF CLIMATE CHANGE IN INDONESIA

Rahmat GERNOWO[1]* , Catur Edi WIDODO[1] , Aris Puji WIDODO[2]

ABSTRACT:
Variability of rainfall, especially in tropical regions like Indonesia has been an important issue that needs to be studied to find out the effect caused. The phenomenon of the occurrence of a flood is more indicated by the heavy rains fall in the region of Jakarta for a few days. This research aims to analyze the characteristics of heavy rain through the approach of atmospheric dynamic anomaly using the WRF model. The method used in this research was Weather Research and Forecasting (WRF) using the scheme of Kain Fritsch's cumulus parameter. The method of this research was applied to the occurrence of the most extreme rainfall of the data from 2007 and 2015 in Jakarta. The analysis result shows that the extreme rainfall was caused by the growth of rail clouds type of Cumulonimbus. The analysis of atmospheric dynamics and the numeric calculation shows that there has been a growth of extreme rain clouds above Jakarta skies indicating the occurrence of climate change.

Key-words: Flood, Could dynamics, Satellite image, Climate change, Cloud model

1. INTRODUCTION

Indonesia is a country located in the equator line which astronomically is located between 6 NL - 11 SL and 95 EL - 141 EL. Such location makes Indonesia become a wet tropical country with sufficiently high rainfall. The phenomenon of extreme rainfall is caused more by climate change occurrence, i.e. the occurrence of climate change compared to its long-term average in a certain time. The climate deviation usually comes from non-seasonal climate factors such as the phenomenon of ENSO (El Nino Southern Oscillation).

During ENSO, the transition season starts from rain and drought. In terms of atmospheric dynamics, this is caused by heating of the ocean in the Pacific Ocean region and it occurs annually. It occurs because of Sea Surface Temperature arising between the West and East Pacific Ocean (Aldrian, 2008). The phenomenon of ENSO occurs globally from the sea atmospheric interaction system in the Pacific Region. The influence of ENSO in each region in Indonesia, in general, occurs during the transition season (Siswanto, et al., 2015).

Based on the event of floods occurring from 2002 to 2020 (**Table 1**), there have been four heavy floods in Jakarta, i.e. on 26th January - 1st February 2002, 4th-14th February 2007, 15th-24th January 2013, and 9th-12th February 2015, and 31st December - 2nd January 2020. Precursors of flood in Jakarta were mainly caused by extreme rainfall, land subsidence, and the contribution of the rising sea surface level (Sakurai et al., 2005, Abidin et al., 2015).

Based on the above research and the data of flood occurrence, it has been important to discuss the comparison of analysis of clouds growth, extreme rainfall, and flood occurrence in Jakarta in the maximum extreme time within the period of 2007 to 2015 seen based on the effect of the inundated width. The analysis of the heavy flood historical atmospheric dynamic in Jakarta becomes the evidence that climate change is happening.

[1]Physics Department, Faculty of Sciences and Mathematics, Diponegoro University, Semarang, Indonesia,
gernowo@yahoo.com, catur.ediwidodo@gmail.com
[2]Informatics Department, Faculty of Sciences and Mathematics, Diponegoro University, Semarang, Indonesia,
arispw@gmail.com

Extreme rainfall data and affected areas in Jakarta.

Date of Occurrence	2 February 2002	2 February 2007	17 January 2013	11 February 2015	1 January 2020
Highest Rainfall (mm/day)	168	340	100	277	377
RW Flooded	353	955	599	702	390
Flooded Area (km^2)	168	455	240	281	156
Strategic Area	Yes	Yes	Yes	Yes	Yes
Number of Refugees	154.270	276.300	90.913	45.813	36.445
Low tide> 95% inundation (days)	6	10	7	7	4
Data Source; BPBD, Bappenas, BMKG, Open Data Jakarta					

2. STUDY AREA AND DATA

This research area, including the Jakarta and surrounding areas affected by flooding in 2007 and 2015. As shown in **Fig.1** is a morphological map of the Jakarta area which is implemented from the scaling of the terrain height (m).
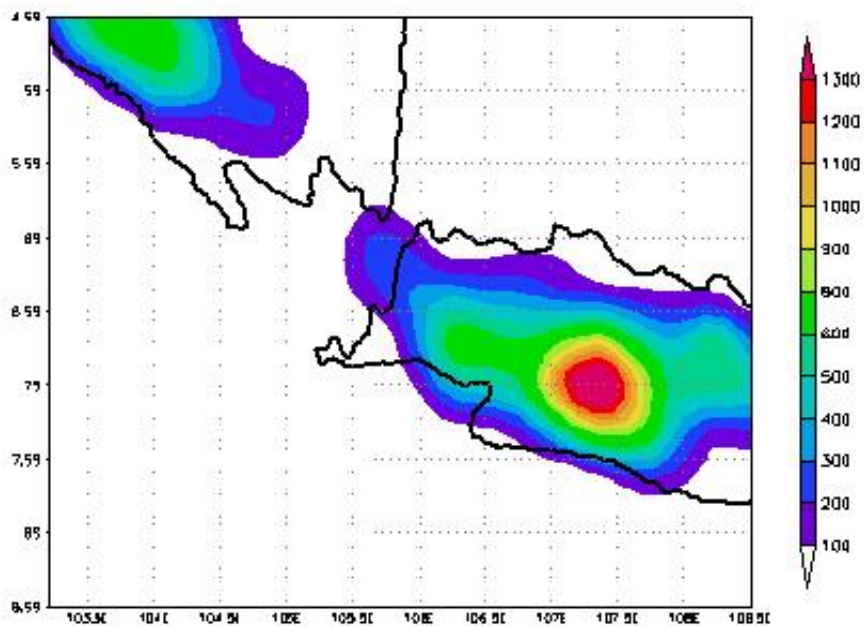
Fig. 1. Topographic map of the study area based on the results of Terrain height (m).

2.1. Data Global

As mentioned above, as the data input on the WRF model, FNL (Final Global Data Assimilation System) data is needed, it constitutes operational data from National Centres for Environmental Prediction (NCEP). Data NFL is located at 90 NL - 90 SL, 0 EL - 360 E with the resolution of 1^O x 1^O, with the format data is WMO GRIB1 data available for about 6 hours for 00Z, 06Z, 12Z, and 18Z every day.

A preliminary simulation was carried out to see the pattern of convection growth and the pattern of rainfall when extreme rainfall 2007 and 2015 occurred. Simulation regions were divided into three domains; domain 1 resolution 30 km, domain 2 resolution 10 km, domain 3 resolution 5 km. Domain 1 and 2 used 2 direction nesting, while domain 3 ran separately (offline nesting). micro-physics parameterization scheme determination was carried out using the WRF scheme of Single-Moment 6-Class (WSM6) (Hou et al., 2016). This was carried out based on the previous research and the convection process assumption could be determined by the micro-physics process.

2.2. Sonde Data Radio and Other Data

Determining the limit required and the preliminary requirements are highly necessary, therefore, the result obtained was the pattern representing the condition of the research area, in this case Jakarta. Preliminary treatment from FNL data to obtain limit requirement and preliminary requirements that go along with Jakarta, i.e. by validating FNL data with radiosonde.

Radiosonde data representing Jakarta was obtained from BMKG (Meteorology Climatology and Geophysics Council) observation station, Cengkareng-Jakarta (-6, 110 SL - 106,650 EL), within the duration of January-February 2007, and January-February 2015. Other data used in this research covered weather data within a daily period for January-February 2007 and 2015.

3. METHODOLOGY

3.1. Weather Research and Forecast Model

WRF Model has developed an advanced generation of forecasting models of mesoscale assimilation systems to help to understand and forecast the mesoscale system about the rain. WRF model is the newest model developed from model MM5 (Mesoscale Model 5) applied in various issues and it covers some advantages such as (Skamarock, et al., 2005):

1. The model uses vertical coordinate following the terrain, hydrostatic pressure with constant pressure surface peak model with grid horizontal from Arakawa.
2. The model is compatible either for ideal application or real data with various choices of the lateral condition and upper limit.
3. Micro physics calculation
4. Parameterization of cumulus.

The basic equation on the atmospheric circulation model consists of a partial differential equation, for the completion of the dynamic issue. Several input variables are wind velocity component u and v, temperature T, specific moisture q, and surface pressure ps.

Hydrostatic equation

$$\frac{\partial \Phi}{\partial \eta} = -\frac{R_d T_v}{P} \frac{\partial p}{\partial \eta} \tag{1}$$

Thermodynamic Equations

$$\frac{\partial T}{\partial t} = -\frac{u}{a \cos \theta} \frac{\partial T}{\partial \lambda} - \frac{v}{a} \frac{\partial T}{\partial \theta} + \frac{k T_v \omega}{(1 + (\delta - 1)q)p} + P_T + K_T \tag{2}$$

Moisture equations

$$\frac{\partial q}{\partial t} = -\frac{u}{a \cos \theta} \frac{\partial q}{\partial \lambda} - \frac{v}{a} \frac{\partial q}{\partial \theta} - \eta \frac{\partial q}{\partial \eta} + P_q + P_q \tag{3}$$

Equation continuity

$$\frac{\partial}{\partial \eta}\frac{\partial p}{\partial t} + \nabla.\left(V_h \frac{\partial p}{\partial \eta}\right) + \frac{\partial}{\partial \eta}\left(\eta \frac{\partial p}{\partial \eta}\right) = 0 \qquad (4)$$

Definition of ξ

$$\xi = \frac{1}{a\cos\theta}\left(\frac{\partial v}{\partial \lambda} - \frac{\partial}{\partial \theta}[cos\theta u]\right) \qquad (5)$$

$$\text{And } E = \frac{1}{2}(u_2 + v_2) \qquad (6)$$

Where $\Phi(= gz)$ is a geopotential factor, $f = 2\,\Omega sin\theta$ the Coriolis parameter, Ω is the angular velocity, a is the radius of the earth, $T_v = (1 + (\varepsilon - 1 - 1)q)$, T is a virtual temperature, R_d is the gas constant for dry air, R_v is the gas constant for water vapor, $k = R_d/C_{pd}$ with C_{pd} is the specific heat for dry air at constant pressure, $\delta = C_{pv}/C_{pd}$ with C_{pv} is the specific heat for dew air at constant pressure and ω is the velocity of vertical pressure.

4. RESULTS AND DISCUSSIONS

Atmospheric dynamic analysis of extreme rainfall event in Jakarta was caused by weather anomaly change, the existence of MJO (Madden Julian Oscillation) periodicity and IOD (Indian Oscillation Dipole) which were the dominant effects as flood precursor (Aldrian, 2008), in the period of 2007 and 2015, however, from the climate analysis data showed growth to the dominant direction (Report BMKG, 2015).

A low-pressure anomaly occurred in Indies Ocean as shown in (**Fig. 2**) was the characteristics of a flood event on 11th February 2015 (**Fig. 2a**) and 2nd February 2007, like in (**Fig. 2b**). From the streamline map, it could be seen that there was convergence and wind divergent area (shoreline), this triggered the growth of convective clouds that could produce heavy rain in the areas of wind meeting. Such low-pressure synoptic effect dominated the occurrence of extreme rainfall, therefore, extraordinary rainfall that caused a flood in 2015 and 2007 in Jakarta was dominated by a local factor of clouds growth. Regional factor showed Asian cold monsoon that had been active, vibrant that triggered the formation of rain clouds which had the potential to occur in Java island in general and specifically in Jakarta (Gernowo et al., 2017, Masouleh et al., 2019).
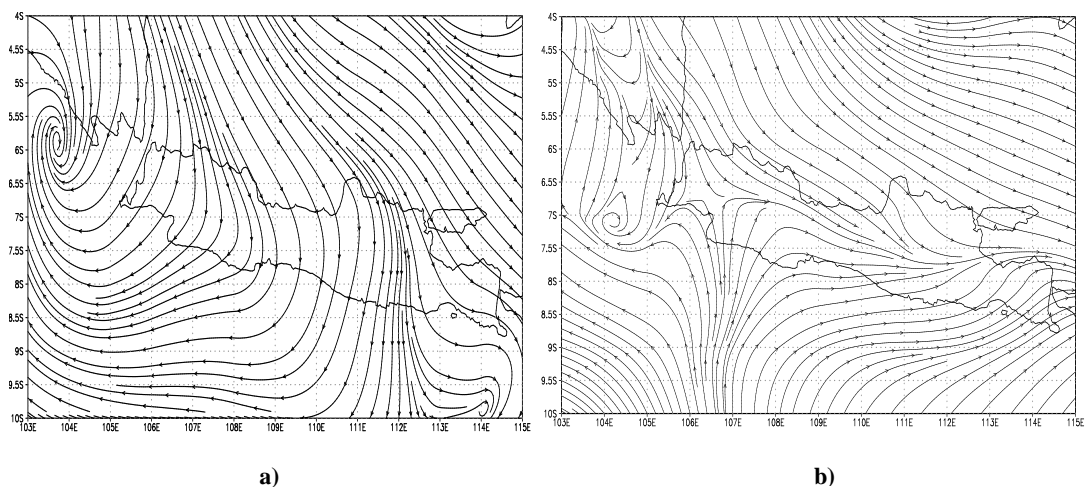

a)   b)

Fig. 2. The wind (vortex) is from 9th to 12th February 2015 – **a**),
the wind (vortex) is from 25th January to 5th February 2007 – **b**).

This study was analyzed based on data AVN from 9th to 12th February 2015, and from 25th January to 5th February 2007, in Jakarta. The 2007 analysis was based on the previous result (Gernowo et al., 2018, Hidayat et al., 2017 and Diaz et al., 2001), as for the analysis in 2015 based on BMKG data (Report BMKG, 2015). Absolute vorticity on 11th February 2015, between the Java Sea and Indies Ocean, there had been negative vorticity anomaly in Java island and it ended on 12th February 2015. It proved that tropical convection activities in the ocean were more active with sufficiently big variations. (Roxana and Wajsowicz, 2005, Roy et al., 2019, Siswanto et al., 2015).

Vorticity anomaly dynamic in February 2015 became maximum in Java on 11th February 2015 and ended on 12th February 2015. Then on 1st February 2007, negative vorticity anomaly occurred in several parts of Java and ended on 2nd February 2007 as shown (in **Fig. 3a** and **Fig. 3b**). This proved that tropical convection activities above the ocean were more active with big variation compared to the land especially in Jakarta (Masouleh et al., 2019 and Aldrian, 2008). Local atmospheric circulation caused the clouds' growth patterns in Jakarta. It showed that the change of anomaly of convection clouds growth in February 2015 and February 2017 was influenced by local atmospheric dynamics, regionally and globally caused by climate change effects.
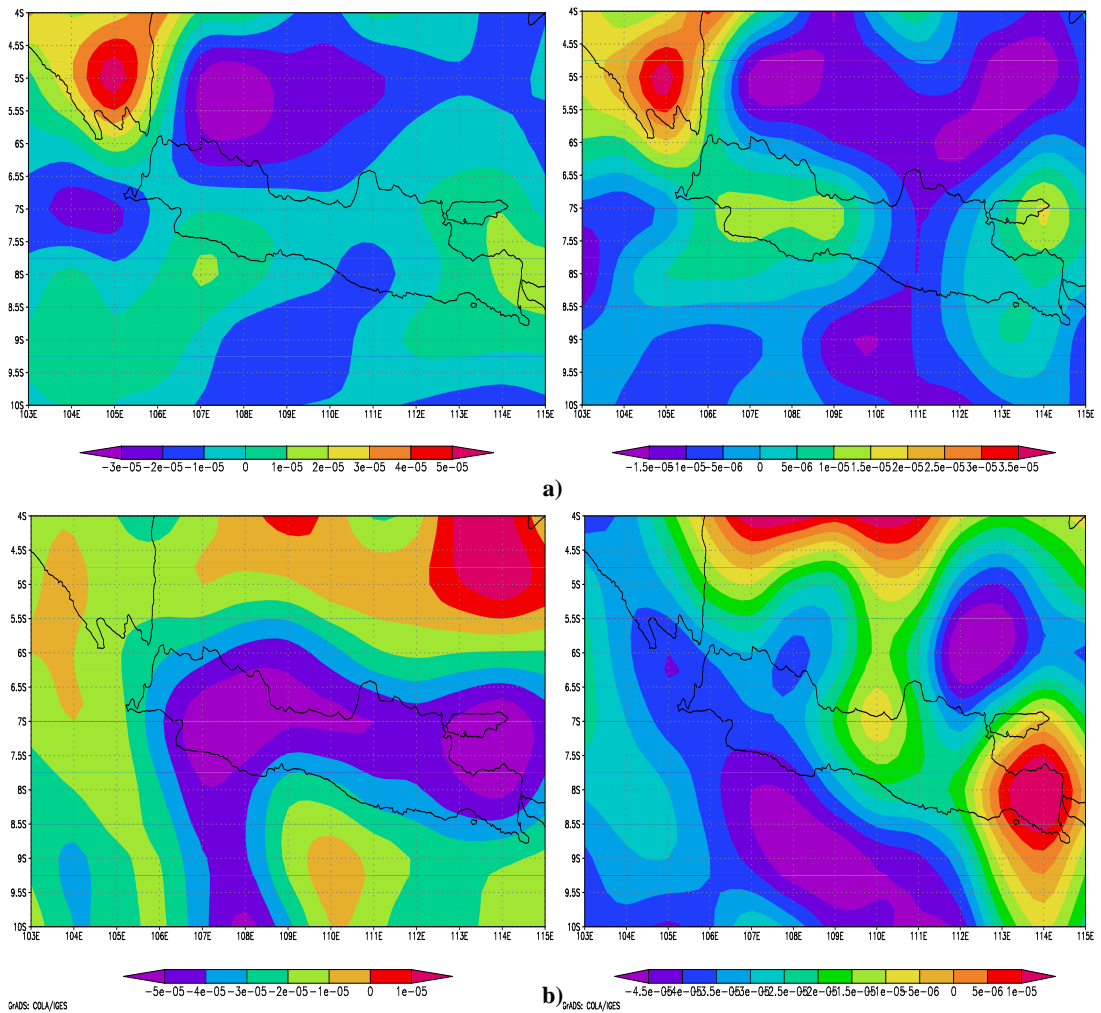
Fig. 3. Wind divergence of DKI-Jakarta on 11th February 2015 and 2nd February 2007 – **a)**, absolute Vorticity [m/s] of DKI-Jakarta Date on 11th February 2015 and 2nd February 2007 from data NCEP/NCAR – **b)**.

4.1. Analysis Model Weather Regional Forecast (WRF)

The atmospheric dynamic numeric analysis is quantitative simulation research to explain the occurrence of extreme rainfall in January/February 2007 and 2015 in the event of a flood in Jakarta. In this research WRF modelling System version 2 was used, non-hydrostatic regional scale or mesoscale model (Skamarock, 2005, Thompson et al., 2016). The application technique of model WRF, first was determining domain area, this was to carry out downscaling of the research area (Skamarock et al., 2005). The application of the model in this research covered the microphysics process, cumulus parameterization, the selection width, or area of research region was meant to obtain a sufficiently realistic result representing the actual condition. In determining the limit of the research area, three nesting stages were used to downscale the data global NCEP-FNL, this was to reach the clouds' growth within the radius of 3 km to horizontal direction connecting the smallest region. The simulation process of domain 1 and 2 was carried out at the same time within a single WRF model system, as for domain 3, it was carried out using Ndown.exe command from model WRF. The resolution of the three domains, i.e. domain 1 with resolution 30 km, domain 2 with resolution 10 km, domain 3 resolution 5km. The domain region of the simulation could be seen in **Fig. 4**.
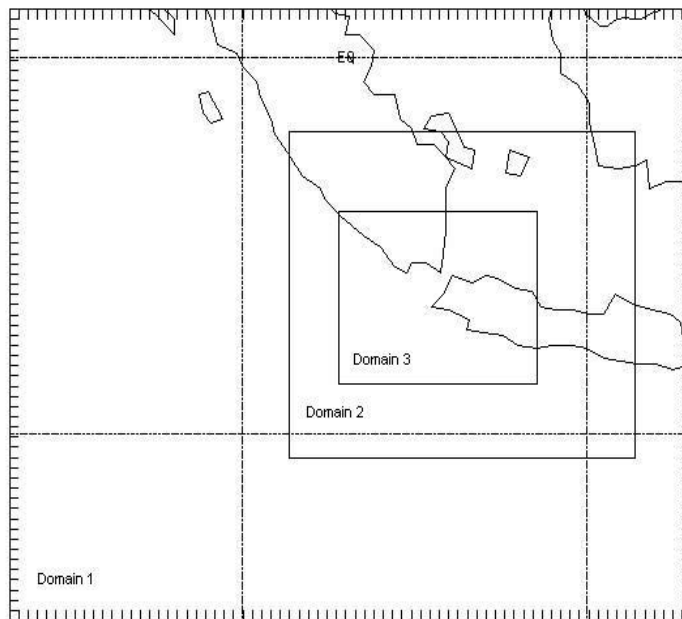
Fig. 4. Downscaling the research area into 3 domains.

4.2. Limit Requirements and Initial Requirement Model

The determination of the initial condition and limit condition in a model is very important since it will determine the output validity produced. The initial input data functions as the initial condition and limit condition used for the WRF model were determined from the FNL data, data validity was carried out through the treatment of comparing FNL data with upper air measurement (radiosonde) in the chosen station. Variable compared including air component of u and v in m/s and the temperature in ^OK (degree Kelvin) as shown in **Fig. 5**., it showed the profile of radiosonde data vertical and FNL on 2nd February 2007, at 00 UTC and 11th February 2015, which had not been filtered. Data from the radiosonde Cengkareng Station with the assumption representing the research region of Jakarta.

The comparison of two vertical profiles in **Fig. 5a** and **Fig. 5b** showed the assimilation process of FNL data with radiosonde data. It showed that data assimilation had succeeded to be done so that radiosonde data was included in FNL data, meanwhile, to obtain a radiosonde data filtered process, filtering could be done. There were some options of filtering presented in the WRF model, Fang's research, (2006) using the Lancos filter to obtain a good result.

a)

b)

Fig. 5. Validation of wind V (m/s) and U (m/s) and Temperature (K) FNL data with radiosonde data Cengkareng-Jakarta station data on 2[nd]February 2007 at 00 UTC – **a)**;
validation of wind V (m/s) and U (m/s) and Temperature (K) FNL data with radiosonde data of Cengkareng-Jakarta station data on 11th February 2015 at 00 UTC – **b)**.

4.3. Cloud Simulation

To see the pattern of clouds growth, the QCLOUD model was used to calculate the clouds in the WRF model. From the result of model simulation for horizontal clouds (**Fig. 6**.) it could be analyzed that the maximum condition occurred after the da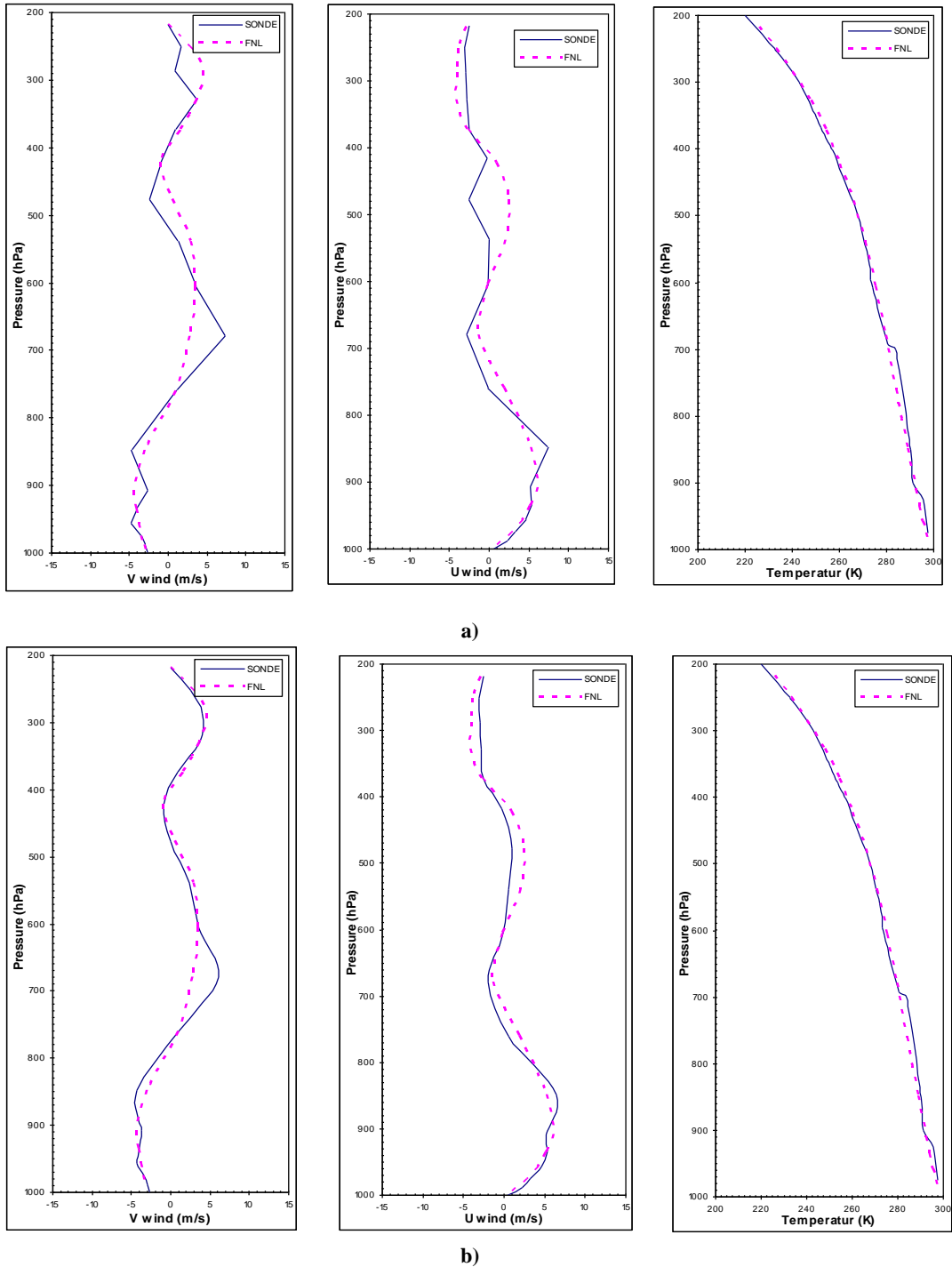ta on 2nd February 2007, at 00 UTC and 11th February 2015, as a model in entering the data. The growth of convective clouds would produce convective rainfall produced from the convection current for the surface heating by sunlight radiation, wind convergence, or because of updraft physical drive when the wind passed through the mountainous area. Convective rainfall had high intensity compared to stratiform rainfall, it occurred in a limited space scale between 10-20 km2 depended on the convection cell dimension itself (Cooley et al., 2007, Gernowo, 2018). In the tropical area, the occurrence of convective clouds and convective rain was very dominant, for the land area, it happened in the afternoon while for convection maritime area, it occurred at noon supported by sea convection during the night.
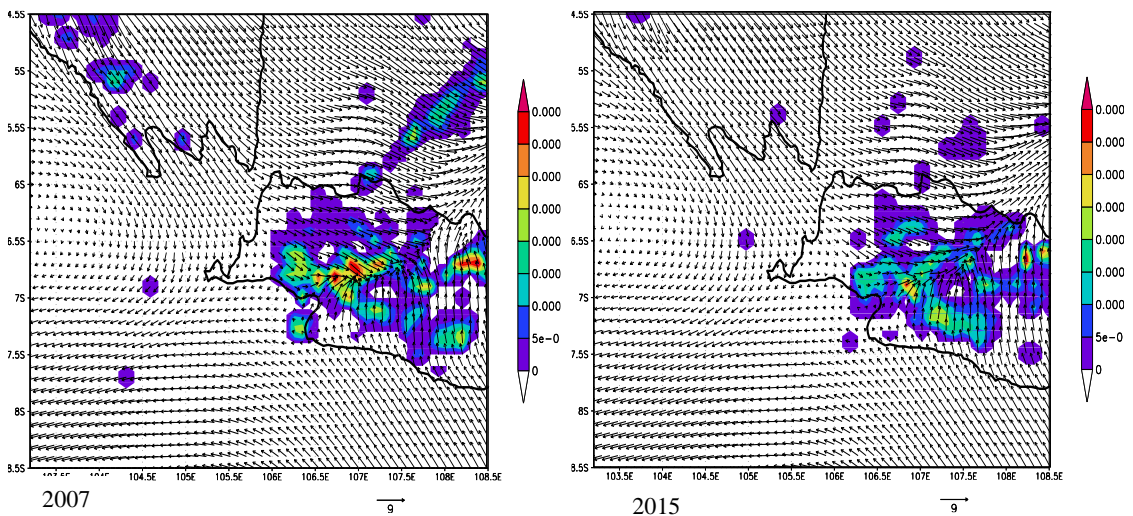
Fig.6. Horizontal rain cloud simulation (kg/kg) data for 2nd February 2007, and 11th February 2015, at 00 UTC Convective cloud growth patterns occur above Jakarta and its surroundings.

The Cloud simulation result for Jakarta region showed high growth, it indicated the occurrence of high-intensity rainfall. The pattern of this growth showed that the period of extreme rainfall on 2nd February 2007, and 11th February 2015, were caused more by local atmospheric dynamic influence, i.e. the existence of thermal convection anomaly. Another analysis for this case was the occurrence of sea-land wind circulation that would boost the development of convection cells above the beach of Jakarta that had the potential to produce heavy rain. Based on the above analysis from the atmospheric dynamics and numeric clouds simulation, showed that the flood disaster around Jakarta and the tropical area was generally caused more by the growth of extreme convective clouds. This became obligatory to enter climate factors in every plan of natural disaster countermeasure as well as generally in the sustainable development plan especially in the tropical area (Prasetyo et al., 2018).

5. CONCLUSIONS

The occurrence of extreme rainfall in Jakarta region from the explanation that had been conveyed, it could be concluded that the extreme weather event that caused a huge flood in February 2007 and 2015 was influenced by various regional and local meteorological factor. Also, weather disturbance causing the occurrence of heavy rain and flood was caused by mechanical and thermal weather disturbances. Where mechanical condition meant was the convergence of under layer, while this

thermal factor was signed by the existence of advection of cold air from Asian land or what was known as Cold Surge.

Based on the analysis of FNL data numeric and radiosonde, in Jakarta in 2007 and 2015, based on the model review, it showed the convective clouds growth result was quite extreme, FNL data scenario assimilating with radiosonde data in the area of study. The tendency of this atmospheric dynamic improvement effect in the tropical area indicated the occurrence of climate change.

ACKNOWLEDGMENTS

R E F E R E N C E S

Aldrian E. (2008) Dominant Factor of Jakarta's Three Largest Flood. *Journal Hidrosfer Indonesia*, **3**, 105-112.

Abidin H. Z., Andreas H., Gumilar I., and Wibowo I. R. (2015) On the correlation between urban development, landsubsidence, and flooding phenomena in Jakarta. *Proc. IAHS*, **370**, 15–20, 2015proc-iahs.net/370/15/2015/ doi:10.5194/piahs-370-15-2015.

Cooley,D., D.Nychka, and P. Naveau (2007) Bayesian spatial modeling of extreme precipitation return levels. *J. Amer.Stat.Assoc.*,**102**, 824–840, https://doi.org/10.1198/016214506000000780.

Diaz, H.F., M.P. Hoerling, and J.K. Eischeid (2001) ENSO variability, teleconnections, and climate change. *Int., J. Climatol*, **21**, 1845-1862.

Gernowo R., Adi K., Yulianto T., Seniyatis S., and Yatunnisa A.A. (2018) Hazard Mitigation with Cloud Model-based rainfall and Convective data. *Journal of Physics: Conference Series*, 1025 (1), 012023.

Gernowo R., Adi K., and Yulianto T. (2017) Convective Cloud model for Analyzing of Heavy rainfall of Weather Extreme at Semarang Indonesia. *Advanced Science Letter*, **23**(7), 6593-6597.

Hou T., Lei H., Yang J., Hu Z., Feng Q. (2016) Investigation of riming within mixed-phase stratiform clouds using Weather Research and Forecasting (WRF) model. *Atmospherics Research Journal*, **178-179**, 291-303.

Hidayat R., Juniarti M.D., and Ma'rufah U. (2018) Impact of La Niña and La Niña Modoki on Indonesia rainfall variability. *IOP Conf. Ser.: Earth Environ. Sci.* **149**, 012046

Masouleh Z.P., Walker D.J. and Crowther J.M. (2019) A Long-Term Study of Sea-Breeze Characteristics: A Case Study of the Coastal City of Adelaide. *J. Appl. Meteor. Climatol.* (2019) **58**(2), 385–400. https://doi.org/10.1175/JAMC-D-17-0251.1

Prasetyo Y., Yuwono B. D., and Ramadhanis Z. (2018) Spatial Analysis of Land Subsidence and Flood Pattern Basedon DInSAR Method in Sentinel Sar Imagery and WeightingMethod in Geo-Hazard Parameters Combination in NorthJakarta Region. *IOP Conf. Series: Earth and Environmental Science*, **123**, 012009.

Roxana C., and Wajsowicz (2005) Forecasting extreme events in the tropical Indian ocean sector climate. *Journal dynamics of atmospheres, and ocean*, pp. 1-15.

Roy I., Tedeschi R.G., and Collins M. (2019) ENSO teleconnections to the Indian summer monsoon under climate changing. *International Journal of Climatology*, **39** (6), 3031-3042.

Sakurai N., Murata F., Yamanaka M.D., Mori S., Hamada J.I., Hasiguchi H., Tauhid Y.I., Sribimawati T., Suhardi B. (2005) Diurnal Cycle of Cloud System Migration over Sumatera Island. *Journal of the Meteorological* , **83** (5).

Skamarock W.C., Klemp J.B., Dudhia J., Gill D.O., Barker D.M., Wang W., and Powers J.G. (2005) A Description of the Advanced Research WRF Version 2, Mesoscale and Microscale Meteorology Division, National Center for Atmospheric Research Colorado USA.

Siswanto, Geert J. V. O. B., Gerald V.D.S., Lende R.K., and Bart V.D.H. (2015) Trends in High-Daily Precipitation Events in Jakarta and Flooding of January (2014) *Special Supplement to the Bulletin of the American Meteorological Society*, **96** (12).

Meteorology Climatology and Geophysics Council (BMKG), Climate Analysis (2015) Progress report, https://www.bmkg.go.id/

Thompson G., Tewari M., Ikeda K., Tessendorf S., Weeks C., Otkin J., Kong F. (2016) Explicitly-coupled cloud physics and radiation parameterizations and subsequent evaluation in WRF high-resolution convective forecasts. *Atmospherics Research Journal*, **168**, 92-104.

INTELLIGENT TECHNOLOGY FOR ESTIMATING OF URBAN ENVIRONMENT QUALITY

Igor PATRAKEYEV[1] , *Victor ZIBOROV[1]* , *Oleksii MIKHNO[2]*

ABSTRACT:
During transiting to the post-industrial era the role of cities and urban environment functions are transformed. A new type of economic system imposes new requirements to the urban environment as a space for the population life and doing business. Today, on the basis of the concept of sustainable development, a general scientific paradigm of cognition is being formed as a result of the synthesis of sciences about nature, society and man. There are many approaches to the concept of sustainable development. The most modern concept, according to the authors of the article, understands of sustainable development, which is based on laws of the conservation of energy or power, as a general law of Nature. The article proposes a comprehensive approach based on the integration of the capabilities of modern GIS and intelligent technologies for estimating the potential, real and missed opportunities of the urban environment in the context of using incomplete and fuzzy information. The application of the proposed approach to estimating the sustainable development of the urban environment on the example of Ukrainian cities is shown.

Key-words: spatial database, knowledge base, fuzzy information, indicator of sustainable development, urban environment.

1. INTRODUCTION

In the last decade, the problem of using intelligent technologies in the study of sustainable urban development has acquired particular importance. This is due to the strengthening of the role of information and communication channels in the world in general and with the actualization of the introduction of information technology in the legal field of state and municipal management. At one time, Aristotle argued that human society governance is a major component of the development process.

The transition to a new paradigm of sustainable development is discussed at international conferences under the auspices of the United Nations since 1999 (Bolshakov & Kuznetsov, 2010). This paradigm provides for a constant increase in free energy. In modern models of sustainable development the capacity is used as a measure of development of the system (Bolshakov & Ryabkova, 2009; Hasanova et al., 2019; Patrakeyev et al., 2017).

There are three groups of system capabilities with a measure of power (Bolshakov, 2007; Newman, 2004). The first group is a potential. It is determined by the measure of full input power to the system. The second group is a real possibility. It is defined as the useful (active) power output of the system. The third group is a lost opportunity. It is determined by the amount of power, which losses on the system output.

It should be noted that to ensure decision-making on sustainable development management, it is necessary to estimate the potential, real and missed opportunities of the urban environment. This estimation is based on the receipt and processing of non-numeric, inaccurate and incomplete information (Shtovba et al, 2016). Non-numeric, inaccurate and incomplete information on the condition of such complex system as the urban environment is used to obtain an integrated estimation

---

[1]*Kyiv National University of Construction and Architecture, Faculty of Geoinformation systems and territory management technologies, 03037, Kyiv, Ukraine, ipatr@ukr.net; ziborov@ukr.net*

[2]*Taras Shevchenko National University of Kyiv, Faculty of Geography, 03127, Kyiv, Ukraine, almikhno@ukr.net*

of sustainable development based on the estimation of potential, actual and lost opportunities of the urban environment.

The aim of the article is to develop the intelligent technology for making decisions on managing the sustainable urban development based on potential, real and lost opportunities of the urban environment. Using the proposed intellectual technology, an integral estimation of the sustainable development of the urban environment and its individual subsystems, is obtained on Ukrainian cities Odessa and Kryvyi Rih. A comparison of the integrated estimations of sustainable development with the level of sustainable development of European cities is made (Sustainable Urban Metabolism for Europe, 2009).

2. CONCEPT OF SUSTAINABLE DEVELOPMENT OF URBAN ENVIRONMENT

Modern science of sustainable development is based on the fundamental laws of the real world. Modern research on sustainable development states that the laws of power conservation are the foundation of the science of sustainable development. A system is open if and only if it exchanges energy flows with the environment. A fundamental feature of open systems is the fact that the total flow N at the entrance to the system is equal to the sum of the active P and passive L (or loss) flows at the exit from the system (Bettencour et al., 2007; Bolshakov & Ryabkova, 2009; Yanitsky, 2013):

$$N = P + L = const, \qquad (1)$$

From the expression (1) it follows that the loss power (L) is under control of the total (N) and useful (P) powers. A decrease in loss power (L) can be achieved (assuming constant full power) only by increasing the net (P) power (productivity), which, in turn, depends on increasing the efficiency of using a full (N) power. That is connected with using modern innovative technologies, improving the quality of production, using renewable energy sources, optimizing the rotation of household and industrial waste, improving the safety of the population, increasing mobility population by improving public transport and more (Kennedy et al., 2015).

We define a set of subsystems of the urban environment that are most important to ensure the concept of sustainable development. Such subsystems may be (Acebillo, 2013; Giordano et al., 2014; Paola et al, 2016):

− transport subsystem, which provides the mobility of population;

− subsystem of city economy, which characterizes conditions of population comfortable life;

− socio-economic subsystem, that provides a healthy standard of living for the population.

The interaction scheme of considered subsystems of urban environment in accordance with expression (1) is shown in **Fig.1**. Supporting the life of urban environment is the circulation of substances. This energy is necessary for the vital activity of living organisms, as well as for the production of materials, substances, products, resources and services.

Each subsystem receives a certain amount of different types of energy, matter and information N(t). In this case, the subsystem produces two types of products. One type is negative production, it is determined by the loss stream L(t). The second type of product is used by each subsystem to ensure its own life, this is a flow of useful work P(t).

The information model of the interaction of city economy subsystem of the urban environment with the environment is shown in **Fig.2** (Acebillo, 2013). Indicators of the total flows of matter, energy, information, as well as indicators of the flow of losses and indicators of the negentropic flow of the subsystem of urban economy have a heterogeneous and multi-scale character.

For example, the real opportunity of the subsystem of urban economy is determined by such indicators of flows of matter, energy and information: the population density with dimensionality in person/ha; building density with dimensionality m^2/ha; building density coefficient with dimensionality m^2/ha; annual energy consumption for heating residential buildings with dimensionality MWh/year; annual water supply in residential buildings with dimensionality l/person; total electricity consumption in residential buildings with dimensionality kWh/year.
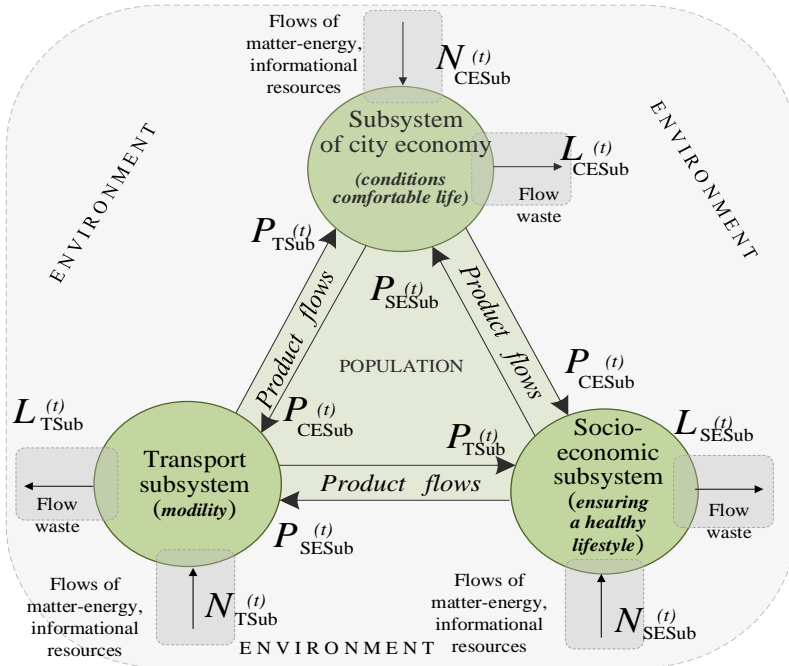
Fig. 1. Scheme of exchange of material resources, information and energy between the environment and subsystems of urban environment.
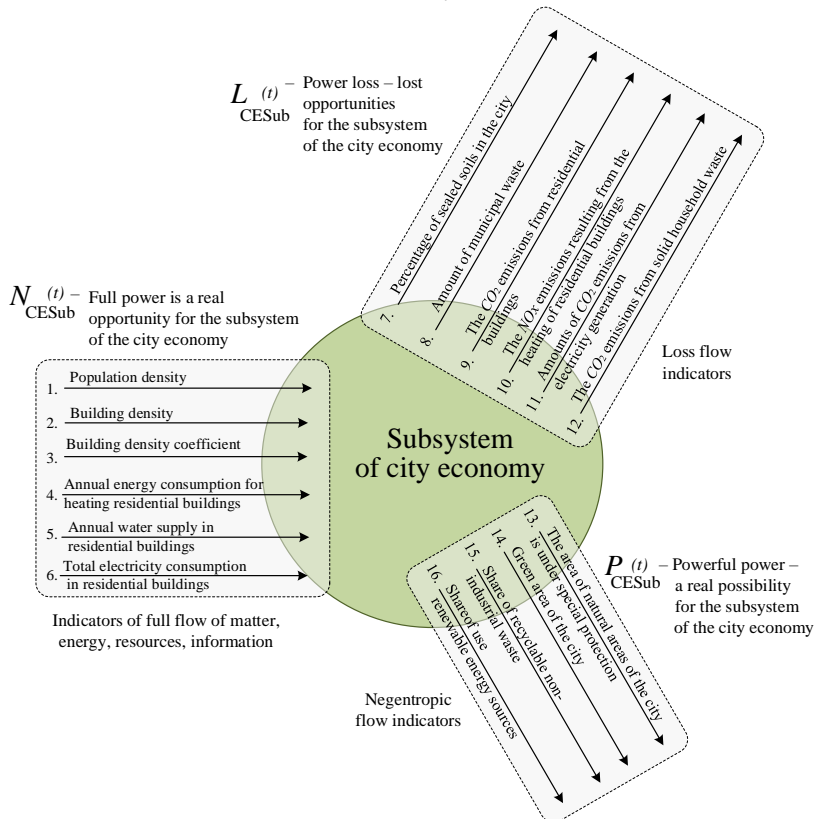
Fig. 2. Information model of the interaction of subsystem of city economy with the environment.

Thus, we have measured flows of different nature. **Table 1** shows an example of indicators of material and energy flows of urban environment for subsystem of city economy, which includes 16 indicators (see **Fig. 2**).

Example of indicators of material and energy flows of urban environment (city economy subsystem)

	Indicators of material and energy flows	Designation	N(t)	P(t)	L(t)	Units of measurement
1.	Population density	I_1	●			*inhabit. /ha*
2.	Building density	I_2	●			m^2/ha
3.	Building density coefficient	I_3	●			m^2/ha
	....	....				....
8.	Amount of household waste	I_8			●	*kg/inhabit.*
	....	....				....
11.	Amounts of CO_2 emission from electricity generation	I_{11}			●	$kg/(m^2 \cdot year)$
	....	....				....
16.	Share of using renewable energy sources	I_{16}		●		%

Depending on types of spatial objects to which they are applied, indicators of material and energy flows can be generalized (have a single value) or distributed (over the territory or along the length of linear object). Distributed over the territory indicator I_2 – building density as a GRID-surface for cities Krivyi Rih, Odessa, Lugano and Barcelona are presented in **Fig. 3** as an example.
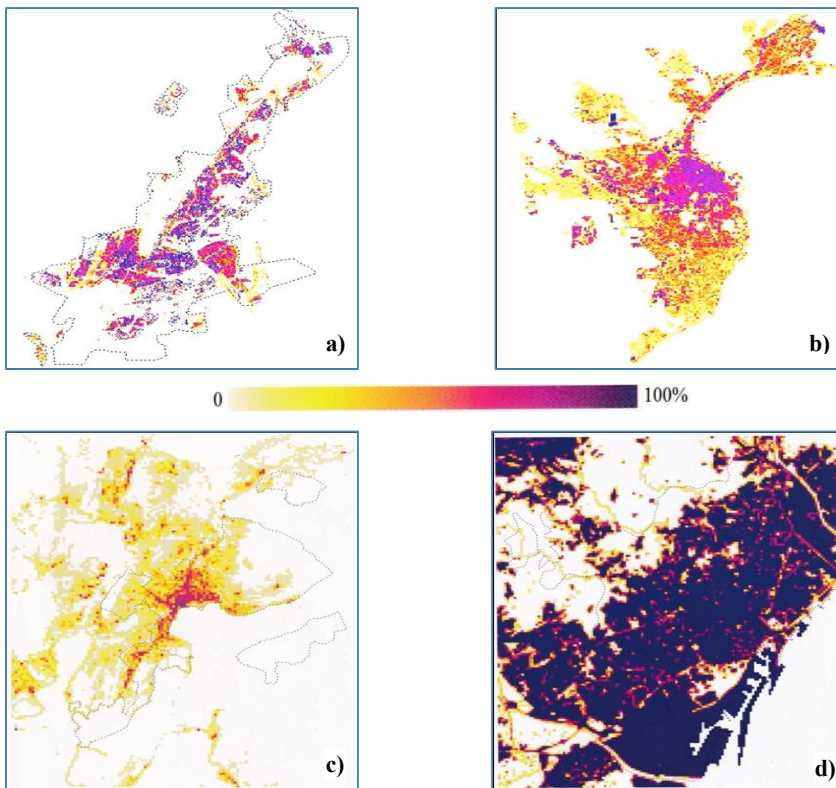
Fig. 3. Examples of indicator I_2 for cities (a) Krivyi Rih, (b) Odessa, (c) Lugano and (d) Barcelona.

3. INTELLIGENT TECHNOLOGY FOR ESTIMATING OF SUSTAINABLE DEVELOPMENT OF URBAN ENVIRONMENT

The proposed intelligent technology for estimating the sustainable development of urban environment based on an indicator of metabolic efficiency is shown in **Fig.4** (Mikhno & Patrakeyev, 2018; Patrakeyev & Ziborov, 2019). The technology consists of four main steps.
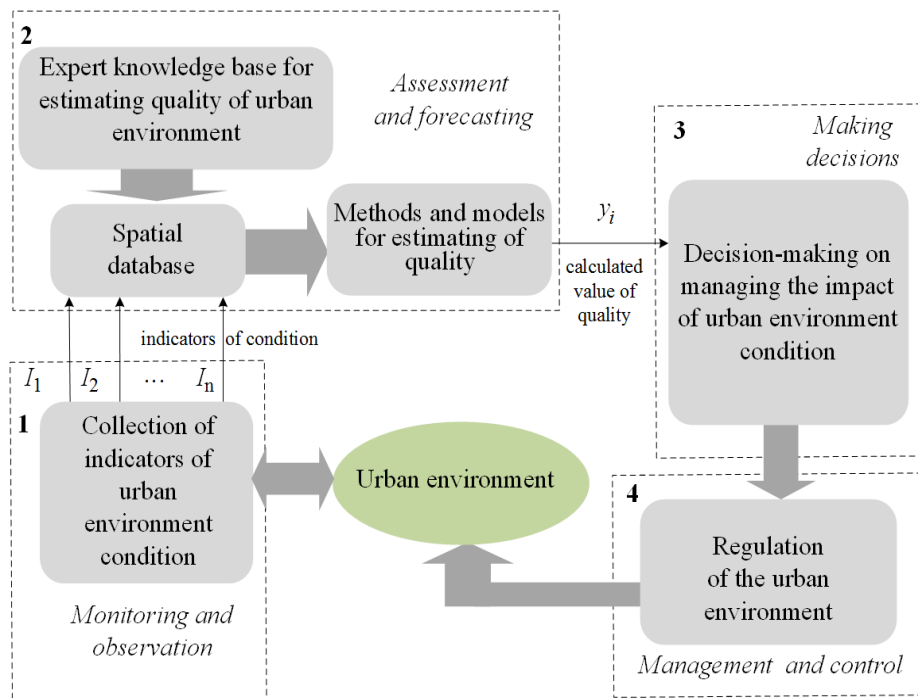
Fig. 4. Structure of intelligent technology for estimating of sustainable development of urban environment.

Consider phased intelligent technology components:

1 – monitoring and observation. The following types of information interaction Φ with the monitoring object can be used: $\{\phi^1, \phi^2, \phi^3, \phi^4, \phi^5, \phi^6, \phi^7, ..., \phi^d\} \in \Phi$, where ϕ^1 — photogrammetric survey, ϕ^2 — aerospace survey, ϕ^3 — satellite measurements, ϕ^4 — geodetic measurements on the ground, ϕ^5 — information processing by means of geoinformation technologies, ϕ^6 — data processing of field measurements, ϕ^7 — infrared, radar survey, d — cardinal number of set Φ.

In the course of complex information interaction with the monitoring object, the characteristics of the current state of urban environment are determined:

$$\{X_l^P\} \supseteq \{X_l^{PA}\}, \ l \in L, \tag{2}$$

where X_l^P is the set of defined parameters,
X_l^{PA} is the set of significant characteristics of the condition of urban environment.

2 – assessment and forecasting of sustainable urban development. At this stage, three interrelated components are used: a spatial object-relational database, a fuzzy knowledge base, and knowledge-oriented methods for calculating the estimation of urban environment quality.

The spatial object-relational database schema is formally represented as:

$$SBD = \langle R, L, C \rangle, \tag{3}$$

where $R = \{r_q, \,| \, q = \overline{1, \, n} \,\}$ is the set of database relations for which the attributes $A_q = \{a_{qp}, \,| \, p = \overline{1, \, m} \,\}$ and restrictions are defined as $S_q = \{s_{qk}, \,| \, k = \overline{1, \, h} \,\}$;

$L = \{l_v, \,| \, v = \overline{1, \, z} \,\}$ is the set of relationships between the relations R;

C — set of rules and restrictions that ensure database integrity and maintain data consistency.

A fragment of classes of objects of spatial database and classes of objects of fuzzy knowledge base for estimating the quality of urban environment is shown in **Fig. 5**. In addition to feature classes, class attributes, class operations and constraints that are imposed on relationships between feature classes are shown.

Creating justified decisions on managing sustainable development of urban territories requires the ability to analyze and optimize flows of energy, water and material resources in order to reduce the consumption of natural resources (Gerasimov et al., 2004; Greg et al., 2017). Therefore, the spatial database focuses on the spatial distribution of large number of buildings and households by functional zones and street blocks. Feature classes have been defined in accordance with the requirements of INSPIRE Data Specification (INSPIRE Data Specification, 2013). Using detailed information about residential buildings: type of building, size, location, year of construction and methods of regression analysis, can define the intensity of consumption of water, electricity, fuel for heating, which allows compensate the lack of small-scale data.

In order to unify the collection, storage and calculation of indicators of material and energy flows of urban environment in the database, it is proposed to create additional classes of thematic objects for storing indicators, which are classified in three sections: full flow of energy, that consumed by urban environment, products flow of energy and loss flow of energy. For example, object classes such as *DomesticWaterConsum, HeatingInBuildingGas, ElectricityBuildingCup* characterize, respectively, water consumption, natural gas consumption for heating and electricity consumption by each household or residents of residential buildings throughout the year. The considered classes of thematic objects model the consumed flow of resources, which for certain time and with certain efficiency has been used by society to meet its needs. Thematic classes of objects *WasteRecycled, RenewableBuildingEnergy* determine the total product produced (non-entropic energy flow (Rebane, 1984; Liiv, 1998)) in a certain time and technological capabilities of city economy subsystem. Thematic object classes *EmissionCO2DomesticWaste, DomesticWaste, EmissionCO2HeatingBuild* model energy loss flow, which characterizes missed opportunities of city economy subsystem. Proposed thematic classes of objects of city economy subsystem model a system of indicators of sustainable development that reflect technological, economic, environmental, social and other opportunities of urban environment as a whole.

Fuzzy Knowledge Base (FKB) provides storage, retrieval and generation of knowledge for estimating of urban environment quality. Knowledge is described by experts in the form of production rules. The knowledge base implements Sugeno logical inference algorithm. (Shtovba et al., 2016; Borisov et al., 2007).

To implement Sugeno algorithm (Rotshtein, 1999; Globa, 2008) an object-oriented approach was used. The diagram (**Fig. 4**) shows the most significant relationships and relationships between the classes of objects that are involved in the algorithm. Fuzzy Rules consist of Conditions and Conclusions, which in turn are Fuzzy Statements. Fuzzy Statement includes Linguistic Variable (*SetLinguisticVariable*) and term that is represented by fuzzy set (*TermSetOfLinguisticVariable*). Membership function is defined on fuzzy set, the value of which can be obtained using method (*getValue*). The relationship between FKB and SDB is provided through *LinguisticVar* class of objects. In general, *FKB* provides storage of production rules in next form:

$$\left[\prod_{k=1}^{n} \left(p_k = A_k^j \right] \rightarrow y_i \left(p_1, \ldots, p_n \right), \ i = \overline{1, m}. \tag{4}$$
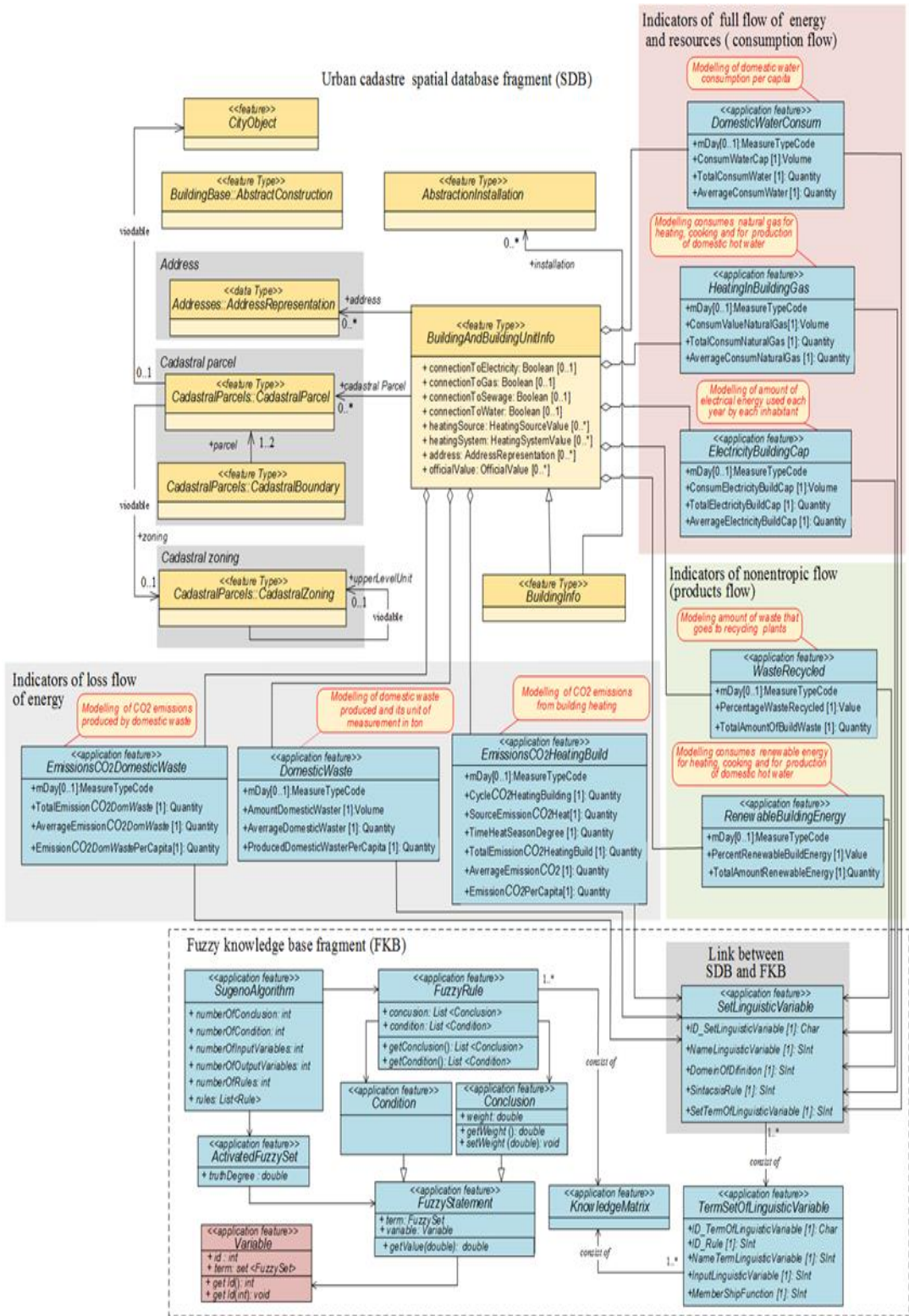
Fig. 5. Conceptual model for estimating of urban environment quality.

Based on a fuzzy knowledge base and expert knowledge on the importance of characteristic values, fuzzification of indicators is carried out, which characterize the full flow of material and energy and information resources for certain time — $N(t)$, the free energy flow that ensures the life of city — $P(t)$ and loss energy flow — $L(t)$.

Fig. 6 shows an example of fuzzification of *population density* indicator I_1 of the city with using appropriate term sets $A_{p_1}^1$ — "*low density*", $A_{p_1}^2$ — "*average density*", $A_{p_1}^3$ — "*high density*".

Each of term sets is characterized by corresponding membership function, which can be analytically defined by the following expression:

$$\mu_{p_1}^1(p) = \begin{cases} 1, & p \leq 200 \\ \frac{p-400}{200}, & 200 \leq p \leq 400 \\ 0, & p \geq 400 \end{cases} ;$$

$$\mu_{p_1}^2(p) = \begin{cases} 0, & p \leq 250 \\ \frac{580-p}{330}, & 250 \leq p \leq 580 \\ \frac{p-580}{220}, & 580 \leq p \leq 800 \\ 0, & p \leq 600 \end{cases} ;$$

$$\mu_{p_1}^3(p) = \begin{cases} 1, & p \geq 960 \\ \frac{960-p}{260}, & 700 \leq p \leq 900. \\ 0, & p \leq 600 \end{cases}$$

The third part − methods and models for quality estimating of urban environment (**Fig. 4**) − calculates the integral estimation of the efficiency indicator of urban environment metabolism based on Sugeno algorithm.
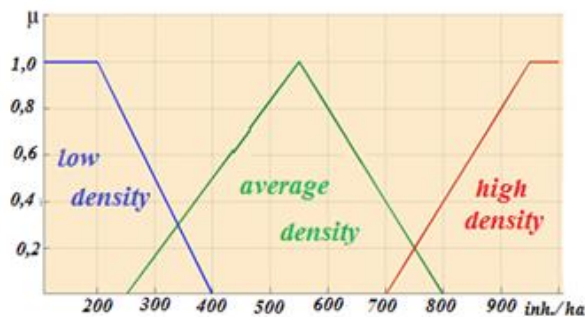
Fig. 6. Example of fuzzification of the city *population density* indicator.

Fuzzy mathematical model for estimating the efficiency indicator of urban environment *as a set of Sugeno rules can be presented as (Giordano et al., 2014):*

$$R^{(i)}: IF \prod_{i=1}^{m}\left(p_k \ IS \ A_k^j\right) THEN \ y_i = \sum_{k=1}^{n} \frac{w_k}{W} \cdot f_k^j(x) \qquad (5)$$

where i is number of TSK rules $(i = \overline{1, \ m})$;

n – number of conditions;

k – input variable number;

p_k – input variable $(k = \overline{1, \ n})$;

A_k^j – fuzzy set with associated membership function of μ_k^j, $j \in \{1,2,3\}$;

w_k – coefficient of an importance of input variable p_k; $W = \sum_{i=1}^{n} w_k$.

The function f_k^j is non-decreasing and complies with restrictions:

$$0 \le f_k^j(x_k) \le 100. \tag{6}$$

3 – decision-making on managing the impact of urban environment condition. At this stage, the indicator of urban environment metabolism efficiency is used as a tool for preparing and making managerial decisions to improve the quality of population life. This **indicator** provides a multidimensional and multifactorial approach in making decisions on managing sustainable urban development.

4 – regulation of the urban environment. At this stage, the choice of alternative scenarios of urban planning is implemented, which will allow end users to change the goals and indicators of the city sustainable development.

4. RESULTS AND DISCUSSIONS

For testing the proposed intelligent technology for estimating of potential, real and lost opportunities of urban environment, two specific post-Soviet cities Odessa and Krivyi Rih were selected. Extremely different in terms of size and population, these cities were chosen because of their specificity: Odessa is a vivid example of tourist city on seashore, while Krivyi Rih represents a vivid example of post-industrial city with difficult environmental situation. The reliability and validity of obtained integrated estimations of sustainable development of cities Odessa and Krivyi Rih is confirmed by similar indicators of sustainable development for cities Barcelona and Lugano.

For preparing the initial data, GIS capabilities were used to form geospatial models and thematic layers according to indicators that presented in table 1. **Table 1** has 37 basic indicators that characterize metabolism of each from three urban environment subsystems of cities Krivyi Rih and Odessa.

The basic component of the urban metabolism efficiency is geographical data, that presented in digital form on spatial objects and includes information about their spatial and non-spatial properties. Intelligent technology is implemented in MatLab software (*The MathWorks Inc*) based on thematic cartographic data generated in ArcGIS 10.

The initial data for cities Krivyi Rih and **Odessa** are based on open sources (Kryvyi Rih strategic development plan till 2025, 2016; Strategy of economic and social development of the city Odessa until 2022, 2013)**.**

Fig. 7 shows changes in the indicator of urban environment efficiency depending on changes in the share without carbon transport and average mileage of vehicles in urban cycle for cities (a) Odessa and (b) Kryvyi Rih. The surface can be interpreted as the landscape of efficiency for the scenario that includes changes to only two of considered input variables. For comparison, landscapes of the urban environment efficiency of the city (c) Lugano in space of these two variables are shown.

a)

b)

c)
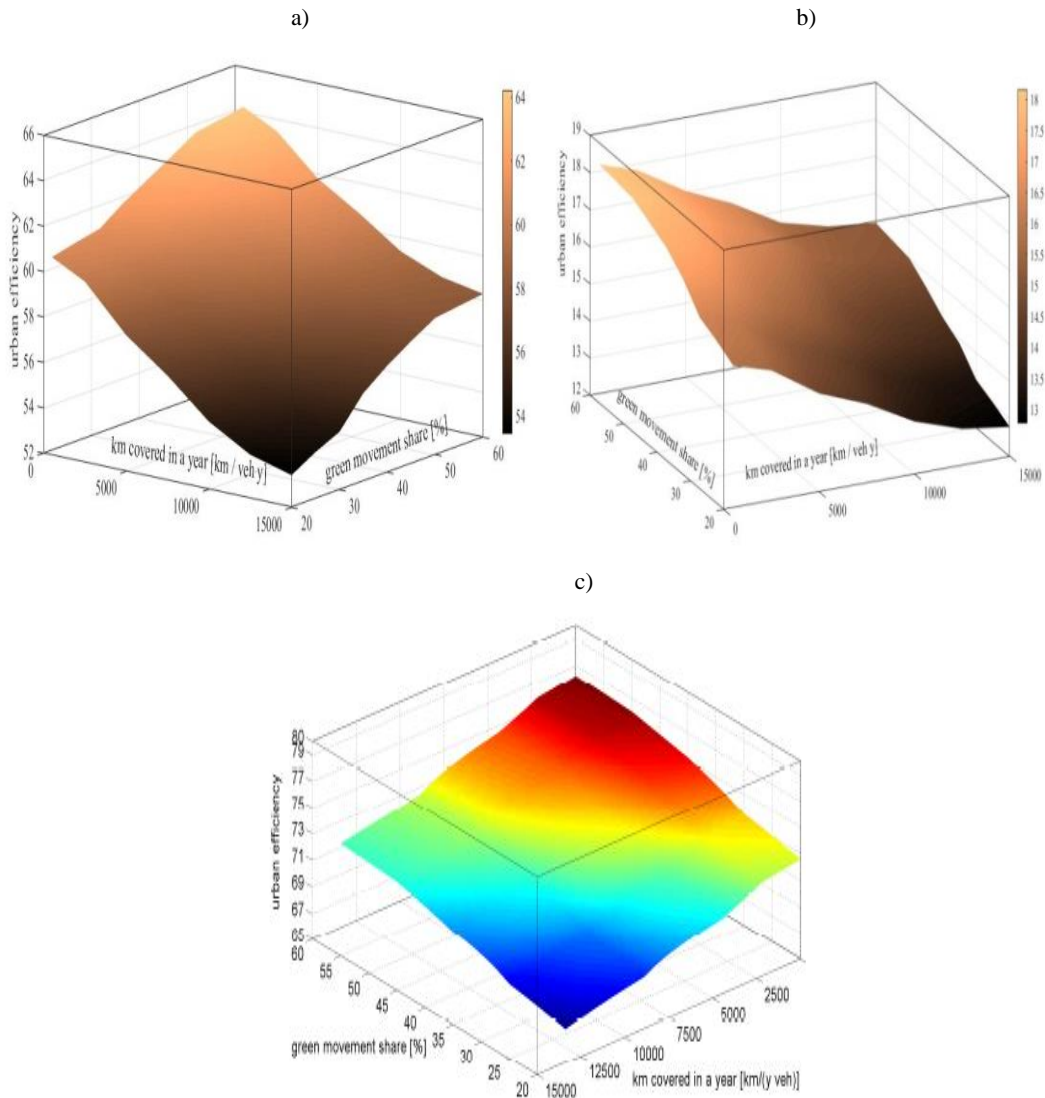
Fig. 7. The influence of green movement share and average volume of km covered in a year on changes of urban environment efficiency for cities (a) Odessa, (b) Kryvyi Rih in comparison with city (c) Lugano.

Fig. 8. shows the contour lines of the estimation indicator of sustainable urban development of cities a) Odessa and b) Kryvyi Rih in context of two-dimensional input space. This performance gives a new knowledge about ways of the urban environment enhancing and, consequently, facilitates the adoption of evidence-based decisions: for example, the contour lines show the direction of changes in variables that are neutral from the point of view of the efficiency of cities. Each contour line is interpreted as a possible compromise between the real and lost possibilities of possible transformation of the urban environment.

In **Fig. 8** we can see how the increase in the average car mileage in the urban cycle can be compensated by increasing shares of no carbon transport. The share without carbon transport, which can compensate for the increase in the average mileage of cars in the urban cycle, is different for (a) Odessa and (b) Kryvyi Rih. The direction, along which the contour lines are closer to each other, shows the maximum sensitivity of the indicator sustainable development of the urban environment.
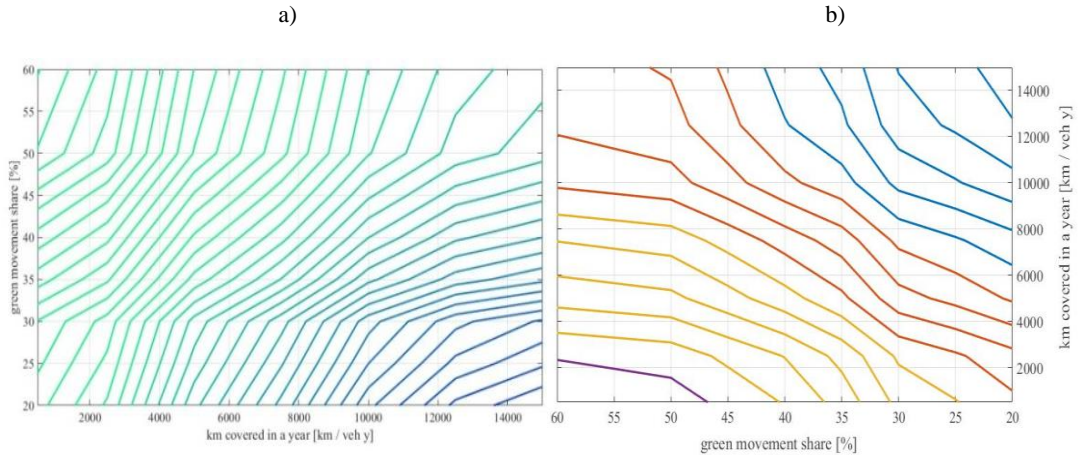
Fig. 8. Contour lines of the indicator of urban environment efficiency: (a) Odessa, (b) Kryvyi Rih.

The following **Fig. 9** shows the reaction of the indicator of the effectiveness of the urban environment to changes in emissions of NO_x (recall that NO_x emissions have two main sources: heating and transport). The surfaces in **Fig. 9** characterize a scenario change indicator of the effectiveness of the urban environment for the case of only changes in NO_x emissions on example of cities Odessa and Kryvyi Rih.

a)

b)

c)
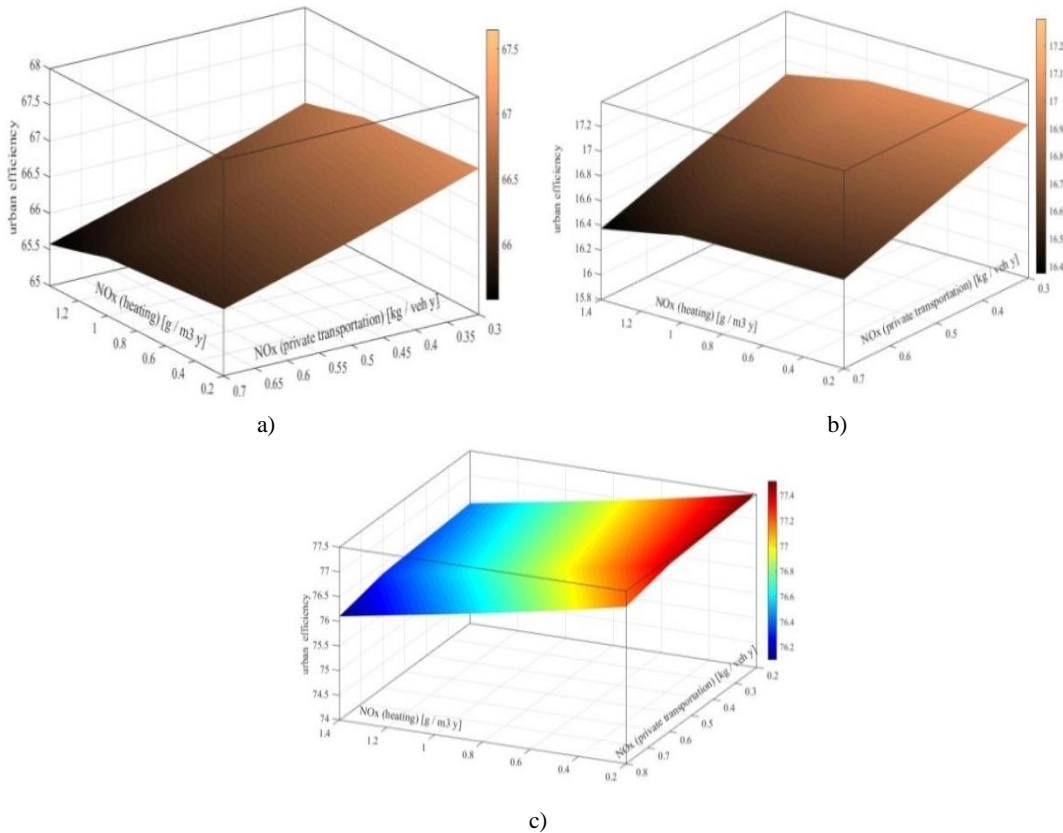
Fig. 9. The indicator of urban environment efficiency for changes in NO_x emissions:
(a) Odessa, (b) Kryvyi Rih, (c) Barcelona.

The calculated values of potential, real and lost opportunities for each of the subsystems of the urban environment (see **Fig. 1**) are presented as Kiviat Diagram (**Fig. 10**).
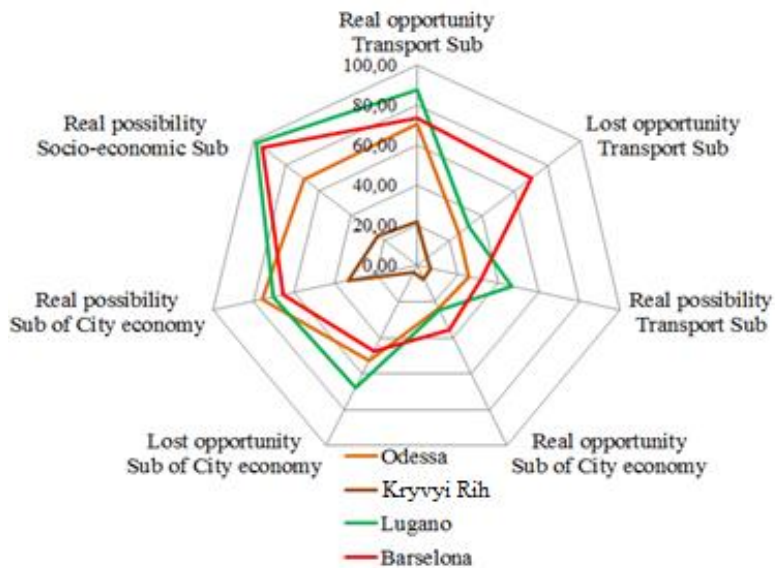
Fig. 10. Values of seven intermediate performance indicators of urban environment subsystems for cities Odessa, Kryvyi Rih in comparison with cities Lugano and Barcelona.

A comparison of indicators of integrated estimations of sustainable urban development for cities Odessa, Kryvyi Rih with similar estimations for cities Barcelona and Lugano, which were obtained as a part of the program for monitoring the sustainable development of European Union cities, is shown in **Fig. 11**.
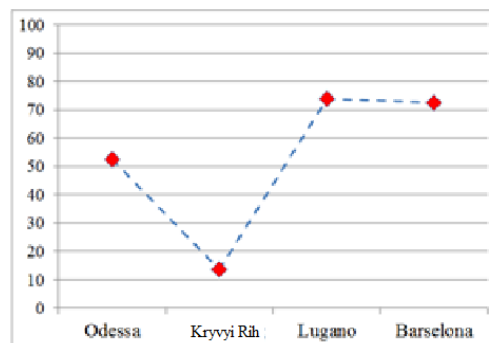
Fig. 11. Computation results for cities Odessa, Kryvyi Rih in comparison with cities Lugano and Barcelona.

A brief analysis of results based on proposed intelligent technology of potential real and lost opportunities of urban environment revealed key problems of the socio-economic and territorial development of post-Soviet cities. Low indicators are explained by the strong zoning of the territory (for industrial and residential), low mobility of the population, low incomes, lack of modern technologies for processing industrial and household waste and poor market development without carbon vehicles. Thus, the new conditions that shape the modern urban environment — globalization, the neo-tertiary economy, and new intellectual information technologies — should reconsider the modern urban planning paradigm so that modern urban projects are based on assessing potential, real and lost opportunities in order to ensure sustainable development of the urban environment.

5. CONCLUSIONS

Approach based on the integration of capabilities of modern GIS and intelligent technologies for estimating the quality of the urban environment is a new, promising area for the development of tools for managing the sustainable development of urban areas. In the framework of proposed intellectual information technology, the following results were obtained:

− the principle of information system creating in the form of an object-oriented database of spatial data has been developed, which contains large arrays of heterogeneous spatially distributed indicators of real, lost and potential capabilities of Ukrainian cities;

− production-type knowledge base has been created for storing expert knowledge on the boundary and maximum permissible environmental, socio-economic and urban development indicators of the urban environment;

− based on formal methods and using expert estimates, a methodology has been developed for estimating the potential, real and lost capabilities of the urban environment based on qualitative characteristics;

− proposed intelligent technology for estimating the quality of the urban environment allows to generate possible scenarios for changing the efficiency indicator depending on the selected space of input characteristics.

Using of proposed intelligent technology for estimating of urban environment quality is deeply interdisciplinary in nature and is important for ensuring decision-making on managing sustainable development of urban areas.

R E F E R E N C E S

Acebillo J. (2013). New Urban Metabolism. Barcelona / Lugano. Barcelona − New York: Editorial ActarD., 244 p.

Bettencour L. A., Lobo J., Helbing D., Kühnert V., West G. B. (2007) Growth, innovation, scaling, and pace of life in cities. *Proceedings of the National Academy of Sciences*, 104 (17), 7301-7306.

Bolshakov B. E., Kuznetsov O. L. (2010) Sustainable development: universal principle for the synthesis of natural, technical and social knowledge. *Bulletin of the Russian Academy of Natural Sciences*, 10 (3), 3-9, (in Russian).

Bolshakov B. E., Ryabkova. S. A. (2009) Emergence and main problems of concept of "Sustainable Development" entering into world politics and science. An appendix to the training complex "Theory and Methodology of Designing the Sustainable Development of Socio-Natural Systems". Dubna, 210 p, (in Russian).

Bolshakov B. E. (2008) Theory and Methodology of Designing Sustainable Development of Socio-natural Systems. 143 p. Available: http://www.aup.ru/books/m536 [Accessed June 2020], (in Russian).

Borisov V., Kruglov V., Fedulov A. (2007) Fuzzy models and networks. – M.:Hot line - Telecom, 284 p, (in Russian).

D2.8.III.2 INSPIRE Data Specification on Buildings – Draft Technical Guidelines. (2013) *INSPIRE Thematic Working Group Buildings*, 309 p.

Gerasimov B., Devisinuck M., Subach I. (2004) Decision support systems: design, application, estimation of efficiency. *Monograph*, Sevastopol, 320 p. Available: https://studfile.net/preview/5367046 . (in Russian).

Giordano P., Capuno P., Vancheri A. (2014) Fuzzy Evaluation of Heterogeneous Quantities: Measuring Urban Ecological Efficiency. *Ecological Modeling*, 288, 112-126. Available: https://doi.org/10.1016/j.ecolmodel.2014.06.001 .

Globa L., Ternovoy O., Shtogrina M. (2008) Creating fuzzy knowledge bases for intelligent control systems. *Computing, International Scientific and Technical Journal,* 7 (1), 70-79. (in Ukrainian).

Greg Scott, Abbas Rajabifard. (2017) Sustainable development and geospatial information: a strategic framework for integrating a global policy agenda into national geospatial capabilities. *Geo-spatial Information Science*, 20:2, 59-76. Available: https://doi.org/10.1080/10095020.2017.1325594 .

Hasanova S. S., Pogosyan L. V., Novikov A. V., Batashev R. V. (July 2019) Urban Geographic Information System: Features of Implementation and Management. *International Journal of Innovative Technology and Exploring Engineering*, 8 (9). Available: https://doi.org/10.35940/ijitee.H7505.078919/ .

Kennedy C.A. et al., (2015). Energy and Material Flows of Megacities. *PNAS,* 112 (19), 5985–5990. Available: https://doi.org/10.1073/pnas.1504315112 .

Kryvyi Rih strategic development plan till 2025. (2016) Executive Committee of Kryvyi Rih City Council. Department of Economics. Public Utilitym Kryvyi Rih City Development Institution of Kryvyi Rih City Council, 100 p. Available: https://kr.gov.ua/ua/st/pg/100415583959267_s [Accessed July 2020]. (in Ukrainian).

Liiv E.H. (1998) Infodynamics, Generalized Entropy and Negentropy. – Tallinn: Juhisjelu, 200 p.

Mikhno O., Patrakeyev I. (2018) Quality evaluation method of the city environment. *Visnyk Taras Shevchenko National University of Kyiv.* Military-Special Sciences, 2 (39), 29-39. Available: https://doi.org/10.17721/1728-2217.2018.39.29-39 . (in Ukrainian).

Newman P. (1999) Sustainability and Cities: Extending the Metabolism Model. *Landscape and Urban Planning,* 44, 219–226.

Paola C., Giulia P., Marco B. (2016) Urban Metabolism Analysis as a Support to Drive Metropolitan Development. *Procedia Engineering*, 161, 1588 – 1595, Available: https://doi.org/10.1016/j.proeng.2016.08.631 .

Patrakeyev I, Ziborov V. (2019) Using fuzzy sets in the estimation system of the efficiency of urban environment metabolism (on the example of cities of Ukraine). *Geodesy and cartography*, 45 (3). 102-109. Available: https://doi.org/10.3846/gac.2019.7699 .

Patrakeyev I., Ziborov V., Lazorenko-Hevel N. (2017) Methods of Evaluation of the State and Efficiency of the Urban Environment, ISPRS *Ann. Photogramm. Remote Sens. Spatial Inf. Sci.*, IV-5/W1, 43–49, Available: https://doi.org/10.5194/isprs-annals-IV-5-W1-43-2017 .

Rebane K.K. (1984) Energy, Entropy, Habitat. Tallinn: Valgus, 159 p, (in Russian).

Rotshtein P. (1999) Intelligent identification technologies. Vinnytsia: University-Vinnytsia, 320 p. (in Russian).

Shtovba S.D., Mazurenko V.V., Tylets R.O. (2016) Fuzzy identification information technology for the synthesis of accurate, compact and interpretable knowledge bases. *Computer Sciences and Telecommunications.* 1 (47). 8–22, (in Russian).

Strategy of economic and social development of the city Odessa until 2022. (2013) Odessa:TPP, 80 p. Available: https://omr.gov.ua/images/File/DODATKI2013/Strategiya_Odessa_Ukr.pdf [Accessed July 2020], (in Ukrainian).

Sustainable Urban Metabolism for Europe (2009). Urban development and urban metabolism: A spatial approach. *Work Package 1*. Available: http://sume.at/project_downloads [Accessed July 2020].

Yanitsky O. N. (2013) Metabolic concept of the modern city. *Sociological science and social practice*, 3, 6-32, (in Russian).

THE REGIONAL AND GEOGRAPHICAL ASPECTS OF FOOD SECURITY: A SPATIAL ANALYSIS IN THE CASE OF AZERBAIJAN, HUNGARY, AUSTRIA, SINGAPORE AND GEORGIA

László VASA[1] , Ragif HUSEYNOV[2] , Imre VARGA[3] , Lóránt DÁVID[4] *

ABSTRACT

Achieving food security is crucial, and a primary development goal world-wide. However, there is a difficulty in finding reliable data on the topic, which raised a problem for policymakers and researchers as well. Therefore, the present study aimed to fill in this gap by examining the dynamics of regional food security. The main research objective was to identify the determinants of food security in Azerbaijan, Singapore, Austria, Georgia and Hungary. Furthermore, a specific objective was to investigate the short- and long-term impacts of both endogenous and exogenous shocks on the food security of the selected countries. The study collected large scale panel dataset between 1992 and 2019. The empirical model suggested that food import, foreign direct investment, inflation, annual per capita income and Human Development Index had a positive, while the flow of food export had an adverse impact on the food security status of the selected countries. The study recommended to the governments of selected countries and to developmental organisations to achieve national food security through indigenous agricultural interventions along with supporting domestic growers by investing in agricultural education, skill development and infrastructure programs.

Keywords

spatial approach, geography of food supply, regional food availability, sustainability

1. INTRODUCTION

Under the Sustainable Development Goals (SDG), countries made a commitment to eliminating all kinds of nutritional and food insecurity (UN, 2015; Popp and Lakner and Oláh eds. 2020). And still, food and nutritional insecurity remains one of the most critical sources of hunger and poverty, particularly in the developing world (FAO, 2017a). The prevalence of undernourishment in young children, the micro and macro nutrients deficiency in women are the highest in the less developed countries (Stevens et al., 2015). Many international institutions pay great attention to the food security problems, especially in developing countries, where a huge amount of people suffers from them (Asatiani, 2009). In this regard, Asian nations are facing two major challenges: food insecurity and promotion of trade. Food prices increased in 2007/2008 and have become volatile due to some critical issues and a great threat to food security. Nevertheless, it should be controlled by the cooperation of nations since it is an important factor in preserving regional stability (Chandra and Lontoh, 2010). Food represents the basic need of humans that provides energy for living. In the meantime, Asian countries are facing several other challenges as well, such as high, rapid growth in population, adverse environmental conditions, rural poverty and only a little growth in agriculture (Marzęda-Młynarska, 2017). Problems related to food insecurity arose frequently, their number showed a sharp increase

---

[1] *Széchenyi István University, 9026 Győr, Hungary, laszlo.vasa@ifat.hu*

[2] *Szent István University, Faculty of Economics and Social Sciences, 2100 Gödöllő, Hungary, ragif_h@yahoo.de*

[3] *Eötvös Loránd University, ELTE Savaria University Centre, Eötvös Loránd University, Faculty of Social Sciences, Institute of Economics, Savaria Department of Business Economics, HU-9700 Szombathely, Hungary, varga.imre@sek.elte.hu*

[4] *Corresponding author, Szent István University, Faculty of Economics and Social Sciences, 2100 Gödöllő, Hungary, david.lorant.denes@szie.hu*

between 2007 and 2012. The main reason for food insecurity lies in the inequality of the society where the poor, due to insufficiently available food or not affordable healthy food, suffer from many diseases (Vasa, 2005; Schlichting et al., 2019).

Regional food security has become a sustainable development issue as well in the past few decades (ADB, 2006; Vasa, 2002). A country is said to be food secure when all its people at all times have sufficient economic and physical economic access to nutritious and safe food to meet their food requirements, in order to maintain an active and healthy lifestyle (FAO, 2003). Therefore, this question has become a primary focus of the millennium development goals (MDGs). And as such, food security is observed and examined in the different countries, thus it is measured through the progress of any government, and as part of social well-being (Carter et al., 2010). However, achieving regional and country-level sustainability of food is still a great challenge (Smith, 2011). While many countries have presented social development programs and carried out policy interventions, none of these efforts led to reaching the desired goals (Keszi-Szeremlei and Magda, 2015; Chaaban et al., 2018;). Particularly, food security in Asian countries did not increase enough to meet the regional demand. The gap between the national food supply and demand has led to an increase in the import of food and livestock (Zahrnt, 2011; Vásáry et al., 2013). Furthermore, there is a difficulty in finding reliable data on regional and national food security in the Asian region, which raised a problem both for policymakers and researchers. The policymakers and implementers of the regional food security program have been gradually seeking tools for measuring food security, which are reliable, easy to use and help to interpret the dynamics of food security (Feizizadeh et al., 2015; Godor, 2016). The analysis of regional and national food security determinants and their status is, therefore, useful for not only policymaking but implementation as well (FAO, 2015b). Hence, it is not surprising that there have already been several factors examined empirically that directly or indirectly impacted food security in the Asian region (Islam and Wrong, 2017). However, according to the literature review, no study applied macro-level or large-scale data to estimate the regional dynamics of the food security situation and its key determinants from a macro perspective recently. Studies investigating the determinants of food security while focusing on a target population or maintaining a micro-perspective could not only mislead policymakers but also could give a spurious situation analysis on Asia or other less developed countries (Oglu, 2018). Therefore, the current paper aims to fill in this gap by examining the dynamics of regional food security. The main research objective is to identify the determinants of food security in Azerbaijan, Singapore, Austria, Georgia and Hungary. These countries have small population size and had quite comparable socioeconomic situations and demographical profile. So, we selected them for examining the food security dynamics. Moreover, a specific objective is to investigate the short- and long-term impacts of both endogenous and exogenous shocks on the food security of the selected countries.

2. LITERATURE REVIEW

A few recent papers focused on the analysis of food security, on short- and medium-term. They highlighted that the dynamics of food security were not dependent on the food balance sheets but on the countries' ability to maintain food consumption through domestic food production and to finance food import. On the short-run, hunger was just increased by such social policies as food aid, and on the medium-run, it was maintained by income inequality (i.e. the higher income of certain people). Higher trading prices for food were found beneficial for agricultural development but could not be expected to drive directly the agricultural growth. Herein, two factors were involved: first, the change in trade prices, and then, in response to it, the rise in agricultural production (Herrmann, 2009). For the argument on food security and the increase in agricultural growth, the European Union's Common Agricultural Policy (CAP) was taken under scrutiny. Hunger was and is a major issue in developing countries which unfortunately did not receive the right attention and response from European farmers. Clearly, in order to boost the agricultural sector, financial investments were needed in the developing countries (Zahrnt, 2011).

Another paper provided knowledge on the agricultural sector's development in Hungary, and explored the creation of an Agricultural Knowledge System (AKS) in the country. Significant changes were implemented in the agricultural sector to beat the challenges of traditional AKS institutions, which sometimes failed to meet new requirements. The study was based on the perspective of a national stakeholder workshop and meetings with professionals, where the literature review gave recommendations for the development of the agricultural sector and the Hungarian AKS institutions, and established a platform or organisation for further communication among concerned parties and for solving the major problems which were related to the creation of the system (Dávid and Szűcs 2009). Therefore, the findings are also important in terms of agricultural knowledge in Europe and food security in general (Nemes and High, 2013). Since many developing countries already had to face food insecurity, it is considered as a major issue. Another paper suggested that in order to improve the food security system, a food policy council should be established, and the locally determined work should be promoted. Work might be related to growth and development in the food system. Food policy, as such, has defined many goals and planning schemes, involving food retail, waste management, urban agriculture, community health, and economic development. Although the findings of the study are wide-ranging, the author highlighted the determining role of local government in addressing food security. Therefore, it was found important to provide a toolkit that could guide local governments in that activity, and in developing the aforementioned council, or in conducting local food and environmental research. Hence, with the collaboration of the local government and the community, moving toward food security could be possible (Stevenson, 2013).

According to another study, food availability was determined by local supply through agricultural and industrial activities. In its measurement, the food security was assessed by GIS multi-criteria analysis through the depiction of a food security map. In that map, 905 villages (57 percent of rural area) were found to be located in the insecure zones and 544 villages (22.15 percent of rural area) were found to be located in the secure ones. The results of that research were particularly important for authorities in East Azerbaijan and Iran (e.g. Ministry of Water Resource Management, Ministry of Agriculture, Ministry of Natural Resources) (Feizizadeh et al., 2015). According to Farmar-Bowers (2015), Australia exported more than the half of its agricultural production. According to the study, Australia failed to control its food security problems and to provide a healthy diet for its people, and to expand the natural resources. In the next decades, a lower yield production is expected due to the changing climate conditions and the higher prices, which together will challenge the food supply systems. Australian people had many interests in the food security-related issues partly because food security forms a necessary part of a healthy food plan. This research suggested that a new policy could not be acceptable for problems in food security and agriculture. It used a seven-method structure for the classified goals of economic growth and other techniques for the improvement of food security. The study explained these basic goals and ideas for the improvement of food security and agriculture system and suggested further techniques for the resolution of problems in the food supply system in Australia. In the beginning of the 20th century, the level of expenditure on food was much lower than in recent decades, when food production significantly increased. Moreover, a significant relationship was found between the quality of food and the income level since healthier food was more expensive than simple cereal and fat. Consumer attitude toward food could change due to a change in the level of income. Hence, consumer preference toward choosing food was different in case of people with lower income. The personal income per capita was (and is) higher in the developed regions and lower in the less developed regions, therefore, developed regions spent more money on better quality, healthier food. In the consumer basket, foodstuff accounted for approximately one-third of the overall expenditure.

Another paper explained that the problem of climate change was a major issue in economic growth and identified its effects on the quality of life and standard of living. It had often been assumed that food security and agricultural food production would be affected by climate change. The paper, upon identifying the effects of climate change on food security, gave some recommendations on how to overcome that situation. The study provided much information on the relationship between food security and climate change by critically examining both of them (Islam and Wrong, 2017). Another

study (Tortajada and Zhang, 2017) proposed some important policies for Singapore's economy, among them to extend the agricultural trade and investment. The authors found that the proposed export-led policies would increase the research and development, the overall national welfare and the control over food insecurity. They explained how the climate condition and some other major problems were related to irrigated agricultural land, hydrography, vegetation, soil erosion and salinity in the respective area. Another research defined the agriculture-related problems in Azerbaijan and the role of the country in economic development. The findings determined the current situation of agriculture and its possible development strategy and priorities (Oglu, 2018). Another study was carried out to investigate the role of price volatility among the import-dependent countries in Central Asia, particularly among wheat exporters in order to check the efficiency of the wheat market. The purpose of the study was to see the availability of wheat on the market so that food insecurity could be reduced. It applied the OLS model and concluded that the major threat to food security in Central Asia was the low production of wheat and the high transporting costs. However, the volatility of prices was also a major issue in the examined countries which also reduced the efficiency of the wheat market. And finally, the food insecurity was just created. According to the study, in order to secure ghee food and to meet the needs of people in these countries, the market infrastructure should be developed, the unofficial payments should be eliminated, and the geopolitical conflicts should be resolved. Thus, the trade-enhancing policies should be linked to wheat sufficiency policies so that food security may improve (Svanidze et al., 2019). Another research examined the four major pillars that might affect food security: the availability of food, the access to it, its utilisation and the stability of food. The issues created around these pillars meant a great challenge that should be resolved. Herein, a systematic study was conducted to analyse the future problems of agriculture and food. According to the findings, both were affected by climate change as well as by many other socioeconomic factors. They also highlighted that political interference was a major issue in some countries where the food departments were not properly established and showed no improvement in self-sufficiency of wheat and other staple foods. The authors suggested that to maximise the effects of the possible policy, actions should be taken by the countries' governments (Calicioglu et al., 2019).

3. ECONOMETRIC MODELLING FRAMEWORK

This study assessed the dynamics of food security of five selected regional economies by employing the Panel GMM estimation approach as proposed by Arellano and Bover (1995) and Blundell and Bond (1998). In order to study the empirical dynamics, we will estimate the moment conditions for $f(FPI, \lambda)$ that is used as proxy of the food security (Eq.1):

$$m(\lambda_0) \cong E[f(FPI, \lambda_0)] = 0, \tag{1}$$

where FPI is the proxy of food security dynamics in a given moment condition $\lambda \neq \lambda_0$.

The estimation of moment condition represents the simple average function (Eq.2):

$$\hat{m}(\lambda) \cong \frac{1}{n} \sum_{n=1}^{n} f(FPI, \lambda) \tag{2}$$

Let us minimise the $f(FPI, \lambda)$ with respect to the λ, using the Eq.2. The estimator results will depend on the choice of the norm function as given (Eq.3):

$$\left\| \hat{m}(\lambda) \right\|_{W}^{2} = \hat{m}(\lambda)^{n} W \hat{m}(\lambda), \tag{3}$$

here W represents the weight norm function bases of the given data set.

The Eq.4 represents the final equation of the GMM, based on all properties of GMM (consistent, efficient, and asymptotically normal):

$$\hat{\lambda} = \arg\min_{\lambda \varepsilon \Theta} \left(\frac{1}{n} \sum_{n=1}^{n} f(FPI, \lambda) \right)^{n} \hat{W} \left(\frac{1}{n} \sum_{n=1}^{n} f(FPI, \lambda) \right). \qquad (4)$$

Econometric Model

$$\ln FPI_{ij} = \beta_{ij,1} FPI_{t-1} + \beta_{ij,2} CPI + \beta_{ij,3} FII + \beta_{ij,4} FEI + \beta_{ij,5} PCGDP + \beta_{ij,6} FDIGDP + \beta_{ij,7} HDI + \varepsilon_{ij}$$
$$(5)$$

where "I" represents cross section (number of countries) and j represents data spam (1992-2019).

Data Description

Panel data were used to examine the regional dynamics of food security of selected five economies (Azerbaijan, Singapore, Austria, Georgia, Hungary). The annual data were taken from the World Development Indicators (WDI) published by the World Bank for the period 1992 to 2019. **Table 1** represents the detailed description and the unit of all variables used to estimate the dynamics of food security of selected countries.

Table 1

Variable Description

Sr.	Variables	Unit	Description
1	Food Production Index	Index	FS
2	Per capita GDP	Dollar	PCGDP
3	Consumer Price Index	Index	CPI
4	Food Import Index	Percentage (%)	FII
5	Food Export Index	Percentage (%)	FEI
6	Human Development Index	Index	HDI
7	Foreign Direct Investment to GDP Ratio	Percentage (%)	FDIGDP

4. RESULTS AND DISCUSSION

The results of descriptive statistics explain the dynamics of the food security of the selected economies. The value of average food production value is 70.27, while 339.02 was the maximum and 3.17 was the minimum value, respectively (**Table 2**). The average ratio of foreign direct investment to GDP was 9.62 percent between 1992 and 2019. The maximum and minimum values of foreign direct investment to GDP were 55.08 to -15.98 percent, respectively, where 55.08 was the maximum foreign direct investment to GDP in the selected countries during 2003. The lowest foreign direct investment to GDP ratio was observed during 2010. Similarly, the average human development index value was around 0.79, while 0.94 was the maximum and 0.61 was the minimum value of HDI, respectively. The average value of CPI was 89.63 between 1992 and 2019, the maximum and minimum CPI values were 155.22 and 48.02. The average food import index value was about 9.22, while the average food export index value was 3.60. (**Table 2**)

Table 2

Descriptive Statistics

	FDIGDP	HDI	CPI	FII	FEI	PCGDP	FPI
Mean	9.62	0.79	89.63	9.22	3.60	25556.85	70.27
Median	7.03	0.79	86.05	5.70	3.48	30413.93	89.68
Maximum	55.08	0.94	155.22	39.10	8.34	59754.99	339.02
Minimum	-15.98	0.61	48.02	2.26	1.11	1238.48	3.17
Std. Dev.	13.15	0.09	25.58	7.18	1.59	19524.17	57.46
Skewness	0.50	-0.12	0.43	1.48	0.98	0.06	0.82
Kurtosis	8.21	2.17	3.08	6.11	3.79	1.54	4.87

Table 3 presents the results of the correlation matrix that explains the dynamics of the food security of the selected regional economies. The main diagonal of the correlation matrix shows the self-association of each variable which was 1 implying that self-association was 100 percent. The estimated results show that the food production index as the proxy of the food security situation is strongly and positively correlated to the foreign direct investment inflow (r=0.77). Likewise, there is a 0.29 correlation between the food production index and the human development index. The food production index is moderately and positively (r=0.55) correlated to the consumer price index. The food security situation was massively dependent (r=0.63) on the food import index. Per capita income also played an important role (r=0.61) for attaining the regional food security dynamics in the selected countries.

Table 3

Correlation Matrix

	FPI	FDIGDP	HDI	CPI	FII	FEI	PCGDP
FPI	1.00						
FDIGDP	0.77	1.00					
HDI	0.29	0.64	1.00				
CPI	0.55	-0.70	0.54	1.00			
FII	0.63	0.31	-0.78	-0.16	1.00		
FEI	0.83	0.51	-0.57	-0.33	0.43	1.00	
PCGDP	0.61	-0.45	0.93	0.26	-0.82	-0.48	1.00

Table 4 reports the estimated results of the panel GMM estimation approach for examining the regional food security dynamics. In order to establish the reliability of the results of the model, the Sargan over identification restriction test was applied as post estimation test (**Table 5**). **Table 4** reports the elasticities, standard error (SE), probability and t-statistics of all model variables, where

the food production index was the dependent variable. Food security was found to have a positive and statistically significant relationship with it that was explained by its lag values. The result indicates that one percent change in the lag values leads to 0.60 percent increase in food security of selected countries. Similarly, CPI inflation also had a positive and statistically significant relationship with the food security of selected countries. This type of positive relationship suggests that the price of agricultural output is a key motivation for farmers to grow more and more food. The estimated result shows that one percent change in the inflation leads to 0.40 percent increase in food production in the selected countries (Oglu, 2018).

The estimated results show that food import has a positive impact on the food security of Azerbaijan, Singapore, Austria, Georgia and Hungary. The empirical results show that the flow of food import has a positive and significant impact on food security because the national food security of these selected countries largely depends on the import of food products. The coefficient of food import suggests that 1 percent of increase in food import could lead to 0.05 percent increase in national food availability in the selected economies. The evidence exists which supports this long-term positive relationship (Zahrnt, 2011). But long-term estimates show that the food export index has a negative and significant impact on the access to food security. The food export leads to an increase in food insecurity in the selected economies. The estimated results show that one percent change in food export leads to a reduction in the domestic food availability by 0.05 percent. The results suggest that the governments of the selected countries and certain developmental organisations make efforts to achieve national food security through indigenous agricultural interventions, which should support domestic growers by investing in agricultural education and skill development, and infrastructure programs. The ratio of income per capita to and the foreign direct investment to GDP of the selected economies positively affects food security. The estimated coefficient of income per capita and foreign direct investment suggests that one percent increase in the income per capita and FDI inflow leads to an improvement of 0.16% and 0.08% in the access to food security on the long-term, respectively. Similarly, HDI as a proxy of human capital and development also has a positive and significant impact on long-term food security dynamics. The coefficient of HDI in the selected economies is interpreted as one percent increase in the quality of human capital that leads to an improvement of 0.045 percent in national food utilisation on the long-term. HDI actually determines food utilisation at national level. The results suggest that human development played a significant role to achieve the sustainable and long-lasting food security goals.

Table 4

Results of Panel GMM estimation approach

System dynamic panel-data estimation				
Dependent Variable: Food Production Index				
	Coef.	**Std. Err.**	**T-Stat**	**Prob.**
lnFPI$_{t-1}$	0.60***	0.08	7.15	0.00
lnCPI	0.40***	0.12	3.41	0.00
lnFII	0.05***	0.02	3.06	0.00
lnFEI	-0.05***	0.01	-3.41	0.00
lnPCGDP	0.16**	0.07	2.15	0.04
lnFDIGDP	0.08**	0.03	2.46	0.02
lnHDI	0.045	0.08	0.55	0.81
Constant	-0.97***	0.18	-5.43	0.00
Wald chi2(8)		285.76	**Prob > chi2**	0.00

Legend: * p<0.10; ** p<0.05; *** p<0.01

Table 4 results disclose that the long-term coefficient of food import has a significant and positive effect on food production, it indicates that the selected countries' governments are successfully filling in the local food supply and demand gap. The GDP per capita, inflation, FDI and HDI also have a positive and significant impact on food security. In these economies, rural people have limited purchasing power, therefore, they face many problems to access and afford food because of poverty. The rapid urbanisation and urban population growth are inversely correlated to national food security.

Table 5

Sargan post-estimation test

Sargan Identification Restrictions test	
H_0: Over Identifying Restrictions are Valid	
Model Post Estimation Results	
chi2(277)	67.31737***
Prob > chi2	0.0002

Legend: * p<0.10; ** p<0.05; *** p<0.01

Table 5 above reports the results of the Sargan test post-estimation for examining the reliability of the model. The Sargan test examines the over identification restrictions of the model. The results show that there was no problem of over identification restrictions in the model and that instrumental variables were uncorrelated with the error term and were correctly specified. The estimated value of the chi square was greater than the critical value of 1,5, while the level of significance was 10 percent.

5. CONCLUSIONS AND POLICY RECOMMENDATIONS

This paper aimed to analyse the dynamics of regional food security in the selected countries, such as Azerbaijan, Singapore, Austria, Georgia and Hungary, by using the panel GMM approach. This approach recommends that food import, FDI, income per capita, inflation and HDI have a positive impact on the dynamics of the national food security in the selected economies. The findings indicate that food security is associated with caloric availability and food consumption in some aspects but not completely. A study by Warrant et al. (2015) similarly found a positive relationship between food availability and food intake and consumption level. It is also essential to identify that food availability does not necessarily attain and improve health and nutritional outcomes (Berti et al., 2004). Our findings suggest a direction for upcoming research: to investigate the health and nutritional characteristics of food security at regional, national and household levels. On the other hand, food export has a negative impact on food availability and access. This finding is quite comparable to existing studies because they also examined food security dynamics and its linages with socio-economic determinants and human development. Evidence reveals that food import provides a greater access to exclusive food baskets, such as fruits and vegetables, which might increase national food security, and the food accessibility and utilisation of adequate healthy food. Future food security research should also focus on food availability, diversity and quality, more specifically, on vegetable and fruit consumption.

Normally, in the less developed countries, there is a limited adaptive and innovation capacity to develop agriculture, besides there is a limitation on small farmers' agricultural production, and on the creation of income and investment. Our findings show that agriculture may be the only source of rural household income in these countries. The agriculture sector promotes food security by providing income for rural households, to meet their daily needs including the purchase of food. The findings suggest that future food security studies should assess the role of agriculture on intra-household distribution of food (e.g. to vulnerable groups of rural households like children and women).

Food import in these economies was seen as an effective policy that improved food security at national level and regional level. However, for achieving the sustainable food security goals, trade liberalisation and more economic integration is required, which could bring mutual benefits. These types of trade policies will contribute immensely to the improvement of national and regional food security. Moreover, the GDG 2 (sustainable development goals) target the eradicating of hunger and malnourishment and the attainment of sustainable food security in such countries like Azerbaijan, Singapore, Austria, Georgia and Hungary by the end of 2030. The present paper also helped to provide new knowledge and to enable policymakers to overcome the problem of food insecurity. As we have shown, human development has a potential impact on regional food security dynamics. Although human development is valuable due to its comparability across regions (Maxwell et al., 2008), it may not be the best indicator for food security. Thus, the present study suggests that future studies should pay attention to food access and utilisation in order to achieve long-term food security. This study suggests that the governments of the selected countries and developmental organisations, in their efforts to achieve national food security through indigenous agricultural interventions, should support domestic growers by investing in agricultural education and skill development, and infrastructure programs.

R e f e r e n c e s

ADB. (2006) Central Asia: Increasing Gains from Trade Through Regional Cooperation in Trade Policy, Transport, and Customs Transit. Philippines: Asian Development Bank.

Berti, P.R., Krasevec, J., M.T.Gamian (2004) A review of the effectiveness of agriculture interventions in improving nutrition outcomes. *Public Health Nutrition*, 7(5), 599–609.

Asatiani, S. (2009). Food security concept, condition and trends in Georgia. *IBSU Scientific Journal*, 3(2), 35-54.

Calicioglu, O., Flammini, A., Bracco, S., Bellù, L. & Sims, R. (2019) The future challenges of food and agriculture: An integrated analysis of trends and solutions. *Sustainability* 11(1), 222.

Carter, K. N., Lanumata, T., Kruse, K. & Gorton, D. (2010) What are the determinants of food insecurity in New Zealand and does this differ for males and females? *Australian and New Zealand Journal of Public Health* 4(6), 602-608.

Chaaban, J., Ghattas, H., Irani, A., & Alban, T. (2018) Targeting mechanisms for cash transfers using regional aggregates. *Food Security* 10(2), 457–472.

Chandra, A. C. & Lontoh, L. A. (2010) Regional food security and trade policy in Southeast Asia: The role of ASEAN. Manitoba: International Institute for Sustainable Development.

Dávid, L. & Szűcs Cs. (2009) Building of networking, clusters and regions for tourism in the Carpathian Basin via information and communication technologies. *NETCOM - Networks and Communications Studies* 23:1-2. 63-74.

FAO (2015) FAOSTAT statistics database. Food Balance Sheets (Updated Feb 2017).

FAO (2003) World summit on food security: Draft declaration of the world summit on food security. Rome: FAO.

Farmar-Bowers, Q. (2015) Finding ways to improve Australia's food security situation. Agriculture, 5(2), 286-312.

Feizizadeh, B., Pourmoradian, S. & Pourmoradian, S. (2015) Food Security Assessment Based on GIS Spatial Analysis in the Rural Area of East Azerbaijan Province, Iran. GI_Forum, 475-483.

Godor, A. K. (2016) The Major Trends of Food Consumption in Hungary. *Deturope-The Central European Journal for Regional Development and Tourism* 8(3), 202-211.

Godrich, S. L., Davies, C. R., Darby, J. & Devine, A. (2017) What are the determinants of food security among regional and remote Western Australian children? *Australian and New Zealand Journal of Public Health*, 41(2), 172-177.

Hameed, M., Moradkhani, H., Ahmadalipour, A., Moftakhari, H., Abbaszadeh, P. & Alipour, A. (2019) A Review of 21st Century Challenges in Food-Energy-Water Security in the Middle East. *Water* 11(4), 682.

Herrmann, M. (2009) Food security and agricultural development in times of high commodity prices (No. 196). United Nations Conference on Trade and Development.

Islam, M. & Wong, A. (2017) Climate change and food in/security: A critical nexus. *Environments* 4(2), 38.

Keszi A. Szeremlei & Magda R. (2015) Sustainable production and consumption. *Visegrad Journal on Bioeconomys and Sustainable Development* 4 (2) pp. 57-61.

Marzęda-Młynarska, K. (2017) Food Security Governance in the Southeast Asia Region: from National to Regional Governance. *Historia i Polityka* 27(20), 31-48.

Maxwell, D. & Caldwell, R. (2008) Measuring food insecurity: can an indicator based on localized coping behaviours be used to compare across contexts? *Food Policy* 33, 533-540.

McKay, F. H., Haines, B. C. & Dunn, M. (2019) Measuring and Understanding Food Insecurity in Australia: A Systematic Review. *International Journal of Environmental Research and Public Health*, 16(3), 476.

Nemes, G., & High, C. (2013) Old institutions, new challenges: the agricultural knowledge system in Hungary. *Studies in Agricultural Economics*, 115(2), 76-84.

Oglu, A. Z. H. (2018) Agriculture in Azerbaijan and its Development Prospects. *International Journal of Medical and Biomedical Studies* 2(4).

Popp, J (Ed.), Lakner, Z. (Ed.), Judit Oláh (Ed.) (2020) Sustainability in Food Consumption and Food Security Basel, Switzerland, *Sustainability*, MDPI, 239.

Schlichting, D., Hashemi, L. & Grant, C. (2019) Infant food security in New Zealand: A multidimensional index developed from cohort data. *International Journal of Environmental Research and Public Health* 16(2), 283.

Smith, C. (2011) Barriers and solutions to achieving food security for New Zealand families (Doctoral dissertation, University of Otago).

Stevens, G.A., Bennett, J.E., Hennocq, Q., Lu, Y., De-Regil, L.M., Rogers, L., Danaei, G., Li, G., White, R.A. & Flaxman, S.R. (2015) Trends and mortality effects of vitamin A deficiency in children in 138 low-income and middle-income countries between 1991 and 2013: a pooled analysis of population-based surveys. *Lancet Glob. Health* 3, e528–e536. https://doi.org/10.1016/S2214-109X(15)00039-X.

Stevenson, S. (2013) Edible impact-Food security policy: A review of literature and synthesis of key recommendations for Toi Te Ora-Public Health Service.

Svanidze, M., Götz, L., Djuric, I. & Glauben, T. (2019) Food security and the functioning of wheat markets in Eurasia: A comparative price transmission analysis for the countries of Central Asia and the South Caucasus. *Food Security* 1-20.

Tortajada, C. & Zhang, H. (2016) Food policy in Singapore. *Elsevier Food Sciences* 1-7.

UN. (2015) Transforming Our World: The 2030 Agenda for Global Action. United Nations, New York Online available at: https://www.eda.admin.ch/content/dam/ agenda2030/en/documents/recent/7603-final-draft-outcome-document-UN-Sept- Summit-w-letter-08072015_EN.pdf

Vasa, L (2002) Behaviour patterns of farm managing households after the agricultural restructuring – socio-economic analysis. Journal of Central European Agriculture 1 (3) pp. 312-320

Vasa, L. (2005) Economic coherences between food consumption and income conditions in the Hungarian households. Annals of Agrarian Sciences, Vol. 1. pp. 228-232.

Vásáry, M., Vasa, L. & Baranyai, Zs. (2013) Analysing competitiveness in agro-trade among visegrad countries Actual Problems of Economics 150 (12) pp. 134-145.Warren, E. & Hawkesworth, S. (2015) Investigating the association between urban agriculture and food security, dietary diversity, and nutritional status: a systematic literature review. *Food Policy* 53, 54–66.

Zahrnt, V. (2011) Food security and the EU' s common agricultural policy: Facts against fears (No. 01/2011). *ECIPE working paper*.

Zsarnoczky, M., Zsarnoczky-Dulhazi, F., Gogo Fredrick Collins Adol, Barczak, M., David, L.D. (2019) Food Safety Challenges in the Tourism Processes. *Rural Sustainability Research* 41 (336) 26-31.

USING OPTICAL SATELLITE AND AERIAL IMAGERY FOR AUTOMATIC COASTLINE MAPPING

Domenica COSTANTINO [1] , Massimiliano PEPE [1] , Gino DARDANELLI [2],*
and Valerio BAIOCCHI [3]

ABSTRACT:
The continuous availability and rapid accessibility to multispectral data from satellite platforms within the Copernicus Programme represents a great opportunity for users in different fields of applications as: agriculture, observation of coastal zones, monitoring land cover change. The aim of this paper is to identify a suitable method to map coastline using Sentinel-2 optical satellite image. The method provides the use of two indexes developed in remote sensing field for water environment: NDWI (Normalized difference water index) and MNDWI (Modified Normalized difference water index). Starting from the construction of maps of these indexes and, identifying appropriate threshold values, it has been possible to extrapolate the coastline. The coastlines derived from the use of the NDWI and MNDWI index were compared with a coastline obtained from the photointerpretation of a very high resolution orthophoto obtained through photogrammetric techniques. The results show that it is possible to map the coastline automatically and quickly with an intrinsic accuracy close to the geometric resolution bands of Sentinel-2 satellite images.

Key-words: Sentinel-2, optical satellite images, Coastline; NDWI; MNDWI; cliffs; photogrammetry.

1. INTRODUCTION

Coastline mapping and coastline change detection are critical for safe navigation, coastal resource management, coastal environmental protection, sustainable coastal development and planning in many coastal zone applications (Di et al., 2003). Several coastline definitions are reported in literature, one of the most spread is the portion of land that contains the emerged and submerged areas and is subject to continental and marine geomorphologic processes (Dominici et al., 2019). Mapping the coastline and its evolution is of fundamental importance since most of the coasts (from 24% to 70%) are subject to the erosion phenomenon (Sui et al., 2020; Mentaschi et al., 2018; Zhou et al., 2017). Italy's coast is approximately 8300 km. long, recent studies have shown that on the Italian coasts, in the period between 2000 and 2007, over 37% of the coastline suffered variations of over 10 m and about 1000 km of coastline are subject to erosion. In particular, many areas of Salento (Southern Italy) are subject to continuous phenomena of collapse of the rocky coastline. The last collapse took place on December 8, 2019 where there were rock falls generating damages from a geological and landscape point of view.

A variety of data sources are available to observe the variation of the coastline. Potential data sources for coastline investigation include historical photographs, coastal maps and charts, aerial photography, beach surveys, in situ geographic positioning system shorelines, and a range of digital

---
[1]*Politecnich of Bari, DICATECh, 70125 Bari, Italy; domenica.costantino@poliba.it,*
   massimiliano.pepe@poliba.it
[2]*Università degli Studi di Palermo, 90128 Palermo, Italy; gino.dardanelli@unipa.it*
[3]*Sapienza University of Rome, Department of Civil, Constructional and Environmental Engineering, I-00184*
   Rome, Italy, Valerio.Baiocchi@uniroma1.it

elevation or image data derived from remote sensing platforms (Boak & Turner, 2005; Holman & Haller, 2013; Harley et al., 2019). High and very high resolution satellite images and the related feature extraction techniques have proven to be particularly suitable for these applications (Teodoro, 2016). Further benefits are identified in rapid and more frequent data acquisition, faster and more automated processing and a greater sampling intensity, such as in the case of Sentinel-2 images.

Mapping the coastline, to distinguish water bodies from land surfaces, is an important activity in the field of Remote Sensing. Indeed, the exponential growth of satellite-based information over the last decade offers opportunities for mapping coastal lines.

Starting from the Landsat missions, it was possible to detect surface water body changes in the last three decades for the entire globe (Pekel et al., 2016, Aguilar et al., 2010). In addition, the increasing availability of multispectral images from satellite, airplane, UAV and terrestrial, combined with recent developments in automatic image processing algorithms, are making possible more and more complex applications in the environmental and surveying field in general (Palazzo et al., 2012; Mentashi et al., 2018; Lo Brutto & Dardanelli, 2017; Baiocchi et al., 2010; Baiocchi et al., 2014).

In order to extract water bodies from different remote sensing images, various methods have been developed. The methods of water body extraction can generally be divided into two categories, i.e. one is the traditional supervised/unsupervised classifications using single or multiple bands and the other one based on the water-related spectral index and threshold-based approach (Casadei et al., 2019) or using thermal imagery (Costantino and Angelini, 2016).

In water environment, two indexes for water mapping are widely used, the Normalized Difference Water Index (NDWI) and the modified NDWI, called MNDWI. NDWI index was developed by McFeeters (1996) using near-infrared (NIR) and green band from Landsat TM in order to delineate open water features according to the following terms:

$$NDWI = \frac{Green - NIR}{Green + NIR} \qquad (1)$$

NDWI was introduced by McFeeters [1996] to difference land surface water and vegetation in Landsat TM images and modified by Xu [2006] that changed the combination of the bands.

NDWI, as well as the earlier NDVI, presents a range of variability between -1 and 1: considering the spectral signatures of the same 3 main categories, the sequence, compared to NDVI, is reversed with the water characterized by high values (Maglione et al., 2014).

This index was used with success in several case studies in water body identification (Saeed & Fatima, 2016; Parente & Pepe, 2018). Although the NDWI could suppress and remove the non-water features, it failed to efficiently suppress built-up ground signals. As consequence, the extracted characteristics could be a mixture of water and accumulated earth noises (Toure et al, 2019). For this reason, subsequently, Xu (2006) modified NDWI and named after MNDWI by replacing origin NIR band with shortwave-infrared (SWIR) obtaining:

$$MNDWI = \frac{Green - SWIR}{Green + SWIR} \qquad (2)$$

and MIR (middle infrared) band (Wang et al., 2018).

The specific application to the single spectra of the indexes described may vary depending on the images used (Maglione et al., 2015); for the Sentinel images used in this experiment it is reported in more detail below under the specific paragraph 2.3.

MNDWI index produces three results: (i) water will have greater positive values than in the NDWI as it absorbs more MIR light than NIR light; (ii) built-up land will have negative values as mentioned above; and (iii) soil and vegetation will still have negative values as soil reflects MIR light more than NIR light and the vegetation reflects MIR light still more than green light (Jakovljević et al., 2019). Therefore, taking into account the high temporal and spectral resolution of Sentinel-2 images, the NDWI and MNDWI indexes was tested on three studies area in order to evaluate the potential of the latter indexes in mapping coastlines automatically and quickly. To evaluate the results on accuracy about the developed method, a comparison with high-resolution orthophotos derived from the aerial photogrammetric method was performed.

2. MATERIALS AND METHODS

2.1. Study areas

In this paper, three test areas have been considered. In particular, these areas are located along the coasts of the Apulia region, in South Italy, as shown in **Fig. 1**.
The first area under investigation ("polygon A") stretches about 2 km and it is a portion of the Salento coast. In particular, the area is northern of the city of Otranto (Lecce) and is characterized by high and rocky coasts (**Fig. 2**).

(a)   (b)
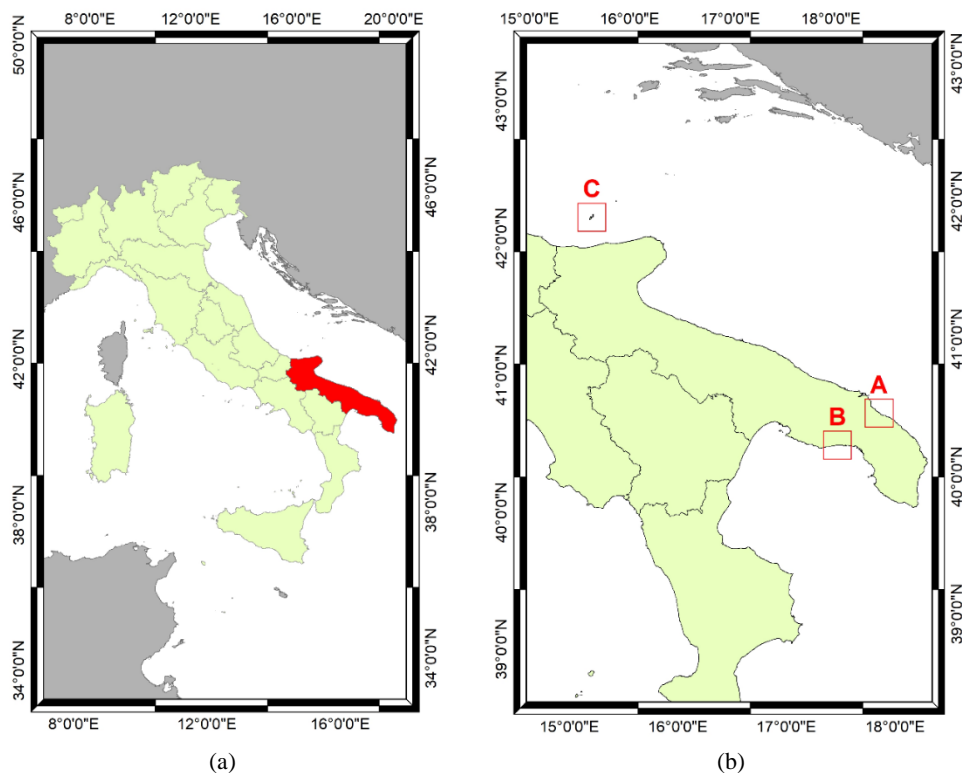
Fig. 1. Identification of the area of interest: localization of Apulia Region in South Italy (a) and localization of three area studies (b).

(a)   **(b)**

Fig. 2. Identification of the study area called "A" (approximate geographic coordinates: 40°15' 16.30"N, 18°26'38.68"E, WGS84) (a) and panorama image of the cliff (b).

In this area, it is possible to identify the presence of "cliffs" with rocky walls that descend steeply to the sea, and are continuously subject to the action of the sea. The cliffs are characterized by typical elements: base, crest, flat surface, face (inclined surface exposed to the sea with steepness up to 90°), cone, where there is loose material of varying sizes, accumulated at the base and consisting of the deposit of rock debris. The crags are in permanent evolution; the erosive process involves a continuous loss of territory ranging from 2 mm to 2 m per year.

The second area is located on the Ionian coast of the Apulia region "polygon B". This area is characterized mostly sandy coastline, as shown in **Fig. 3**.

The third study area concerns the island of San Domino, within the Trèmiti Islands (or Diomedèe, from the Greek Diomèdee). The Trèmiti Islands are an archipelago of the Adriatic Sea located about 20 km north of the Gargano promontory, the northern part of the Apulia region. The islands are characterized by rocky coasts, composed of calcareous deposits, referring to Cenozoic marine successions, and Quaternary deposits consisting of continental successions. The island of San Domino (**Fig. 4**) covers an area of about 208 ha (a length of 2,600 meters and a width of 1,700 meters) with a coastal development of 11,000 metres.

(a)   (b)

Fig. 3. Identification of the study area called "B" on Google Earth platform (approximate geographic coordinates: 40°17'42"N, 17°31'18"E, WGS84) (a) and a particular of the coastline (b).

Fig. 4. Identification of the San Domino Island (the whole island is the area called "C") on Google Earth platform (approximate geographic coordinates: 42°06' 50"N, 15°29'15"E, WGS84.

It should be emphasized that all the study areas are located in areas where the effect of tides in the short term (i.e. the time elapsed between the survey carried out with the different methodologies) is negligible for the determination of the coastline derived through satellite images that have a spatial resolution of at least 10 metres.

2.2. Satellite Sentinel-2 Dataset

According to the accessibility of the images, sensors can be divided into two groups: commercial and free data sources (open data). This latter type of data can be obtained in free, full, and open data policy adopted by the Copernicus and Landsat programs. In this way, it was possible to obtain quickly free multispectral data on global coverage with high temporal resolution. However, the spatial resolution of the images may represent a limitation for some applications.

The Copernicus Sentinel-2 mission consist of a constellation of two satellites polar-orbiting in the same sun-synchronous orbit, phased at 180° to each other (Sentinel-2, 2020).

Frequent revisits of five days at the equator require two identical Sentinel-2 satellites (called Sentinel-2A and Sentinel-2B units) and each one carrying a single imaging payload named MSI (Multi-Spectral Instrument). Sentinel-2 carries an optical instrument payload that samples 13 spectral bands: four bands (blue, green, red and NIR) at spatial resolution of 10 metres, six bands (including SWIR band) at 20 m and three bands at 60 m spatial resolution. The orbital swath width is 290 km.

The coverage limits of Sentinel-2 satellites are from latitudes 56° south to 84° north.

Sentinel-2 products available for users (generated either by the ground segment or by the SENTINEL-2 Toolbox) are listed in the following Table 1.

Table 1.

Sentinel-2 Product Types.

Name	High-level Description	Production & Distribution	Data Volume
Level-1C	Top-Of Atmosphere reflectance in cartographic geometry	Systematic generation and online distribution	≈ 600 MB (each 100 x 100 km)
Level-2A	Bottom-Of Atmosphere reflectance in cartographic geometry	Systematic and on-User side (Sentinel-2 toolbox)	≈ 800 MB (each 100 x 100 km)

Products are a composing of elementary granules of fixed size, along with a single orbit. A granule is the minimum indivisible partition of a product (containing all possible spectral bands). For Level-1C and Level-2A, the granules, also called tiles, are ortho-images in UTM/WGS84 projection.

The satellite optical dataset used for the automatic extraction of the coastline was extracted from the Sentinel open access hub website. In particular, the datasets are reported below.

- "S2B_MSIL1C_20190120T094319_N0207_R036_T33TYE_20190120T115009.SAFE" (acquired on 2019-01-20 at 09:43:19.024Z);
- "S2A_MSIL1C_20150715T094306_N0204_R036_T34TBK_20150715T094315.SAFE" (acquired on 2015-07-15 at 09:43:06.029Z);
- "S2A_MSIL1C_20160702T095032_N0204_R079_T33TWG_20160702T095806" (acquired on 2016-07-15 at 09:50:32.020Z)

All the datasets used in this study are processed at Level-1C.

2.3. Use of the NDWI and MNDWI in Satellite Sentinel-2 Dataset

The NDWI algorithm proposed by McFeeters (1996) is based on (3)

$$NDWI = \frac{\varrho_{green} - \varrho_{NIR}}{\varrho_{green} + \varrho_{NIR}} \tag{3}$$

where ϱ_{green} is the TOA (Top-Of Atmosphere) reflectance value of the green band and ϱ_{NIR} is the TOA reflectance value of the NIR band. Using Sentinel-2 images, the NDWI, can be calculated by following formula:

$$NDWI = \frac{\varrho_3 - \varrho_8}{\varrho_3 + \varrho_8} \tag{4}$$

where ϱ_3 is the TOA reflectance value of the green band and ϱ_8 is the TOA reflectance value of the NIR band.

As regards the MDWI index, it can be expressed as:

$$MNDWI = \frac{\varrho_{green} - \varrho_{SWIR}}{\varrho_{green} + \varrho_{SWIR}} \tag{5}$$

where ϱ_{green} is the TOA reflectance value of the green band and ϱ_{SWIR} is the TOA reflectance value of the SWIR band. Using Sentinel-2 images, the MNDWI, the previous formula becomes [19]:

$$MNDWI = \frac{\varrho_3 - \varrho_{11}}{\varrho_3 + \varrho_{11}} \tag{6}$$

where ϱ_3 is the TOA reflectance value of the green band and ϱ_{11} is the TOA reflectance value of the SWIR band. It is important to empathize that while the band 3 has a geometric resolution of 10 m, the band 11 has a resolution of 20 m.

2.4. Method

The Sentinel-2 bands can be imported in a GIS (Geographic Information System) environment, such ArcGIS (developed by ESRI Company) or Quantum GIS software. Since it is required to calculate the RS indexes, i.e. the NDWI and the MNDWI, only the bands necessary for the calculation of these indices are imported into the software. In addition, in order to speed up the processing time,

the images (raster) can be clipped in relation to the area under investigation. Next, using map algebra operations, the RS indexes can be obtained. In particular, it is necessary to perform the normalized ratio between the bands taken into consideration.

As known, the NDWI index varies between -1 and 1; usually water features have positive values and thus are enhanced, while vegetation and soil usually have zero or negative values and therefore are suppressed (Palazzo et al., 2012).

Since some regions of the observed scene, such as the built-up region, can change the usual threshold values or introduce a noise in the image, it is necessary to apply the criterion of Maximum Likelihood classification, which is a supervised classification method based on the Bayes theorem (Du et al., 2016; Ahmad & Quegan, 2012). In this way, several training areas (water, not-water) can be identified within the study area. Indeed, in binary classification image, 0 indicates a land pixel and 1 indicates a water pixel.

The same approach applied to the NDWI index can also be applied to the MNDWI index. Since the band 11 has a different spatial resolution, before to perform the calculation of MNDWI index, it was necessary to resample this band to the same size as the other bands, i.e. at resolution of 10 metres.

This task can be obtained in the several ways (geometric interpolation, pan-sharpening, etc.); in this case study, a resample with "cubic" interpolation was adopted. Indeed, this latter interpolation performs a cubic convolution and determines the new value of a cell based on fitting a smooth curve through the 16 nearest input cell centres. The consequent loss of data is in any case to be considered limited and the overall integrity of the data is guaranteed.

Once identified the water and not-water regions using both indexes, it is possible to obtain the coastlines quickly using the tools developed in GIS software.

This task may be realized by conversion from "raster to vector". In order to improve the quality of the coastlines derived by this latter automatic process, an operator's editing may be necessary.

The coastline derived by the application of RS indexes must be compared with one obtained by the photo-interpretation of the orthophoto with higher geometric resolution. The orthophoto can be carried out by the use of images acquired UAV (Unmanned Aerial Vehicle) platform or airborne imagery. In this way, according a photogrammetric pipeline processing, it is possible to obtain a 3D model and so a high geometric quality of the orthophoto.

Therefore, it is possible to define strategic transects and evaluate transect by transects the difference (d_i) between coastline derived by photo-interpretation (reference) and the coastline obtained by the application of RS indexes.

This task may be realized in commercial computer-aided design (CAD) software or GIS commercial or open source.

As regards the evaluation of the accuracy, we decided to use the classical statistics parameters: maximum, minimum, mean and standard deviation (σ).

The formula used for the calculation of the standard deviation is intended as:

$$\sigma = \sqrt{\frac{\sum_{i=1}^{n}(d_i - \bar{d})^2}{n-1}} \tag{7}$$

Where:

n   number of transects;

d_i distance between the coastline calculated by remote sensing (NDWI and MNDWI) indexes and the reference coastline;

$\bar{d}$ mean of d_i values.

The pipeline of the method developed can be summarized as shown below (Figure 5).
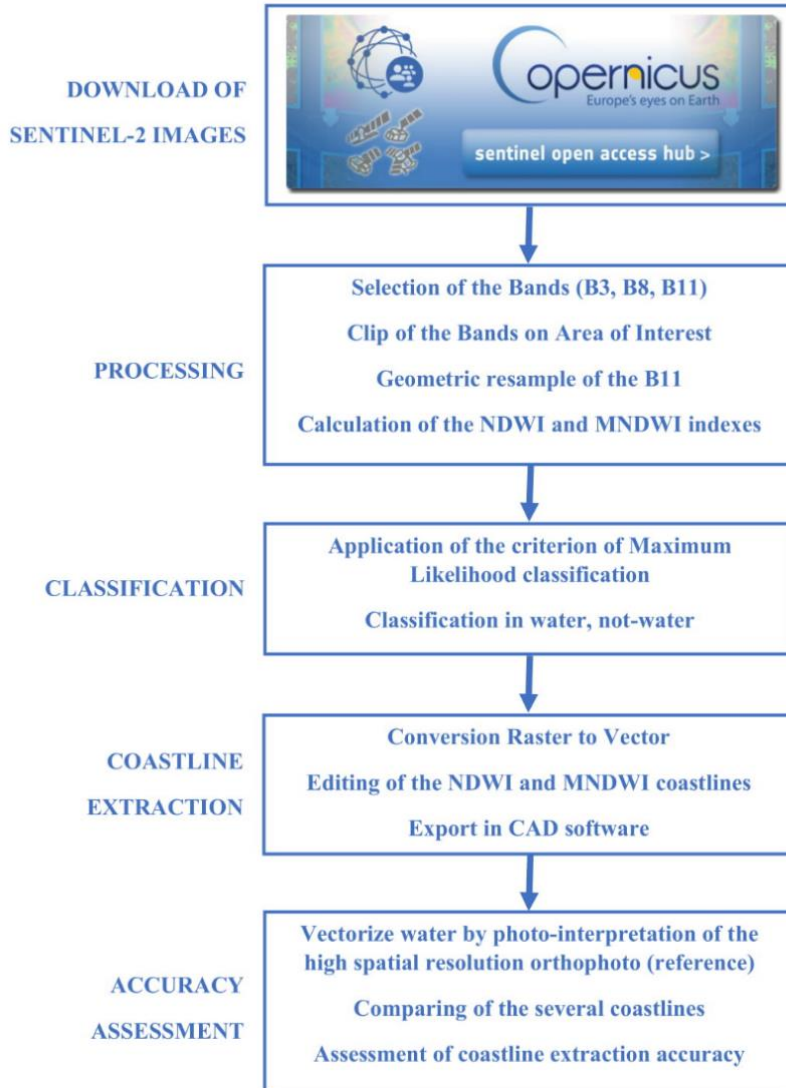

Fig. 5. Pipeline of the developed method to evaluate the assessment of coastline extraction using sentinel-2 images and NDWI-MNDWI indexes.

3. RESULTS

3.1 Application of the RS indexes

Before the elaboration of RS indexes, a clip of the single bands on the AOI (Area of interest) was performed; the elaborations of the NDWI and MNDWI indexes were performed using raster

calculator implemented in a GIS environment. Both the indexes were obtained at the geometric resolution of 10 metres (**Fig. 6**). In the case of the estimation of the MNDWI, the SWIR band was resampled at a higher geometric resolution by the use of "cubic" interpolation that is implemented in "resample" tool of ArcMap software.

(a)   (b)
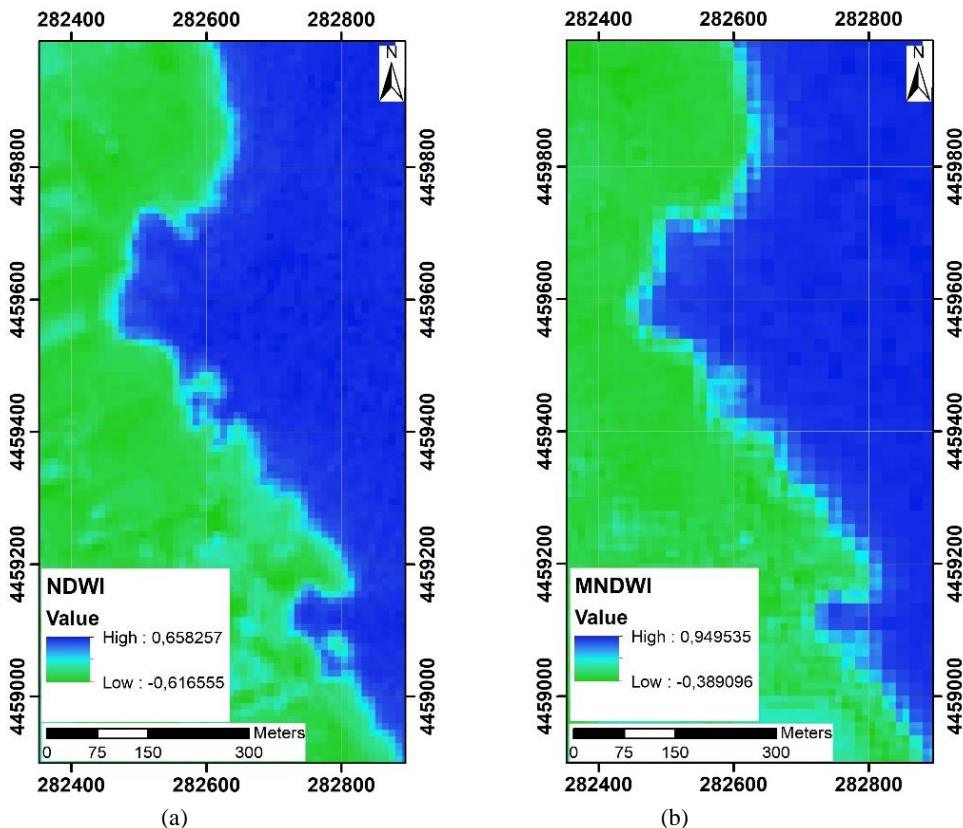
Fig. 6. Raster values of RS indexes of test site "A", represented in Universal Transverse of Mercator (UTM)-zone 34 North reference system: NDWI (a) and MNDWI (b).

3.2. Coastline extraction by the use of photogrammetric techniques, oblique and nadir aerial images

3.2.1. Photogrammetric approach

To assess the accuracy of the coastline extracted from satellite images, it was compared with a coastline obtained from aerial images processed with the SfM/MVS approach (Structure from motion/Multi View Stereo) approach. Through this approach, it is possible, starting from a set of images, to obtain a three-dimensional model of the acquired scene. Structure from Motion (SfM) allows reconstructing the geometry of the scene from a limited set of points identified on a bundle of images. The output of the process is the sparse Point Cloud (PC) and the external orientation (EO) of the images. Using the Multi-View Stereo technique, it is possible to obtain a dense reconstruction of a static scene and, consequently, densify the point cloud obtained in the previous SfM approach. Subsequently, a texturized mesh model is constructed from the dense point cloud. Once generated the polygonal mesh, it is possible to build a colour orthophoto of the observed scene.

3.2.2. Sensor and Flight planning

Presently, a variety of image-based sensors can be used for 3D photogrammetric documentation, indeed, the images can be acquired with different types of sensors, such as CCD/CMOS (Charge Coupled Device/complementary metal-oxide semiconductor) sensors, frame, linear, multiple head, (Digital single-lens reflex) DSLR-type, etc. For this project the aerial survey was performed with a Nikon D5500 digital SLR with 24.2-megapixel resolution and an ultra-fast autofocus system with dual contrast and phase detection modes. A Nikkor 18-70 mm lens was used, adopting a focal length of 70 mm for all photos, with ISO values of 1600 (deliberately kept low compared to the maximum of 25600 ISO available to minimize electronic noise). The availability of a high sensitivity and resolution of the sensor, a fast autofocus system (to obtain images always sharp and in focus), a professional lens (very bright and with low aberrations and colour optics), an SD card (Secure Digital) storage class 10 ultra (SDXC ultra-fast for recording images even at maximum resolution and in RAW format without loss of quality) have ensured a safe and comfortable acquisition phase, minimizing the number of unusable photos. The flight plan was realized with strips (or Flight Lines – FLs) along the coast by the use of nadir and oblique images (Pepe et al., 2018). The nadir strips were designed with an 80% overlap at a flight height of about 1000 metres (about 3300 feet) AGL (Above Ground Level). The oblique FLs were designed for 45° image acquisition. In this way, it is also possible to acquire the part of the coast that has significant slopes in the direction of the sea. The entire mission of the aerial survey was carried out with a single-engined aircraft. The flight (photogrammetric) mission was carried out in the middle hours of the day and lasted about 1 hour.

3.2.3. Post-processing of the images

The dense point cloud of the coast was obtained using 3DF Zephyr Aerial software (Pepe et al., 2020); in this way, it was possible to generate three-dimensional models from the acquired images (**Fig. 7**).

Fig. 7. Screenshot of the 3D point cloud and camera poses.

The dense point cloud was georeferenced by means of a rapid static GNSS (Global Navigation Satellite System) survey of the Ground Control Points (GCPs) identified on the acquired photos.

Table 2.

Coordinates of the GCPS, EPSG: 6709

ID Point	East	North	Ellipsoidal height
(#)	(metres)	(metres)	(metres)
1	282835.08	4458952.14	47.41
3	282791.26	4459026.04	46.24
4	282725.49	4459019.82	48.20
6	282668.90	4459126.06	41.40
7	282671.01	4459163.22	43.48
8	282783.46	4459189.18	47.07
9	282639.73	4459250.48	48.90
10	282695.47	4459262.73	48.05
11	282683.06	4459294.32	48.33
12	282636.20	4459390.23	48.35
13	282530.57	4459360.44	51.36
14	282562.04	4459434.99	50.27
15	282509.14	4459531.57	51.32
16	282399.56	4459495.78	54.30
17	282464,75	4459676.75	51.06
18	282553.98	4459748.22	49.77
19	282621.24	4459852.80	49.09
20	282567.27	4459959.39	49.76

In particular, twenty points were surveyed by Leica Viva GS14 GNSS, which is able to receive 120 channels (up to 60 satellites simultaneously on two frequencies). The post-processing of the data was carried out using LGO (Leica Geo Office software ver. 8.4). The spatial coordinates of the GCPs are shown below (Table 2). The accuracy in determining the planimetric coordinates was about 0.05 metres; in this case, the permanent station used for data processing was "Melendugno" of the Italpos CORS network (Continuously Operating Reference Station) (Pepe, 2018), framed in EPSG: 6709; the baselines were about 10 km long. The ellipsoidal heights were converted into orthometric height using a high accuracy geoid local model named ITALGEO05 (Barzaghi et al., 2007), realized by the Politecnico di Milano and distributed by the "Istituto Geografico Militare Italiano" (IGMI, Italian Military Geographic Institute): its resolution is 1' and the overall accuracy is around 0.01 metres. The undulations of the geoid are stored in the form of a grid and with the algorithms developed in Geotrasformer software (Baiocchi et al., 2017). With surveyed GCPs (with orthometric elevation), it was possible to scale the model and, at the same time, to evaluate its precision and accuracy. The precision achieved on photogrammetric model was about 0.08 metres and the accuracy around 0.10 metres. The high number of photos (more than 50) in the project, the high geometric resolution, the high quality of the images and the high coverage of the images have allowed obtaining a very detailed and dense cloud point (over 7 million points) of the study area; more details can be found on (Pepe et al., 2020). Starting from the georeferenced point cloud, the mesh and, subsequently, the colour

orthophoto with a spatial resolution of 0.02 metres were generated. Lastly, a polyline of the coastline (about 2000 metres) was drawn by photo-interpretation in a GIS environment.

3.3 Evaluation of the accuracy of the coastline in the first study area (polygon A)

In addition to performing operations on the individual satellite bands, it is also possible to build a map in false colour or, simply to colour (**Fig. 8a**) in order to obtain a visive information of the study area (Ciritci & Türk, 2020; Zhang & Hou, 2020). The coastlines obtained by NDWI and MNDWI were compared with the coastline obtained through photogrammetric method (**Fig. 8b**).

The difference between the two coastlines, both obtained through the RS indexes, has been measured on transects every 50 metres along the direction of the coast itself. In other words, in 20 transects were measured the normal distance between the coastline obtained by the use of high-resolution orthophoto and the coastline obtained by the use of NDWI and MNDWI. This task was carried out in CAD environment by following steps:

- division of the polyline into equal parts; this operation has created points which, in turn, indicate the place where the transects are carried out;
- in each transect a specific UCS (User Coordinate System) was identified which takes into account the coastline trend taken as reference;

the normal line containing the point was drawn and, of consequence, (along this line) the distance between the coastline (taken as reference) and that obtained by means of the NDWI and MNDWI were measured

(a)   (b)
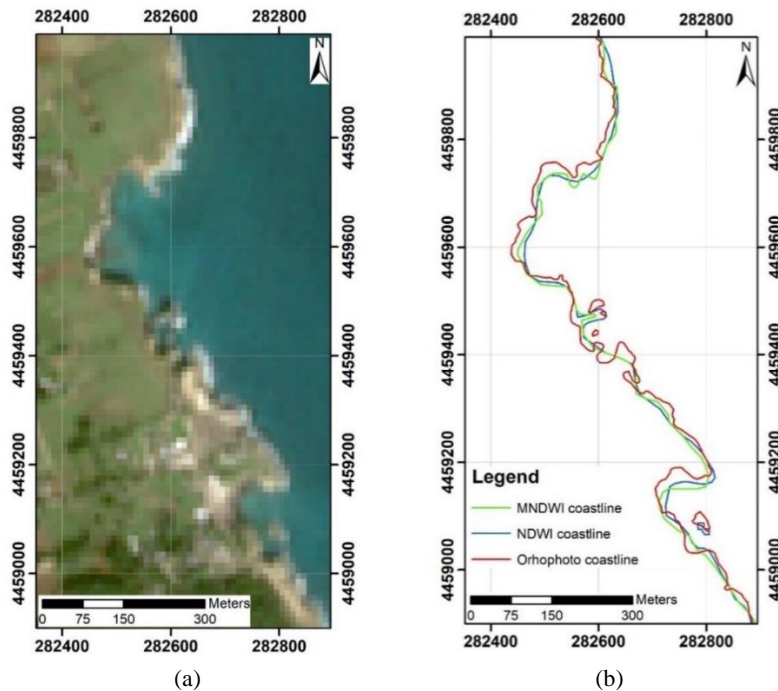
Fig. 8. Raster (a) and vector representation of the coastline of the "A" test site (in WGS84-UTM34N reference system, EPSG: 6709): natural colour composite, bands 432 (Red Green Blue - RGB); coastline obtained by the use of RS indexes and by photo-interpretation of the orthophoto generated by photogrammetric method (b).

The statistics parameters (mean, standard deviation, minimum, maximum) were calculated and are shown below (Table 3).

Table 3.

Statistic parameters about distance between reference coastline and NDWI-MNDWI indexes coastline obtained within the polygon A.

Name	Mean (m.)	Standard Deviation (m.)	Minimum (m.)	Maximum (m.)
Coastline obtained NDWI index	4.52	9.42	-9.80	24.72
Coastline obtained MNDWI index	4.35	10.81	-16.00	16.90

3.4 Evaluation of the accuracy of the coastline in the second area study (polygon B)

In order to obtain more information about the quality of the coastline that can be achieved through the use of the tested indexes and Sentinel-2 images, a second area study was taken into consideration. In particular, the coastline is about 10 km long. The NDWI and MNDWI indices have been calculated using the same procedure used for the first test area. (**Fig. 9a** & **9b**).
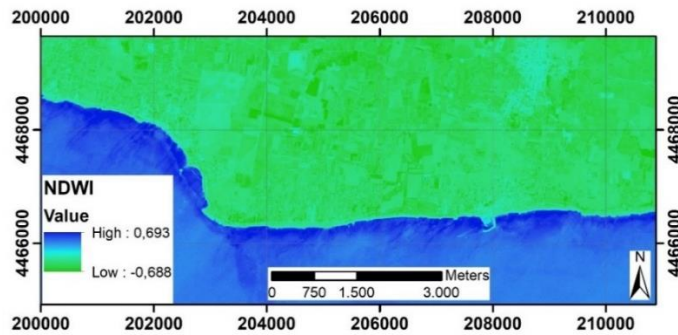
(a)
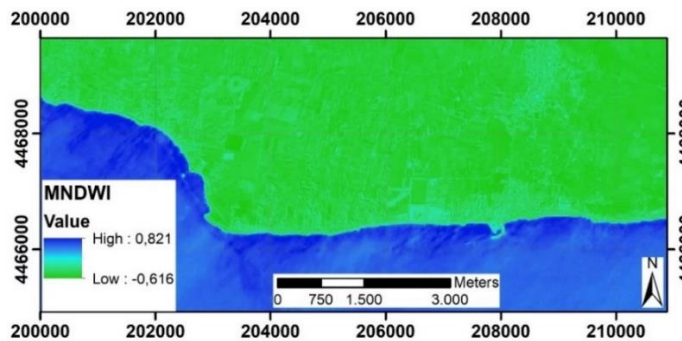
(b)
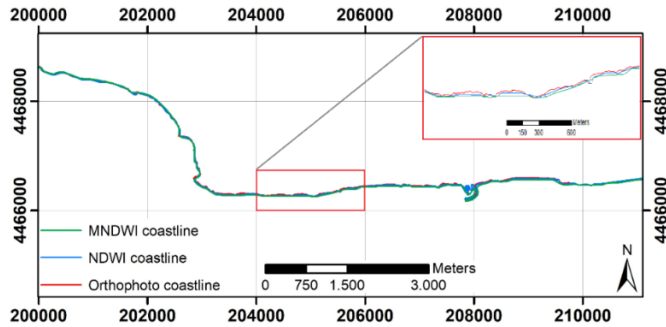
(c)

Fig. 9. Raster and vector representation of the coastline (in WGS84-UTM34N reference system): NDWI (a), MNDWI (b) and coastline obtained by the use of RS indexes and by photo-interpretation of the orthophoto generated by photogrammetric method (c).

Subsequently, the coastline extracted with Remote Sensing techniques were compared with the one obtained with photo interpretation of a high spatial resolution orthophoto (**Fig. 9c**). In this latter case, the orthophoto, generated by traditional aerial-photogrammetric approach, was provided by the administrative body of the Apulia Region. The accuracy of this latter orthophoto is less than 1 m.

In this way, it was possible to calculate the distance between the coastline obtained by photointerpretation and the other obtained by RS techniques. This distance was evaluated along the transects taken into consideration; also in this case 20 of them were considered. The statistic parameters obtained within the polygon B are listed below (see Table 4).

Table 4.

Statistic parameters about distance between reference coastline and NDWI-MNDWI indexes coastline obtained within the polygon B.

Name	Mean (m)	Standard Deviation (m)	Minimum (m)	Maximum (m)
Coastline obtained NDWI index	-5.18	8.27	-21.63	20.37
Coastline obtained MNDWI index	-7.21	15.59	-34.00	28.00

The statistical values obtained in polygon B are comparable to those obtained in polygon A. However, within the polygon B, the MNDWI index showed a higher standard deviation value than NDWI index. This mean that the MNDWI index showed greater uncertainty in determining the coastline under consideration. In addition, the NDWI index has made it possible to better represent the harbour area and the small coves than the MNDWI index. These latter aspects are related to the lower geometric resolution of the native SWIR band.

3.5 Evaluation of the accuracy of the coastline on the third test site.

The accuracy on the determination of the coastline was also evaluated on the island of San Domino, within the Tremiti Islands which represent the third test site that we'll call "Poligon C" as

in Fig. 1b . The evaluation on this additional study area allows us to make further assessments of the accuracy achievable from the indexes tested on Sentinel-2 images. Following the procedure established by the pipeline, the two MNDWI and NDWI indexes have been calculated (see **Fig.10a** and **10b**). Subsequently, it was possible to obtain the three coastlines (**Fig. 10c**) and calculate the differences still on 20 transects. In this case the high resolution orthophoto was provided by the Apulia Regional administration which has a stated scale of 1:5000, more details can be found on the specific web site (sit.puglia.it).
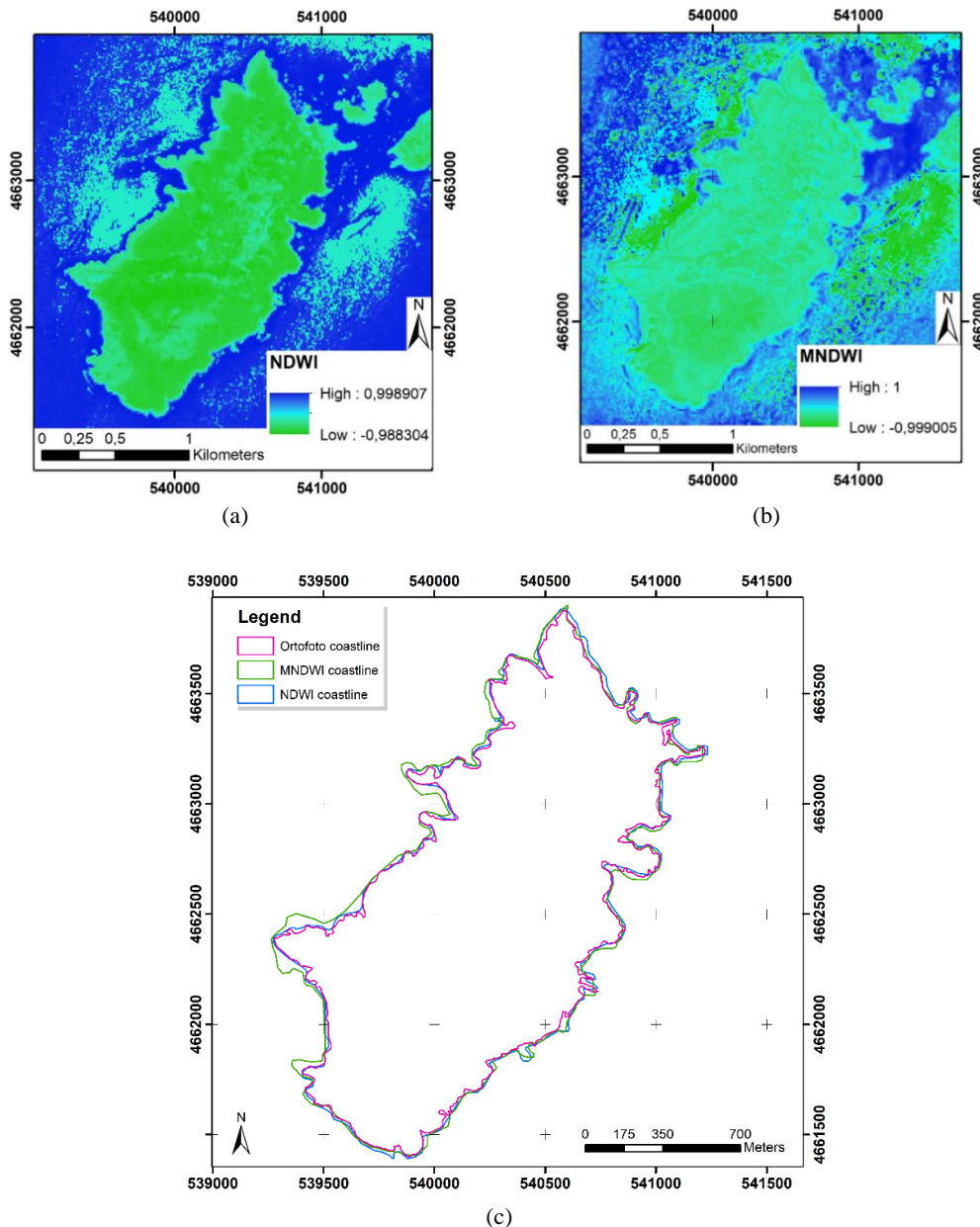

(a)

(b)

(c)

Fig. 10. Raster and vector representation of the coastline (in WGS84-UTM34N reference system) on San Domino Island: NDWI (a), MNDWI (b) and coastline obtained by the use of RS indexes and by photo-interpretation of the orthophoto (c).

The statistical parameters related to the comparison between the various coastlines obtained in Polygon C are shown in the following table 5.

Statistic parameters about distance between reference coastline and NDWI-MNDWI indexes coastline obtained within the polygon C.

	Mean (m.)	Standard Deviation (m.)	Minimum (m.)	Maximum (m.)
Coastline obtained NDWI index	8.66	6.40	-9.34	21.89
Coastline obtained MNDWI index	10.39	10.75	-11.00	-33.77

4. DISCUSSION

Two indexes have been tested along the coasts of all three test sites for a total length of 23.250 km.

The accuracy achieved when comparing coastlines is between 4 and 10 m and with a standard deviation between 8 and 16 m. In addition, the coastlines derived from the two indices tested, are very close to each other. However, the NDWI index, which uses bands at a higher spatial resolution than those used in the MNDWI index, allowed to better discriminate the coasts of small islands.

The statistic results obtained in the several areas respect to NDWI and MNDWI index are reported in the following "whiskers plot" (**Fig. 11**).
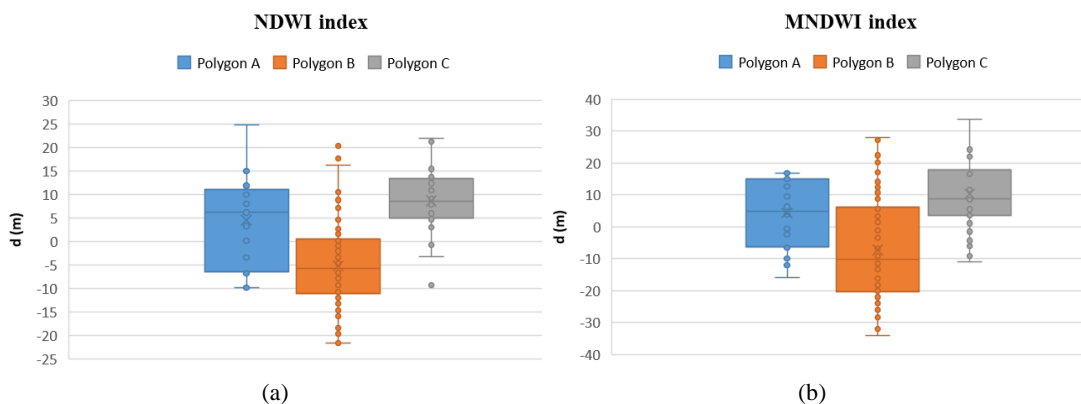
Fig. 11. Statistic evaluation of the accuracy of coastline by remote sensing indexes where on the y-axis the distance d, i.e. the distance between the coastlines calculated by RS index and the reference coastline: NDWI (a) and MNDWI (b).

Figure 11 shows the normal distribution parameters; in particular it is observed that the analysis of transects data using the NDWI index has less dispersion than the MNDWI index. Therefore, in the case of the analysis of the values obtained using the MDNWI index, the values of the population are closer to the average values, i.e. the deviations assume lower values. To validate what has been described above, we analysed how the population of observed data is distributed around the minimum values. To achieve this aim, statistical analysis was carried out using the "Extreme Value Distribution"

(EV) function. This form of the probability density function is suitable for modelling the minimum value, as shown in the case studies. The probability density function for the extreme value distribution with location parameter $\bar{d}$ and scale parameter σ is:

$$y = f(d|\bar{d}, \sigma) = \sigma^{-1} exp\left(\frac{d - \bar{d}}{\sigma}\right) exp\left(-exp\left(\frac{d - \bar{d}}{\sigma}\right)\right) \tag{5}$$

Therefore, it is possible to build suitable graphs about the data distribution in the three case study examinated, as shown in the **Fig. 12**.

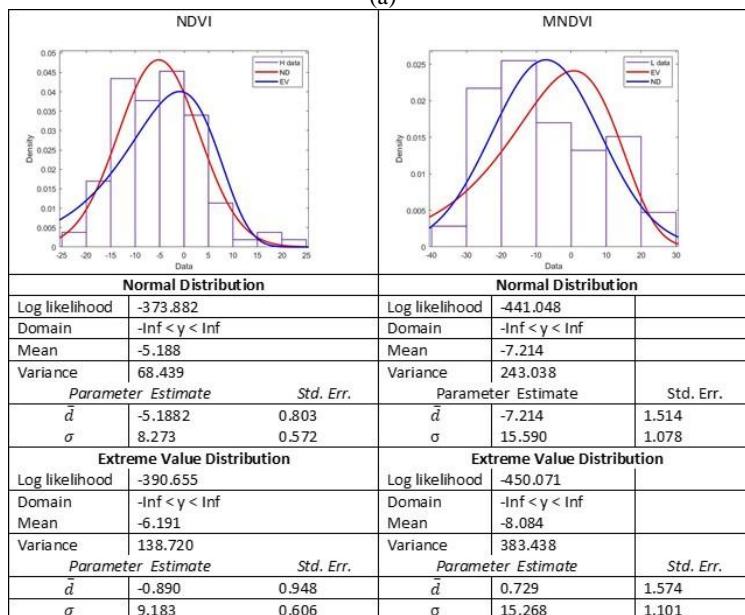| Normal Distribution			Normal Distribution		
Log likelihood	-91.065		Log likelihood	-94.507	
Domain	-Inf < y < Inf		Domain	-Inf < y < Inf	
Mean	4.522		Mean	4.355	
Variance	88.880		Variance	117.061	
Parameter Estimate		Std. Err.	Parameter Estimate		Std. Err.
$\bar{d}$	4.522	1.88552	$\bar{d}$	4.355	2.164
σ	9.428	1.37516	σ	10.819	1.578
Extreme Value Distribution			**Extreme Value Distribution**		
Log likelihood	-92.348		Log likelihood	-93.612	
Domain	-Inf < y < Inf		Domain	-Inf < y < Inf	
Mean	4.048		Mean	4.472	
Variance	126.355		Variance	122.121	
Parameter Estimate		Std. Err.	Parameter Estimate		Std. Err.
$\bar{d}$	9.107	1.857	$\bar{d}$	9.446	1.817
σ	8.764	1.286	σ	8.616	1.409

(a)

Normal Distribution			Normal Distribution		
Log likelihood	-373.882		Log likelihood	-441.048	
Domain	-Inf < y < Inf		Domain	-Inf < y < Inf	
Mean	-5.188		Mean	-7.214	
Variance	68.439		Variance	243.038	
Parameter Estimate		Std. Err.	Parameter Estimate		Std. Err.
$\bar{d}$	-5.1882	0.803	$\bar{d}$	-7.214	1.514
σ	8.273	0.572	σ	15.590	1.078
Extreme Value Distribution			**Extreme Value Distribution**		
Log likelihood	-390.655		Log likelihood	-450.071	
Domain	-Inf < y < Inf		Domain	-Inf < y < Inf	
Mean	-6.191		Mean	-8.084	
Variance	138.720		Variance	383.438	
Parameter Estimate		Std. Err.	Parameter Estimate		Std. Err.
$\bar{d}$	-0.890	0.948	$\bar{d}$	0.729	1.574
σ	9.183	0.606	σ	15.268	1.101

(b)

	Normal Distribution			Normal Distribution	
Log likelihood	-127.233		Log likelihood	-147.482	
Domain	-Inf < y < Inf		Domain	-Inf < y < Inf	
Mean	8.663		Mean	10.397	
Variance	40.958		Variance	115.695	
Parameter Estimate		Std. Err.	Parameter Estimate		Std. Err.
$\bar{d}$	8.663	1.025	$\bar{d}$	10.397	1.722
σ	6.400	0.739	σ	10.756	1.242
Extreme Value Distribution			Extreme Value Distribution		
Log likelihood	-128.309		Log likelihood	-149.482	
Domain	-Inf < y < Inf		Domain	-Inf < y < Inf	
Mean	8.342		Mean	9.893	
Variance	56.408		Variance	165.587	
Parameter Estimate		Std. Err.	Parameter Estimate		Std. Err.
$\bar{d}$	11.723	0.993	$\bar{d}$	15.684	1.703
σ	5.856	0.685	σ	10.033	1.193

(c)

Fig. 12. Plot of the Normal Distribution and Extreme Value Distribution evaluated on the three study areas and related estimated statistical parameters: polygon A (a), polygon B (b) and polygon C (c).

The indication deduced from the normal distribution (ND) of average values and variances confirms the reliability of the method comparable with the spatial resolution of the satellite image. From the analysis of the results obtained through the EV distribution and comparing it with the Gauss distribution, it can be observed that the dataset of the polygon A and C show values comparable to each other and, in any case, comparable with a normal distribution. For the dataset of polygon B, instead, the population of the minimum values has more individuals that present values close to 0, that is, closer to the real trend of the coast. This result is consistent with the morphological structure of the coast.

5. CONCLUSIONS

The use of NDWI or MNDWI indices and the development of an appropriate methodology made it possible to quickly map the coastlines of the area taking into account the free satellite images acquired by the Sentinel-2 platform.
The coastline obtained by the use of these remote sensing indexes was compared with one obtained by aerial photogrammetry. Indeed, this latter approach allowed to obtain a high geometric resolution orthophoto and, as consequence, to obtain a faithful reconstruction of the coastline.
The results show that the mean value of the distance values between the coastline lines extracted through the use of NDWI and MNDWI index than the "real" one is in the order of the sub-pixel of the visible bands of the Seninel-2 images. It should also be considered that generally, it is not possible to find satellite images that match exactly the same time of the data surveyed on the ground or

acquired with aerophotogrammetric acquisition. Even in this study, the acquisitions refer to different times and therefore do not represent exactly the same instantaneous coastline. However, although the results are different in time, in the short acquisition interval between the different methodologies, the variations in time of the coastlines due to tides and possible wave movements are not influential. The purpose of the analysis carried out is not the erosive verification but the evaluation of the accuracy of the methodology adopted. Therefore, the results of the comparison show that the studied methodologies allow to automatically extract the instantaneous coastline in a rapid way and with a precision that can be obtained from this type of satellite images.

R E F E R E N C E S

Aguilar, F.J., Fernández, I., Pérez, J.L., López, A., Aguilar, M.A., Mozas, A. & Cardenal, J. (2010) Preliminary results on high accuracy estimation of shoreline change rate based on coastal elevation models. *Int. Arch. Photogramm. Remote Sens. Spat. Inf. Sci*, 33, 986–991.

Ahmad, A. & Quegan, S. (2012) Analysis of maximum likelihood classification on multispectral data. *Appl. Math. Sci*, 6, 6425–6436.

Baiocchi, V., Camuccio, P., Zagari, M., Ceglia, A., Del Gobbo, S., Purri, F., Cipollini, L., (...), Vatore, F. (2017) Development of a geographic database of a district area in open source environment. *Geoingegneria Ambientale e Mineraria,* 151 (2), pp. 97-101.

Baiocchi, V., Brigante, R., Dominici, D., Milone, M.V., Mormile, M. & Radicioni, F. (2014) Automatic three-dimensional features extraction: The case study of L'Aquila for collapse identification after April 06, 2009 earthquake. *Eur. J. Remote Sens*, 47, 413–435.

Baiocchi, V., Brigante, R. & Radicioni, F. (2010) Three-dimensional multispectral classification and its application to early seismic damage assessment. *Riv. Ital. Telerilevam*, 42, 49–65.

Barzaghi, R., Borghi, A., Carrion, D. & Sona, G. (2007) Refining the estimate of the Italian quasigeoid. *Bollettino di Geodesia e Scienze Affini*, 3, 145-160.

Boak, E.H. &Turner, I.L. (2005) Shoreline definition and detection: *A review. J. Coast. Res*. 21, 688–703.

Casadei, S., Di Francesco, S., Giannone, F. & Pierleoni, A. (2019) Small reservoirs for a sustainable water resources management. *Adv. Geosci*, 49, 165–174.

Ciritci, D. & Türk, T. (2020) Analysis of coastal changes using remote sensing and geographical information systems in the Gulf of Izmit, Turkey. *Environmental Monitoring and Assessment*, 192 (6).

Constantino, D. & Angelini, M.G. (2016) Thermal monitoring using an ASTER image. *Journal of Applied Remote Sensing*, 10(4), 046031.

Dominici, D., Zollini, S., Alicandro, M., Della Torre, F., Buscema, P.M. & Baiocchi, V. (2019) High Resolution Satellite Images for Instantaneous Shoreline Extraction Using New Enhancement Algorithms. *Geosciences* 9, 123.

Di, K., Ma, R. & Wang, J., Li, R. (2003) Coastal mapping and change detection using high-resolution IKONOS satellite imagery. In *Proceedings of the 2003 annual national conference on Digital government research*, 1-4. Digital Government Society of North America.

Du, Y., Zhang, Y., Ling, F., Wang, Q., Li, W., & Li, X. (2016) Water bodies' mapping from Sentinel-2 imagery with modified normalized difference water index at 10-m spatial resolution produced by sharpening the SWIR band. *Remote Sensing*, 8(4), 354.

Harley, M. D., Kinsela, M. A., Sánchez-García, E. & Vos, K. (2019) Shoreline change mapping using crowd-sourced smartphone images. *Coastal Engineering*, 150, 175-189.

Holman, R. & Haller, M. C. (2013) Remote sensing of the nearshore. *Annual Review of Marine Science*, 5, 95-113.

Jakovljević, G., Govedarica, M. & Álvarez-Taboada, F. (2019) Waterbody mapping: a comparison of remotely sensed and GIS open data sources. *International Journal of Remote Sensing*, 40(8), 2936-2964.

Lo Brutto, M. & Dardanelli, G. (2017) Vision metrology and Structure from Motion for archaeological heritage 3D reconstruction: A Case Study of various Roman mosaics, *Acta IMEKO*, 6 (3), 35-44.

Maglione, P., Parente, C & Vallario, A. (2014) Coastline extraction using high resolution WorldView-2 satellite imagery, *European Journal of Remote Sensing*, 47:1, 685-699, DOI: 10.5721/EuJRS20144739

Maglione, P., Parente, C. & Vallario, A. (2015). High Resolution Satellite Images to Reconstruct Recent Evolution of Domitian Coastline. *American Journal of Applied Sciences,* 12(7), 506-515. https://doi.org/10.3844/ajassp.2015.506.515

Mc Feeters, S.K. (1996) The use of the Normalized Difference Water Index (NDWI) in the delineation of open water features. *Int. J. Remote Sens*, 17, 1425–1432.

Mentaschi, L., Vousdoukas, M. I., Pekel, J. F., Voukouvalas, E. & Feyen, L. (2018) Global long-term observations of coastal erosion and accretion. *Scientific reports*, 8(1), 1-11.

Palazzo, F., Latini, D., Baiocchi, V., Del Frate, F., Giannone, F., Dominici, D. & Remondiere, S. (2012) An application of COSMO-Sky Med to coastal erosion studies. *Eur. J. Remote Sens*, 45, 361–370.

Parente, C. & Pepe, M. (2018) Bathymetry from WorldView-3 satellite data using radiometric band ratio. *Acta Polytechnica*, 58(2), 109-117.

Pekel, J.F., Cottam, A., Gorelick, N. & Belward, A.S. (2016) High-resolution mapping of global surface water and its long-term changes. *Nature*, 540, 418–422.

Pepe, M. 82018) CORS architecture and evaluation of positioning by low-cost GNSS receiver. *Geod. Cartogr*, 44, 36–44.

Pepe, M., Costantino, D. & Restuccia Garofalo, A. (2020) An Efficient Pipeline to Obtain 3D Model for HBIM and Structural Analysis Purposes from 3D Point Clouds. *Applied Sciences*, 10(4), 1235.

Pepe, M., Fregonese, L. & Scaioni, M. (2018) Planning airborne photogrammetry and remote sensing missions with modern platforms and sensors. *European Journal of Remote Sensing*, 51, 412–436.

Saeed, A. M. & Fatima, A. M. (2016) Coastline extraction using satellite imagery and image processing techniques. *International Journal of Current Engineering and Technology*, 6(4), 1245–1251.

Sentinel-2 mission, Available online: *https://sentinel.esa.int/web/sentinel/missions/sentinel-2* (accessed on 22 May 2020)

Sui, L., Wang, J., Yang, X. & Wang, Z. (2020) Spatial-temporal characteristics of coastline changes in Indonesia from 1990 to 2018. *Sustainability* (Switzerland), 12 (8), 1-28.

Teodoro, A. C. (2016) Optical satellite remote sensing of the coastal zone environment—An overview. *Environment Applications of Remote Sensing*, InTechOpen, 165-196, London, UK

Toure, S., Diop, O., Kpalma, K. & Maiga, A.S. (2019) Shoreline Detection using Optical Remote Sensing: A Review. *ISPRS Int. J. Geo-Inf*, 8, 75.

Wang, Z., Liu, J., Li, J. Zhang, D. (2018) Multi-Spectral Water Index (MuWI): A Native 10-m Multi-Spectral Water Index for Accurate Water Mapping on Sentinel-2. *Remote Sensing*, 10(10), 1643.

Xu, H. (2006) Modification of normalised difference water index (NDWI) to enhance open water features in remotely sensed imagery. *Int. J. Remote Sens*.

Zhang, Y. & Hou, X. (2020) Characteristics of coastline changes on southeast Asia Islands from 2000 to 2015. *Remote Sensing*, 12 (3).

Zhou, Y., Dong, J., Xiao, X., Xiao, T., Yang, Z., Zhao, G., Zou, Z. & Qin, Y. (2017) Open surface water mapping algorithms: A comparison of water-related spectral indices and sensors. *Water*, 9, 256.

WHAT CAN WE LEARN FROM BROWNFIELD DATABASES? EXPLORING SPECIFICS OF THE LOCATION OF BROWNFIELDS IN THE CZECH REPUBLIC

Jaroslav SKRABAL[1] ⓘD

ABSTRACT:
The aim of this paper is to advance our understanding of brownfield locations in municipalities and cities situated in the Czech Republic. The data on brownfields was obtained from the National Brownfield Database which is coordinated by the CzechInvest Agency in the Czech Republic. The analysed period of the paper are the years 2018 and 2020. In 2018, 460 brownfields were analysed with an area of 2,334.65 hectares and in 2020 there were 572 abandoned buildings and sites with a total area of 2,320.09 hectares. The data on brownfields are based on the regions of NUTS 3 level. Each brownfield was then divided according to its location, i.e. whether it is located in the centre, in the inner part, outer part or within the development area of the municipalities and cities of the given regions. Based on the obtained data, relative proportions within each region were calculated on the NUTS 3 level for the years 2018 and 2020. It was discovered that brownfields are mostly located in the outer parts of municipalities and cities in both analysed years (2018, 2020). Such finding may influence also the possibility of potential brownfield regeneration. Abandoned buildings and sites that are located in the centres or the inner part of municipalities and cities are generally better preconditioned for a potential regeneration and utilization compared to brownfields that are located in the outer parts or on the margins of the cadastral areas of municipalities and cities of the given country.

Keywords: Brownfields, NUTS 3, Location, Spatial Analysis, Czech Republic

1. INTRODUCTION

Spatial planning is considered to be one of the key tools of how to increase the sustainability of cities and contribute to their development on a global scale (UN, 2015). One of the key aspects of sustainable spatial planning is sustainable land use, i.e. more deliberate approach towards which type of land is used for the development of cities. It is particularly necessary with cities with a growing population to take a decision which areas are most suitable for future development. A promising approach seems to be a re-development of formerly used sites that are now vacant, such as brownfields, for new projects of city developments, especially the ones that are situated in central localities (Bartke & Schwarze, 2015). Brownfields are defined as „any land which was formerly used or developed and is now not fully used, even though it can be partially occupied or used as well as unoccupied, vacant or contaminated" (Alker et al., 2000). Another definition emphasizes the need for location and development and it indicates that brownfields are predominantly located in developed urban areas and require some intervention in order to be used repeatedly (CABERNET, 2006).

Brownfields represent significant social and environmental issues across the world (Thornton et al., 2007), and are recognized by the international association (OSN, 2015) and the European Union (EC, 2012). Brownfields are of various origin, are distributed across the entire country, yet they represent a significant issue in densely urbanized areas, such as cities in particular (Burinskiene et al., 2017). Abandoned buildings and sites are an integral part of cities in Central Europe (Tureckova et al., 2017). Brownfields that are located in the inner city, in the vicinity of the inner city or near other municipal subcentres are generally well-connected with the current technical and social infrastructures (Koch et al., 2018). The level of brownfield regeneration reflects the cultural and

---

[1] *School of Business Administration in Karvina, Silesian University in Opava, Univerzitni Nam. 1934/3,*
   733 40 Karvina, Czech Republic, skrabal@opf.slu.cz

economic development of the country, region, city or village as it reflects the strategies of sustainable development of sites (Wedding & Crawford-Brown, 2007).

Tools for dealing with disagreements between the interests of involved parties and the aims of sustainable development are rare (Bartke et al., 2016). Former studies showed that the location of brownfields in the inner city is influenced by the type of regeneration (Bjelland, 2004; Temelova, 2007). The type of regeneration may or may not reflect the opinions of local inhabitants (De Sousa, 2006) and sustainability (Bleicher & Gross, 2010). However, while planning brownfield regeneration, opinions of the local inhabitants should be taken into consideration (Meyer & Lyons, 2000), especially if the regeneration is co-financed using public funds (Rizzo et al., 2015). A major argument in favour of brownfield regeneration is the necessity to retain the compactness of cities and thus prevent their uncontrolled and non-regulated expansion (Tureckova et al., 2018). The planning of brownfield regeneration according to the principles of sustainable development presents a significant challenge, especially with rural brownfields that have small chances of attracting private investment (Sardinha, Craveiro & Milheiras, 2013). The balance between the development of cities and countryside is not only a common trend, but it is also a common objective for all countries in order to achieve sustainable integration between cities and countryside. Even though the countries across the world have a distinct history, culture, ideology, economic growth and other aspects, they also suffer from uneven growth between municipal and rural areas (Abrham, 2011; Dong et al., 2011; Gurrutxaga, 2013; Zitti et al., 2017). In the past, the rural countryside was perceived mainly as a tool for agricultural production. One of the most important values of the landscape was thus soil fertility, accessibility of field and suitability of the field for agricultural purposes and use of machines (Prishchepov et al., 2012). The current approach allows for agricultural, residential and tourist functions of the landscape. One of the most important fucntions of the landscape are the characteristic of the landscape, aesthetics of the landscape, diversity and function of the environment. Some parts of rural landscape are undergoing serious changes, especially the landscape in the vicinity of large cities (Stastna et al., 2018). Despite all this effort, the loss of agricultural soil in certain European countries is still rather dramatic. Agricultural land needs to be protected against several threats. This is deeply influenced by the development of agriculture and its adaptation to the changing domestic as well as global driving forces, including the volatility of the market, climate disruption of global food supply and a growing demand for local foodstuffs (Connell et al., 2013).

Urbanization belongs to one of the biggest trends of this century across the world, which means that the most important factor that changes urban landscape is the expansion of built-up sites, which is connected to urban sprawl (Luck & Wu, 2002; Van Eetvelde & Antrop, 2004). Urban sprawl has plenty of negative impacts on the environment, such as higher energy consumption, higher air pollution, reduced regional open space, loss of agricultural land, reduced species variety and fragmentation of ecosystems (Johnson, 2001). Green areas suitable for recreation must be preserved withing urban regions as by creating large parks, green belts and local recreational areas mental and physical well-being of inhabitants of the cities is improved (von Hertzen, Hanski & Haahtela, 2011).

Brownfields remain one of the biggest challenges of contemporary urbanists and developers (Frantal et al., 2015). With ongoing global economic stagnation, many industrial sectors either disappear or are moved to countries with lower labour costs – new brownfields emerge and their sustainable development is still restricted by many obstacles (Alexandrescu et al., 2014; Frantal & Martinát, 2013; Ganser & Williams, 2007; Payne, 2013; Vojkovska et al., 2013). As global economic stagnation continues, the investments fall and many industries disappear or are moved to countries with lower labour costs – new brownfields emerge, and their sustainable redevelopment is still constrained by many barriers and associated with several dilemmas (Alexandrescu et al., 2014; Frantal & Martinát, 2013; Ganser & Williams, 2007; Payne, 2013; Vojkovska et al., 2013). Abandoned buildings and sites left without any effort to find some alternative use prevent a further development of built-up sites, unfavourably influence the environment and have a bad impact on the given region in general (Tureckova et al., 2019).

The aim of the paper is to better understand the shift in the location brownfields in municipalities and cities in the Czech Republic as is evidenced in official brownfield databases in the years 2018

and 2020. The paper is structured as follows: after the introduction, a chapter follows focusing on data on brownfields in the Czech Republic, focusing particularly on their number and location. The next chapter deals with the methodology of the contribution. The fourth chapter deals with the results that were achieved by the author. The conclusion at the end summarizes existing findings.

2. DATA

The second chapter focuses on the number and size of brownfields in the Czech Republic. The Czech Republic is situated in Central Europe and has an area of 7,886,600 hectares. Currently (2020), approximately 10,694,364 inhabitants are living in the Czech Republic (CSO, 2020). There are 14 regions of NUTS 3 level (Eurostat Database, 2020). The Figure below (**Fig. 1**) displays the mentioned regions of NUTS 3 level in the Czech Republic.

Fig. 1. NUTS 3 regions in the Czech Republic *(Source: Eurostat, 2020).*

For the purposes of the paper, the data on brownfields was obtained from the National Brownfield Database which is coordinated by the CzechInvest Agency in the Czech Republic. Prague is not included in the results as there is only one abandoned building registered according to the database and it does not reflect the reality and problematics of the brownfield incidence in the capital city of Prague. In 2018, a total of 460 abandoned buildings and sites with an area of 2,335 hectares were registered. In 2020, the number of brownfields increased to 572, yet the area was reduced to 2,320 hectares. It follows that the number of registered abandoned building and sites between the two analysed years increased by 112, yet the total area decreased by 15 hectares.

In the Czech Republic, there are approximately 10 to 12 thousand brownfields with an area of 25 to 35 thousand hectares (National Brownfield Regeneration Strategy, 2019). The reason for the non-existence of these buildings and sites in the National Brownfield Database is influenced by the owners of the individual land and sites who are not interested in registering the involved sites as brownfields.

The table below (**Table 1**) focuses on information regarding the area of individual regions of NUTS 3 level in the Czech Republic, on the number of brownfields in 2018 and 2020 and their area. The highest occurrence of these abandoned buildings and sites is predominantly in Ústí nad Labem Region, Liberec Region and South Moravian Region. The largest area of brownfields is recorded mainly in Central Bohemian Region, Ústí nad Labem Region and Moravian-Silesian Region.

The number of brownfields and their size in individual regions of NUTS 3 level.

NUTS 3	Area of the region in (ha)	Number of brownfields (2018)	Area of brownfields in (ha) (2018)	Number of brownfields (2020)	Area of brownfields in (ha) (2020)
Karlovy Vary Region	331,400	32	**216**	43	**183**
Ústí nad Labem Region	533,500	62	**209**	80	**220**
Liberec Region	316,300	61	**188**	58	**166**
Pardubice Region	451,900	28	**66**	25	**35**
Hradec Králové Region	475,900	24	**110**	34	**166**
Vysočina Region	679,600	24	**29**	30	**35**
South Bohemian Region	1,005,700	33	**74**	37	**56**
Plzeň Region	756,100	24	**103**	34	**195**
Central Bohemian Region	1,101,500	30	**774**	38	**768**
Olomouc Region	526,700	35	**160**	44	**107**
South Moravian Region	718,800	52	**186**	67	**122**
Zlín Region	396,400	15	**18**	13	**8**
Moravian-Silesian Region	542,700	40	**203**	69	**260**
Total	7,836,500	460	2,335	572	2,320

Source: CzechInvest, 2018; 2020, adopted.

Another table (**Table 2**) describes the share of the area of brownfields on the area of the given region where the abandoned building or site is located. The data on the area of brownfields and regions is adopted from the previous table (Table 1). Information in the table below (**Table 2**) is in relative numbers. In both years (2018, 2020), the largest share of brownfield area on the area of the given region is mainly in Central Bohemian Region, Karlovy Vary Region and Liberec Region. In 2018, the total proportion of the area of brownfield sites registered in the National Brownfield Database in the Czech Republic was 0.0298% in relative terms; two years later, the proportion was 0.0296%. It should be emphasized that the proportion of acreage involved is actually larger, as most abandoned properties and sites are not on the register.

Share of the area of brownfields on the area of individual regions of NUTS 3 level.

NUTS 3	Share of BF area in NUTS 3 region area (2018) in %	Share of BF area in NUTS 3 region area (2020) in %
Karlovy Vary Region	0.0651	0.0551
Ústí nad Labem Region	0.0391	0.0413
Liberec Region	0.0593	0.0523
Pardubice Region	0.0146	0.0088
Hradec Králové Region	0.0232	0.0349
Vysočina Region	0.0037	0.0050
South Bohemian Region	0.0074	0.0056
Plzeň Region	0.0136	0.0257
Central Bohemian Region	0.0700	0.0698
Olomouc Region	0.0302	0.0202
South Moravian Region	0.0258	0.0169
Zlín Region	0.0044	0.0020
Moravian-Silesian Region	0.0373	0.0480
Total	0.0298	0.0296

Source: based on own survey, 2020.

3. METHODOLOGY

The third chapter is focused on the methodology of the paper. The aim of the paper is to better understand the shift in the location brownfields in municipalities and cities in the Czech Republic as is evidenced in official brownfield databases in the years 2018 and 2020. The reason for choosing this topic is that the author wishes to locate the abandoned buildings and sites within the structure of municipalities and cities in individual regions of the Czech Republic. For the purposes of the paper, the data on brownfields from 2018 and 2020 was obtained from the National Brownfield Database. As it was mentioned above, in 2018, 460 abandoned buildings and sites were registered and in 2020, it was 572.

For the purposes of the paper, brownfields were localized using an exact location of brownfields that are mentioned with every registered abandoned building and site in the database. The data on brownfields is based on the regions of NUTS 3 level. Each brownfield was then divided according to its location, i.e. whether it is located in the centre, in the inner part, outer part or within the development area of the municipalities and cities of the given regions. Based on the obtained data, relative shares within individual regions on the NUTS 3 level were calculated for the years 2018 and 2020. The table below (**Table 3**) shows the characteristics of the parts.

The characteristic of parts

Centre	• The center, or also the central zone, is the accumulation of all functions, areas prevail here and areas of higher public amenities serving residents. • The functional composition is accompanied by a varied structure of public spaces made up of equally varied constructions with a range of architectural values.
Inter Part	• This section is mainly characterised by functionally mixed multi-storey development with a higher proportion of built-up areas. • Usually one of the basic functions prevails in these parts of cities, most often housing.
Outer part	• Within this section, it is a territory that is mixed. • This applies not only in functional but also spatial terms. • The mixture of functional areas and objects is supported by a loose-knit form of construction mostly of individual architectural design and without the ambition of creating a public space or an architectural file.
Development area	• Immediately following link into stoppable territory. • However, these are hugely important areas and spaces that convey the optimal transition of urbanised environments and free economically exploited landscapes.

Source: URR, 2020; adopted.

4. RESULTS

The next part of the paper will be dealing with the localization of brownfields. First, the results for 2018 and 2020 in relative numbers will be mentioned and at the end of this chapter, the summary of the results will be performed. The table below (**Table 3**) displays the results of the localization of abandoned buildings and sites in 2018 in individual regions on NUTS 3 level in the Czech Republic. It can be seen from the table that the majority of brownfields in all analyzed regions of the country are largely located in the outer parts of municipalities and cities. The majority of such abandoned buildings and sites are located in Olomouc Region, Moravian-Silesian Region and Central Bohemian Region. The second largest group is represented by abandoned buildings and sites located in the outer parts of municipalities and cities. The largest number of localized brownfields in this group are mainly in Karlovy Vary Region. Another group is represented by abandoned buildings and sites that are located in the inner parts of municipalities and cities. The largest number of localized abandoned buildings and sites in this group is predominantly in Hradec Králové Region. Brownfields that are located in the centres of municipalities and cities belong to the last group. It is evident that in this group the largest localization is mainly in Zlín Region.

The following table (**Table 4**) displays the results of localization of brownfields in 2020. The largest relative shares of localized abandoned buildings and sites are mainly in the outer parts of municipalities and cities, such as in 2018 (see Table 3). Within this group, Moravian-Silesian Region, Pardubice Region and Olomouc Region dominate. Next, it was discovered that the second group of brownfields is represented by the ones located in the inner parts of municipalities and cities. Here, Karlovy Vary Region, South Bohemian Region and Central Bohemian Region dominate. The third part involves abandoned buildings and sites that are located on the margins of cadastral areas of municipalities and cities. This includes mainly Liberec Region and Vysočina Region. The last group includes abandoned buildings and sites that are localized in the centres of municipalities and cities. This group includes mainly brownfields localized in Zlín Region, Ústí nad Labem Region and Central Bohemian Region.

Localization of brownfields within the regions on NUTS 3 level in the Czech Republic in 2018 in %.

NUTS 3	Centre	Inner part	Outer part	Development area
Karlovy Vary Region	0	6.3	65.6	28.1
Ústí nad Labem Region	14.5	12.9	66.1	6.5
Liberec Region	8.2	21.3	59	11.5
Pardubice Region	10.7	17.9	64.3	7.1
Hradec Králové Region	16.7	25	45.8	12.5
Vysočina Region	17.4	21.7	52.2	8.7
South Bohemian Region	12.1	18.2	51.5	18.2
Plzeň Region	16.7	12.4	54.2	16.7
Central Bohemian Region	6.7	13.3	70	10
Olomouc Region	0	11.8	76.4	11.8
South Moravian Region	15.7	9.8	56.9	17.6
Zlín Region	21.4	7.1	57.1	14.4
Moravian-Silesian Region	5.3	2.5	71.1	21.1

Source: based on own survey, 2020.

Localization of brownfields within the regions on NUTS 3 level in the Czech Republic in 2020 in %.

NUTS 3	Centre	Inner part	Outer part	Development area
Karlovy Vary Region	9.3	32.6	41.9	16.2
Ústí nad Labem Region	16.5	21.5	50.6	11.4
Liberec Region	6.9	22.4	50	20.7
Pardubice Region	12	20	64	4
Hradec Králové Region	14.7	17.7	52.9	14.7
Vysočina Region	13.8	17.2	48.3	20.7
South Bohemian Region	8.1	27.1	45.9	18.9
Plzeň Region	14.7	23.5	52.9	8.9
Central Bohemian Region	15.8	26.3	44.7	13.2
Olomouc Region	7	20.9	58.1	14
South Moravian Region	13.4	19.5	53.7	13.4
Zlín Region	16.7	25	58.3	0
Moravian-Silesian Region	7.5	13.4	64.2	14.9

Source: based on own survey, 2020.

The figure below (**Fig. 2**) presents the complete results of the localization of brownfields in the Czech Republic in 2018 and 2020. The values shown in the chart below show the relative expression of localized abandoned objects and areas in given parts (Center, Inter part, Outer part, Development area) following the period. It is evident from the figure that within the analysed period the abandoned buildings and sites are to be found mainly in the outer parts of municipalities and cities.

During the year 2018, it involves 61.7% of localized brownfields in the area of the Czech Republic. In 2020, it oscillates around 52.3%. The second group is represented by abandoned buildings and sites located in the inner parts of municipalities and cities. In 2018, the relative number was 13.9% and in 2020, it reached 21.4%. It was discovered that the third group was represented by brownfields located in the outer parts of municipalities and cities where the relative number was 13.9% in 2018 and in 2020, the number was similar to the previously analysed year, i.e. 14%. The last group is formed by abandoned buildings and sites localized in the centres of municipalities and cities. The relative number reached 10.5% in 2018 and increased to 12.3% in 2020.
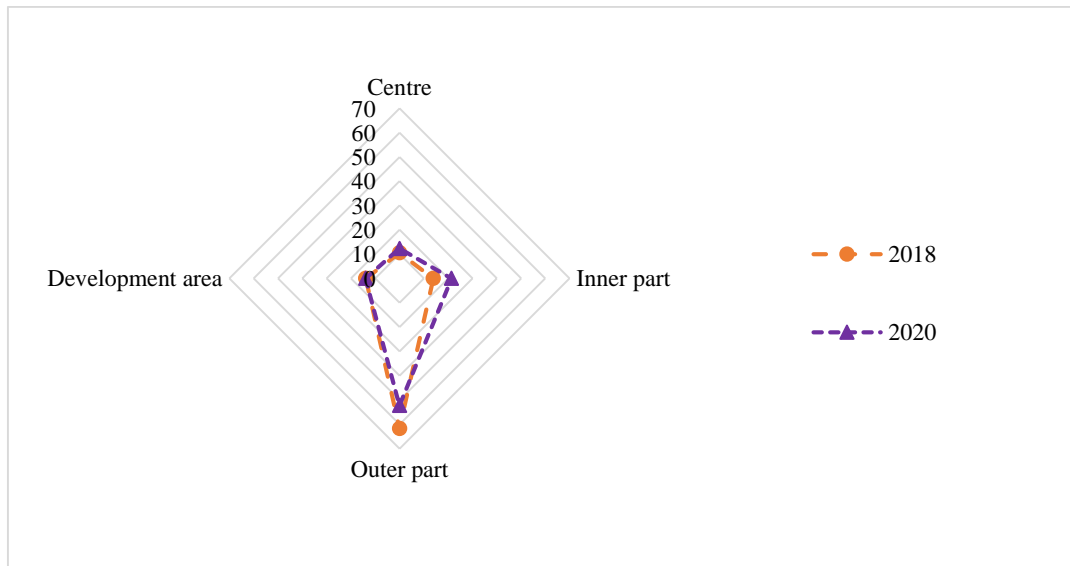
Fig. 2. The resulting evaluation of localized brownfields for the years 2018 and 2020 in the Czech Republic.
(***Source: based on own survey).***

5. CONCLUSION

The paper dealt with the issue of brownfields in individual regions of NUTS 3 level in the Czech Republic based on the localization using an exact location of brownfields. The aim of the paper was to better understand the shift in the location brownfields in municipalities and cities in the Czech Republic as is evidenced in official brownfield databases in the years 2018 and 2020. The analysed period of this contribution covered the years 2018 and 2020. It was discovered that the largest number of abandoned buildings and sites is mostly in Ústí nad Labem Region, Liberec Region and South Moravian Region.

The paper then analysed the area of NUTS 3 regions in the Czech Republic and the area of the individual abandoned buildings and sites in the analysed years. It was discovered that the largest share of brownfield area on the area of the given region is primarily in Central Bohemian Region, Karlovy Vary Region and Liberec Region. In addition, the author examined the localization of abandoned buildings and areas based on an exact location of brownfields that are quoted with each registered brownfield in National Brownfield Database.

It was discovered that brownfields are mostly located in the outer parts of municipalities and cities in both analysed years (2018, 2020).

The mentioned finding may also impact potential brownfield regeneration. Abandoned buildings and sites that are located in the centres or the inner parts of municipalities and cities generally stand a better chance to be potentially regenerated and reused. Abandoned buildings and sites located in the outer parts of municipalities and cities are rather little attractive for potential investors and developers who are interested in the opportunity to regenerate and reuse brownfields. These include primarily areas more distant from the centres that are of no added value for the investors.

Generally, it can be stated that the most attractive localities with the biggest chance to be regenerated are the ones in the vicinity of the centres with accessible transport infrastructure. There is a huge difference regarding the utilization opportunities of abandoned buildings and sites depending on whether they are located in the cities or municipalities. Cities are more suitable for brownfield regeneration than municipalities. Potential investors and developers primarily search abandoned buildings and sites that are located near the city centres as these are attractive due to their location and transport accessibility. By contrast, brownfields located within municipalities do not feature any added value for their potential investors regarding their reuse.

The paper managed to locate brownfields within the structure of municipalities and cities in individual regions of the Czech Republic based on an exact location of brownfields. As it was mentioned above, abandoned buildings and sites are primarily located in the outer parts of municipalities and cities. Here, they can be possibly regenerated and reused provided that the potential investors or developers are interested in those particular brownfields.

As part of the contribution, it should be noted that there are limited data sources that also influence the existence of the results. As mentioned in the post above, the registration of abandoned objects and sites in the National Brownfield Database in the Czech Republic is influenced by the owners of the brownfield sites concerned, who are not interested in the registration and declaration of the brownfield properties. This may also have an effect on the results achieved in the post.

ACKNOWLEDGMENT

R E F E R E N C E S

Abrham, J. (2011) Rural development and regional disparities of the new EU Member State. *Agricultural Economics*, 57 (6), 288–296.

Alexandrescu, F., Martinat, S., Klusacek, P. & Bartke, S. (2014) The path from passivity toward entrepreneurship public sector actors in brownfield regeneration processes in Central and Eastern Europe. *Organization & Environment*, 27 (2), 181–201.

Alker, S., Joy, V., Roberts, P. & Smith, N. (2000) The definition of brownfield. *Journal of Environmental Planning and Management*, 43 (1), 49–69.

Bartke, S. & Schwarze, R. (2015) No perfect tools: Trade-offs of sustainability principles and user requirements in designing support tools for land-use decisions between greenfields and brownfields. *Journal of Environmental Management*, 153, 11–24.

Bartke, S., Stanislav, M., Klusacek, P., Pizzol L., Alexandrescu, F., Frantal B., Critto, A. & Zabeo, A. (2015) Targeted selection of brownfields from portfolios for sustainable regeneration: User experiences from five cases testing the Timbre Brownfield Prioritization Tool. *Journal of Environmental Management*, 184 (1), 94–107.

Bjelland, M. D. (2004) Brownfield Sites in Minneapolis-St. Paul: The Interwoven Geographies of Industrial Disinvestment and Environmental Contamination. *Urban Geography*, 25 (7), 631–657.

Bleicher, A. & Gross, M. (2010) Sustainability assessment and the revitalization of contaminated sites: operationalizing sustainable development for local problems. *International Journal of Sustainable Development & World Ecology*, 17 (1), 57–66.

Burinskiene, M., Bielinskas, V., Podviezko, A., Gurskiene, V. & Maliene, V. (2017) Evaluating the significance of criteria contributing to decision-making on brownfield land redevelopment strategies in urban areas. *Sustainability*, 9 (5), 759–776.

CABERNET (2006). Sustainable brownfield regeneration: CABERNET network report Nottingham: University of Nottingham.

Connell, D. J., Bryant, C. R., Caldwell, W. J., Churchyard, A., Cameron, G., Johnston, T., Margulis, M. E., Ramsey, D. & Marois, C. (2013) Food sovereignty and agricultural land use planning: the need to integrate public priorities across jurisdictions. *Journal of Agriculture, Food Systems, and Community Development*, 3 (4), 117–124.

CSO (2020). - Czech Statistical Office. Avaiable from: https://www.czso.cz/csu/czso/home [Accessed July 2020].

De Sousa, C. A. (2006) Unearthing the benefits of brownfield to green space projects: an examination of project use and quality of life impacts. *Local Environment*, 11 (5), 577–600.

Dong, X., Song, S. & Zhu, H. (2011) Industrial structure and economic fluctuation evidence from China. *The Social Science Journal*, 48 (3), 468–477.

EC (2012). Guidelines on best practice to limit, mitigate or compensate soil sealing. SWD (2012) 101 final.

Frantal, B., Greer-Wrootten, B., Klusacek, P., Krejci, T., Kunc, J. & Martinat, S. (2015). Exploring spatial patterns of urban brownfields regeneration: The case of Brno, Czech Republic. *Cities*, 44, 9-18.

Frantal, B. & Martinát, S. (2013) Brownfields: A geographical perspective. *Moravian Geographical Reports*, 21 (2), 2–4.

Ganser, R. & Williams, K. (2007). Brownfield development: Are we using the right targets? Evidence from England and Germany. *European Planning Studies*, 15 (5), 603–622.

Gurrutxaga, M. (2013) Changes in rural–urban sex ratio differences in the young professional age group as an indicator of social sustainability in rural areas: a case study of continental Span, 2000–2010. *Area*, 45 (3), 337-347.

von Hertzen, L., Hanski, I. & Haahtela, T. (2011) Natural immunity. *EMBO Reports*, 12 (11), 1089–1093.

Johnson, M. P. (2001) Environmental impacts of urban Sprawl: A survey of the literature and proposed research agenda. *Environment and Planning A: Economy and Space*, 33 (4), 717–735.

Koch, F., Bilke, L., Helbig, C. & Schlink, U. (2018) Compact or cool? The impact of brownfield redevelopment on inner-city micro climate. *Sustainable Cities and Society*, 38, 31–41.

Luck, M. & Wu, J. G. (2002) A gradient analysis of urban landscape pattern: A case study from the phoenix metropolitan region, Arizona, USA. *Landscape Ecology*, 17 (4), 327–339.

Meyer, P. B. & Lyons, T. S. (2000) Lessons from private sector Brownfield redevelopers -planning public support for urban regeneration. *Journal of the American Planning Association*, 66 (1), 46–57.

MPO (2020). Narodni strategie regenerací brownfieldu 2019-2024. Available from: https://www.mpo.cz/cz/podnikani/dotace-a-podpora-podnikani/podpora-brownfieldu/narodni-strategie-regeneraci-brownfieldu-2019-2024--248322/ [Accessed July 2020].

Payne, S. (2013) Pioneers, pragmatists and sceptics: Speculative house builders and brownfield development in the early twenty-first century. *Town Planning Review*, 84 (1), 37–62.

Prishchepov, A. V., Radeloff, V., Baumann, M., Kuemmerle, T. & Müller, D. (2012) Effects of institutional changes on land use: agricultural land abandonment during the transition from state-command to market-driven economies in post-Soviet Eastern Europe. *Environmental Research Letters*, 7 (2), 68–85.

Rizzo, E., Pesce, M., Pizzol, L., Alexandrescu, F. M., Giubilato, E., Critto, A., Marcomini, A. & Stephan. B. (2015) Brownfield regeneration in Europe: identifying stakeholder perceptions, concerns, attitudes and information needs. *Land Use Policy*, 48, 437–453.

Sardinha, I. D., Craveiro, D. & Milheiras, S. (2013) A sustainability framework for redevelopment of rural brownfields: stakeholder participation at SÃO DOMINGOS mine, Portugal. *Journal of Cleaner Production*, 57, 200–208.

Stastna, M., Vaishar, A., Vavrouchova, H., Masícek, T. & Perinkova, V. (2018) Values of a suburban landscape: Case study of Podoli u Brna (Moravia), The Czech Republic. *Sustainable Cities and Society*, 40, 383-393.

Temelova, J. (2007) Flagship developments and the physical upgrading of the post-socialist inner city: the golden angel project in Prague. *Geografiska Annaler: Series B, Human Geography*, 89 (2), 169–181.

Thornton, G., Franz, M., Edwards, D., Pahlen, G. & Nathanail, P. (2007) The challenge of sustainability: incentives for brownfield regeneration in Europe. *Environmental Science &Policy,* 10 (2), 116–134.

Tureckova, K., Martinat, S., Skrabal, J., Chmielova, P. & Nevima, J. (2017) How local population perceive impact of brownfields on the residential property values: some remarks from postindustrial areas in the Czech Republic. Geographia Technica, 12 (2), 150–164.

Tureckova, K., Nevima, J., Skrabal, J. & Martinat, S. (2018) Uncovering patterns of location of brownfields to facilitate their regeneration: Some remarks from the Czech Republic. Sustainability, 10 (6), 224–234.

Tureckova, K., Nevima, J. Skrabal, J. & Tuleja. P. (2019) Categorization of Impact of the Selected Variables for Potential Brownfield Regeneration in the Czech Republic by Means of Correspondence Analysis. Geographia Technica, 14 (2), 120–130.

UN (2015). - Sustainable development goals: 17 goals to transform our world. Available from: http://www.un.org/sustainabledevelopment/ [Accessed July 2020].

URR (2020) - Institute For Spatial Development. Available from: www.uur.cz/principy/pap/KapitolaB/B3311_MestaSidla_20061206.pdf+&cd=1&hl=cs&ct=clnk&gl=cz [Accessed July 2020].

Van Eetvelde, V. & Antrop, M. (2004) Analysing structural and functional changes of traditional landscapes - two examples from Southern France. *Landscape and Urban Planning*, 67 (1–4), 79–95.

Vojkovska, D., Vojvodíkova, B. & Maceckova, B. (2013) Underused land, brownfields, future use and effects – BROWNTRANS Project outputs. *WIT Transactions on Ecology and the Environment,* 173, 205–216.

Wedding, G.C. & Crawford-Brown, D. (2007) Measuring site-level success in brownfield redevelopments: a focus on sustainability and green building. *Journal of Environmental Management*, 85 (2), 483–495.

Zitti, M., Efstathios, G & Salvati, L. (2017) Beyond the "Divided City ": a manifesto for spatially–balanced, sprawl–free post–crisis metropolises. *Review of Applied Socio-Economic Research*, 13 (1), 95–109.

SPATIAL ANALYSIS AND GEOMORPHIC CHARACTERISTICS OF CORAL REEFS ON THE EASTERN PART OF LOMBOK, INDONESIA

Bachtiar MUTAQIN[1,2] (ID)

ABSTRACT:
The eastern part of Lombok Island is a highly dynamic environment with many physical processes as well as very complex landuse. In addition to the anthropogenic origin, sedimentation in this area also occurs due to natural origins, such as volcanic processes. Due to hydrological processes since the 1257 CE eruption of Samalas volcano, almost half of the materials were transported and deposited to the coastal area. These deposits can affect the state of the aquatic environment, so they, directly and indirectly, affect the coral reef conditions. However, the spatial information of coral reefs in this area is rarely known. Therefore, the spatial distributions of coral reefs in this area should be investigated to distinguish and determine the factors that regulate its patterns. The multidisciplinary approach, including geomorphological survey, remote sensing and geographic information system (GIS), as well as geostatistical analysis, has been used to gain a deep understanding of the spatial distribution and geomorphic features of coral reefs in the eastern part of Lombok. Our results show that coral reefs on the eastern part of Lombok are mostly fringing reefs and developed on shallow continental shelves in depth between 0-20 m and located close to the main island. In addition, coast typology in the eastern part of Lombok divided into river deposition coast and wave erosion coast. Finally, the absence of coral reefs in some areas in the eastern part of Lombok can be caused by sedimentation and pollution from the river as well as the extraction of remnant coral reefs.

Key-words: *Sedimentation; Coastal; Coral reef; DEM; Samalas; Lombok.*

1. INTRODUCTION

The existence of primary ecosystems in the coastal area, i.e., coral reefs, mangroves, and seagrass (Guannel et al. 2016; Mutaqin et al., 2020; Marfai et al., 2020) may affect the coastal landscape dynamics. Coral reef as the first barrier can reduce the energy of waves that strike the shore (Ferrario et al., 2014; Costa et al., 2016; Hongo et al., 2018; Harris et al., 2018). Coral reef as coastal protection may also minimize coastal erosion (Silva et al., 2016; Reguero et al., 2018) and significantly reduce the risk from coastal hazards for about 200 million people in the world (Ferrario et al., 2014). Coral typically live in tropical and subtropical areas with favorable oceanographic conditions, such as water temperatures between 18-29 °C, salinity between 32-42‰, as well as clear water where the intense sunlight still can penetrate it (Davidson-Arnot, 2010). Disturbances in those advantageous conditions and environment undoubtedly can affect the existence of coral's life.

One of these disturbances is from volcanic origins. Volcanic materials may reach the sea following to the eruption, either directly and indirectly through the river, and it can result in disturbances in the ocean environment (Maniwavie et al., 2001; Vroom and Zgliczynski, 2011; Mutaqin et al., 2019a; Mutaqin et al., 2019b; Mutaqin and Lavigne, 2019). Disturbances in the ocean due to volcanic ash, pumice rafts, as well as Pyroclastic Density Current (PDC) deposits, may affect the coral reefs, e.g., coral bleaching which triggers mortality of corals (Maniwavie et al., 2001; Schils, 2012). In addition to the mortality of corals, there are other negative impacts of lahars, lava flows, and volcanic ash that deposited on coral reefs: 1) sunlight penetration has decreased that affect the

---

[1]*Universitas Gadjah Mada, Faculty of Geography, Coastal and Watershed Research Group, 55281 Yogyakarta, Indonesia, mutaqin@ugm.ac.id.*

[2]*Université Paris 1 Panthéon Sorbonne, Laboratoire de Géographie Physique UMR 8591, 92190 Paris, France, mutaqin@ugm.ac.id*

coral's photosynthesis, changes in the chemical elements in the ocean (Reuter and Piller, 2011), and 2) nutrient enrichments triggering transformations in the benthic structure (Tomascik et al., 1996; Vroom and Zgliczynski, 2011; Schils, 2012).

As the most powerful case in the recent eruptive history of Lombok (Lavigne et al., 2013; Vidal et al., 2015; Mutaqin et al., 2019a), volcanic materials that were expelled by the Samalas volcano in 1257 CE covered the entire of Lombok Island, and until now it still remains and exploited by the local people through the extraction (**Fig. 1**). The exploitation of materials from the Samalas eruption in Lombok started intensively since the early 1980s. The pumices (**Fig. 1a**) are exported mainly to Asia (China 59.4%, South Korea 20.1%, Vietnam 8.7%, and Thailand 3.2%) as a building material in the manufacture of concrete and as an abrasive material (Statistics Indonesia, 2017). The extraction, which is widespread all over Lombok Island (**Fig. 1b**), has accelerated the natural landscape evolution. As a result, their exploitation allows the extension of cultivated areas from under-exploited land to large rice fields (**Fig. 1c**) as well as causes the sediment in the rivers, which then flows into the sea and leads to sedimentation.

Fig. 1. Location of volcanic materials extraction in Lombok Island: a) pumice from the extraction, b) pumice quarry, and c) rice-fields area as a "benefit" from the exploitation.

Based on **Fig. 1**, we can identify that the pumices extractions are mostly found in the eastern part of Lombok and may disturb the ocean conditions. However, the spatial configuration of coral reefs in this area is largely unexplored. Coral reefs monitoring and research mostly located in the western part of Lombok and limited to their ecosystem services (Pradjoko et al., 2015; Kurniawan et al., 2016; Chen et al., 2019). The novelty of this research is related to the spatial distributions of coral reefs in

the eastern part of Lombok in relation to landscape dynamics, especially from volcanic origins, which should be investigated to distinguish and determine the factors that regulate its patterns.

This research aims at the investigation of spatial distributions of coral reefs in the eastern part of Lombok as well as its correlation with the volcanic activities on Lombok Island. In the present study, we, therefore, also compared the spatial distribution of coral reefs and bathymetric information as well as coast typologies on the eastern part of Lombok.

2. METHODS

The multidisciplinary approach between geomorphological surveys, remote sensing and geographic information system (GIS) techniques, as well as geostatistical analysis, were used to acquire comprehensive information on the subject of spatial distribution and geomorphic characteristics of coral reefs on the eastern part of Lombok Island. There are five data as an input to further analyze, both in the field and in the laboratory, i.e., coral reefs database; the 1998 Indonesian topographic map with a scale of 1:25,000; the 2014 Indonesian bathymetric map with a scale of 1:200,000; satellite imagery of SPOT 6 and 7; and Indonesian Digital Elevation Model with a spatial resolution of 0.27-arcsecond (**Fig. 2**). This study collected three kinds of data: (1) spatial distribution of coral reefs, (2) digital elevation model (DEM), and (3) coast typology.
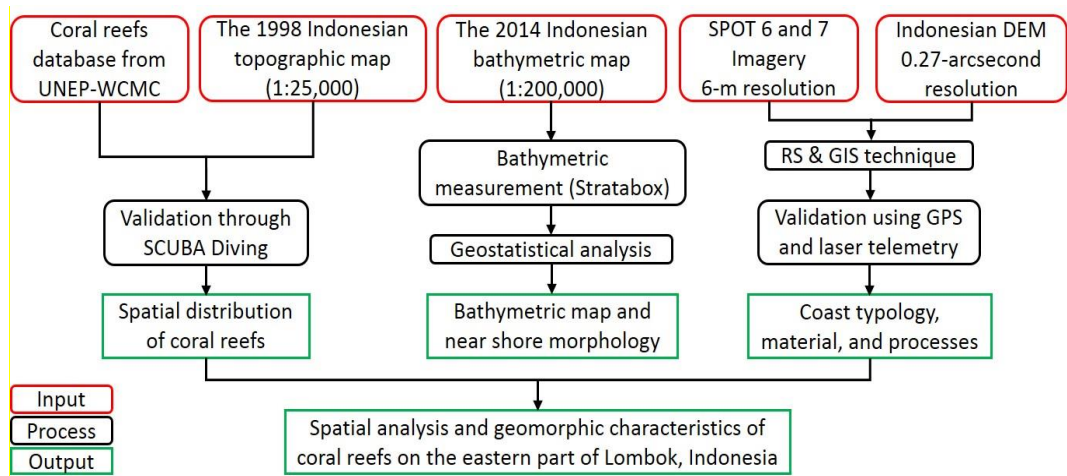
Fig. 2. Research methodology on the spatial analysis and geomorphic characteristics of coral reefs.

We used the most comprehensive distribution data of coral reefs from the UNEP World Conservation Monitoring Centre (UNEP-WCMC) and the WorldFish Centre (UNEP-WCMC et al., 2018), combined with data from the Indonesian Geospatial Information Agency (BIG) as a baseline map for a detailed survey conducted in 2016 and 2017 (**Fig. 3a**). The use of GIS technologies will help to perform spatial analysis here. The next step is to develop a DEM from the 2014 bathymetric map of Indonesia at a scale of 1:200,000, produced by the Indonesian Hydro-Oceanographic Agency, which detailed with field measurements using a high-resolution marine geophysical instrument, called StrataBox (**Fig. 3b**).

DEM data is essential while studying the Earth's morphology (Nistor et al., 2019; Kongmuang et al., 2020). DEM data generated using geostatistical analysis, i.e., the simple Kriging process with the first order for trend removal and an exponential semivariogram model. Kriging was used in this study since the data is normally distributed and stationary. Furthermore, Kriging is the most excellent interpolation method since it is unbiased, it performs better, and had the smallest error values (Zimmerman et al., 1999; Schwendel et al., 2012; Arun, 2013; Arétouyap et al., 2016; Mutaqin et al., 2019a).

Classification of coast typology refers to the most dominant processes in the coast from Shepard (1973), i.e., the primary coast, which is mainly formed and controlled by land processes, and the secondary coast, which is shaped primarily by the sea or by marine organisms.

Fig. 3. Survey and field measurements of: a) coral reefs, b) bathymetric data, and c) coast typology.

Coast typology identified from a 2016 of SPOT 6 and 7 imagery satellite provided by the National Institute of Aeronautics and Space of Indonesia, which combined with Indonesian DEM data with a spatial resolution of 0.27-arcsecond provided by BIG (http://tides.big.go.id/DEMNAS/), as well as field measurements in 2017 and 2019 (**Fig. 3c**).

3. RESULTS AND DISCUSSIONS

3.1. Computational analysis

The value of the mean, RMSE, mean standardized error, root mean squared standardized error, and average standard error is shown in **Table 1** which calculates automatically in ArcGIS software based on Equations (1)-(5):

Mean:
$$\sum_{i=1}^{n} \left(\hat{Z}(s_i) - z(s_i) \right) \Big/ n \tag{1}$$

RMSE value:
$$\sqrt{\sum_{i=1}^{n} \left(\hat{Z}(s_i) - z(s_i) \right)^2 \Big/ n} \tag{2}$$

Mean standardized error:
$$\frac{\sum_{i=1}^{n} \left(\hat{Z}(s_i) - z(s_i) \right) \Big/ \hat{\sigma}(s_i)}{n} \tag{3}$$

Root mean squared standardized error:
$$\sqrt{\frac{\sum_{i=1}^{n} \left[\left(\hat{Z}(s_i) - z(s_i) \right) \Big/ \hat{\sigma}(s_i) \right]^2}{n}} \tag{4}$$

Average standard error: (5)

$$\sqrt{\frac{\sum_{i=1}^{n} \hat{\sigma}^2(s_i)}{n}}$$

where $Z(s_i)$ is the measured value at the ith location; n is the number of measured values; and σ is variance parameter.

Table 1.

Cross-validation for the bathymetric model.

Parameters	Value
Mean	0.16
RMSE value	3.85
Mean standardized error	0.04
Root mean squared standardized error	1.66
Average standard error	2.26

The quality of DEM can be identified through a small RMSE value. The smallest RMSE implies that the algorithm has accurately estimated the calculated values. Furthermore, the validity of DEM data generated using geostatistical analysis can be identified through several criteria, among others: 1) the mean standardized error is near zero; 2) the value of average standard error and the root mean squared prediction error is not far adrift; 3) the value of root mean squared standardized error is approximately 1 (Li and Tang, 2011; Zhu, 2016; Mutaqin et al., 2019a). Based on those parameters, bathymetric models in our study can be categorized as a valid model. The bathymetric model of the Alas Strait, which has 10-m spatial resolution, shows depths varying from 0 m in the shoreline to a maximum depth of approximately 200 m in the mid-channel.

3.2. Spatial distribution of coral reefs

Based on the bathymetric model and field measurements, we can identify that spatially, coral reefs coverage on the eastern part of Lombok is the most extensive in Lombok Island with an area of 61.89 km^2 from total coverage of 137.34 km^2 (45.1%). Furthermore, coral reefs on the eastern part of Lombok are mostly fringing reefs and developed on shallow continental shelves in depth between 0-20 m and located close to the main island. Fringing reefs are frequently found on mainland coasts, morphologically simple, and appear as shore-attached organisms (Kennedy and Woodroffe, 2002; Davidson-Arnott, 2010). In the eastern part of Lombok, coral reefs develop mostly in areas with linear sandy beaches as well as in bay heads. However, coral reefs did not found in all areas in the eastern part of Lombok. Four bathymetric profiles were created to obtain detailed information about the spatial distribution of coral reefs which also compare with bathymetric data and coast typology. Profiles A and D were used to represent areas with coral reefs, while profiles B and C represent areas without coral reefs. In bathymetric profile A (**Fig. 4a**), coral reefs were located in a relatively flat nearshore morphology (slope up to 0.6 degrees), sandy seabed materials, with a distance up to 1 km seaward, and the depth reach 19 m. Bathymetric profile D (**Fig. 4d**) shows that coral reefs were located on a very gentle slope (up to 1.1 degrees), sandy seabed materials, up to 13 meters of depth, and a distance of up to 1 km from the shoreline. In front of the affected area from the 1257 CE Samalas eruption (Mutaqin et al., 2019a), we identified that there were no living coral reefs, represents by profiles B and C (**Fig. 4b** and **Fig. 4c**). In a distance of 1 km toward the sea, profiles B and C have similar morphological characteristics with profiles A and D, i.e., very gentle slope. Still, the depth is only up to 10 m with the conditions of murky water.

This phenomenon may be triggered by the landscape evolution following the 1257 CE Samalas eruption that produces more than 4.4 x 10^6 m^3 of pumice-rich PDCs. Following the 1257 CE eruption, volcanic materials from Samalas reached the Alas Strait and resulted in the coast progradation at specific locations along the shoreline, e.g., in Korleko. The 1257 CE materials had buried almost all the pre-eruption coral reefs in this area and highly eroded since then (Mutaqin et al., 2019a). Several studies have also mentioned the impacts of volcanic materials at sea from different perspectives. In 1988, the lava from the eruption of Gunung Api in Banda Island, Indonesia, entered the sea and buried about 70,000 m^2 (Casadevall et al., 1989) of the coral reef (Sutarna, 1990) to a depth more than 50 m.

In other cases, suspended volcanic ash following the 2003 CE eruption in Anatahan, the Northern Mariana Islands reduced the underwater visibility up to 2-meter (Vroom and Zgliczynski, 2011). Consequently, the maximal living coral cover has decreased by about 35% with poor conditions, and most of them displayed signs of stress in the form of coral bleaching (Vroom and Zgliczynski, 2011).
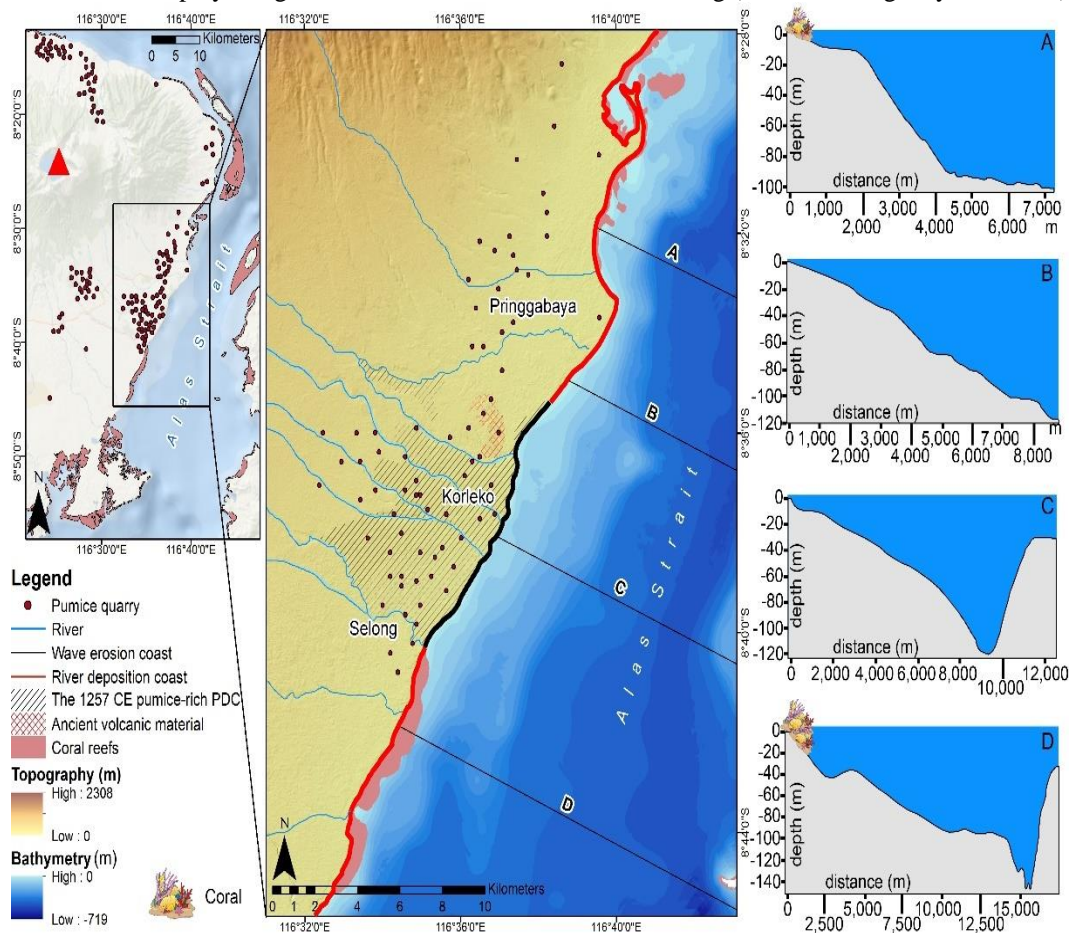

Fig. 4. Spatial distribution of coral reefs and coast typology in the eastern part of Lombok.

In 1994, a volcanic eruption in Rabaul Caldera, Papua New Guinea, produced large volumes of ash and pumice, which completely buried the coral reefs around Rabaul Harbor (Maniwavie et al., 2001). Although the coral reefs had extensively recolonized in the two years following the eruption, the volcanic ash had succeeded in decreasing the live coral cover from 50% before the eruption to 0% in the aftermath of the eruption. This rapid recolonization may have happened if the remobilization of volcanic materials from the mainland (i.e., suspended solid sediments and lahars) that reach the sea through the rivers did not disturb the underwater conditions.

Profiles graph of A, B, C, and D show the same patterns of gradient changes in the waters of eastern Lombok. In general, the seabed material of the Alas Strait consists mostly of rock and sand. Nevertheless, there were different materials and dominant processes in the coast of Selong, Korleko, and Pringgabaya. In Korleko, the materials are mostly from the Samalas volcano (pumice-rich PDC and flood derived sand deposits), while in Pringgabaya and Selong are undifferentiated volcanic rocks (e.g., lava, breccia, and tuff) and an ancient debris avalanche, respectively. Coast typology in Korleko also categorized as a wave erosion coast since a straightened, and irregular high cliff only can be found in Korleko.

3.3. Coastal dynamics and its geomorphic impacts on coral reefs

Coastal sedimentation occurs when the eroded material has deposited downstream by runoff into surface waters such as estuaries. In past years, sediment input has dramatically increased in coastal areas due to material from the volcanic eruption (Vogel and Märker, 2010; Ramalho et al., 2013; Mutaqin et al., 2019a). From the end of the 13th to the beginning of the 20th century, coastal evolution in the eastern part of Lombok is dominated by fluvial origin rather than by marine and anthropic origin. After being relatively stable since the 13th century, the coastline on the eastern part of Lombok has receded several hundred meters since the 1980s, probably due to a combination of natural factors (sea level rise driven by climate change; earthquakes) and human factors.

Since coral reefs are very vulnerable ecosystems, pumice quarry on the eastern part of Lombok, as well as the destruction of the remnant coral reefs for building materials and lime production (**Fig. 5a),** could have geomorphic impacts and worsen the existence of coral reefs in this area. Eroded volcanic material, either due to natural processes or from quarries, transported by rivers and deposited on estuaries (**Fig. 5b**). Deposited material from the river, which consists of sand deposits and pumices, accumulated in the nearshore zone and causing murky waters. Furthermore, those materials, along with eroded material from volcanic deposits along the coast, are then transported southward by longshore currents in the Alas Strait. Field measurement shows that within 24 hours, seawater current velocity is more than 1.7 m/s that occurs for 9 hours, at the interval between the first and second low water tides and flowing towards the south.
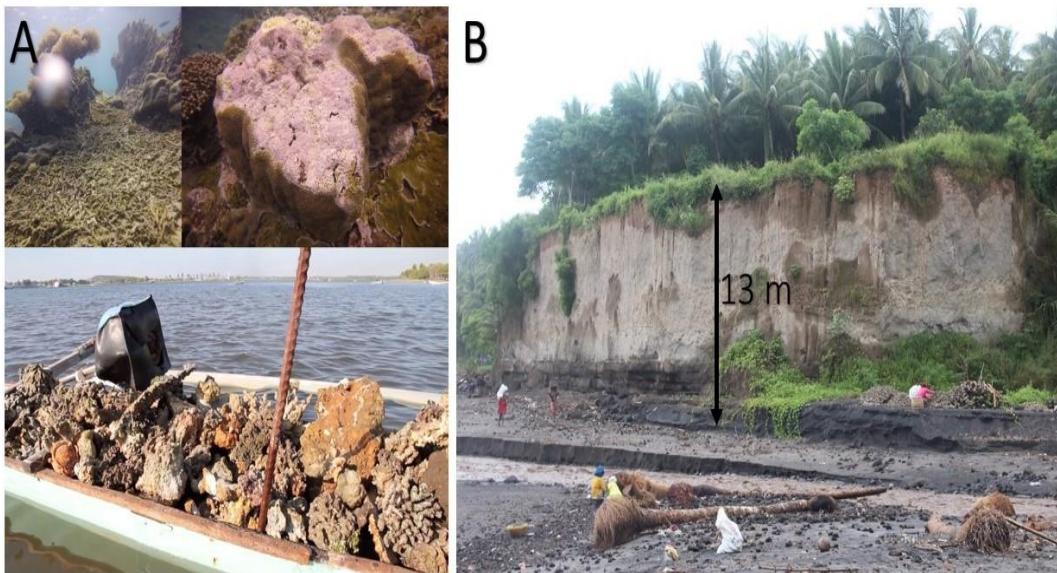
Fig. 4. a) Coral reefs conditions following dynamite fishing, anchor dragging, and coral extraction (Courtesy: A. Landa, 2016); b) sedimentation in the estuary with a background of a cliff (pumice-rich PDC) in Korleko.

Moreover, the activity of dynamite and cyanide fishing also still exists and practiced by some people in Lombok Island, including in the eastern part of Lombok. Since the Holocene era, human activities are mentioned as one of the factors that can affect coastal dynamics (Alizadeh et al., 2015). Thenceforth, human pressures in the coastal area in the form of coral reef extraction had increased due to their needs related to economic factors (Aretano et al., 2017; Mutaqin, 2017), including in the eastern part of Lombok although there is already regulation about it.

4. CONCLUSIONS

The bathymetric model on the eastern part of Lombok was reconstructed using the kriging technique. The model is valid and has the RMSE with the smallest value; hence, in other words, the model is reasonably accurate. In general, coast typology in the eastern part of Lombok consists of two types, i.e., river deposition coast as well as wave erosion coast, like in Korleko. The results show a correlation between the 1257 CE eruption of Samalas with the existence of coral reefs in the eastern part of Lombok. Currently, there is no living coral reef in the nearshore of Korleko. This condition can be caused due to several factors, among others: 1) sedimentation from the river, 2) regular input of acid pumice material in the sea which transported in suspension by the rivers; and 3) illegal activities of coral reefs extraction and destruction of coral reefs for lime production and building materials. These types of studies are important to carry out, not only in Lombok Island but also in another area in Indonesia to understand more detail the impact of volcanic, fluvial, and anthropogenic activities on the coastal ecosystems and its dynamics. Furthermore, the results in this article might be used by the local government and related institutions as a basis for policy-making, especially on the management of coral reefs, sand mining regulation, and marine protected area.

R E F E R E N C E S

Alizadeh, K., Cohen, M., and Behling, H. (2015). Origin and dynamics of the northern South American coastal savanna belt during the Holocene - the role of climate, sea-level, fire, and humans. *Quaternary Science Reviews*. 122, 51-62. https://doi.org/10.1016/j.quascirev.2015.05.009.

Aretano, R., Parlagreco, L., Semeraro, T., Zurlini, G., Petrosillo, I. (2017). Coastal dynamics vs beach users attitudes and perceptions to enhance environmental conservation and management effectiveness. *Marine Pollution Bulletin*. 123, 142–155. https://doi.org/10.1016/j.marpolbul.2017.09.003.

Arétouyap, Z., Njandjock Nouck, P., Nouayou, R., Kemgang, F.E.G.K., Toko A.D.P., and Asfahani, J. (2016). Lessening the adverse effect of the semivariogram model selection on an interpolative survey using kriging technique. *SpringerPlus* 5, 549. https://doi.org/10.1186/s40064-016-2142-4.

Arun, P. (2013). A comparative analysis of different DEM interpolation methods. *The Egyptian Journal of Remote Sensing and Space Sciences* (16), 133-139. https://doi.org/10.1016/j.ejrs.2013.09.001.

Casadevall, T., Pardyanto, L., Abas, H., and Tulus. (1989). The 1988 eruption of Banda Api volcano, Maluku, Indonesia. *Geologi Indonesia*. 12, 1, 603-635.

Chen, F., Wu, J., Liu, J., Hu, Y., Chen, X., Lim, P-E., Abdullah, W.M.A., Sjafrie, N.D.M., Adirianto, B. (2019). Comparison of social-value cognition based on different groups: The case of Pulau Payar in Malaysia and Gili Matra in Indonesia. *Ocean & Coastal Management*. 173, 1-9. https://doi.org/10.1016/j.ocecoaman.2019.02.010.

Costa, M.B.S.F., Araújo, M., Araújo, T.C.M., Siegle, E. (2016). Influence of reef geometry on wave attenuation on a Brazilian coral reef. *Geomorphology*. 253, 318–327. https://doi.org/10.1016/j.geomorph.2015.11.001.

Davidson-Arnott, R. (2010). An *Introduction to Coastal Processes and Geomorphology*. Cambridge University Press, New York. 458p.

Ferrario, F., Beck, M.W., Storlazzi, C.D., Micheli, F., Shepard, C.C., and Airoldi, L. (2014). The effectiveness of coral reefs for coastal hazard risk reduction and adaptation. *Nature Communications*. 5:3794. https://doi.org/10.1038/ncomms4794.

Guannel, G., Arkema, K., Ruggiero, P., Verutes, G. (2016). The Power of Three: Coral Reefs, Seagrasses, and Mangroves Protect Coastal Regions and Increase Their Resilience. *PLoS ONE* 11(7): e0158094. https://doi.org/10.1371/journal.pone.0158094.

Harris, D.L., Rovere, A., Casella, E., Power, H., Canavesio, R., Collin, A., Pomeroy, A., Webster, J.M., Parravicini, V. (2018). Coral reef structural complexity provides important coastal protection from waves under rising sea levels. *Science Advances*. 4, 2, eaao4350. https://doi.org/10.1126/sciadv.aao4350.

Hongo, C., Kurihara, H., and Golbuu, Y. (2018). Coral boulders on Melekeok reef in the Palau Islands: An indicator of wave activity associated with tropical cyclones. *Marine Geology*. 399, 14–22. https://doi.org/10.1016/j.margeo.2018.02.004.

Kennedy, D.M., and Woodroffe, C.D. (2002). Fringing reef growth and morphology: a review. *Earth-Science Reviews*, 57, (3–4), 255-277. https://doi.org/10.1016/S0012-8252(01)00077-0.

Kongmuang, C., Tantanee, S., Seejata, K. (2020). Urban Flood Hazard Map Using GIS of Muang Sukhothai District, Thailand. *Geographia Technica,* 15(1), 143-152. http://doi.org/10.21163/GT_2020.151.13.

Kurniawan, F., Adrianto, L., Bengen, D.G., Prasetyo, L.B. (2016). Vulnerability assessment of small islands to tourism: The case of the Marine Tourism Park of the Gili Matra Islands, Indonesia. *Global Ecology and Conservation.* 6, 308-326. https://doi.org/10.1016/j.gecco.2016.04.001.

Lavigne, F., Degeai, J.-P., Komorowski, J.-C., Guillet, S., Robert, V., Lahitte, P., Oppenheimer, C., Stoffel, M., Vidal, C.M., Surono, Pratomo, I., Wassmer, P., Hajdas, I., Hadmoko, D.S., de Belizal, E. (2013). Source of the great A.D. 1257 mystery eruption unveiled, Samalas volcano, Rinjani Volcanic Complex, Indonesia. *PNAS*. 110(42), 16742-16747. https://doi.org/10.1073/pnas.1307520110.

Li, F., and Tang, G. (2011). DEM-based Terrain Factor of Soil Erosion at Regional Scale and Soil Erosion Mapping. In Ruas, A. *Advances in Cartography and GIScience* (Volume 2). Springer-Verlag Berlin Heidelberg. https://doi.org/10.1007/978-3-642-19214-2.

Maniwavie, T., Rewald, J., Aitsi, J., Wagner, T.P., and Munday, P.L, (2001). Recovery of corals after volcanic eruptions in Papua New Guinea. *Coral Reefs*. 20:24. https://doi.org/10.1007%2Fs003380100114.

Marfai M.A., Ahmada B., Mutaqin B.W., Windayati R. (2020). Dive Resort Mapping and Network Analysis: Water Resources Management in Pemuteran Coastal Area, Bali Island, Indonesia. *Geographia Technica*. 15(2), 106-116. http://doi.org/10.21163/GT_2020.152.11.

Mutaqin, B.W. (2017). Shoreline Changes Analysis in Kuwaru Coastal Area, Yogyakarta, Indonesia: An Application of the Digital Shoreline Analysis System (DSAS). *International Journal of Sustainable Development and Planning* 12(7):1203-1214. https://doi.org/10.2495/SDP-V12-N7-1203-1214.

Mutaqin B.W. and Lavigne F. (2019), Oldest Description of a Caldera-forming Eruption in Southeast Asia Unveiled in Forgotten Written Sources, *GeoJournal*. https://doi.org/10.1007/s10708-019-10083-5.

Mutaqin B.W., Lavigne F., Sudrajat Y., Handayani L., Lahitte P., Virmoux C., Hiden, Hadmoko D.S., Komorowski J.C., Hananto N., Wassmer P., Hartono, Boillot-Airaksinen K. (2019a), Landscape evolution on the eastern part of Lombok (Indonesia) related to the 1257 CE eruption of the Samalas Volcano, *Geomorphology* 327, 338-350. https://doi.org/10.1016/j.geomorph.2018.11.010.

Mutaqin B.W., Lavigne F., Hadmoko D.S., Malawani M.N. (2019b), Volcanic Eruption-Induced Tsunami in Indonesia: A Review, *IOP Conf. Ser.: Earth Environ. Sci*. 256 012023. https://doi.org/10.1088/1755-1315/256/1/012023.

Mutaqin B.W., Marfai M.A., Helmi M., Rindarjono M.G., Windayati R., Sunarto (2020), Spatio-temporal Mapping of Ecotourism Activities in Buleleng Conservation Zone: A Methodological Review, *IOP Conf. Ser.: Earth Environ. Sci*. 451 012095. https://doi.org/10.1088/1755-1315/451/1/012095.

Nistor, M-M., Rahardjo, H., Satyanaga, A., Leong, E-C., Hao, K.Z., Sham, A.W.L., Wu, H. (2019). GIS-Based Approach to Identify the Suitable Locations for Soil Sampling in Singapore. *Geographia Technica*, 14(1), 103-117. http://doi.org/10.21163/GT_2019.141.08.

Pradjoko, E., Bachtiar, I., Matalatta, N., Sugihartono, G. (2015). The Submerged Breakwater as Prototype of Coastal Protection in Gili Trawangan, Lombok, Indonesia. *Procedia Engineering*. 125, 284-290. https://doi.org/10.1016/j.proeng.2015.11.041.

Ramalho, R., Quartau, R., Trenhaile, A., Mitchell, N., Woodroffe, C., & Ávila, S. (2013). Coastal evolution on volcanic oceanic islands: A complex interplay between volcanism, erosion, sedimentation, sea-level

change and biogenic production. *Earth-Science Reviews*. (127), 140-170. https://doi.org/10.1016/j.earscirev.2013.10.007.

Reguero, B.G., Beck, M.W., Agostini, V.N., Kramer, P. (2018). Coral reefs for coastal protection: A new methodological approach and engineering case study in Grenada. *Journal of Environmental Management*. 210, 146-161. https://doi.org/10.1016/j.jenvman.2018.01.024.

Reuter, M., and Piller, W.E. (2011). Volcaniclastic events in coral reef and seagrass environments: evidence for disturbance and recovery (Middle Miocene, Styrian Basin, Austria). *Coral Reefs*. 30, 889–899. https://doi.org/10.1007/s00338-011-0798-3.

Schils, T. (2012). Episodic Eruptions of Volcanic Ash Trigger a Reversible Cascade of Nuisance Species Outbreaks in Pristine Coral Habitats. *PLoS ONE* 7(10): e46639. https://doi.org/10.1371/journal.pone.0046639.

Schwendel, A., Fuller, I., & Death, R. (2012). Assessing DEM interpolation methods for effective representation of upland stream morphology for rapid appraisal of bed stability. *River Research and Applications*, 28(5), 567-584. https://doi.org/10.1002/rra.1475.

Shepard, F.P. (1973). *Submarine Geology* (3rd edition). Harper and Row, New York. 517p.

Silva, R., Mendoza, E., Mariño-Tapia, I., Martinez, M.L., and Escalante, E. (2016). An artificial reef improves coastal protection and provides a base for coral recovery. *Journal of Coastal Research*. SI (75), 467-471. https://doi.org/10.2112/SI75-094.1.

Statistics Indonesia. (2017). *Ekspor Menurut Kelompok Komoditi dan Negara*. Buletin Statistik Perdagangan Luar Negeri. Jakarta: CV Josevindo.

Sutarna, I.N. (1990). Shape and condition of living coral colonies in the waters around Banda Islands, Central Maluku. In: Praseno D. P., Atmadja, W. S. (eds) *Waters of the Maluku and its Environments*. Indonesian Institute of Sciences (LIPI), Ambon. 135-147.

Tomascik, T., van Woesik, R., and Mah, A.J. (1996) Rapid coral colonization of a recent lava flow following a volcanic eruption, Banda Islands, Indonesia. *Coral Reefs*. 1, 169–175. https://doi.org/10.1007/BF01145887.

UNEP-WCMC, WorldFish Centre, WRI, TNC. (2018). *Global distribution of coral reefs, compiled from multiple sources including the Millennium Coral Reef Mapping Project. Version 4.0, updated by UNEP-WCMC*. Includes contributions from IMaRSUSF and IRD (2005), IMaRS-USF (2005), and Spalding et al. (2001). Cambridge (UK): UNEP World Conservation Monitoring Centre. URL: http://data.unepwcmc.org/datasets/1.

Vidal, C.M., Komorowski, J.-C., Métrich, N., Pratomo, I., Kartadinata, N., Prambada, O., Michel, A., Carazzo, G., Lavigne, F., Rodysill, J., Fontijn, K., Surono. (2015). Dynamics of the major Plinian eruption of Samalas in 1257 A.D. (Lombok, Indonesia). *Bulletin of Volcanology*. 77(9), 73. https://doi.org/10.1007/s00445-015-0960-9.

Vogel, S., & Märker, M. (2010). Reconstructing the Roman topography and environmental features of the Sarno River Plain (Italy) before the AD 79 eruption of Somma–Vesuvius. *Geomorphology* (115), 67-77. https://doi.org/10.1016/j.geomorph.2009.09.031.

Vroom, P.S., and Zgliczynski, B.J. (2011). Effects of volcanic ash deposits on four functional groups of a coral reef. *Coral Reefs*. 30, 1025–1032. https://doi.org/10.1007/s00338-011-0793-8.

Zhu, X. (2016). *GIS for Environmental Applications: A practical approach*. Routledge, London, 490p. https://doi.org/10.4324/9780203383124.

Zimmerman, D., Pavlik, C., Ruggles, A., & Armstrong, M. (1999). An Experimental Comparison of Ordinary and Universal Kriging and Inverse Distance Weighting. *Mathematical Geology*, 31(4), 375-390. https://doi.org/10.1023/A:1007586507433.

PRECIPITATION USED AS KEY FACTOR IN TAPERED LINE BASED RIVER REPRESENTATION

Zsolt MAGYARI-SÁSKA[1]

ABSTRACT:

GIS and cartography represent two different study areas but both of them share the map concept. Nowadays, most GIS software incorporates advanced representation and labeling possibilities, and thanks to the database, which is an essential component of any geoinformation system, there are multiple symbolization possibilities, using the stored data. Taking into account this symbiosis between the two components of modern GIS: analysis and advanced representation this study wants push further the cartographic possibilities of them taking advantage of their analysis and modelling part. Through this study we wanted to develop and test a method for river symbolization in which the river's line width to be proportional with the average precipitation amount at every part of the river. The idea of this study came by working with hand drawn historical maps in which this type of representation is common and very suggestive. Although there are some interesting approaches which want to symbolize river courses based on data, this type of approach presented in this study has not been found. The result obtained from a situation where inaccuracies are inevitable due to very different data sources: a recent DEM with 25m resolution and a map from the beginning of the 20th century with scale of 1: 300000, has shown that this method based on modeling, analysis and GIS operations can be used successfully to have a more accurate, more real and eye catching symbolization of watercourses.

Key-words: river symbolization; realistic representation; historical map; python scripting; QGIS

1. INTRODUCTION

Cartographic representations have several important roles. Maps as valuable information holding and presenting tools are used not just in orientation but also for illustrating content, phenomena, processes in an eye captivating manner (Cosgrove, 2005). This latter use of maps sometimes relies on exaggerating the reality, sometime simplifying it or in many cases just trying to reflect the reality as much as possible (Thorwer, 2007; Petersen, 2014). When it's about reality GIS can provide useful backend data analysis methods to precisely calculate data and based on these results to achieve a more suggestive cartographic representation (Hardy et al., 2005; Mei and Li, 2008; Brewer, 2015).

Our research intends to make a contribution in river mapping. The most common method for representing watercourses is the use of lines, which width suggests the importance and size of the river mainly based on its water flow quantity or in some cases based on river length. In such cases the width is maintained constant through the line length especially if it's created using GIS. In some vector illustration software may exists possibilities to gradually increase the line width but these approaches can use just the length of the line as base value.

If we look at historical maps in many cases, we can observe that the rivers width is gradually growing as it flows from their spring to inflow (**Fig. 1**). As in many other fields such in architecture or furniture design also in cartography meticulous work in the creation process was not intended just to reveal the beauty but to create a practical, a usable thing. A few years ago we started to analyze how we could digitally recreate in an automatized way the hachure lines used in relief representation (Magyari-Sáska, 2017). With this research we want to continue and to investigate the automatic recreation possibilities for historical and not just historical maps, presenting a GIS based method for river flows representation based on mean annual rainfall data.

---

[1] *Babes-Bolyai University Cluj, Faculty of Geography, Gheorgheni Extension, 535500 Gheorgheni, Romania, zsmagyari@gmail.com.*
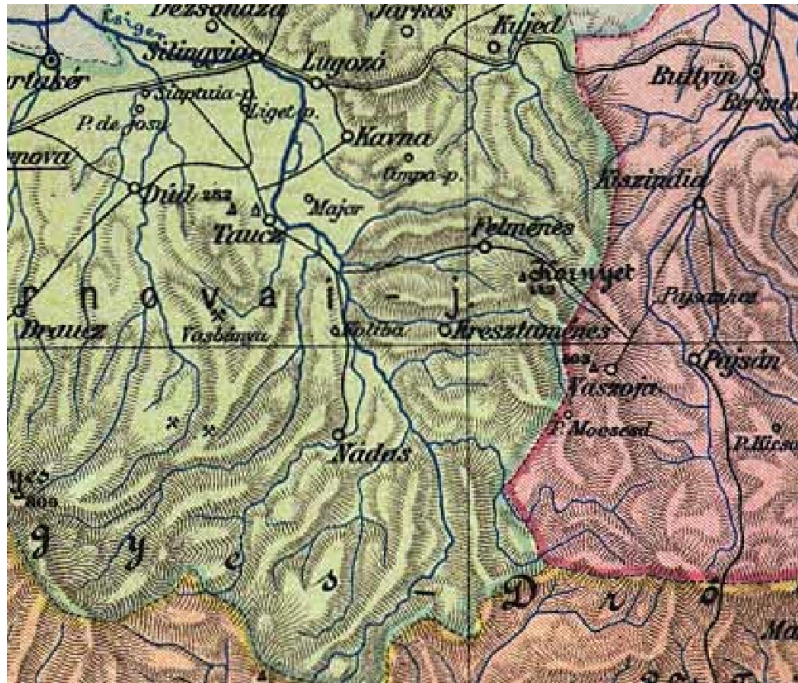
Fig. 1. Gently thickening river representation in a historical map

Although there are studies related about the processing (Piovan, 2019; Timár and Biszak, 2010; Rumsey and Punt, 2004) and automatic vectorization of old maps (Iosifescu et al., 2016), there is no such research or method regarding symbolization, although the importance of suggestive representation is shown up in several studies (Punt et al., 2006; Yamg and Lin, 2008).

2. METHODS AND RESULTS

The objective of the research was to develop a method for creating vector layers representing rivers, which are suitable for the desired symbolization. This layers should have an attribute value based on which the gradually growing line representation can be made. The symbolization should respect the reality considering that the line width should grow in correspondence with that rainfall which contributes to the river water quantity at every part of the river.

The existing vector data-model doesn't provide many possibilities to achieve the desired representation as a line feature could have a single (even if it's calculated from several fields) value based on which it's width is determined by scaling it to different intervals. The existing symbolization methods can be groups as below:

- methods in which a single symbology (including width) is used for a line depending on line attributes or their combinations. This is the most widely use method, with drawback, that the width is constant through all course (**Fig. 2a**).
- methods in which the line forming segments are identified in the symbolization process and treated separately in generating the width (**Fig. 2b**). This method is presented by A. Graser in 2017 in an on-line article *Better river styles with tapered lines* and further developed by M.R. Lombardo in 2019 in another on-line article: *Improved tapered rivers in QGIS*.
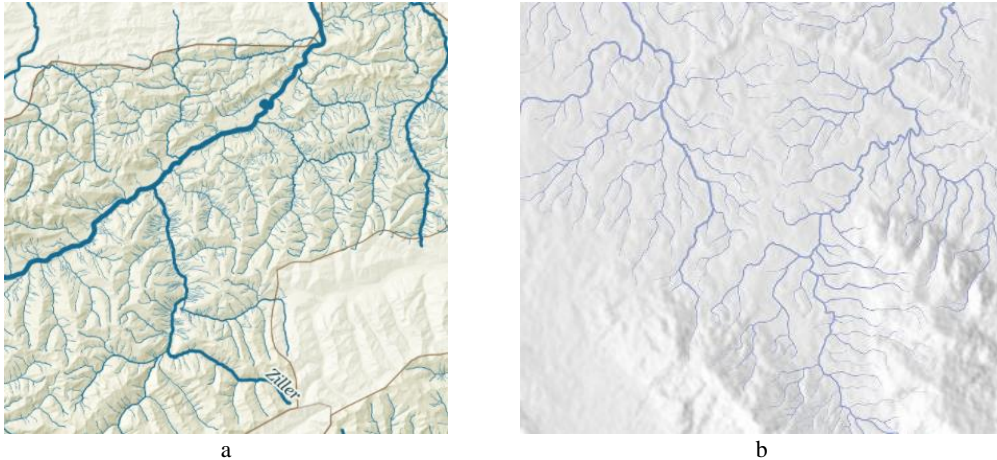
Fig. 2. Existing river symbolization ways: a) with constant width (source: Graser, A. – Tirol riverset) b) with tapered lines (source: Lombardo, M.R. – Cuencas de los ríos Sansón y Sansoncito)

This second method category catches the main idea but the actually varying factors that controls the line width are: the current segment number divided to the total number of segments which forms the line, and values (hard coded or attribute based) which are constant for a line. This means that the middle line segment will have approximately the average width of the first and last line segments' width. Moreover, this approach being a software dependent possibility, doesn't represent a general solution in symbolization process. With all this, the method (if present in given GIS.) has the advantage of not exploding the line to segments, from which we can benefit at feature labeling.
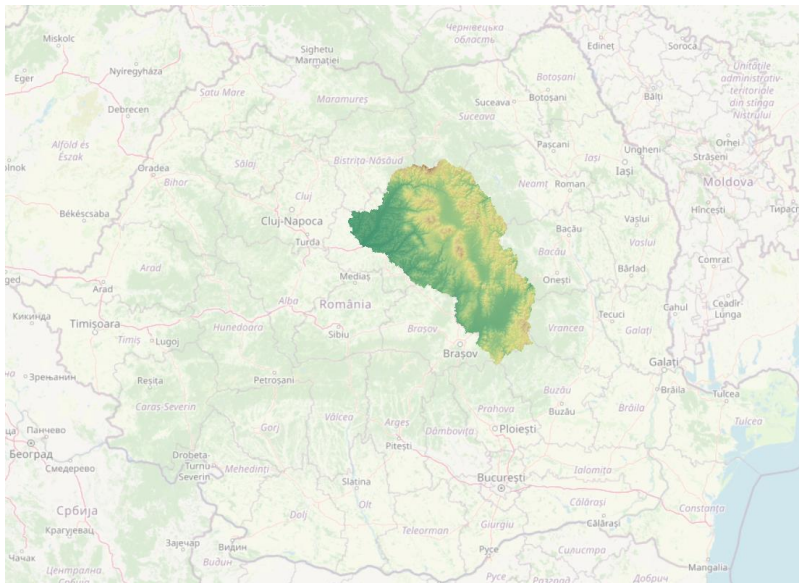
Fig. 3. Test area in Romania's central region

Our developed method wants to assign different values for different line segments proportional to the water quantity that could be present at a given line segment. As this is practically impossible we had to split every line feature representing a river, obtaining in fact as much features as it's the number of segments that forms the original line feature. The attached values indicating the water quantity can be modelled at various complexity levels. As our research is more exploratory then applicative for a given region, we don't want to focus on achieving the best possible modelling of rivers runoff values we did not take into account the pedagogical characteristics of soil nor the

vegetation's impact or evapotranspiration which may contribut to the runoff value (Crăciun et al., 2009).

As we will present below the study has the following main parts: achieving a fair spatial interpolation of average annual rainfall, calculating and attaching a rainfall based attribute to each exploded line segment to use it in symbolization. Even if the current study is methodological, we selected a test area, which was the central region of Romania covering part of Harghita and Covasna and Mureș counties as presented in **figure 3**.

2.1. Rainfall interpolation

Starting from the simplest IDW to complex geostatistical methods such as Krieging, there are various techniques for rainfall interpolation which are in used and compared in many studies (Hartkamp et al., 1999; Naoum and Tsanis, 2004; Taesombat and Sriwongsitanon, 2009; Mair and Fares, 2011; Noori et al., 2014). The efficiency off these methods depends on many factors which has the origin mainly in the number and spatial distribution of measurement sites (Di Piazza et al, 2011; Chen et al., 2017;). Because in our case there are just a few meteorological stations in the study region, we considered more appropriate to take all measurement data existing at different meteorogical stations in Transylvania region and apply a less common but suitable method based on multiple regression (Efroymson, 1960; Hastie and Pregibon, 1992). Due to the fact that we don't want to interpolate the rainfall value obtained in a short time period (hours or days) to see the spatial distribution of values, but to characterize the annual average precipitation distribution over a multi-decade period, we have considered that identifying factors that influences the precipitation could be a fair try.

Accordingly, we used the backward stepwise multiple linear regression in R statistical software package (Venables and Ripley, 2002). The method takes all linear combination of the specified factors, named predictors and based on various statistical criteria (in case of R the Akaike Information Criterion is used) identifies that combination which has the highest correlation value to predict the give result dataset (Chatterjee and Hadi, 2012).
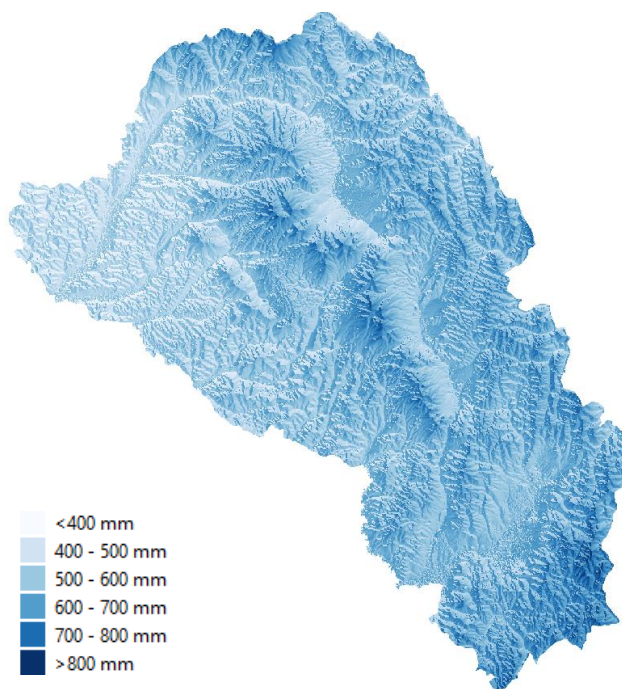

Fig. 4. Annual average rainfall map interpolated using backward stepwise multiple regression

As candidate factors, we used the height (source: EU-DEM v.1.1, resolution: 25m) which is considered an important factor (Modallaldoust et al., 2008; Huang and Hu, 2009), the coordinates, and the aspect. From the mentioned 4 predictors only the x coordinate was considered by the model not influential for the given region and for the annual average precipitation value. Based on the obtained predictors we made the interpolation and got the rainfall distribution map (**Fig. 4**).

2.2. Calculating accumulated precipitation values

In the beginning we performed the necessary hydrological operations such as fill sinks to can create a correct flow accumulation image. In creating the flow accumulation, the interpolated precipitation values were considered as weighting factor. Analyzing the accumulation values the channel network can be identified, which has an important role in watershed basins generation. The presented process was realized in SAGA (**Fig. 5** – blue part).
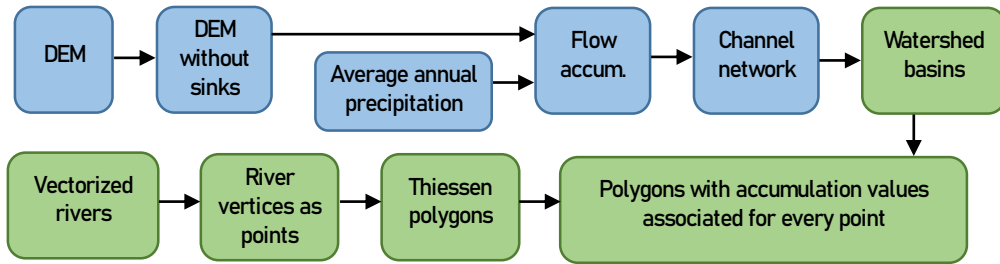

Fig. 5. Determining flow accumulation for every vertices representing river line segments endpoints (raster layers with blue, vector layers with green background)

Having the accumulated precipitation values it seems to be very easy to attach these values to the vertices defining the rivers. Due to the fact that the DEM on which the hydrological analysis was done and the historical map from which the rivers were vectorized could not have proper overlay the vertices in many cases were positioned on such cells which had very improper accumulated precipitation value. We had to find a way to attach an appropriate cell value even if this are relatively far from the vertex but its value surely is most correct than those below the vertex.

We needed a spatial splitting method. For this we created Thiessen polygons based on river vectorization vertices. In such way we've got an own region for every river vertex which of course could pass over several catchments. To overcame this unwanted situation, we made an intersection between the created Thiessen polygons and the watershed basins layer. (**Fig. 5** – green part) From the obtained polygons we always took the highest accumulated precipitation value, considering that in fact this value should have been under the vertices in case of spatially precisely corresponding data layers. Even if for our test case the dislocation of map elements maybe it's more pronounced than in other situations, in most cases this kind of inaccuracies appears and the presented method could represent a solution for it.

2.3. Attaching accumulated precipitation values to line segments

After we got the accumulated precipitation values in polygons representing intersection between catchment areas and the Thiessen polygons defined by the endpoints of river segments, we had added their values to the proper line segments. For this we the mean precipitation values present at the end points of the line segments were used. Because this process could not be performed with existing QGIS operations we had to develop a Processing script in Python which has two input: a line layer with vectorized rivers and a polygon layer with the accumulated precipitation values for the catchment area slices.

The accumulated precipitation values along every vectorized river, this should form a monotonically increasing data series. Unfortunately, this isn't true due to the following situations:

- the flow may have incorrect vectorized direction from inflow to spring resulting a theoretical monotonically decreasing series. Although this may be considered a vectorization error it could frequently appear.
- the vectorized river path may cross through different catchments (**Fig. 6**) for different reasons (scale, resolution or precision difference between the digital elevation model and original map sheet)
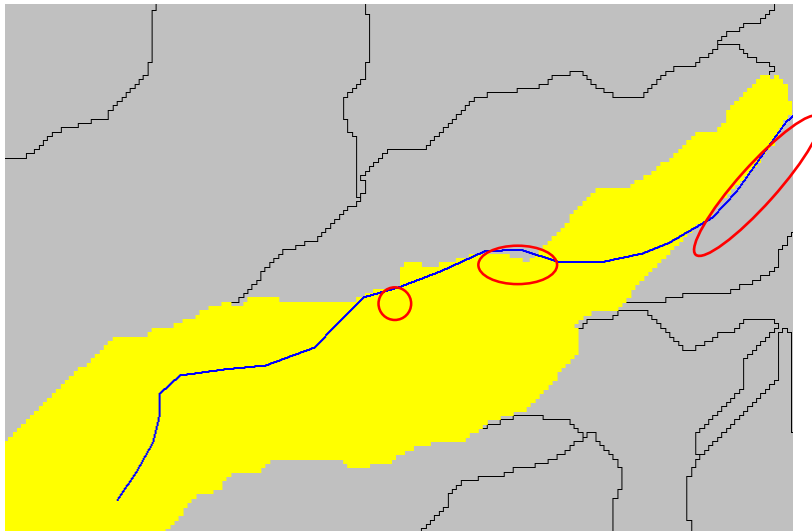

Fig. 6. Vectorized rivers touches multiple catchments resulting improper accumulation data

While the first situation obviously should be corrected by detecting and inverting the direction the second situation raises the question of should the streamflow path corrected or not? The answer of course depends on the effective situation. In our case the concept was to create a digital version of a historical map with the highest representation fidelity. In this case even if the original map had a weak precision, we wanted to keep its look, maintaining the internal positional proportions between the cartographic elements. Considering this, for both problematic situations we developed one method at each to overcome them as follows.

Incorrect streamline direction

The direction of a vectorized line is stored inside the associated data structure and can visualized by using arrow symbol in visual representation. Even if most of the time the line direction is not important in several cases it could be crucial. Such applications are network routing with one-way connections or river flow modelling. In our case we should have a method to detect whether the vectorization direction was correct or not. This could be done using gradient analysis along the line but as we already had the accumulated precipitation values, we decided to make use of it.

The detection method is simple based on signum function with the assumption that the number of vertices positioned in proper catchments are higher than for those in incorrect catchments. In this case by counting and comparing the number of cases at which the accumulated precipitation values doesn't follow an increasing trend to total number of vertices we succeeded to identify with high probability the lines vectorized on incorrect direction. The ratio was calculated for every river using equation 1

$$\frac{\sum_{i=1}^{n-1} sgn(v_{i+1}-v_i)}{n-1} \tag{1}$$

where *n* indicates the number of vertices that forms the line and v_i is the accumulated precipitation value at vertex *i*. A line was considered having an incorrect direction is the value of the ratio in equation 1 was higher than 0.6.

Anomalies in precipitation accumulation data series

As mentioned before due to spatial dislocation between DEM and original map sheets, which are caused especially by scale/resolution differences, in many cases a streamflow touches or crosses other catchment areas than its own. In these cases, the accumulate precipitation values are inappropriate for the current flow and can significantly differ from the real values. **Figure 7** shows an example for such cases. There are observable that many vertices which are positioned in other catchments. For this example, in the majority of cases the precipitation values of wrong catchments are much lower, undershooting the values for the normal course of the river and in a few cases the vertices are positioned in catchment with higher precipitation value, overshooting the values. As these misplaced values has negative influence on the desired symbolization we should identify and treat them properly.
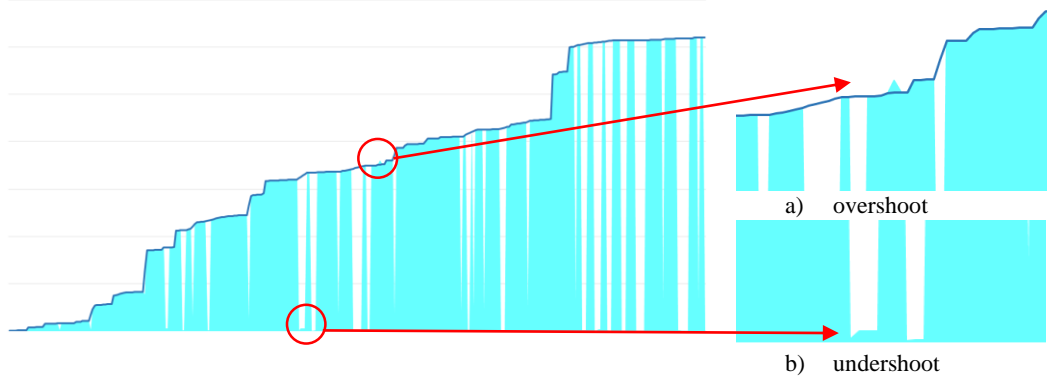

a) overshoot

b) undershoot

Fig. 7. Incorrect data series (with cyan) resulted from accumulated precipitation value due to vertices in incorrect catchment areas. Correct flow values are presented with the top blue line.

As these values can't be considered time series or series with a specific statistical distribution the well-known anomaly detection or outlier detection algorithms could not be applied successfully.

Taking in consideration the real-life imposed monotonicity that should be present for every stream we developed a rank-based algorithm where two type of ranks are associated to every vertex one based on their appearance order and the other based on accumulated precipitation value order. When the values of two rank type are identical, we got a monotonic increasing series and the goal was reached. The main steps of the algorithm are presented in **figure 8.** which was implemented in PyQGIS, which is a valuable scripting language to extend the processing capabilities of QGIS (Sherman, 2018).

```
set initial position-based ranks
set initial value-based ranks
while pairwise ranks are different
        identify and exclude from dataset the rightmost data with the highest rank difference
        set new position-based ranks
        set new value-based ranks
for all excluded data
        set their new values using linear trend based on not excluded head and end data
```

Fig. 8. Processing algorithm for detecting and correcting anomalous data in accumulation value series

2.4. Final result

Applying the PyQGIS processing script we got a vector layer in which every line feature corresponds to an original line segment of the vectorized rivers. As an attribute of the layer, for every feature the corrected accumulated precipitation value is present.
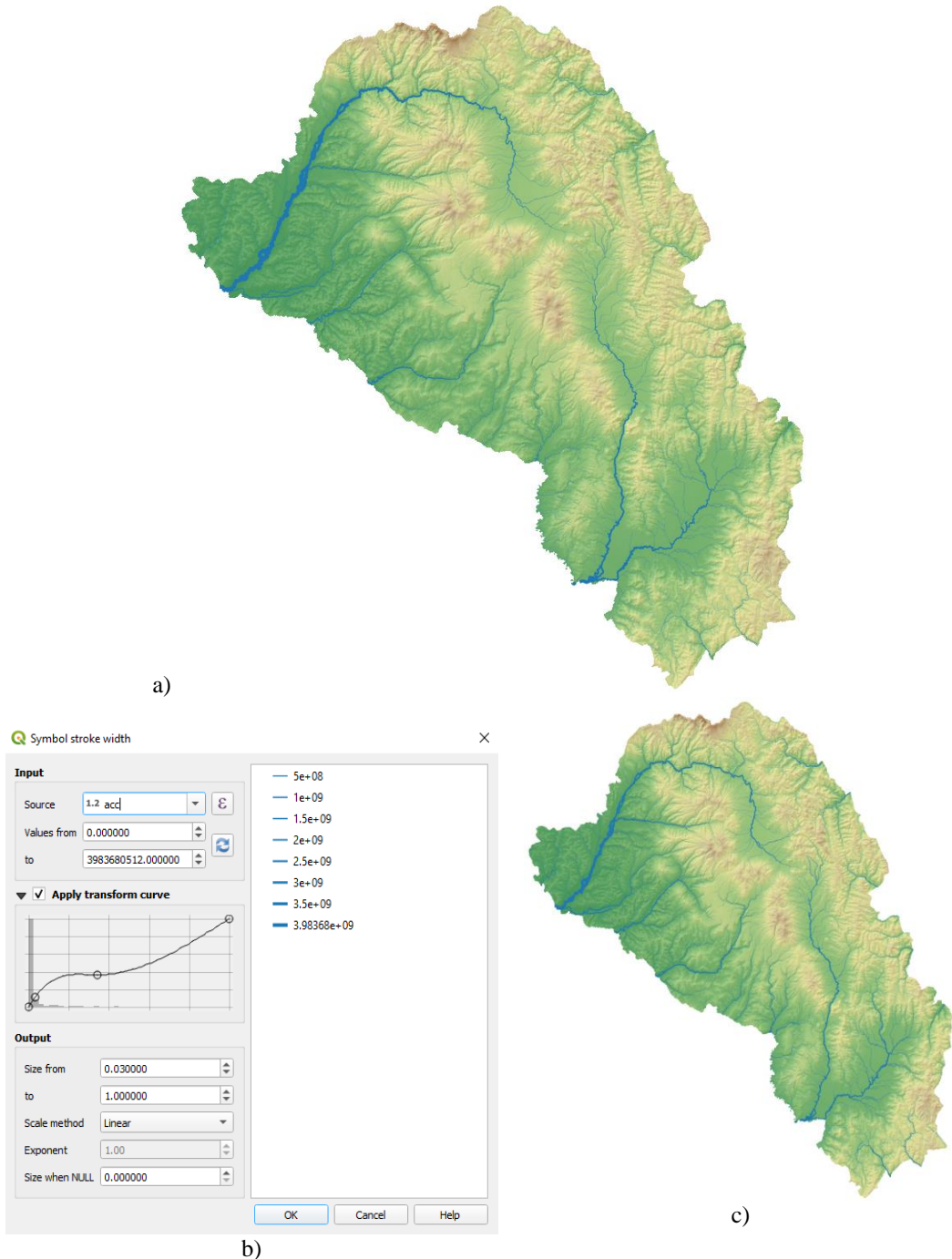

Fig. 9. Resulted river representation. Growing width is modelled based on precipitation in catchment areas. a) line width after linear scaling b) manually definable scaling curve in QGIS c) line width using manually adjusted scaling curve emphasizing smaller creeks and brooks

These values can be used in line symbolization. From now on the visual effect depends on the symbolization possibilities of the used GIS. The values can be scaled in a linear way, determining the representation width, or other functions (logarithmic, exponential) can be applied on data to emphasize higher or lower values before rendering them (**fig. 9**). QGIS also has an advanced method, called Assistant, in which the transformation curve between the existing data and the selected visualization width range can be manually adjusted.

Whatever the possibilities are in a given GIS the segments width now is proportional with the presumed water quantity that can be assumed for that river portion.

3. CONCLUSIONS

The aim of this study was to develop a methodology for representing rivers according to their water quantity. To test our methodology, we considered solely the interpolated precipitation values as contributing factor to line width, but the methodology permits to consider any other more sophisticated method to estimate the flow value. As only individual line features can have their width determined by attribute table values, we had to split every line to its line segments resulting multiple features for every river. This is the most disadvantageous element of our study because it affects the labelling possibilities of original line features. The most challenging part of the study was how to maintain data consistency of the accumulated values in case of rivers because the spatial position of vectorized river network in some cases doesn't correspond to catchment areas derived from DEM.

We think that the developed methodology presents a possibility not just to create more beautiful visual representations but also more realistic ones. Even if the real width of a river is not determined just by its water quantity in cartographic representations this is the key factor indicating the magnitude of the river.

The developed methodology, as shown in figure 5 not just gradually increases the river width according to the water amount, but inflows from other water sources are clearly observable as steps in the data series. Another benefic effect of this approach is that the line width is maintained even if the river splits around small islands which is usually vectorized as separate line features with different lengths.

Beside the fact that using our method the rivers width is not rendered based on their length or category as in most of the current representations, there are some other advantages. It does not matter the vectorization direction, because in case of wrong direction it is detected and changed accordingly. It does not matter if the lines are not merged together or if the river network topology is incorrect as these elements are not considered.

In the final the methodology can be used even if we want to illustrate just a smaller portion of the river network from a larger area, as the data used on which the representation is made relies on accumulated precipitation values and if we have this data, the accumulation values are propagated automatically to the interested locations where the vectorized rivers are present.

REFERENCES

Brewer, C. A. (2015). *Designing Better Maps: A Guide for GIS Users*, 2nd ed. Esri Press, Redlands, CA.

Chatterjee, S., Hadi, A. (2012), *Regression Analysis by Example*. 5th ed. N.p.: John Wiley & Sons

Chen, T., Ren, L., Yuan, F., Yang, X., Jiang, S., Tang, T., Liu, Y., Zhao, C., Zhang, L. (2017) Comparison of Spatial Interpolation Schemes for Rainfall Data and Application in Hydrological Modeling, *Water*, 9(5), 342, DOI: https://doi.org/10.3390/w9050342

Cosgrove, D. (2005) Maps, Mapping, Modernity: Art and Cartography in the Twentieth Century, *Imago Mundi*, 57(1), 35-54, DOI: 10.1080/0308569042000289824

Crăciun, I., Haidu, I., Magyari-Sáska, Zs., Imbroane, A.I. (2009), Estimation of Runoff Coefficient According to Soil Moisture Using GIS Techniques, *Geographia Technica*, 4(2), 1-10

Di Piazza, A., Lo Conti, F., Noto, L.V., Viola, F., La Loggia, G. (2011), Comparative analysis of different techniques for spatial interpolation of rainfall data to create a serially complete monthly time series of precipitation for Sicily, Italy, *International Journal of Applied Earth Observation and Geoinformation*, 13(3), 396-408, https://doi.org/10.1016/j.jag.2011.01.005

Efroymson, M.A. (1960) Multiple regression analysis. In Ralston, A. and Wilf, HS, editors, *Mathematical Methods for Digital Computers.* Wiley.

Hardy, P., Eicher, C., Briat, M., Kressmann, T. (2005) Database-stored Representations and Overrides, Supporting Automated Cartography with Human Creativity, *Auto-Carto 2005 Proceedings*, Las Vegas

Hartkamp, D., De Beurs, K., Stein, A., White, J.W. (1999), *Interpolation Techniques for Climate Variables*, International Maize and Wheat Improvement Center, Mexico, 26

Hastie, T.J., Pregibon, D. (1992) *Generalized linear models.* Chapter 6 of *Statistical Models in S* eds J. M. Chambers and T. J. Hastie, Wadsworth & Brooks/Cole.

Huang B., Hu T. (2009) Spatial Interpolation of Rainfall Based on DEM. In: *Advances in Water Resources and Hydraulic Engineering*. Springer, Berlin, Heidelberg. DOI: 10.1007/978-3-540-89465-0_15

Iosifescu, I., Tsorlini, A., Hurni, L. (2016), Towards a comprehensive methodology for automatic vectorization of raster historical maps, *e-Perimetron*, 11(2), 57-76

Magyar-Sáska, Zs. (2017) Automatic generation of hachure lines, *Geographia Technica* 12(1), 78-81, DOI: 10.21163/GT_2017.121.08

Mair A., Fares A. (2011), Comparison of Rainfall Interpolation Methods in a Mountainous Region of a Tropical Island, *Journal of Hydrologic Engineering* 16(4), 371-383, DOI: 10.1061/(ASCE)HE.1943-5584.0000330

Mei Y., Li, L. (2008), A Cartographic data model for Better Geographical Visualization based on Knowledge, *The International Archives of the Photogrammetry, Remote Sensing and Spatial Information Sciences*. Vol. XXXVII. Part B2. 611-616

Modallaldoust, S., Bayat, F., Soltani, B., Soleimani, K., (2008), Applying Digital Elevation Model to Interpolate Precipitation. *Journal of Applied Sciences*, 8: 1471-1478, DOI: 10.3923/jas.2008.1471.1478

Naoum, S., Tsanis, I.K. (2004), Ranking Spatial Interpolation Techniques Using a GIS-Based DSS, Global Nest Journal. 6(1), 1-20, DOI: https://doi.org/10.30955/gnj.000224

Noori, M.J., Hassan, H.H., Mustafa, Y.T. (2014), Spatial Estimation of Rainfall Distribution and Its Classification in Duhok Governorate Using GIS, *Journal of Water Resource and Protection*, 6, 75-82, DOI: 10.4236/jwarp.2014.62012

Petersen, G. (2014). *GIS Cartography: A Guide to Effective Map Design* (2nd edition) CRC Press, Boca Raton, FL.

Piovan, S. (2019). Historical Maps in GIS. *The Geographic Information Science & Technology Body of Knowledge* (1st Quarter 2019 Edition), John P. Wilson (Ed.).

Rumsey, D., Punt, E. M. (2004) *Cartographica Extraordinaire: The Historical Map Transformed*. Redlands, CA: ESRI Press.

Sherman, G. (2018), *PyQGIS Programmer's Guide*, Locate Press, 252

Taesombat, W., Sriwongsitanon, N. (2009), Areal rainfall estimation using spatial interpolation Techniques, *ScienceAsia*, 35, 268-275, DOI: 10.2306/scienceasia1513-1874.2009.35.268

Thrower, N. J. W. (2007). *Maps and Civilization: Cartography in Culture and Society* (3rd edition), University of Chicago Press, Chicago.

Tímár, G., Biszak, S. (2010), Digitizing and georeferencing of the historical cadastral maps (1856-60) of Hungary, *5th International Workshop on Digital Approaches in Cartographic Heritage*, Vienna, Austria, 22–24 February 2010

Venables, W.N., Ripley, B.D. (2002) *Modern Applied Statistics with S.* New York: Springer (4th ed.).

THE RELATIONSHIP BETWEEN NORMALIZED DIFFERENCE VEGETATION INDEX AND CANOPY TEMPERATURE THAT AFFECTS THE URBAN HEAT ISLAND PHENOMENON

Tissadee PROHMDIREK[1] *Poramate CHUNPANG[1]*, *Teerawong LAOSUWAN[1*]*

ABSTRACT:
The objective of this research is to analyze the relationship between Normalized Difference Vegetation Index (NDVI) and canopy temperature that affects the Urban Heat Island (UHI) phenomenon in Mueang Maha Sarakham Municipality. The operational methods were divided into three main steps: 1) Analyzing NDVI by using Landsat 8 OLI satellite data 2) Monitoring canopy temperature with mobile traverses installed with digital thermometer and auto-record GPS receiver 3) Analyzing the relationship between NDVI and canopy temperature that passed through the spatial interpolation process using the kriging method. The results of the operational methods indicated that the trend of average atmospheric temperature in the urban area was higher than the outer area. Mueang Maha Sarakham Municipality had the highest UHI in the atmosphere at 4.65° C. And from the buffer zone with a distance of 800 m around the centroid point, the highest UHI in the atmosphere was 5.08° C. From the regression analysis between NDVI and the atmospheric temperature, it could be found a negative relationship between the data with a significance level of 0.01 and the decision coefficient (R^2) of 0.9392. This can be explained that if the area from the buffer zone decreased towards the centroid point, the value of NDVI decreased as well. In addition, when the equation set from the regression analysis was brought to predict the difference in atmospheric temperature in the area of Mueang Maha Sarakham Municipality and the surrounding area, the UHI sizes at all periods (16.00-20.00 hrs.) increased in accordance with the decreases of NDVI values. Meanwhile, considering the tendency between the changes in UHI size in the atmosphere in each period and NDVI values with the polynomial regression analysis (degree 4), it was found that the maximum formation of UHI was during 18.00-19.00 hrs.'. The decreases in NDVI values resulted in a higher UHI size in each period. In addition, when the NDVI values in Mueang Maha Sarakham Municipality were less than 0.302, the largest size of UHI in the atmosphere will change at the time approaching 19.00hrs.

Key-words: *Normalized Difference Vegetation Index (NDVI); Urban Heat Island (UHI); Remote Sensing; Landsat 8.*

1. INTRODUCTION

At present, the rapid development progress in urban areas for human economic prosperity, namely business areas, industrial areas and famous educational centers, has resulted in increasing demand for land uses, especially in central cities or prosperous places with a high population density, for the purposes of operations or performing activities. These land uses have led to the increase in instructions of buildings and roads that affects the changes in environment and atmospheric temperature continuously (IPCC, 2019). This is because, if buildings are exposed to sun heat during daytime, the heat will be released into the atmosphere after sunset. For this reason, when comparing between urban areas and rural areas that are nearby each other, it can be seen that the atmospheric temperature after sunset in urban areas is still higher than rural areas (Huang & Lu, 2017), which caused occurrence of the Urban Heat Island (UHI) phenomenon in the atmosphere with a tendency of rising temperature from surrounding areas to the highest temperature in central cities (United States Environmental Protection Agency, 2008). Generally, the atmospheric temperature will drop sharply after sunset in rural areas due to most of rural areas or suburbs have more vegetation cover than urban

---

[1] *Department of Physics, Faculty of Science, Mahasarakham University, Maha Sarakham, 44150, Thailand*
[*] *Corresponding author email: teerawong@msu.ac.th*

areas. By comparison, during a day, the UHI's size will emerge distinctly after sunset. And during different seasons, the UHI's size will emerge distinctly during the winter (Yokobori & Ohta, 2007; Singhachantra, 2012).

The result of the increase in land uses is one of the causes that decreases in the amount of vegetation and land covers, that are green space (Zhang et al., 2010; Mathew et al., 2017; Ursu, 2019). Vegetation and green space can help reduce air temperature or the rate of UHI formation in urban areas effectively from water release of trees (Kophim, 2013), including reduction of flux values and heat radiation of buildings that accumulate heat energy from solar radiation throughout daytime, will result in the change in atmospheric temperature after sunset (Takebayashi & Moriyama, 2009; Perini & Magliocco, 2014; Yang et al., 2018). According to the previous cause, some periods of time, air temperatures between urban areas and surrounding areas are not balanced. Generally, considering the changes in air temperature at different time periods in the study area, the actual data from ground measurement stations can be analyzed by spatial analysis interpolation in order to predict the quality value trend of the atmospheric temperature in the areas or positions between the points that have the actual measurement data from measurement stations (Gopal & Kaufmann, 2000; Kambi et al., 2018) in order to obtain the actual air temperatures from measurement stations which have the number of sample points spread as much as possible in the study area. From the study of related documents, it has been found that there are many researchers conducted the measurement of the air temperature by using mobile traverses. The sample points were collected the data continuously along the routes in the study area. Also, locations and air temperatures were automatically recorded. The height of each temperature measurement point was set at 1.5 meters above the earth ground. And the resolution of the measurement tool was generally set at 0.1°C. The data obtained from the measurement were brought to evaluate and compare the air temperatures around outer areas with urban areas (Vicente-Serrano et al., 2005; Sodoudi et al., 2014; Cardoso & Amorim, 2018) that led to the study of UHI occurrence in the canopy atmosphere, which is a change in the levels of height from the ground in several time periods or areas with a large numbers of living creatures (Dupont & Ching, 2004; Srivanit & Hokao, 2012; Mukhelif et al., 2016).

Many researchers had analyzed the relationship of air or surface temperature changes from the UHI phenomenon and land covers by classifying land cover types using remote sensing technology in order to detect vegetation-covered areas or green spaces, buildings, constructions and so on. For example, the study relationship of land surface temperature changes from the UHI phenomenon and the percentage of green spaces was studied by calculating the data from the QuickBird, SPOT, Landsat 5 TM satellite in Beijing, China. The result was found that the green spaces in the range of 10-20% resulted in the increase in land surface temperature approximately $31\text{-}35^{\circ}$C. If the percentage of vegetation cover increases, the trend of land surface temperature will decrease in accordance with a linear regression relationship (Li et al, 2013). From several researches, there are studies and testing the relationship with regression analysis between UHI size and NDVI of areas in Delhi and Mumbai, India in 2010. The results indicated that the relationship between those values had a negative direction and tendency. The thermal expansion revealed that the covers of buildings and bare soils indicated high air temperatures. While areas covered with vegetation and water sources indicated lower air temperatures. The areas that represented the UHI sizes clearly could be found to be the areas densely covered by buildings (Grover & Singh, 2015). In addition, the Landsat 8 satellite data were used to analyze the expansion of UHI sizes in Skopje, Macedonia area which had the change of land covers over the period of 5 years from 2013 - 2017. The results indicated that the NDVI values decreased while buildings increased from to the expansion of urban area. The thermal expansion showed the highest land surface temperature that changed from the original temperature at 12°C. This result was consistent with the data of the air temperature change from the weather station of Meteorological Department. And the UHI size expanded from the original area approximately 4 km^2 (Kaplan et al, 2018). According to the increase in the temperatures in urban areas as previously mentioned, this research aims to analyze the relationship between NDVI and canopy temperature that affects the UHI phenomenon in Mueang Maha Sarakham Municipality, that will lead to the assessment of the changed relationship of vegetation and UHI sizes.

2. MATERIALS AND METHODS

Mueang Maha Sarakham Municipality, Talat District, Maha Sarakham Province (**Fig**. **1**) has an area of approximately 24.14 km² and is located at the coordinates of 16°10'38.1" N 103°18'3.5" E.
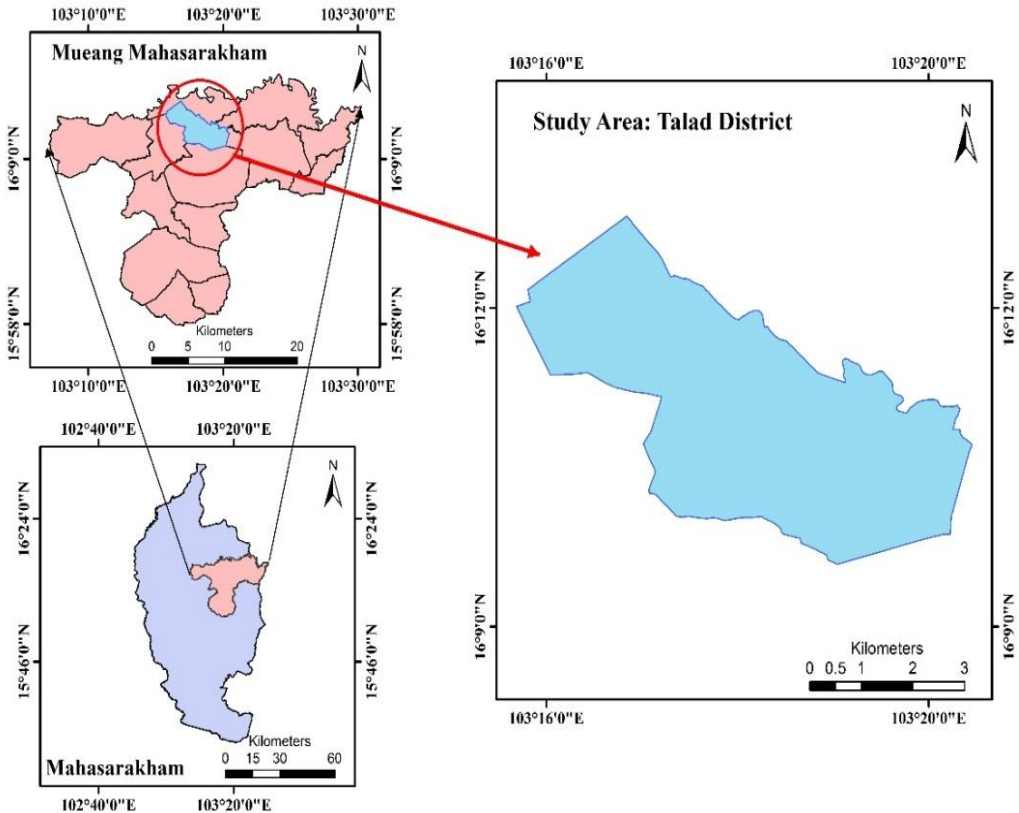

Fig. 1. Study area.

The characteristic of the area is an anticline highland. The general area is approximately 130-230 meters above sea level. According to the data of 2009, the population in Mueang Maha Sarakham Municipality was a total of 39,965 people with a population density of 1,655 people/km² and 16,759 households. In 2019, the population density increased to 2,124 people/km² and the housing rate increased up to 62% (Official Statistics Registration Systems, 2019). This represented that the area of Maha Sarakham Municipality had an expansion of population due to it has played an important role in being a central city for educational services. Moreover, according to the data from Meteorological Department, the average annual temperature was 33.4 °C in 2019(Thai Meteorological Department, 2019).

2.1. Surveying the study area

Studying the routes along the road network in the study area as well as exploring the actual area in order to set a route for the optimal period for collecting sample data and covering the study. In this study, the routes for collecting data in the study area were divided into 2 parts (**Fig**. **2**) including inner routes and outer routes of Mueang Maha Sarakham Municipality.
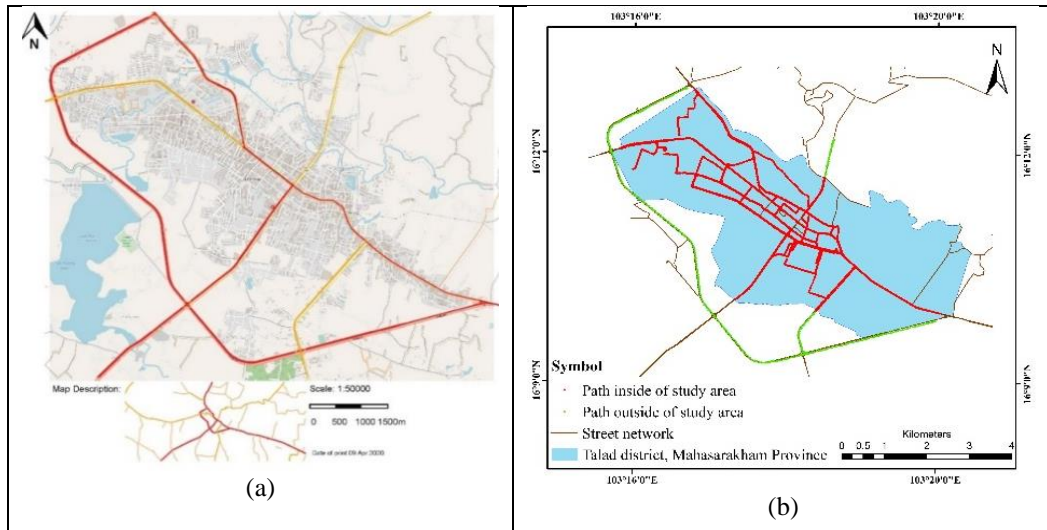
Fig. 2. (a) Road network covering the study area, (b) Path to store sample data inside and outside Mueang Maha Sarakham Municipality.

2.1.1 Conditions and data collection periods

This research collected the sample data during the winter in February 2020. The periods of days were 16.00 hrs., 17.00 hrs., 18.00 hrs., 19.00 hrs. and 20.00 hrs. due to the UHI phenomenon in the atmosphere will generally indicate values clearly after sunset. The sample data were screened and analyzed only on a calm day in order to determine sizes of the UHI phenomenon. Because these weather conditions will prevent formation of the UHI phenomenon (Singhachantra, 2012). After determining the routes to collect sample data, 4 sets of indicators in form of mobile traverses were used, divided into 1 set for outer areas and 3 sets for inner areas. The vehicle speed was controlled not over 40 km/h to obtain approximate air temperature data throughout the study area in adjacent periods. Also, the measurement time for each area was determined to be completed within 10-12 minutes. Meanwhile, the time of the indicator for recording data was set every 5 seconds.

2.1.2 Preparing satellite data

The data at the closest time of collecting sample data was selected to reduce discrepancies caused by land uses over many different periods of time. The radiation reflectivity and solar height angle of Landsat 8 OLI satellite data (recorded on February 12, 2020 from EarthExplorer-USGS) were adjusted in band 4and 5, according to Equation 1 (Laosuwan et al., 2017; Rotjanakusol & Laosuwan, 2018).

$$P\lambda = \frac{P\lambda'}{\sin(\theta_{SE})} = \frac{M_p Q_{cal} + A_p}{\sin(\theta_{SE})} \tag{1}$$

Where;

$P\lambda$ = Planetary TOA reflectance (unitless)

M_p = Reflectance Multi band of band 4 and band 5

Q_{cal} = Digital Number (DN) of band 4 and band 5

A_p = Reflectance add band of band 4 and band 5

θ_{SE} = Sun elevation of band 4 and band 5

2.2 Data Processing

2.2.1 Normalized Difference Vegetation Index (NDVI)

NDVI is a value indicating the proportion of vegetation that covers the earth's surface. NDVI can be obtained from bringing near infrared wavelength and red visible wavelengths reflected from the earth's surface to calculate the difference of reflections. The values of NDVI will display in the range of -1 and +1, which can be calculated according to Equation 2 (Ogunode & Akombelwa, 2017; Rotjanakusol & Laosuwan, 2019). From Equation 2, it can be explained that the NDVI value approaching 0 means that the area is slightly covered with vegetation. While the NDVI value approaching +1 means that the area is densely covered with vegetation.

$$NDVI = \frac{NIR\text{-}RED}{NIR\text{+}RED} \qquad (2)$$

Where;
    NIR = Reflection in the near-infrared spectrum
    RED = Reflection in the red range of the spectrum

2.2.2 Measuring atmospheric temperature

The data from the air temperature measurement and positions were used for spatial interpolation by using ordinary kriging methods to spread the data across the study area and used the equation model for spherical considerations (Al-Mashagbah et al., 2012; Xia et al., 2014; Ruthirako, 2016). The size of the UHI phenomenon in each period could be calculated according to Equation 3 (Oke, 1982; United States. Environmental Protection Agency, 2008; Miles & Esau, 2017).

$$\Delta T = T_U\text{-}T_r \qquad (3)$$

Where;
    T_U =   Average temperature within the boundary of the designated

    T_r = Average temperature of the boundary near the boundary of the boundary of the city

according to the outside or the rural area

2.2.3 Creating buffer zones

This research created buffer zones at equal distances in every 200 m in all directions of the study area. The distances were determined away from the boundary in the range of 200 - 800m (**Fig**. **3** and **Table 1**), which led to spatial display for analysis of NDVI and UHI sizes in the atmosphere that occurred in each period.

NDVI and UHI sizes in the atmosphere was conducted by determining direction of the relationship of data from correlation coefficient (r) at a significance level of 0.01, according to Equation 4. This was consistent with the trend line of linear regression equation that led to the acquisition of decision coefficient (r^2) (Oyler et al., 2016; Liu et al., 2019; Panek, & Gozdowski, 2019).

$$r = \frac{\Sigma(X_i\text{-}\overline{X})\,(Y_i\text{-}\overline{Y})}{\sqrt{\Sigma(X_i\text{-}\overline{X})^2\,\Sigma(Y_i\text{-}\overline{Y})^2}} \qquad (4)$$

Where;
The value r = 1 means a perfect positive correlation and
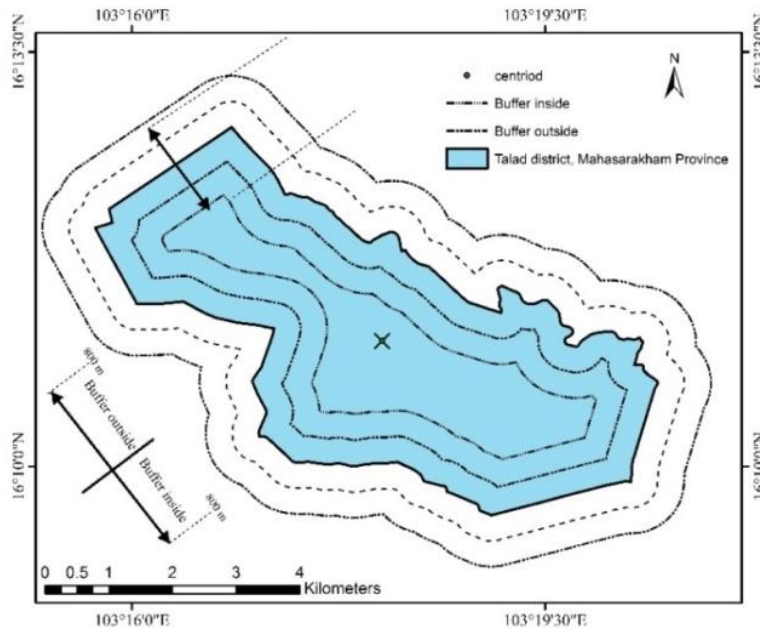The value r = -1 means a perfect negative correlation.

Fig. 3. Illustration boundary areas of collisions based on the boundary of Mueang Maha Sarakham Municipality, each with their common centroid points.

Table 1.

Buffer area.

Arbitrary buffer	Distance (m)	Area (km²)
Buffer outside	800	45.20
	600	39.65
	400	34.28
	200	29.06
	0	23.92
Buffer inside	200	19.02
	400	14.64
	600	10.64
	800	7.00

3. RESULTS AND DISCUSSIONS

3.1 Results of NDVI analysis and buffer zones

The results of NDVI values (**Fig**. **4** and **Table 2**) indicated that the rate of vegetation cover tended to decrease from the outer areas to inner areas. This can be remarked that the boundary of Mueang Maha Sarakham Municipality had a dense rate of land uses.
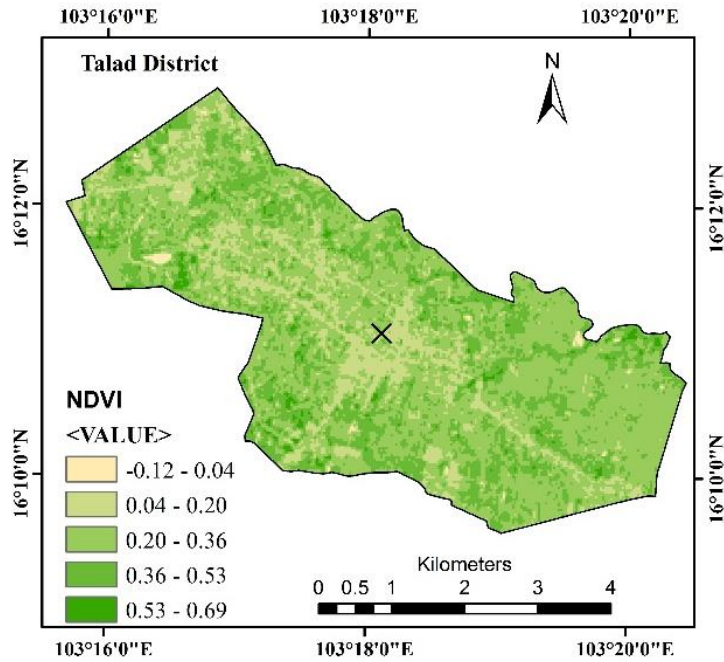
Fig. 4. NDVI covering Mueang Maha Sarakham Municipality.

As a result, the cover of the green spaces was sparse, especially around the centroid point. From determining the boundary for consideration around the centroid point covering an area of 7 km², it indicated NDVI of 0.28, which represented the area at the level of low to medium vegetation cover (Taufik et al., 2016; Hashim et al., 2019).

Table 2.

Average of NDVI by buffer area.

Area (km²)	NDVI
45.20	0.3123
39.65	0.3133
34.28	0.3139
29.06	0.3120
23.92	0.3074
19.02	0.3026
14.64	0.2973
10.64	0.2896
7.00	0.2801

3.2 Analysis results of UHI size in the atmosphere

From the analysis of the difference of air temperatures between inner and outer urban areas at the same time period and spatial interpolation on the atmospheric temperatures from the sample group using the ordinary kriging technique, the expansion of atmospheric temperature in Mueang Maha Sarakham Municipality area was shown in **Fig. 5** and **Fig. 6**.
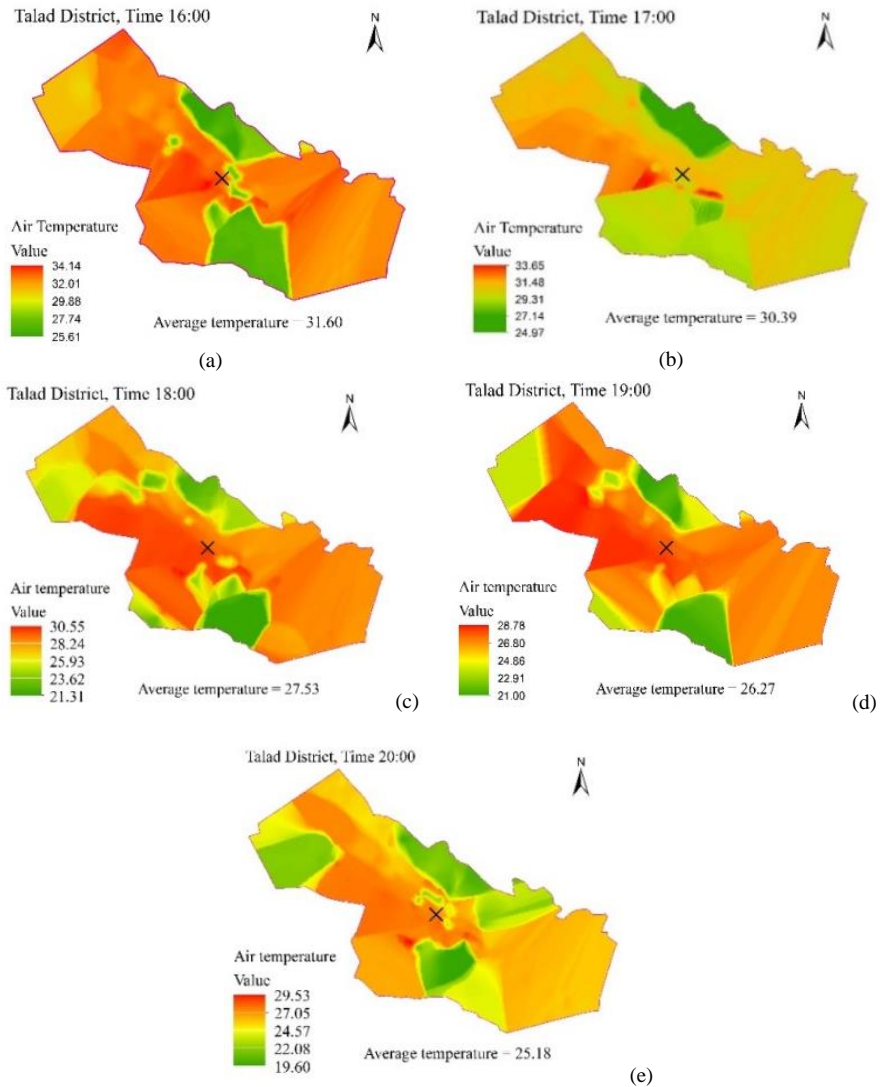
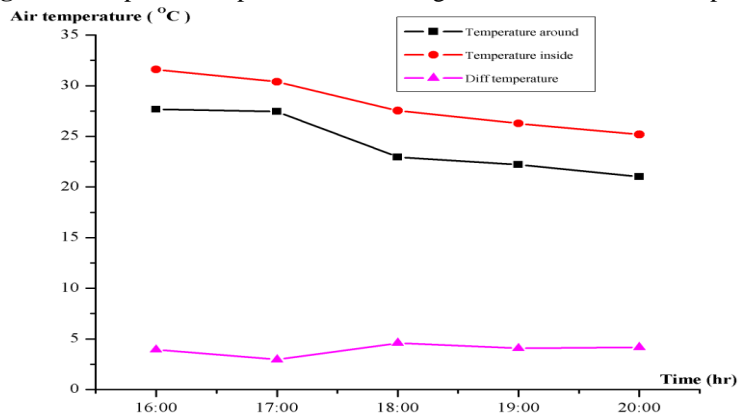**Fig. 5.** Atmospheric temperature in Mueang Maha Sarakham Municipality.

Fig. 6. The trend of changes in the average temperature of each period and the size of the UHI in the atmosphere.

The temperatures in both areas tended to decrease after 17.00 hrs. The outer areas clearly showed the decrease rate of air temperature clearly while the inner areas of the study area still showed higher average air temperature. In addition, during 17.00 - 18.00 hrs., the air temperature in the outer areas changed about 4.5°C while the inner areas decreased by 2.8°C. From the graph, the largest UHI size in the most atmosphere was at 4.58°C during 18.00hrs. The UHI size was still high during 2 00.hrs. with the rate reduced less than 1°C, while the outer areas of the study area indicated the decrease rate of temperatures by approximately 2°C.

3.3 The relationship between NDVI according to the buffer zones and UHI sizes in the atmosphere

The relationship between NDVI according to the buffer zones and the UHI size in the atmosphere can be shown in **Fig. 7**, **Fig. 8** and **Table 3**. The graph in **Fig.7** shows the change of the UHI sizes in the atmosphere along the buffer line areas. It was found that every time period tended to be in the same direction, which represented the negative relationship between data at a significance level of 0.01 and relatively high correlation coefficient (r) and decision coefficient (r^2).
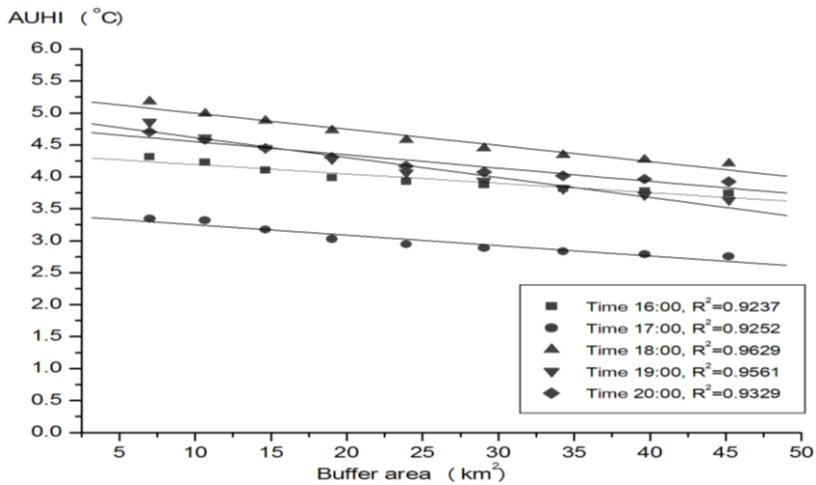

Fig. 7. UHI size in each area of the buffer line areas.
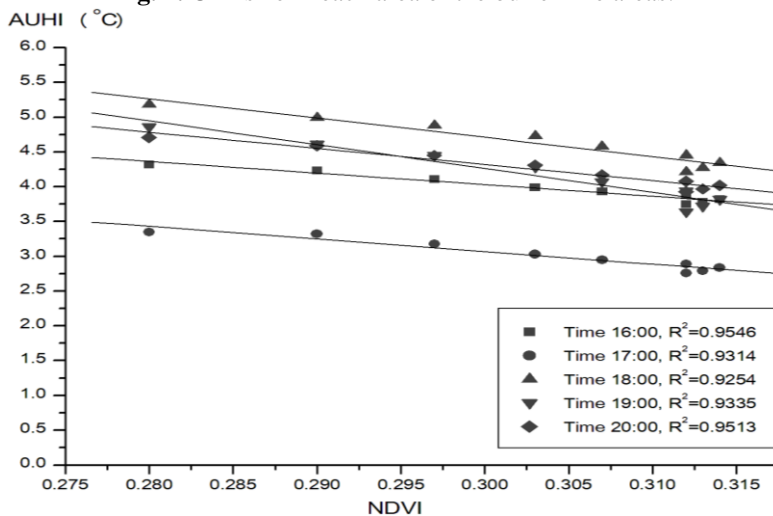

Fig. 8. Decision coefficient from every period.

The average linear regression equations from all time periods were equal to -0.9696 and 0.9402, respectively. Also, when the rate of vegetation decreased along the buffer zone, it caused the higher air temperature that resulted in larger UHI size in the atmosphere as well.

The average correlation coefficient (r) and decision coefficient (r^2) from every period of the graph in **figure 8** were equal to -0.9691 and 0.9392, respectively. While considering the period with the largest UHI size and the linear regression equation $Y = 5.25331 - 0.02529 * X$ and $Y_1 = 12.97746 - 27.55394 * X_1$, when the boundary around the centroid point covered the smallest area of 7 km^2, it was found that the UHI size in the atmosphere was 5.08ºC and NDVI was .0.286At the same time period, the areas in Mueang Maha Sarakham Municipality indicated UHI and NDVI values of 4.65ºC and 0.302, respectively. From the regression equation in the relationship between UHI sizes and the buffer zones, if the distance to the centroid point was determined at 0.001 km^2 (very small compared to the size of the whole study area or approaching zero) during 18.00 hrs., the maximum heat point indicated at 5.25ºC. From the survey of reflection of the electromagnetic wave for checking existence of vegetation (Fig. 4), it was found that the values in the pixel covered the same coordinates represented NDVI value of 0.16, which means that there was very little vegetation cover in such the pixel.

In this research, considering in the concept of ideology, if the boundary of Mueang Maha Sarakham Municipality was covered with dense vegetation in the whole area, the tendency of the air temperature in the area was close to the surrounding area, which did not show UHI clearly. However, if the area has the increase in land uses, it will cause the change in air temperature. From the linear regression equation set ($Y_1 = b_1 + a_1X_1$), it was found that if Mueang Maha Sarakham Municipality area has developed and expanded structures for the whole area, it will cause the decrease of vegetation cover gradually until completely. And if the existence of vegetation and water resources in the area was equal to zero ($X_1 = 0$), the difference in air temperatures approximately 18.00hrs. was equal to 12.98ºC and increased to the highest air temperatures approximately 19.00 hrs. at 14.55ºC. After that, the air temperatures began to decrease until it reached equilibrium onwards. This indicated that NDVI that tended to decrease in the study area caused the increase in air temperature in urban areas. Also, the time period that showed the largest UHI size would change. In addition, this research had tested the trend of UHI changes in urban areas during 16.00 - 20.00 hrs. from the linear regression equation set ($Y_1 = b_1 + a_1X_1$) in case that the study area had decreased NDVI.

Table 3.

Linear regression equation.

Period	UHI size in each area of the buffer line areas Y = b + aX	Standard deviation	UHI size with NDVI in each area $Y_1 = b_1 + a_1X_1$	Standard deviation
16:00	Y = 4.34307 - 0.01467 * X	0.05962	$Y_1 = 9.00329 - 16.57611 * X_1$	0.04599
17:00	Y = 3.41526 - 0.01624 * X	0.06529	$Y_1 = 8.50039 - 18.10612 * X_1$	0.06252
18:00	Y = 5.25331 - 0.02529 * X	0.07013	$Y_1 = 12.97746 - 27.55394*X_1$	0.09951
19:00	Y = 4.92949 - 0.03122 * X	0.09456	$Y_1 = 14.5475 - 34.28796 * X_1$	0.11645
20:00	Y = 4.76042 - 0.02065 * X	0.07829	$Y_1 = 11.2732 - 23.17772 * X_1$	0.06672

The graph in **figure 9** represents the best polynomial regression trend line in the form of the fourth power of the UHI size in the atmosphere in each time period with unequal NDVI values. The results showed that the maximum UHI formation was found between 18.00 - 19.00 hrs. The trend of the decrease in vegetation will result in the increase in UHI size in each period. And when the NDVI value in the area of Mueang Maha Sarakham Municipality was less than 0.30, it can be seen the time period which represented the change of the largest UHI size in the atmosphere, which was likely to approach the period of 19.00 hrs.
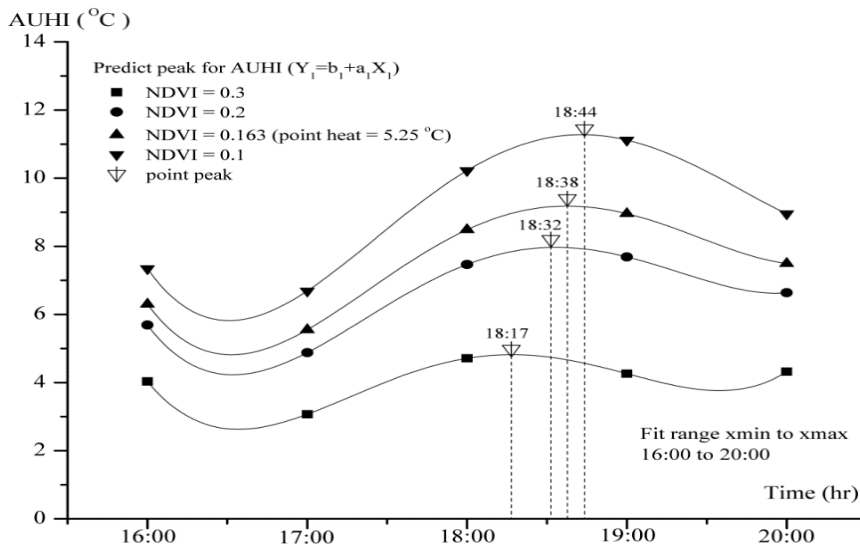
Fig. 9. Polynomial quartic function trend of UHI size change between 16.00 hrs to 20.00 hrs in Mueang Maha Sarakham Municipality when NDVI decreased

4. CONCLUSIONS

The study of air temperatures in the area of Mueang Maha Sarakham Municipality could be found as follows: Throughout the period of 16.00-20.00 hrs., the air temperatures inside the study area tended to be higher than the outer area, which had more dense vegetation cover than the inner area that helped decrease the air temperature. While the area within Mueang Maha Sarakham Municipality showed a slight decrease in temperature, especially in the most inner area of the buffer zone. Therefore, the largest UHI size was displayed in the atmosphere during 18.00 hrs. The trend of air temperature changes in both areas and UHI sizes occurred were in accordance with the study. The relationship of the UHI phenomenon in each buffer zone towards the study area represented the decrease of NDVI that resulted in the increasing trend of air temperature in each area. From the linear regression relationship, it was found that the area of Mueang Maha Sarakham Municipality had the largest UHI size in the atmosphere at 4.65°C and the boundary around the centroid point covering a minimum area of 7 km^2 was equal to 5.08°C.

From the correlation of data between UHI sizes and NDVI values in each buffer zone, all time periods tended to be in the same direction, which represented a negative relationship and obtained the average coefficient of decision (r^2) from every time period at 0.9392. The decrease of NDVI caused the difference in air temperatures in urban areas and surrounding areas. From the prediction of difference in air temperatures by using linear regression equation set in Mueang Maha Sarakham Municipality, it was found that UHI sizes at all time periods increased in accordance with the decrease in NDVI values. Meanwhile, when considering the trend of changes in UHI values in the atmosphere with polynomial regression (degree 4), it represented the highest formation rate of UHI during 18.00 - 19.00 hrs. In other words, if each buffer zone had reduced NDVI values or approaching zero, it will obtain the time period that represents the difference in highest air temperature with a tendency of approaching the period of 19.00 hrs.

ACKNOWLEDGEMENTS

R E F E R E N C E S

Al-Mashagbah, A., Al-Adamat, R. & Salameh, E. (2012). The use of Kriging Techniques with in GIS Environment to Investigate Groundwater Quality in the Amman-Zarqa Basin/Jordan. *Research Journal of Environmental and Earth Sciences*. 4(2), 177-185.

Buttstadt, M., Sachsen, T., Ketzler, G., Merbitz, H. & Schneider, C. (2011). A new approach for highly resolved air temperature measurements in urban areas. *Atmos. Meas. Tech. Discuss*. 4, 1001-1019.

Cardoso, R.S., & Amorim, M.C.C.T. (2018). Urban heat island analysis using the 'local climate zone' scheme in Presidente Prudente, Brazil. *Investigaciones Geográficas*, 69, 107-118.

Dupont, S., & Ching, J. (2004). Implementation of an Urban Canopy Parameterization in a Mesoscale Meteorological Model. *Journal of Applied Meteorology*. 43(11), 1648-1665.

Grover, A., & Singh, R.B. (2015) . Analysis of Urban Heat Island (UHI) in Relation to Normalized Difference Vegetation Index (NDVI): A Comparative Study of Delhi and Mumbai. *Environments,* 2, 125-138.

Gopal, S., & Kaufmann, R. (2000). Spatial Interpolation of Surface Air Temperatures Using Artificial Neural Networks: Evaluating Their Use for Downscaling GCMs. *Journal of Climate*, 13,886-895.

Hashim, H., Abd Latif, Z. & Adnan, A.N. (2019) .Urban Vegetation Classification with NDVI Threshold Value Method with Very High Resolution (VHR) Pleiades Imagery. *Remote Sensing and Spatial Information Sciences*, Volume XLII-/4W16, 237-240.

Huang, Q., & Lu, Y. (2017). Urban heat island research from 1991 to 2015: a bibliometric analysis. *Theoretical and Applied Climatology,* 131, 1055-1067.

IPCC .(2019). *An IPCC Special Report on climate change, desertification, land degradation, sustainable land management, food security, and greenhouse gas fluxes in terrestrial ecosystems* (ISBN 978-92-9169-154-8) Retrieved from https://www.ipcc.ch/site/ assets/uploads/sites//02/2020/4SPM_Updated-Jan.20pdf

Kambi, M., Wang, Z., & Gulemvuga, G. (2018). Determination of the Correlation between the Air Temperature Measured in Situ and Remotely Sensed Data from MODIS and SEVIRI in Congo-Brazzaville *Atmospheric and Climate Sciences*, 8(2), 192-211.

Kaplan, G., Avdan, U., & Avdan, Z.Y. (2018). Urban Heat Island Analysis Using the Landsat 8 Satellite Data: A Case Study in Skopje, Macedonia. *Proceedings of The 2nd International Electronic Conference on Remote Sensing*, 2(7), 1-5.

Kophim, W. (2013). *Impacts of Land Use and Land Cover Toward Surface Urban Heat Island in Bangkok Metropolitan*. (Master of Science). Mahanakorn University, Bangkok.

Liu, H., Zhou, Q., Zhang, S., & Deng, X. (2019). Estimation of Summer Air Temperature over China Using Himawari-8 AHI and Numerical Weather Prediction Data. *Advances in Meteorology*. Article ID 2385310, 10 pages. Retrieved from https://doi.org/10.1155/2019/2385310

Li, X., Zhou, W., & Ouyang, Z. (2013). Relationship between land surface temperature and spatial pattern of greenspace: What are the effects of spatial resolution?. *Landscape and Urban Planning*. 114, 1-8.

Laosuwan, T., Gomasathit, T., & Rotjanakusol, T. (2017). Application of Remote Sensing for Temperature Monitoring: The Technique for Land Surface Temperature Analysis. *Journal of Ecological Engineering*, 18 (3), 53-60.

Mathew, A., Khandelwal, S., & Kaul, N. (2017). Investigating spatial and seasonal variations of urban heat island effect over Jaipur city and its relationship with vegetation, urbanization and elevation parameters. *Sustainable Cities and Society*, 35, 157-177.

Miles, V., & Esau, I. (2017). Seasonal and Spatial Characteristics of Urban Heat Islands (UHIs) in NorthernWest Siberian Cities. *Remote sensing*, 9(10), 1-15.

Mukhelif, A., Al.Ammar, K., & Al.Jooburi, M. (2016). The Seasonal Variation of the Urban Heat Island Effect and Estimating the Human – Discomfort Index at the City of Hillah. *Pure and Applied Sciences*, 24(2), 423-434.

Official Statistics Registration Systems. (2019). Number of citizens of Thailand. Retrieved from http://stat.bora.dopa.go.th/stat/pk/pk_62.pdf

Ogunode, A., & Akombelwa, M. (2017). An algorithm to retrieve Land Surface Temperature using Landsat-8 Dataset. *South African Journal of Geomatics*, 6(2), 262-276.

Oyler, J.W., Dobrowski, Z.A., Holden, Z.A. and Running, S. (2016). Remotely Sensed Land Skin Temperature as a Spatial Predictor of Air Temperature across the Conterminous United States. *Journal of Applied Meteorology and Climatology*, 55(7), 1441-1457.

Oke, T. R., (1982). The energetic basis of the urban heat island. *Quart. J. R. Met. Soc*. 108, 1-24.

Panek, E., & Gozdowski, D. (2019). Analysis of relationship between cereal yield and NDVI for selected regions of Central Europe based on MODIS satellite data. *Remote Sensing Applications: Society and Environment*, 17, 1-11.

Perini, K., & Magliocco, A. (2014). Effects of vegetation, urban density, building height, and atmospheric conditions on local temperatures and thermal comfort. *Urban Forestry & Urban Greening*, 13(3), 495-506.

Rotjanakusol, T., & Laosuwan, T. (2018). Estimation of Land Surface Temperature using Landsat Satellite Data: A Case Study of Mueang Maha Sarakham District, Maha Sarakham Province, Thailand for the Years 2006 and 2015. *Scientific Review Engineering and Environmental Sciences*, 27 (4),401-409.

Rotjanakusol,T., & Laosuwan, T. (2019). An Investigation of Drought around Chi Watershed during Ten-year Period using Terra/modis Data. *Geographia Technica,* 14(2), 74-83.

Ruthirako, P. (2016). Application of Geo-information Technology to Study Urban Heat Island Phenomenon. *SDU Research Journal*, 9(3), 147-163.

Sharifi, E., & Soltani, A. (2017). Patterns of Urban Heat Island Effect in Adelaide: A Mobile Traverse Experiment. *Modern Applied Science*, 11(4), 80-90.

Sodoudi, S., Shahmohamadi, P., Vollack, K., Cubasch, U., & Che-Ani, A.I. (2014). Mitigating the Urban Heat Island Effect in Megacity Tehran. Advances in Meteorology. *Advances in Meteorology*. Article ID 547974, 19 p.

Singhachantra, B. (2012). *Analysis of the Relation Between Land Covers and Urban Heat Island in Chiang Mai Municipal Area*. (Master of Engineering). Chiang Mai University, Chiang Mai.

Srivanit, M., & Hokao, K. (2012). Thermal Infrared Remote Sensing for Urban Climate and Environmental Studies: An Application for the City of Bangkok, Thailand. *Journal of Architectural/Planning Research and Studies,* 9(1), 83-100.

Thai Meteorological Department. (2019). *Weather summary (monthly).* Retrieved from http://www.climate. tmd.go.th/content/category/file

Taufik, A., Ahmad, S., & Ahmad, A. (2016). Classification of Landsat 8 Satellite Data Using NDVI Thresholds. *Journal of Telecommunication, Electronic and Computer Engineering*, 8, 37-40.

Takebayashi, H., & Moriyama, M. (2009). Study on the urban heat island mitigation effect achieved by converting to grass-covered parking. *Solar Energy*, 83(8), 1211-1223.

United States. Environmental Protection Agency. (2008). Urban Heat Island Basics. In U.S. Environmental Protection Agency (Eds.), Reducing urban heat islands: Compendium of strategies (1st., pp. 1-16) Retrieved from https://www.epa.gov/heat-islands/heat-island-compendium

Ursu, C. (2019). The Land Surface Temperature Evolution (LST) using Landsat Scenes. Case Study: The Industrial Platform Săvinești, *Geographia Technica,* 14(2), 131-142.

Vicente-Serrano, S., Cuadrat-Prats, J., & Saz-Sánchez, M. (2005). Spatial patterns of the urban heat island in Zaragoza (Spain). *Climate Research*, 30, 61-69.

Xia, B., Ren, Z., & Koh, C.S. (2014). An Adaptive Optimization Algorithm Based on Kriging Interpolation with Spherical Model and its Application to Optimal Design of Switched Reluctance Motor. *J Electr Eng Technol*, 9(5), 1544-1550.

Yang, Y., Zhang, X., Lu, X., Hu, J., Pan, X., Zhu Q., & Su, W. (2018). Effects of Building Design Elements on Residential Thermal Environment. *Sustainability*, 10(1), 1-15.

Yokobori, T., & Ohta, S. (2009). Effect of land cover on air temperatures involved in the development of an intra-urban heat island. *Climate Research*, 39, 61-73.

Zhang, X.X., Wu, P.F., & Chen, B. (2010). Relationship between vegetation greenness and urban heat island effect in Beijing City of China. *Procedia Environmental Sciences*, 2, 1438-1450.

Aims and Scope

Geographia Technica is a journal devoted to the publication of all papers on all aspects of the use of technical and quantitative methods in geographical research. It aims at presenting its readers with the latest developments in G.I.S technology, mathematical methods applicable to any field of geography, territorial micro-scalar and laboratory experiments, and the latest developments induced by the measurement techniques to the geographical research.

Geographia Technica is dedicated to all those who understand that nowadays every field of geography can only be described by specific numerical values, variables both oftime and space which require the sort of numerical analysis only possible with the aid of technical and quantitative methods offered by powerful computers and dedicated software.

Our understanding of *Geographia Technica* expands the concept of technical methods applied to geography to its broadest sense and for that, papers of different interests such as: G.I.S, Spatial Analysis, Remote Sensing, Cartography or Geostatistics as well as papers which, by promoting the above mentioned directions bring a technical approach in the fields of hydrology, climatology, geomorphology, human geography territorial planning are more than welcomed provided they are of sufficient wide interest and relevance.

Targeted readers:

The publication intends to serve workers in academia, industry and government.
Students, teachers, researchers and practitioners should benefit from the ideas in the journal.

Guide for Authors

Submission

Articles and proposals for articles are accepted for consideration on the understanding that they are not being submitted elsewhere.

The publication proposals that satisfy the conditions for originality, relevance for the new technical geography domain and editorial requirements, will be sent by email to the address editorial-secretary@technicalgeography.org.

This page can be accessed to see the requirements for editing an article, and also the articles from the journal archive found on www.technicalgeography.org can be used as a guide.

Content

In addition to full-length research contributions, the journal also publishes Short Notes, Book reviews, Software Reviews, Letters of the Editor. However the editors wish to point out that the views expressed in the book reviews are the personal opinion of the reviewer and do not necessarily reflect the views of the publishers.

Each year two volumes are scheduled for publication. Papers in English or French are accepted. The articles are printed in full color. A part of the articles are available as full text on the www.technicalgeography.org website. The link between the author and reviewers is mediated by the Editor.

Peer Review Process

The papers submitted for publication to the Editor undergo an anonymous peer review process, necessary for assessing the quality of scientific information, the relevance to the technical geography field and the publishing requirements of our journal.

The contents are reviewed by two members of the Editorial Board or other reviewers on a simple blind review system. The reviewer's comments for the improvement of the paper will be sent to the corresponding author by the editor. After the author changes the paper according to the comments, the article is published in the next number of the journal.

Eventual paper rejections will have solid arguments, but sending the paper only to receive the comments of the reviewers is discouraged. Authors are notified by e-mail about the status of the submitted articles and the whole process takes about 3-4 months from the date of the article submission.